Utrecht University

Institute for Theoretical Physics

Master's Thesis

Phase transitions of the Swedenborgite antiferromagnet & quasiparticle interference in a topological insulator

Author:
G.A.R. van Dalum

Supervisor:
Dr. L. Fritz

September 2015 - June 2016

Universiteit Utrecht

Abstract

In this thesis, we study two separate subjects. First, we examine phase transitions of the antiferromagnetic Heisenberg model on the Swedenborgite lattice. This three-dimensional model contains two different interactions, and there is a critical ratio of these interaction strengths that separates a region with a unique ground state from a region where geometric frustration prevents the existence of such a ground state. First, we explain the possible phase transitions in these different regions by means of phenomenological Landau theory and mean-field theory. Afterwards, a spin wave analysis is performed that shows how thermal fluctuations can destroy the unique ground state. In the vicinity of the critical ratio, we find that the critical temperature that separates the unique ground state from a disordered phase scales linearly with the ratio of interaction strengths. This successfully completes an important section of the phase diagram of this model.

The second part covers quasiparticle interference in the Cu doped topological insulator Bi_2Te_3. The effects of impurity scattering are calculated using an effective low-energy tight-binding model, along with a single local surface impurity. We find two distinct six-fold rotationally symmetric scattering patterns corresponding to two different energy windows. A comparison with the band structure of the system suggests that this distinction is caused by the interplay between edge states among themselves and with the conduction band. We also find that the symmetry and rotational orientation of the model results are in good agreement with experiments. However, this requires a special type of impurity that only couples to the electrons from a single orbital.

Acknowledgements

I would like to take this opportunity to thank some people. First of all, I thank Tycho, for showing continuous interest in my research, and for organizing the useful weekly meetings. I also thank Andrew for the several helpful discussions we shared on the topic of quasiparticle interference. Furthermore, I am grateful to my fellow Master's students, who made the past year a blast. However, most of all I would like to thank my supervisor Lars, for his lasting support, for our frequent motivating discussions, and for being a great supervisor. I could not have done all of this on my own.

Contents

Abstract iii

Acknowledgements iv

I Phase transitions of the antiferromagnetic Heisenberg model on the Swedenborgite lattice 1

1 Introduction to Part I 3
1.1 Classical spin models and frustration . . . 4
1.2 Triangular, Kagomé and Swedenborgite lattices . . . 6
1.3 The Swedenborgite antiferromagnetic Heisenberg model . . . 9
1.4 Phase transition in the $J_2/J_1 \to 3/2$ limit . . . 11

2 Phenomenological Landau theory 13
2.1 The distorted triangular lattice . . . 15
2.1.1 Order parameters . . . 18
2.1.2 Symmetry and the construction of the Landau free energy . . . 20
2.1.3 Primary and secondary order parameters . . . 21
2.2 Landau theory of the Swedenborgite antiferromagnet . . . 23
2.2.1 Octupolar ordering and its absence . . . 24

3 Mean-field theory 26
3.1 Mean-field methods applied to the Heisenberg antiferromagnet on the triangular lattice . 26
3.1.1 A simple mean-field approximation . . . 26
3.1.2 Variational mean-field theory . . . 28
3.1.3 Mean-field approximation using a Hubbard-Stratonovich transformation and the relation with Landau theory . . . 30
3.2 Variational mean-field theory revisited . . . 33
3.2.1 Real space free energy . . . 33
3.2.2 Momentum space free energy . . . 34
3.2.3 A final look at the triangular lattice . . . 36
3.3 Mean-field critical temperature of the Swedenborgite antiferromagnet . . . 37
3.4 Failure of mean-field theory . . . 39

4 Spin waves of the Swedenborgite antiferromagnet 42
4.1 Spin wave Hamiltonian . . . 42
4.1.1 Real space Hamiltonian . . . 42
4.1.2 Momentum space Hamiltonian . . . 44
4.1.3 On the relevance of odd order terms . . . 46
4.2 Lowest order approximation of T_c . . . 47
4.3 Higher order contributions . . . 51
4.3.1 Quadratic corrections to the Hamiltonian . . . 52
4.3.2 Direct perturbation theory of the correlation functions . . . 55
4.4 Conclusions and outlook . . . 56

II Quasiparticle interference in a topological insulator 59

5 Introduction to Part II 61
5.1 Tight-binding models and electronic band structure . . . 61
5.1.1 The square lattice tight-binding model . . . 62
5.1.2 Band theory, electrical properties and topological insulators . . . 63
5.1.3 Mapping complicated models to a square lattice . . . 65
5.2 Green's functions and the density of states . . . 68
5.3 Impurity scattering and quasiparticle interference . . . 70

6 Model description of quasiparticle interference in the topological insulator $Cu_xBi_2Te_3$ 74
6.1 The model Hamiltonian . . . 74
6.2 Methods and results . . . 77
6.3 Discussion . . . 81
6.4 Conclusions and outlook . . . 83

Appendix 85
A.1 Comments on the Monte Carlo simulations . . . 85
A.2 Additional simulation results . . . 86
A.3 Gaussian integrals . . . 88
A.4 Wick's theorem . . . 89
A.5 Perturbation theory and Feynman diagrams . . . 90
B.1 Tight-binding band structure of graphene . . . 93
B.2 Efficient iterative methods for the numerical calculation of surface Green's functions . . . 96

Bibliography 101

Part I

Phase transitions of the antiferromagnetic Heisenberg model on the Swedenborgite lattice

Chapter 1

Introduction to Part I

Over the last century, phase transitions of magnetic materials have received a lot of scientific attention, both theoretically and experimentally. Magnetic properties arise from the underlying lattice structure of such a material, in combination with the interactions between the spins residing on the lattice sites. This interplay between geometry and interactions may lead to different forms of magnetism, for example paramagnetism, ferromagnetism, or antiferromagnetism. The exact properties of a magnet also depend on the temperature of the system, resulting in the emergence of phase transitions at certain temperatures. However, in some situations the interactions between the spins may be incompatible with one another, and the system is said to be frustrated. Magnetically frustrated materials often have extensively degenerate ground states, and they lead to the existence of phases not encountered in conventional non-frustrated materials. An example of such an unusual phase is called a spin-liquid phase. A spin-liquid phase lacks long-range order of any type, much like how liquid water is disordered compared to frozen water. For example, fluctuations between the many degenerate configurations that might make up a spin-liquid phase allow the lack of long-range order to extend to much lower temperatures than it would in absence of frustration [1].

On a theoretical level, much research has been done on frustrated systems, for example on the Heisenberg Kagomé antiferromagnet [2]. Especially classical systems are often found to display a spin-liquid phase. However, it was only recently that the first experimental evidence of spin liquids has been found: in 2012, Han *et al.* [3] found that the material Herbertsmithite, $ZnCu_3(OD)_6Cl$, has key features that are characteristic to spin liquids. The reason for this late discovery is that real systems have a quantum nature, and the ground state degeneracy of frustrated magnets is often easily lifted by small internal or external perturbations. Another class of materials that shows promise for experimental observation of magnetic frustration are the so-called Swedenborgites. The advantage of these materials is the ability to tune their properties by chemical substitution of some of the components. Motivated by the potential experimental relevance, this work will build on the prior theoretical study of classical frustrated magnetism of Swedenborgites by Buhrandt [4].

The remainder of this chapter will first cover the important concepts related to classical spin models and frustrated magnetism. Then, the triangular lattice and the Kagomé lattice will be introduced and described, leading to the Swedenborgite lattice. Afterwards, we will review the possible ground states and the phase diagram of the antiferromagnetic Heisenberg model on the Swedenborgite lattice, which is the model that is the main topic of interest of this part of the thesis. Finally, we will discuss the unanswered questions regarding this model; these will define the main goals of this work.

In Ch. 2, we cover the phenomenological Landau theory that will give us a better qualitative understanding of the phase transitions that are encountered on the Swedenborgite antiferromagnetic Heisenberg model. In order to do so, we first discuss the concepts of phenomenological Landau theory in general. Then, Landau theory will be applied to a simpler model: the antiferromagnetic Heisenberg model on a distorted triangular lattice. The analysis of the distorted triangular lattice will be supported by Monte Carlo simulations, and the results from this model will be generalized to construct a Landau free energy for the Swedenborgite lattice.

In Ch. 3, mean-field theory will be discussed in an attempt to describe the phase transitions of the models of interest in a microscopic way. The chapter starts with a mean-field analysis of the (undistorted)

triangular lattice. Subsequently, a general framework for variational mean-field theory is discussed and then applied to the Swedenborgite lattice. This leads to a mean-field description of the relevant phase transitions. However, we will see that this mean-field description disagrees both with simulations and with the exact theoretical analysis of the model from Ch. 1. The reasons for this will be discussed at the end of Ch. 3.

Finally, Ch. 4 will cover an analysis of spin waves about the unique ground state of the Swedenborgite antiferromagnet. This will allow us to estimate the critical temperature that separates the unique ground state from a disordered phase. This critical temperature will be determined to lowest order, which will reveal the part of the phase diagram that was previously unknown. Then, higher order spin wave contributions will be discussed by describing them as quadratic corrections to the Hamiltonian, and by performing direct perturbation theory of the correlation functions. At the end of this chapter, we wrap up this first part of the thesis by discussing the conclusions.

1.1 Classical spin models and frustration

Spin models provide a successful way to explain magnetism. These models describe a material as a lattice of atoms, each of which carries its own magnetic dipole moment, a quantity that arises from the spin that it carries. Interactions between these dipole moments, and consequently the spins, are responsible for the magnetic properties of the material. Classically, the spins can be described by n-dimensional unit vectors, rather than quantum mechanical operators. Using this description, magnetic properties can be described in the following way. If the interactions between spins are for example ferromagnetic, then it is energetically favourable for different spins to point in the same direction. Hence at low temperature (when the system will occupy the ground state) all spins are aligned and the material becomes *ferromagnetic*. On the other hand, at high temperatures thermal fluctuations will become strong enough to destroy this ferromagnetic ordering and the spins will point in random directions, such that the system becomes disordered. However, applying a strong enough external magnetic field can still force the spins to point in a specific direction, so the material is now *paramagnetic*. The temperature at which the transition between these two phases happens is called the *critical temperature* T_c. In addition to successfully explaining magnetism, spin models also prove to be excellent models to study phase transitions and critical phenomena in general.

The above example focuses on ferromagnetic interactions. Another possible type of interactions are *antiferromagnetic* interactions, where it is energetically favourable for two interacting spins to point in the opposite direction. This kind of interaction can give rise to the concept of *magnetic frustration* [5]. A system is said to be magnetically frustrated if it is unable to satisfy all interactions simultaneously. Frustrated systems often have a highly degenerate ground state, and they allow for interesting phases and behaviour that would not appear in systems that are not frustrated. There are two ways for magnetic frustration to appear, which we will now explain at the hand of examples.

The simplest (but still remarkably useful) spin models are restricted to interactions between nearest neighbour lattice sites. One such nearest neighbour spin model is the Ising model. This model considers spins as one-dimensional unit vectors, so each spin can either take the value $+1$ or -1. Explicitly, this model is described by the Hamiltonian

$$H = J \sum_{\langle i,j \rangle} S_i S_j, \tag{1.1}$$

where $\langle i, j \rangle$ denotes all nearest neighbour pairs on the lattice, S_i is the spin on lattice site i, and J is the coupling constant. Note that the size and units of the spins are absorbed into J, and that J can be negative (ferromagnetic) or positive (antiferromagnetic). In the former situation, there are two ground states: either all spins point up (i.e. they all assume the value $S_i = +1$), or they all point down ($S_i = -1$). However, these two states are simply an $O(1)$ rotation of one another, and we refer to them as a single unique ground state, where "unique" now implicitly means "unique up to global $O(1)$ rotations". If on the other hand J is positive, it depends on the underlying lattice what the ground states are and how many of them exist. It is very well possible that the ground state is still unique, for example on a one-dimensional chain: then the spins simply alternate between up and down, and all interactions are satisfied. However, one can also imagine lattices on which this will not work, such as a single equilateral triangle, which is detailed in Fig. 1.1. On a single triangle, it is impossible for all three pairs to be

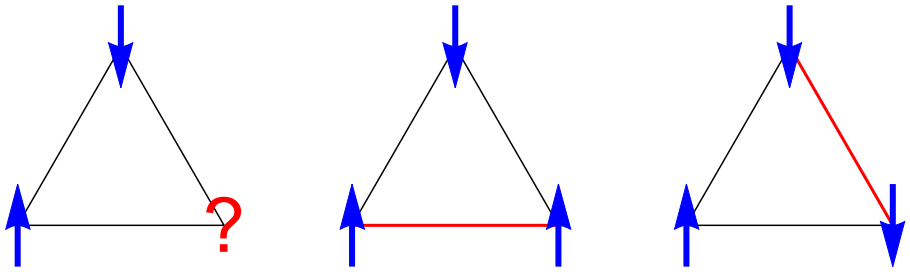

Figure 1.1: Geometric frustration of the antiferromagnetic Ising model on a single triangle. Once two spins are chosen anti-parallel, the third spin can no longer be picked such that all antiferromagnetic interactions are satisfied. Unsatisfied bonds are signified by red lines.

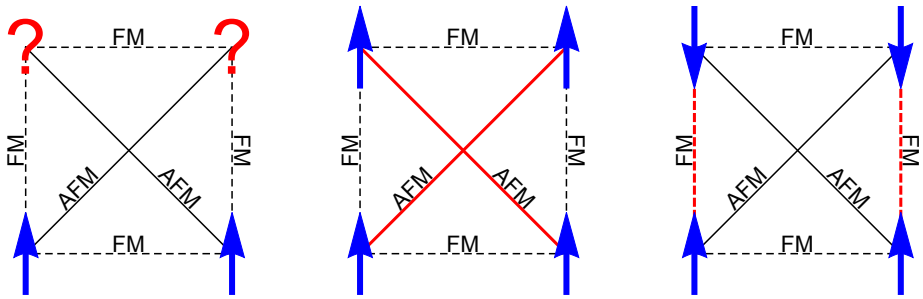

Figure 1.2: Exchange frustration of a next-nearest neighbour Ising model on a single square. The dashed lines signify ferromagnetic (FM) interactions, while the solid lines are antiferromagnetic (AFM) interactions. After choosing the first two spins, it is not possible to choose the remaining spins such that all bonds are satisfied. The best possible choices still leave two unsatisfied bonds (shown in red).

anti-parallel, and therefore there is no unique ground state. The best that this system can achieve, is having two spins pointing up and one spin pointing down, such that the ground state of this system is highly degenerate: six out of the eight possible configurations give the lowest possible energy. This is an example where frustration arises from the incompatibility of the interactions with the geometry of the underlying lattice, which is called *geometric frustration*.

The second type of frustration, called *exchange frustration*, can be caused by introducing conflicting interactions beyond nearest neighbour interactions. Again, this is a concept best explained by means of an example. We start again with the Ising model, but this time we consider the ferromagnetic version of this model. Moreover, we will now include antiferromagnetic next-nearest neighbour interactions as well. This model causes conflicting interactions: the ferromagnetic nearest neighbour interactions prefer all spins to be aligned, while the antiferromagnetic next-nearest neighbour interactions require some spins to point in the opposite direction as well. Therefore, not all of the interactions can be satisfied. As an example, this model can be placed on a single square, which is shown in Fig. 1.2.

Lattices consisting of frustrated unit cells (such as those from the above examples) can have two different types of ground states: either there is some long-range ordering, or the degeneracy of the ground state scales with the system size, leading to a *spin-liquid* phase. The latter happens for example for the antiferromagnetic Ising model on a full triangular lattice, while the former may happen for higher-dimensional (continuous) spins on the same lattice. Both types will be encountered in Sec. 1.3.

In some cases, the ground state degeneracy of the spin-liquid phase is partially lifted by an effect called *order-by-disorder* [6]. This effect is a result from the fact that thermal systems strive to minimize the free energy,

$$F = E - TS, \tag{1.2}$$

where E is the thermal average of the energy of the system, T is the temperature and S is the entropy. The mechanism works as follows. For low but non-zero temperatures, there are thermal fluctuations

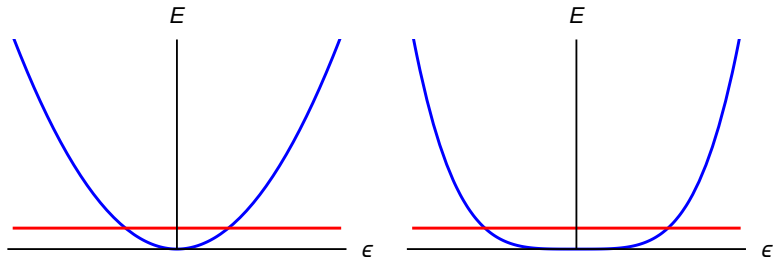

Figure 1.3: Energy as a function of ϵ with fluctuations scaling with ϵ^2 (left) and with fluctuations scaling with ϵ^4 (right). For low temperatures (temperature being indicated by the red line), the ϵ^4 fluctuations cost less energy than the ϵ^2 fluctuations. This means that the system corresponding to the right picture is allowed to fluctuate more than the one on the left for these low temperatures, leading to a larger corresponding entropy. Explanation based on Ref. [4].

about the ground state. Different types of spin configurations may allow different types of fluctuations: for example, a coplanar configuration of a system of three-dimensional spins (i.e. all spin vectors lie in the same plane) can have in-plane and out-of-plane fluctuations, while general configurations lead to all fluctuations being equivalent. Since the temperature is low, the fluctuations (parametrized by ϵ) can be expanded to lowest order in ϵ. Now imagine a situation where fluctuations about some special configurations scale with ϵ^4, while general fluctuations scale with ϵ^2. Then, the special configurations have a larger entropy (more "disorder") than the general configurations (see Fig. 1.3). As a result, the system selects these special configurations, and the degeneracy of the low-T phase is decreased (i.e. the system becomes more "ordered").

The order-by-disorder effect plays an important role in the phase diagrams of many frustrated systems, and we will encounter it several times in the remainder of this thesis. Additionally, the spin fluctuations about the ground state on which the above considerations are based (called *spin waves*), will be covered in much more detail in Ch. 4.

1.2 Triangular, Kagomé and Swedenborgite lattices

As was mentioned in the previous section, a spin model is always accompanied by an underlying lattice. In this section, we will describe the structures of the lattices that form the main interest of this work. We start with the triangular and Kagomé lattices, eventually leading to a complicated lattice called the Swedenborgite lattice.

Lattices consist of repeating *unit cells*. A unit cell may consist of one or more lattice sites, together with the corresponding bonds. The structure of an n-dimensional lattice in terms of unit cells is given by the lattice vectors $\mathbf{a}_1, \mathbf{a}_2, \ldots, \mathbf{a}_n$. In terms of these lattice vectors, there is unit cell located at each

$$\mathbf{r} = \sum_i^n c_i \mathbf{a}_i, \quad c_i \in \mathbb{Z}. \tag{1.3}$$

First, we consider the triangular lattice. The building block of this lattice is the single equilateral triangle that was also seen in Fig. 1.1. The lattice consists of edge-sharing triangles, resulting in the configuration shown in the left panel of Fig. 1.4. Choosing $\mathbf{a}_1$ along the $\hat{\mathbf{x}}$-direction, the lattice vectors corresponding to the triangular lattice are given by

$$\mathbf{a}_1 = a\begin{pmatrix}1\\0\end{pmatrix}, \qquad \mathbf{a}_2 = \frac{a}{2}\begin{pmatrix}1\\\sqrt{3}\end{pmatrix}, \tag{1.4}$$

where a is the lattice constant (i.e. the distance between neighbouring lattice sites). With each lattice site having six nearest neighbours, the connectivity of this lattice is large. This reduces the degeneracy of frustrated spin systems on a triangular lattice when compared to lattices with a smaller connectivity. While frustration still plays a large role on this lattice, the effects are often less prevalent than they are for geometrically frustrated spin systems on other lattices.

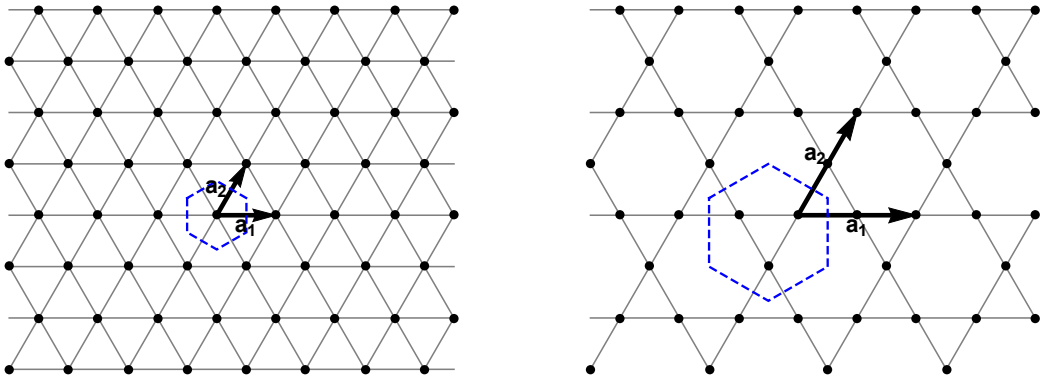

Figure 1.4: Overview of the triangular lattice (left) and the Kagomé lattice (right). The triangular lattice consists of edge-sharing triangles, and a unit cell (indicated by the blue dashed line) consists of a single lattice site. On the other hand, the Kagomé lattice consists of corner-sharing triangles, and a unit cell consists of three lattice sites. The lattice vectors of both lattices are denoted by $\mathbf{a}_1$ and $\mathbf{a}_2$. Notice that the length of the lattice vectors of the Kagomé lattice are twice as long as those of the triangular lattice.

An example of another lattice known to lead to frustration is the Kagomé lattice. Similar to the triangular lattice, the building block of the Kagomé lattice is a triangle. However, this time the lattice consists of corner-sharing triangles, rather than edge-sharing triangles. The resulting configuration can be seen in the right panel of Fig. 1.4. The Kagomé lattice is notably more complicated than the triangular lattice. In particular, the unit cell of the Kagomé lattice consists of three lattice sites rather than just one, such that there are now interactions inside a unit cell on top of the interactions between unit cells. On the level of entire unit cells, the lattice is simply a triangular lattice of unit cells (rather than individual lattice sites), and the corresponding lattice vectors are

$$\mathbf{a}_1 = 2a \begin{pmatrix} 1 \\ 0 \end{pmatrix}, \qquad \mathbf{a}_2 = a \begin{pmatrix} 1 \\ \sqrt{3} \end{pmatrix}, \tag{1.5}$$

i.e. the lattice vectors are twice as long as those of the triangular lattice, in terms of the lattice constant a. In addition, each lattice site has only four nearest neighbours, such that the connectivity of the Kagomé lattice is smaller than that of the triangular lattice. As a result, spin systems on the Kagomé lattice have a larger degeneracy and they often show more frustration than on the triangular lattice; we will encounter an explicit example of this difference at the end of Ch. 2.

Using the knowledge of the triangular and Kagomé lattices, it is possible to construct a complicated three-dimensional lattice known as the *Swedenborgite lattice*. Before we explicitly define this lattice, we take a moment to mention its relevance. In nature, there are many materials (called Swedenborgites) that have the structure of the mineral Swedenborgite, $SbNaBe_4O_7$. This mineral was first discovered

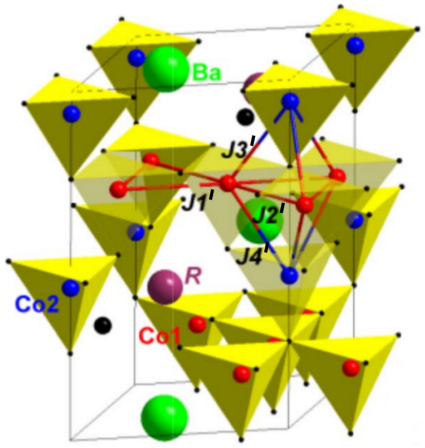

Figure 1.5: Lattice structure of $R\mathrm{BaCo_4O_7}$. The effective lattice structure consists of stacked Kagomé layers of $\mathrm{Co_1}$, connected by intermediate $\mathrm{Co_2}$ sites. The effective spin interactions allowed by the lattice symmetry are denoted by J_1', J_2', J_3' and J_4'. Picture from Ref. [7].

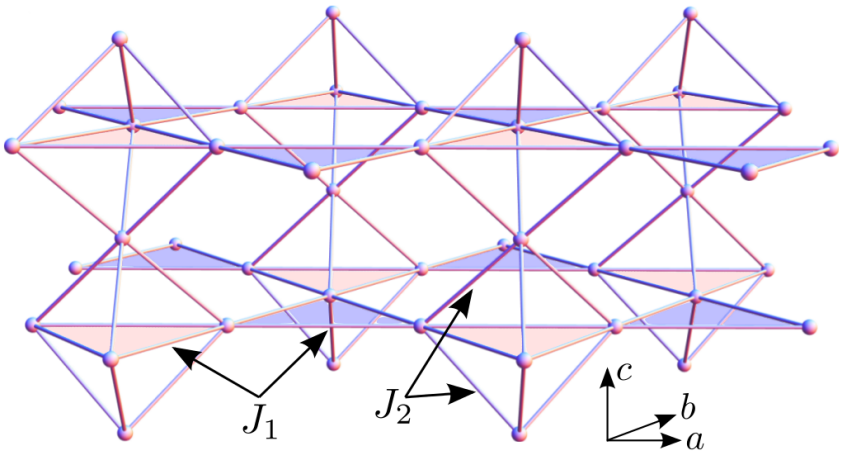

Figure 1.6: The Swedenborgite lattice. It is made up of alternating Kagomé layers that are connected by intermediate triangular layers. As a result, the triangles from the Kagomé layers have one of two roles: either they are part of a bipyramid (red), or they connect different bipyramids (blue). J_1 denotes the in-plane interaction strength, while J_2 gives the intermediate interaction strength between the layers. Picture from Ref. [4].

by Gregori Aminoff in 1924, who named it after Swedish scientist and theologian Emanuel Swedenborg [8]. An example of a Swedenborgite is $R\mathrm{BaCo_4O_7}$, see Fig. 1.5. As several materials with this structure exist, it is of interest to study the consequences of this structure on a theoretical level.

We will now construct the Swedenborgite lattice using the triangular and Kagomé lattices. We start with two Kagomé layers (B and C) with lattice spacing a that are *not* connected to each other, with layer C rotated 180 degrees with respect to layer B. Then, we connect these two layers by placing a triangular layer (A) with lattice spacing $2a$ between the layers B and C. Placing another layer A on top of layer C, we can now fill out the entire space by repeating this configuration of layers. The resulting structure is an ...ABAC...-pattern, and the corresponding lattice vectors are

$$\mathbf{a}_1 = 2a\begin{pmatrix}1\\0\\0\end{pmatrix} \equiv 2a\hat{\mathbf{a}}, \qquad \mathbf{a}_2 = a\begin{pmatrix}1\\\sqrt{3}\\0\end{pmatrix} \equiv 2a\hat{\mathbf{b}}, \qquad \mathbf{a}_3 = 4\sqrt{\frac{2}{3}}a\begin{pmatrix}0\\0\\1\end{pmatrix} \equiv 4\sqrt{\frac{2}{3}}a\hat{\mathbf{c}}, \tag{1.6}$$

where $\hat{\mathbf{a}}$, $\hat{\mathbf{b}}$ and $\hat{\mathbf{c}}$ are the basis vectors that span the lattice structure. For the remainder of this part of the thesis, we rescale the lattice in the $\hat{\mathbf{c}}$-direction, such that $\mathbf{a}_3$ has the same length as $\mathbf{a}_1$ and $\mathbf{a}_2$. In terms of these basis vectors, the layers are stacked in the $\hat{\mathbf{c}}$-direction, while the triangular and Kagomé lattices are spanned by the vectors $\hat{\mathbf{a}}$ and $\hat{\mathbf{b}}$. Keeping only the nearest neighbour bonds, the Swedenborgite lattice resulting from the above description is shown in Fig. 1.6.

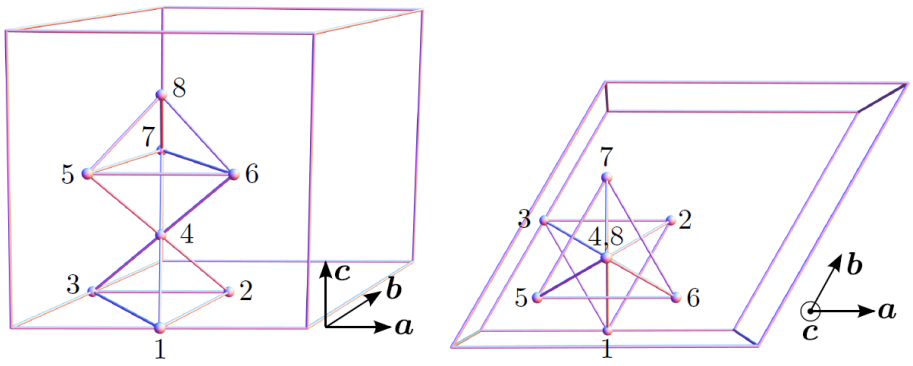

Figure 1.7: Unit cell of the Swedenborgite lattice. Lattice sites 4 and 8 are located on intermediate triangular layers, while the other lattice sites are located on Kagomé layers. Picture from Ref. [4].

As can be seen from the figure, the Swedenborgite lattice is made up of triangle-sharing columns of bipyramids. In other words: the individual frustrated clusters (the bipyramids) are connected by other frustrated clusters (the intermediate triangles), and this will lead to additional frustration. Additionally, the unit cells are quite large. Since two adjacent bipyramids inside a column are rotated by 180 degrees with respect to each other, a unit cell cannot be just a single bipyramid. Instead, a unit cell is given by two stacked bipyramids, resulting in eight-site unit cells, see Fig. 1.7. On the level of entire unit cells, the Swedenborgite lattice reduces to a stacked triangular lattice, similar to what happened with the Kagomé lattice.

Concerning the interactions, Khalyavin *et al.* [7] found that the symmetry of this lattice allows for four different spin interactions, denoted by J_1', J_2', J_3' and J_4' in Fig. 1.5. However, it was also found for $R\mathrm{BaCo_4O_7}$ that these interactions can be simplified using just an in-plane interaction strength J_1 and an intermediate interaction strength J_2 to a good approximation. We will adopt this approximation for the remainder of this thesis, leading to the interactions as shown in Fig. 1.6.

1.3 The Swedenborgite antiferromagnetic Heisenberg model

In this section, we will discuss the spin model that forms our main topic of interest: the Swedenborgite antiferromagnetic Heisenberg model (the final part often being abbreviated to HAFM, which stands for Heisenberg antiferromagnet). The Heisenberg model describes spins as three-dimensional unit vectors that are allowed to point in any direction on the unit sphere. Placing this model on the Swedenborgite lattice and allowing for different antiferromagnetic in-plane and intermediate interactions $J_1, J_2 > 0$, the Hamiltonian of becomes

$$H = J_1 \sum_{\substack{\langle i,j\rangle \in \\ \text{same layer}}} \mathbf{S}_i \cdot \mathbf{S}_j + J_2 \sum_{\substack{\langle i,j\rangle \in \\ \text{adj. layers}}} \mathbf{S}_i \cdot \mathbf{S}_j. \tag{1.7}$$

Here, J_1 and J_2 denote respectively the in-plane and intermediate coupling constants, $\mathbf{S}_i$ is the S^2 spin vector located at lattice site i, the first sum goes over all in-plane nearest neighbour pairs, and the second term sums over all nearest neighbour pairs between adjacent layers (all pairs being shown in Fig. 1.6). Once again, the units and length of the spin vectors have been absorbed into the coupling constants, such that $|\mathbf{S}_i| = 1$. In the following, we will review the analysis of this model that was done by Buhrandt in Refs. [4, 9]. The pictures in this section are from these works as well.

The first thing to note is that the Heisenberg model is invariant under global $O(3)$ transformations: sending all $\mathbf{S}_i \to g\mathbf{S}_i$ with $g \in O(3)$, the dot products that appear in the Hamiltonian are left invariant. This is easily shown by using $g^T = g^{-1}$:

$$\mathbf{S}_i \cdot \mathbf{S}_j = \mathbf{S}_i^T \mathbf{S}_j \to (g\mathbf{S}_i)^T (g\mathbf{S}_j) = \mathbf{S}_i^T g^T g \mathbf{S}_j = \mathbf{S}_i^T g^{-1} g \mathbf{S}_j = \mathbf{S}_i^T \mathbf{S}_j = \mathbf{S}_i \cdot \mathbf{S}_j. \tag{1.8}$$

Hence, configurations that are merely $O(3)$ rotations of each other are equivalent, and the word "unique" therefore means "unique up to $O(3)$ transformations", similar to what we have seen in Sec. 1.1. Of course, the above also holds for more general n-dimensional spins and corresponding global $O(n)$ transformations.

Next, we will derive the ground state of the Swedenborgite HAFM. To do so, it is convenient to split the Hamiltonian in terms of the building blocks of the lattice, which are the bipyramids and the interconnecting triangles. Numbering the individual lattice sites of these components according to Fig. 1.8 and using that $\mathbf{S}_i \cdot \mathbf{S}_i = |\mathbf{S}_i|^2 = 1$, the Hamiltonians corresponding to the building blocks are given by

$$\begin{aligned} H_{\text{triangle}} &= J_1 \left(\mathbf{S}_1 \cdot \mathbf{S}_{2'} + \mathbf{S}_{2'} \cdot \mathbf{S}_{3''} + \mathbf{S}_{3''} \cdot \mathbf{S}_1 \right) \\ &= \frac{J_1}{2} \left(\mathbf{S}_1 + \mathbf{S}_{2'} + \mathbf{S}_{3''} \right)^2 - \frac{3J_1}{2} \\ &= \frac{J_1}{2} \left(\mathbf{S}_1 + \mathbf{S}_{2'} + \mathbf{S}_{3''} \right)^2 + \text{const.}, \end{aligned} \tag{1.9}$$

and similarly

$$H_{\text{bipyramid}} = \frac{J_1}{2} \left(\mathbf{S}_1 + \mathbf{S}_2 + \mathbf{S}_3 + \frac{J_2}{J_1} \left(\mathbf{S}_4 + \mathbf{S}_5 \right) \right)^2 + \frac{J_2^2}{2J_1} \left(\mathbf{S}_4 - \mathbf{S}_5 \right)^2 + \text{const.} \tag{1.10}$$

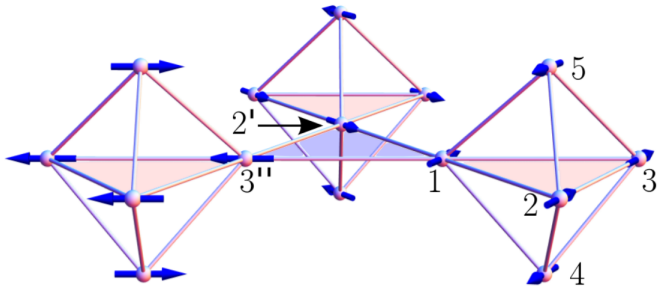

Figure 1.8: Numbering of the individual lattice sites of the building blocks of the lattice. The spin configuration shown is the ground state of the antiferromagnetic Heisenberg model for $J_2/J_1 \geq 3/2$, as derived in the text.

The second term of Eq. (1.10) appears to cancel the unwanted $\mathbf{S}_4 \cdot \mathbf{S}_5$ cross term that arise from the first term. Using these two Hamiltonians, the total Hamiltonian is simply given by the sum over all building blocks. It is now clear that the energy is minimized by minimizing the length of the three vectors that appear inside the squares. Therefore, the optimal configuration would be given by

$$\mathbf{S}_1 + \mathbf{S}_{2'} + \mathbf{S}_{3''} = 0, \tag{1.11}$$

$$\mathbf{S}_1 + \mathbf{S}_2 + \mathbf{S}_3 + \frac{J_2}{J_1}(\mathbf{S}_4 + \mathbf{S}_5) = 0, \tag{1.12}$$

$$\mathbf{S}_4 - \mathbf{S}_5 = 0 \tag{1.13}$$

for all triangles and bipyramids. The third condition is easily satisfied by $\mathbf{S}_4 = \mathbf{S}_5$. Noting that this condition has to hold for all bipyramids, this leads to all intermediate spins of a given column pointing in the same direction.

Condition (1.11) requires the spins of an intermediate triangle to assume a so-called 120° configuration. This can be seen as follows. The unit vectors $\mathbf{S}_1$ and $\mathbf{S}_{2'}$ define a plane. Since the sum of the vectors must be zero, the third vector $\mathbf{S}_{3''}$ must lie in this plane as well. Without loss of generality, we can choose the coordinate system such that the common plane is the $x-y$ plane, and we choose the $\hat{\mathbf{x}}$-direction along $\mathbf{S}_1$. Then, we have $\mathbf{S}_1 = (1,0,0)$, $\mathbf{S}_{2'} = (\cos\theta_{2'}, \sin\theta_{2'}, 0)$ and $\mathbf{S}_{3''} = (\cos\theta_{3''}, \sin\theta_{3''}, 0)$. Solving Eq. (1.11), one finds $\theta_{2'} = -\theta_{3''}$ and $\theta_{2'} = \pm 2\pi/3 = \pm 120°$, leading to $\mathbf{S}_1 = (1,0,0)$, $\mathbf{S}_{2'} = (-1/2, \pm\sqrt{3}/2, 0)$ and $\mathbf{S}_{3''} = (-1/2, \mp\sqrt{3}/2, 0)$. This proves that Eq. (1.11) indeed leads to a configuration where all spins are at an angle of 120° with respect to each other. The above is an example of a frustrated cluster that still leads to a unique ground state, which is one of the possibilities that was mentioned in Sec. 1.1.

The final condition, Eq. (1.12), leads to more complicated situations. Depending on the value of J_2/J_1, there may be many possible solutions, or it can be impossible to satisfy this condition. This originates from the fact that the vector $\mathbf{S}_1 + \mathbf{S}_2 + \mathbf{S}_3$ can at most have length 3, while the vector $\frac{J_2}{J_1}(\mathbf{S}_4 + \mathbf{S}_5)$ has length $2J_2/J_1$ due to Eq. (1.13). As a result, there are three regimes.

First, if $J_2/J_1 = 3/2$, the condition is satisfied by the unique solution $\mathbf{S}_1 = \mathbf{S}_2 = \mathbf{S}_3 = -\mathbf{S}_4$. Together with the other conditions, this leads to a unique ground state: inside a given column, all intermediate spins point in the same direction, while all other spins of that column point in the opposite direction of the intermediate spins. Keeping this in mind, the configuration of an entire column can therefore be described by assigning it a *macrospin* (for example the direction of the intermediate spins). Since the Swedenborgite lattice is a triangular lattice of columns (or macrospins), adjacent triangles are edge-sharing (such that they share two corners). Due to condition (1.11), each of these triangles must assume a 120° configuration. This uniquely determines the configuration on the entire lattice: given the configuration of one triangle, two out of three macrospins of an adjacent triangle are known, and then its third macrospin is automatically imposed as well. This ground state is shown in Figs. 1.8 and 1.9. In the second regime, $J_2/J_1 > 3/2$, it is impossible to satisfy condition (1.12). However, the length of this vector is still minimized by the same configuration as for $J_2/J_1 = 3/2$, and therefore this regime leads to the same unique ground state configuration.

The third regime, $J_2/J_1 < 3/2$, is where the effects of frustration are most prominent. Again, the vector $\mathbf{S}_1 + \mathbf{S}_2 + \mathbf{S}_3$ must be equal to $-2J_2/J_1\mathbf{S}_4$, which is now a vector with length smaller than 3.

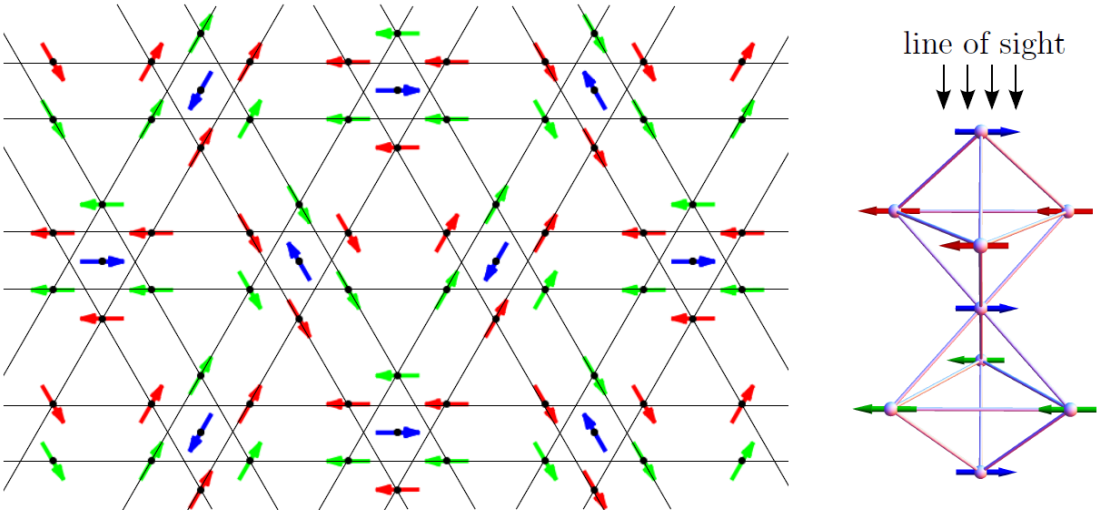

Figure 1.9: Unique ground state of the antiferromagnetic Heisenberg model on the Swedenborgite lattice for $J_2/J_1 \geq 3/2$. Blue, green and red spins denote the spins on the layers A, B and C, respectively.

Hence, there are now many ways to choose $\mathbf{S}_1$, $\mathbf{S}_2$, and $\mathbf{S}_3$, and the number of possible configurations increases with decreasing J_2/J_1. The ground state is therefore highly degenerate in this regime. Part of this degeneracy is removed again when all columns are connected to form the complete lattice, but the effects of frustration are still easily strong enough to destroy all long-range order. This is an example of a spin-liquid phase, which is the second possibility that was mentioned in Sec. 1.1.

Now that the ground state has been determined, we can shift our focus to the phase diagram of the model. For all J_2/J_1, we expect a disordered phase above some finite temperature. For very small J_2/J_1, the Kagomé layers decouple from the triangular layers, and the low-temperature phase will be a two-dimensional spin-liquid phase. On the other hand, for large J_2/J_1 (i.e. $J_2/J_1 \geq 3/2$) the low-temperature phase will be the unique ground state that was found. For $J_2/J_1 < 3/2$, we have seen that the low-temperature phase is a spin-liquid phase. However, something else happens for small but finite temperatures: it has been shown by Buhrandt that order-by-disorder effects remove a large part of the ground state degeneracy by selecting a common plane for all spin vectors. As a result, the low-temperature phase in this regime is a so-called *nematic* phase. For somewhat larger temperature, when entropic order-by-disorder no longer plays a role, the system will occupy a three-dimensional spin-liquid phase before becoming completely disordered.

The full phase diagram by Buhrandt is shown in Fig. 1.10. This phase diagram was constructed by elaborate Monte Carlo simulations based on the above considerations. It was found that the phase transition between the nematic phase and the spin-liquid phase is first order, the phase transition between the unique ground state and the disordered phase is second order, and all other transitions are actually crossovers. However, there are reasons to believe that the simulations did not capture all of the physics relevant to this model. This will be discussed in the next section.

1.4 Phase transition in the $J_2/J_1 \to 3/2$ limit

Although Fig. 1.10 gives a good overview of the different phases and the corresponding phase transitions of the Swedenborgite HAFM, there is one region that the simulations did not capture: the region in the vicinity of $J_2/J_1 = 3/2$. Due to the low resolution of data points in this region, there is not enough information to deduce the behaviour, and the vertical line that is drawn appears only to connect the different parts of the phase diagram. As was mentioned by Buhrandt in Ref. [9], one cannot actually distinguish this vertical phase boundary from a steep slope towards $J_2/J_1 > 3/2$. We do not expect a vertical line for several reasons. For one, a vertical phase boundary would result in an ill-defined critical temperature. More importantly, there is an entropic argument as well. The spin-liquid phase to the left of the boundary and the unique ground state to the right have a similar energy. However, the spin-liquid

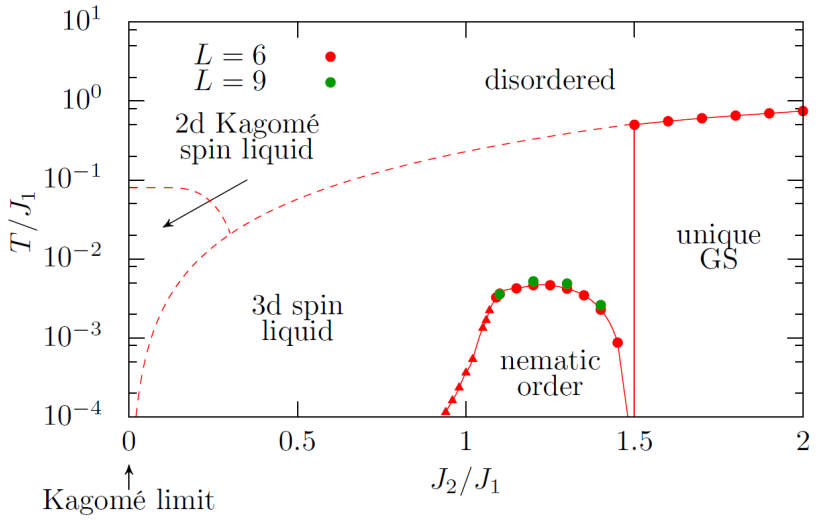

Figure 1.10: Phase diagram of the Swedenborgite antiferromagnetic Heisenberg model, by means of Monte Carlo simulations. The line separating the nematic phase from the spin-liquid phase denotes a first order phase transition, the unique ground state is separated by a second order phase transition, and the dashed lines signify crossovers. Note that the nematic phase exists for all $J_2/J_1 < 3/2$.

phase has a much larger entropy than the unique ground state. Minimization of the free energy therefore leads us to believe that the spin-liquid phase also eats its way into the region $J_2/J_1 > 3/2$, an effect becoming stronger for increasing temperatures. Based on this argument, one would expect the actual boundary between the spin-liquid phase and the unique ground state to have a finite slope.

As discussed above, there is still a region of the phase diagram that has not yet been properly investigated. Moreover, this region is quite special when compared to most other regions: it is this region that contains the physics concerning boundaries between the two types of low temperature phases of frustrated systems that have been covered in the previous sections. It is therefore desirable to complete the phase diagram.

The main goal of the following chapters is to gain a proper understanding of the phase transitions in the region close to the "critical" value $J_2/J_1 = 3/2$, i.e. the boundary between the regions where a unique ground state exists and where it does not. First, we attempt to gain a general understanding by means of Landau theory. Then we will investigate this region microscopically by using mean-field theory, and finally going beyond mean-field theory by examining fluctuations. Since we expect a finite slope towards $J_2/J_1 > 3/2$, we focus mostly on J_2/J_1 approaching the value $3/2$ from above.

Chapter 2

Phenomenological Landau theory

The goal of this chapter is to gain a better qualitative understanding of the phase transitions of the Swedenborgite HAFM by means of phenomenological Landau theory (see for example Chaikin & Lubensky [10] for an elaborate introduction). To reach this goal, we first discuss the principles of the Landau theory of phase transitions. Then, we apply this theory to a simple model: the antiferromagnetic Heisenberg model on the distorted triangular lattice. This is a model that also depends on the ratio of two different interaction strengths J_1 and J_2, and it shares several features with the Swedenborgite antiferromagnet, making it a good introductory example. The results from this example will then be generalized to the Swedenborgite lattice, enabling us to understand the types of phase transitions that appear.

Landau theory, first described in 1937 [11], attempts to describe phase transitions by introducing a function L, called the Landau free energy (not to be confused with the Helmholtz free energy F), that depends on the temperature, microscopic constants and order parameters of the system. An order parameter is a quantity that measures if the system is in an ordered state or not, changing from a non-zero value in the corresponding ordered phase to zero in the disordered phase. An example of such an order parameter would be the magnetization of a ferromagnetic spin model. The actual state of a system is then determined by the global minimum of L with respect to the order parameters. The idea of Landau theory is to expand the Landau free energy in terms of the order parameters in the vicinity of the phase transition, assuming them to be small in this region.

The Landau free energy has several properties. Most importantly, it must be invariant under the symmetry group of the disordered (high-temperature) phase, which is the symmetry group of the microscopic Hamiltonian. As a result, the expansion of L can only contain combinations of the order parameters that are invariant under operations from this symmetry group. We also assume that L is analytic close to the phase transition, allowing us to perform the aforementioned expansion of L. Equating the derivatives of L with respect to the order parameters to zero and noting that the order parameters themselves are zero in the disordered phase, we see that the expansion of L cannot contain linear terms. It is however possible to apply an external field that forces an order parameter to be non-zero even in the high-temperature phase; this can be included by adding a linear coupling term to L. Finally, the highest order term included in the expansion must always be even, and its coefficient must be positive for all temperatures in order to have a global minimum at all.

It turns out that Landau theory is very successful in predicting the types of phase transitions that can appear in a system. The most common types of phase transitions are first order phase transitions and second order phase transitions. First order phase transitions are discontinuous, in the sense that the corresponding order parameter discontinuously jumps from zero to a finite value at the critical temperature; second order phase transitions are continuous, and the order parameter continuously becomes non-zero. To see how all of this works, let us restrict ourselves to a single homogeneous order parameter η for the moment. Following the above description and assuming that the series can safely be truncated above fourth order terms, the Landau free energy takes the form

$$L = \frac{1}{2}c_2(\{J\},T)\eta^2 + \frac{1}{3}c_3(\{J\},T)\eta^3 + \frac{1}{4}c_4(\{J\},T)\eta^4 - h\eta. \tag{2.1}$$

Here η is the order parameter, $c_i(\{J\},T)$ are the expansion coefficients as a function of the temperature T and the set of microscopic constants $\{J\}$, h is the external field, and the numeric prefactors are included

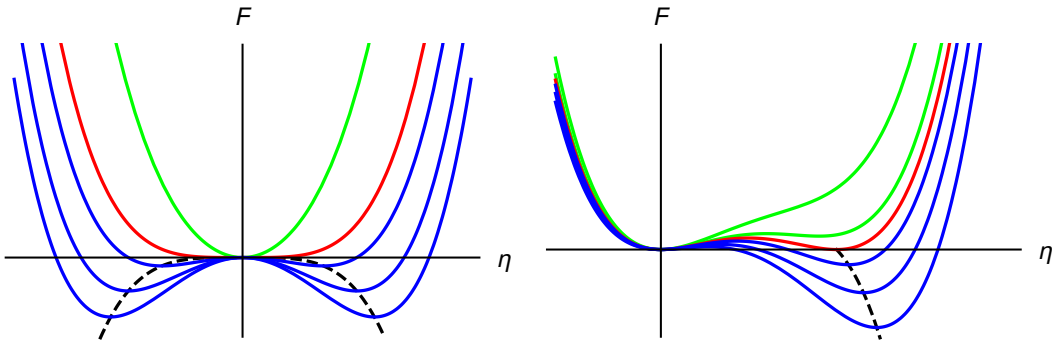

Figure 2.1: Landau free energy as a function of the order parameter η for the two examples discussed in the text. The left plot shows how the global minimum can change continuously from zero to non-zero values (second order phase transition), while the right plot shows how this can happen discontinuously as well (first order phase transition). The green curves are for $T > T_c$, the red curves are for $T = T_c$ and the blue curves are for $T < T_c$. The dashed black lines denote the possible positions of the global minimum for different temperatures. Note that $T_c \neq T^*$ for the second example.

for convenience. We now consider two examples to see how this Landau free energy can distinguish first order and second order phase transitions. For both examples, we set the external field to zero and make the $\{J\}$ dependence of the coefficients implicit.

For the first example, we consider a model that has $\eta \to -\eta$ symmetry. This is for instance realized by the ferromagnetic Ising model: then, the order parameter is simply the average value of the spins S_i (this is called the magnetization), and the $S_i \to -S_i$ symmetry of the Hamiltonian dictates that this symmetry must hold for the order parameter as well. As the Landau free energy must respect this symmetry, the expansion cannot contain any odd order terms. Considering only the region close to some temperature T^* and demanding that c_4 stays positive, we can expand to linear order in $T - T^*$:

$$L = \frac{1}{2}a(T - T^*)\eta^2 + \frac{1}{4}b\eta^4, \tag{2.2}$$

where a and b are positive coefficients. This free energy is plotted in the left panel of Fig. 2.1. We now see that the shape of the free energy, and consequently the position of the global minimum, depends on the temperature T: the global minimum is located at $\eta = 0$ if $T \geq T^*$, but for $T < T^*$ it is located at $\eta = \pm\sqrt{-a(T - T^*)/b}$. The order parameter thus changes continuously from zero to non-zero values. We can conclude that this model has an ordered low-temperature phase and a disordered high-temperature phase, separated by a second order phase transition at critical temperature $T_c = T^*$.

For the second example, we consider a model that allows odd order terms by its symmetry, such that the Landau free energy expansion becomes

$$L = \frac{1}{2}a(T - T^*)\eta^2 + \frac{1}{4}b\eta^4 - \frac{1}{3}c\eta^3, \tag{2.3}$$

where the minus sign in front of the final term has been chosen for convenience. This free energy is shown in the right panel of Fig. 2.1. As can be seen from the figure, the global minimum now jumps discontinuously from zero to non-zero η at some critical temperature T_c, resulting in a first order phase transition. Note that T_c is now different from T^*: solving $L = 0$ and demanding that there are exactly two solutions gives $T_c = T^* + 2c^2/9ab$.

The above examples demonstrate how a simple analysis following from the symmetry group of the Hamiltonian can be used to predict the order of the corresponding phase transitions. However, Landau theory is usually more complicated than in these two situations. To complete this introduction of phenomenological Landau theory, we consider the possibility of an inhomogeneous order parameter $\eta(\mathbf{r})$, which can for instance be achieved by applying an inhomogeneous external field. Defining a local order parameter on a lattice can be tricky, and is usually done by a procedure called *coarse-graining*, where the lattice is divided into small sections and determining the order parameter for each of these sections. As domain walls between sections with different order parameters usually cost energy (for example the

ferromagnetic Ising model with a section with magnetization +1 neighbouring a section with magnetization −1), gradient terms must be added to the Hamiltonian. Once again considering a single order parameter $\eta(\mathbf{r})$ and truncating the series above fourth order, the simplest form of the Landau free energy is given by

$$L[\eta(\mathbf{r})] = \frac{N}{V}\int \mathrm{d}\mathbf{r}\left[\frac{1}{2}c_2\eta(\mathbf{r})^2 + \frac{1}{3}c_3\eta(\mathbf{r})^3 + \frac{1}{4}c_4\eta(\mathbf{r})^4 - h(\mathbf{r})\eta(\mathbf{r}) + \frac{1}{2}C\left[\nabla\eta(\mathbf{r})\right]^2\right], \tag{2.4}$$

where V is the volume of the system, and all of the coefficients can depend on T and $\{J\}$. In principle, higher order derivatives are allowed as well, but this lowest order term often suffices. The partition function can now be calculated as well, by taking a functional integral over the order parameter:

$$Z = \int \mathcal{D}\eta(\mathbf{r}) e^{-\beta L[\eta(\mathbf{r})]}, \tag{2.5}$$

where $\beta = 1/k_B T$ is the inverse temperature and k_B is the Boltzmann constant. Finally, we note that there can be several relevant order parameters in a single system, and they are not always scalar as in the above introduction. Instead, order parameters are often rank-n tensors.

2.1 The distorted triangular lattice

In this section, we will apply phenomenological Landau theory to describe a simple model: the antiferromagnetic Heisenberg model on the distorted triangular lattice. This model shares several properties with the Swedenborgite HAFM, and it will serve as an example of a more complicated Landau theory of which the results can later be generalized to the Swedenborgite lattice. We will start by describing the model itself and its ground states, after which we discuss the order parameters and use it to construct a Landau free energy. We will then finish this section by discussing the consequences of the resulting Landau free energy, supported by Monte Carlo simulations.

In Sec. 1.3, we briefly discussed the ground state of the antiferromagnetic Heisenberg model of the undistorted triangular lattice, following from the constraint $\mathbf{S}^1_\Delta + \mathbf{S}^2_\Delta + \mathbf{S}^3_\Delta = 0$ on each triangle that appears on the lattice. We have seen that this leads to a 120° configuration of the spins on a single triangle, and that this uniquely defines the ground state configuration of the entire system due to the fact that neighbouring triangles share two lattice sites. For the example of this section, we once again consider the antiferromagnetic Heisenberg model on a two-dimensional triangular lattice. This time, however, the bonds in one direction (say the $\mathbf{a}_1$-direction) are stronger than in the other directions. The Hamiltonian is thus given by

$$H = J_1 \sum_{\substack{\langle i,j\rangle \in \\ \mathbf{a}_1\text{-direction}}} \mathbf{S}_i \cdot \mathbf{S}_j + J_2 \sum_{\substack{\langle i,j\rangle \in \\ \text{other directions}}} \mathbf{S}_i \cdot \mathbf{S}_j, \tag{2.6}$$

where $J_1 > J_2 > 0$. We can rewrite this Hamiltonian to a more convenient form:

$$H = \frac{J_1}{2}\sum_\Delta \left(\mathbf{S}^1_\Delta + \mathbf{S}^2_\Delta + \frac{J_2}{J_1}\mathbf{S}^3_\Delta\right)^2 - J_1 N_\Delta \left(1 + \frac{J_2^2}{2J_1^2}\right). \tag{2.7}$$

Here, the sum runs over all triangles of the system, with N_Δ being the total number of triangles, and $\mathbf{S}^i_\Delta$ denotes the i^{th} spin of a triangle. In this notation, $\mathbf{S}^1_\Delta$ and $\mathbf{S}^2_\Delta$ are connected by a J_1-bond, while the other combinations within the triangle are connected by a J_2-bond. To calculate the final term (which is constant), we used the fact that all spins have unit length.

The above Hamiltonian (2.7) is obviously minimized if

$$\mathbf{S}^1_\Delta + \mathbf{S}^2_\Delta + \frac{J_2}{J_1}\mathbf{S}^3_\Delta = 0 \tag{2.8}$$

for all triangles, provided that it is possible. To check if it is possible to satisfy this condition, we will simply try to construct the ground state using Eq. (2.8) and see if it works. We start by numbering the

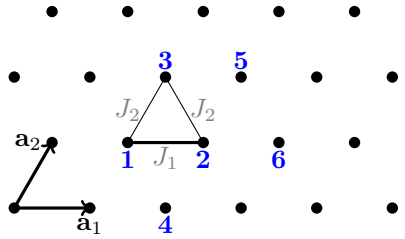

Figure 2.2: Schematic view of the distorted triangular lattice. The numbers denote the lattice sites that are referenced in the text.

spins according to Fig. 2.2 and choosing $\mathbf{S}_3 = \hat{\mathbf{x}}$. To complete the first triangle, we now have to solve

$$\mathbf{S}_1 + \mathbf{S}_2 + \frac{J_2}{J_1}\mathbf{S}_3 = \begin{pmatrix} S_1^x + S_2^x + \frac{J_2}{J_1} \\ S_1^y + S_2^y \\ S_1^z + S_2^z \end{pmatrix} = 0. \tag{2.9}$$

Choosing the $\hat{\mathbf{y}}$-direction such that $\mathbf{S}_2$ lies in the $x-y$ plane, we find

$$\mathbf{S}_1 = \begin{pmatrix} -\frac{J_2}{2J_1} \\ \pm\sqrt{1-\left(\frac{J_2}{2J_1}\right)^2} \\ 0 \end{pmatrix}, \qquad \mathbf{S}_2 = \begin{pmatrix} -\frac{J_2}{2J_1} \\ \mp\sqrt{1-\left(\frac{J_2}{2J_1}\right)^2} \\ 0 \end{pmatrix}, \qquad \mathbf{S}_3 = \begin{pmatrix} 1 \\ 0 \\ 0 \end{pmatrix}. \tag{2.10}$$

Obviously, $(\mathbf{S}_1)^2 = (\mathbf{S}_2)^2 = (\mathbf{S}_3)^2 = 1$ holds as required.

From this first triangle, we will try to construct the rest of the ground state. There are two types of nearest neighbours of a triangle: like $\mathbf{S}_4$ and $\mathbf{S}_5$ (see again Fig. 2.2). $\mathbf{S}_4$ has to obey the same equation as $\mathbf{S}_3$, so we immediately find $\mathbf{S}_4 = \mathbf{S}_3$. Now let us calculate $\mathbf{S}_5$:

$$\mathbf{S}_3 + \mathbf{S}_5 + \frac{J_2}{J_1}\mathbf{S}_2 = \begin{pmatrix} 1 + S_5^x - \frac{J_2^2}{2J_1^2} \\ S_5^y \mp \frac{J_2}{J_1}\sqrt{1-\left(\frac{J_2}{2J_1}\right)^2} \\ S_5^z \end{pmatrix} = 0 \quad \Rightarrow \quad \mathbf{S}_5 = \begin{pmatrix} \frac{J_2^2}{2J_1^2} - 1 \\ \pm\frac{J_2}{J_1}\sqrt{1-\left(\frac{J_2}{2J_1}\right)^2} \\ 0 \end{pmatrix}. \tag{2.11}$$

$\mathbf{S}_5$ is a unit vector as well:

$$\begin{aligned} (\mathbf{S}_5)^2 &= \left(\frac{J_2^2}{2J_1^2} - 1\right)^2 + \frac{J_2^2}{J_1^2}\left(1 - \left(\frac{J_2}{2J_1}\right)^2\right) \\ &= \frac{J_2^4}{4J_1^4} - \frac{J_2^2}{J_1^2} + 1 + \frac{J_2^2}{J_1^2} - \frac{J_2^4}{4J_1^4} \\ &= 1. \end{aligned} \tag{2.12}$$

From this, we see that it is possible to construct neighbouring triangles in both directions. Therefore, we can conclude that it is indeed possible to construct the entire ground state configuration from Eq. (2.8), once the initial $\pm$ choice (see Eq. (2.10)) has been made. Note that this $\pm$ choice is simply a reflection about the $x-z$ plane (an $O(3)$ transformation), and they are regarded as the same configuration.

From the above analysis, it is apparently possible to choose the basis such that $S_i^z = 0$ for all i, leading to the conclusion that the ground state configuration is coplanar. Next, we will look at the angles between neighbouring spins by considering the dot products between them. To further support the following analysis, let us first calculate one additional spin, $\mathbf{S}_6$:

$$\mathbf{S}_2 + \mathbf{S}_6 + \frac{J_2}{J_1}\mathbf{S}_5 = \begin{pmatrix} -\frac{J_2}{2J_1} + S_6^x + \frac{J_2}{J_1}\left(\frac{J_2^2}{2J_1^2} - 1\right) \\ \mp\sqrt{1-\left(\frac{J_2}{2J_1}\right)^2} + S_6^y \pm \frac{J_2^2}{J_1^2}\sqrt{1-\left(\frac{J_2}{2J_1}\right)^2} \\ S_6^z \end{pmatrix} = 0 \tag{2.13}$$

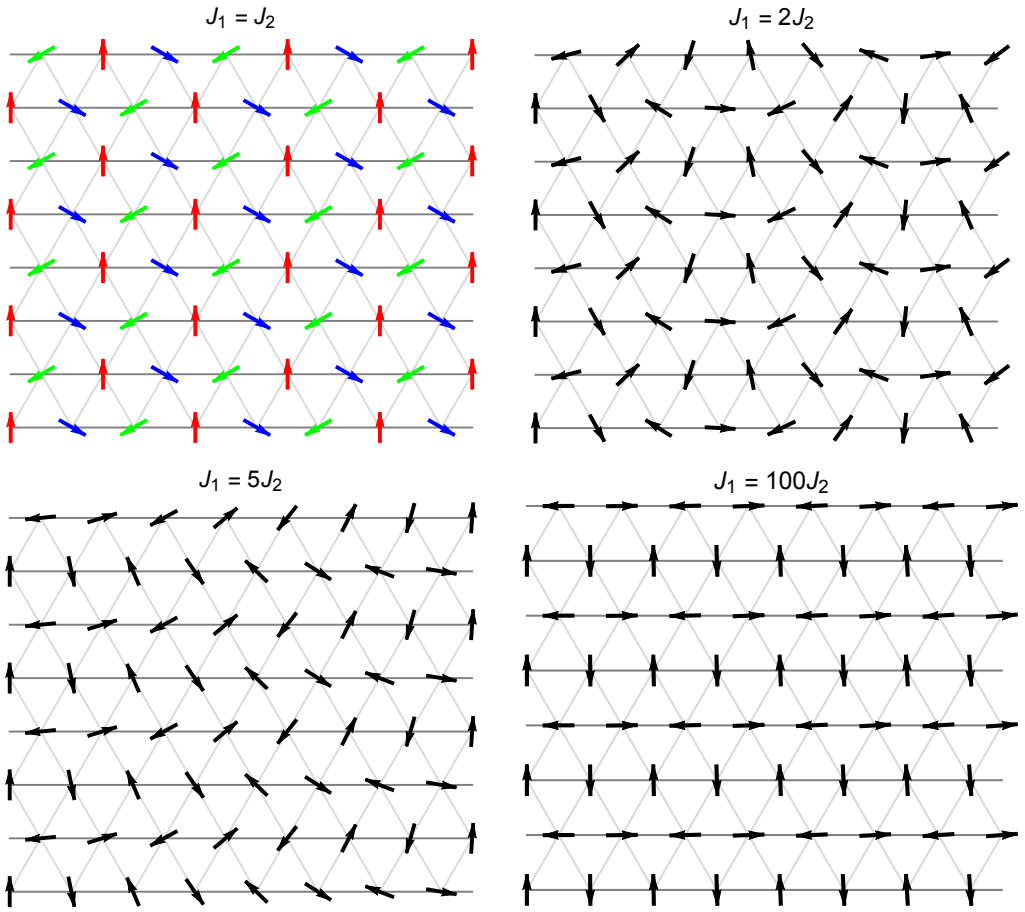

Figure 2.3: Ground state of the antiferromagnetic Heisenberg model on the distorted triangular lattice for different values of J_1/J_2, unique up to global $O(3)$ rotations. The darker lines correspond to the strong bonds J_1, while the lighter lines signify the weaker bonds J_2. The periodic case $J_1 = J_2$ has been divided into three sublattices, denoted by the different colours.

$$\Rightarrow \quad \mathbf{S}_6 = \begin{pmatrix} \frac{J_2}{2J_1}\left(3 - \frac{J_2^2}{J_1^2}\right) \\ \pm\left(1 - \frac{J_2^2}{J_1^2}\right)\sqrt{1 - \left(\frac{J_2}{2J_1}\right)^2} \\ 0 \end{pmatrix}. \tag{2.14}$$

It is easily checked that $\mathbf{S}_6$ is a unit vector as required. Using all these spins, we can calculate the dot products between neighbouring spins in the $\mathbf{a}_1$-direction:

$$\mathbf{S}_1 \cdot \mathbf{S}_2 = \left(\frac{J_2}{2J_1}\right)^2 - \left(1 - \left(\frac{J_2}{2J_1}\right)^2\right) = \frac{J_2^2}{2J_1^2} - 1, \tag{2.15}$$

$$\begin{aligned} \mathbf{S}_2 \cdot \mathbf{S}_6 &= -\left(\frac{J_2}{2J_1}\right)^2 \left(3 - \frac{J_2^2}{J_1^2}\right) - \left(1 - \frac{J_2^2}{J_1^2}\right)\left(1 - \left(\frac{J_2}{2J_1}\right)^2\right) \\ &= -\left(\frac{J_2}{2J_1}\right)^2 \left(3 - \frac{J_2^2}{J_1^2} - 1 + \frac{J_2^2}{J_1^2}\right) - 1 + \frac{J_2^2}{J_1^2} \\ &= \frac{J_2^2}{2J_1^2} - 1, \end{aligned} \tag{2.16}$$

$$\mathbf{S}_3 \cdot \mathbf{S}_5 = \frac{J_2^2}{2J_1^2} - 1. \tag{2.17}$$

Seeing how the spins are constructed, this pattern must extend over the entire system, such that all neighbouring spins in the $\mathbf{a}_1$-direction (so all neighbouring spins in a *chain*) are at the same angle between one another. The same statement holds for neighbouring spins in the other directions (between chains), as can be checked:

$$\mathbf{S}_1 \cdot \mathbf{S}_3 = \mathbf{S}_2 \cdot \mathbf{S}_3 = \mathbf{S}_1 \cdot \mathbf{S}_4 = \mathbf{S}_2 \cdot \mathbf{S}_4 = \mathbf{S}_2 \cdot \mathbf{S}_5 = \mathbf{S}_6 \cdot \mathbf{S}_5 = -\frac{J_2}{2J_1}. \tag{2.18}$$

We conclude that spins inside a chain are at an angle $\pm \arccos\left(\frac{J_2^2}{2J_1^2} - 1\right)$ with respect to each another, while the different chains are at an angle $\mp \arccos\left(-\frac{J_2}{2J_1}\right)$ between one another. Either the upper or the lower sign must be chosen for all spins, which can be seen from the above example spins. It is important to note that this ground state is generally *not* periodic in the $\mathbf{a}_1$-direction, since in general $\arccos\left(\frac{J_2^2}{2J_1^2} - 1\right)/\pi$ is irrational, and in that case a multiple of this angle can never be a multiple of 2π. Unless the fraction J_1/J_2 is chosen exactly such that the ground state is periodic, the lattice distortion is called *incommensurate*, meaning that the periodicity of the ground state and the periodicity of the lattice are incompatible, leading to a perfectly predictable yet not periodic ground state configuration that lacks translational symmetry.

Fig. 2.3 shows the ground state that follows from the above analysis for several different values of the ratio J_1/J_2. As can be seen in the figure, the ground state for $J_1 = J_2$ (i.e. the undistorted triangular lattice) indeed reduces to the 120° configuration that was found before.

2.1.1 Order parameters

In order to write down a Landau free energy, we need suitable order parameters that can be used to identify the ground state. First, we can use the fact that the ground state selects a common plane for all spins. Consider the following vector [2]:

$$\boldsymbol{\kappa}_\Delta \equiv \frac{1}{\mathcal{N}_\kappa}\left(\mathbf{S}_\Delta^1 \times \mathbf{S}_\Delta^2 + \mathbf{S}_\Delta^2 \times \mathbf{S}_\Delta^3 + \mathbf{S}_\Delta^3 \times \mathbf{S}_\Delta^1\right), \tag{2.19}$$

where $\mathcal{N}_\kappa$ is a normalization constant. In the disordered phase, all spins independently point in random directions, such that this vector is zero on average. On the other hand, in the ordered phase $\boldsymbol{\kappa}_\Delta$ is a unit vector normal to the selected plane. To see this, we choose the basis such that the configuration from Eq. (2.10) holds for one of the triangles. Then, the normal vector is simply the basis vector $\hat{\mathbf{z}}$. Using the fact that the configurations on all triangles are rotations of each other, this immediately gives

$$\frac{J_1}{J_2}\mathbf{S}_\Delta^1 \times \mathbf{S}_\Delta^2 = \mathbf{S}_\Delta^2 \times \mathbf{S}_\Delta^3 = \mathbf{S}_\Delta^3 \times \mathbf{S}_\Delta^1 = \pm\sqrt{1 - \left(\frac{J_2}{2J_1}\right)^2}\,\hat{\mathbf{z}} \tag{2.20}$$

for all triangles on the lattice. Choosing

$$\mathcal{N}_\kappa = 2\left(1 + \frac{J_2}{2J_1}\right)\sqrt{1 - \left(\frac{J_2}{2J_1}\right)^2}, \tag{2.21}$$

this leads to the conclusion that $\boldsymbol{\kappa}_\Delta = \pm\hat{\mathbf{z}}$ holds for all triangles on the lattice, given that the system occupies the ground state.

Since the direction of the normal vector $\boldsymbol{\kappa}_\Delta$ has no relevance, the order parameter associated with the selection of a common plane cannot be a vector. Instead, it must at least be a rank-2 tensor that is invariant under $\boldsymbol{\kappa}_\Delta \to -\boldsymbol{\kappa}_\Delta$. The selection of a common plane (and consequently a normal direction) is similar to the selection of a preferred direction in nematic liquid crystals, hence the relevant order parameter is the so-called *nematic order parameter* [10]:

$$Q_\kappa^{\alpha\beta} \equiv \frac{1}{N_\Delta}\sum_\Delta\left(\kappa_\Delta^\alpha \kappa_\Delta^\beta - \frac{1}{3}|\boldsymbol{\kappa}_\Delta|^2\delta^{\alpha\beta}\right). \tag{2.22}$$

As before, the sum goes over all triangles of the lattice, while N_Δ is the total number of triangles. The tensor $Q_\kappa^{\alpha\beta}$ is symmetric and traceless, and all components become zero in the disordered phase due to

$O(3)$ symmetry of this phase. On the other hand, the ordered phase gives some non-zero components. Returning to the basis that led to $\boldsymbol{\kappa}_\Delta = \pm\hat{\mathbf{z}}$, we find the ground state value

$$\mathbf{Q}_\kappa = \begin{pmatrix} -\frac{1}{3} & 0 & 0 \\ 0 & -\frac{1}{3} & 0 \\ 0 & 0 & \frac{2}{3} \end{pmatrix}. \tag{2.23}$$

For later reference, we note that it is possible to construct simpler forms of the nematic order parameter, for example [12]:

$$Q_S^{\alpha\beta} \equiv \frac{1}{N}\sum_i \left(S_i^\alpha S_i^\beta - \frac{1}{3}\delta^{\alpha\beta} \right). \tag{2.24}$$

Although this form of the nematic order parameter does not give the same numeric values as $Q_\kappa^{\alpha\beta}$, it still describes the same type of ordering, and we are free to choose the preferred form of the nematic order parameter.

While the nematic order parameter $Q^{\alpha\beta}$ does a good job detecting the selection of a common plane, it is not sufficient: it may be possible that all spins lie in a common plane (giving a non-zero $Q^{\alpha\beta}$), but still being randomly distributed inside this plane. In order to distinguish between random coplanar configurations and the actual ordered ground state, we introduce an additional order parameter: the *sublattice magnetization*

$$\mathbf{M} \equiv \frac{1}{N}\sum_i \left(\mathbf{S}_i \cos(\mathbf{q}\cdot\mathbf{r}_i) + \frac{1}{\mathcal{N}_M}\mathbf{S}_i \times (\mathbf{S}_{i+1}\times\mathbf{S}_{i+2}) \sin(\mathbf{q}\cdot\mathbf{r}_i) \right) \equiv \frac{1}{N}\sum_i \mathbf{M}_i. \tag{2.25}$$

Here, the sum goes over all lattice sites i (with i counted along the direction of $\mathbf{a}_1$), $\mathcal{N}_M$ is the normalization constant of the triple cross product, $\mathbf{r}_i$ is the two-dimensional position of lattice site i and $\mathbf{q}$ is the wave vector corresponding to the ground state periodicity. The normalization constant $\mathcal{N}_M$ is easily derived by noting that the triple cross product from the second term should have unit length for the ground state configuration:

$$\begin{aligned} \mathcal{N}_M &= \sin\left(\arccos\left(\frac{J_2^2}{2J_1^2} - 1 \right) \right) \\ &= \frac{J_2}{J_1}\sqrt{1 - \left(\frac{J_2}{2J_1} \right)^2}. \end{aligned} \tag{2.26}$$

Moreover, the wave vector $\mathbf{q}$ is given by $(2\pi/\lambda_x, 2\pi/\lambda_y)$, where $\lambda_{x,y}$ are the wavelengths corresponding to the ground state periodicity. Noting that two chains are separated by a distance $\sqrt{3}a/2$ and referring back to Fig. 2.3, we immediately get $\lambda_y = \sqrt{3}a$. For the other direction (i.e. the direction of $\mathbf{a}_1$), we note that each distance a yields a phase shift of $\arccos\left(\frac{J_2^2}{2J_1^2} - 1\right)$, such that the wavelength is given by $\lambda_x = 2\pi a/\arccos\left(\frac{J_2^2}{2J_1^2} - 1\right)$. Combining these results, we find

$$\mathbf{q} = \left(\arccos\left(\frac{J_2^2}{2J_1^2} - 1 \right)/a, 2\pi/\sqrt{3}a \right). \tag{2.27}$$

As with $Q^{\alpha\beta}$, $\mathbf{M}$ becomes zero in the disordered phase due to $O(3)$ symmetry. For the ground state, $\mathbf{M}_i$ is a unit vector that points in the same direction for every i due to the definition of the wave vector $\mathbf{q}$. To see this, we consider the periodic case $J_1 = J_2$ as an example. We place lattice site $i = 1$ at the origin and divide the lattice sites into three *sublattices* in such a way that each sublattice only contains one of the three possible spin states when considering the ground state (see the top-left panel of Fig. 2.3). The value of $\mathbf{q}\cdot\mathbf{r}_i$ is fixed for each of these sublattices: it equals 0 for sublattice 1, $2\pi/3$ for sublattice 2 and $4\pi/3$ for sublattice 3. We find

$$\mathbf{M}_{i_1} = \mathbf{S}_{i_1}, \tag{2.28}$$

$$\mathbf{M}_{i_2} = -\frac{1}{2}(\mathbf{S}_{i_2} - 2\mathbf{S}_{i_2}\times(\mathbf{S}_{i_2+1}\times\mathbf{S}_{i_2+2})), \tag{2.29}$$

$$\mathbf{M}_{i_3} = -\frac{1}{2}(\mathbf{S}_{i_3} + 2\mathbf{S}_{i_3}\times(\mathbf{S}_{i_3+1}\times\mathbf{S}_{i_3+2})), \tag{2.30}$$

where i_n denotes that we are looking at a lattice site that resides on sublattice n. For the ground, this reduces to

$$\mathbf{M}_{i_1} = \mathbf{S}_1, \tag{2.31}$$

$$\mathbf{M}_{i_2} = -\frac{1}{2}(\mathbf{S}_2 - 2\mathbf{S}_2 \times (\mathbf{S}_3 \times \mathbf{S}_1)), \tag{2.32}$$

$$\mathbf{M}_{i_3} = -\frac{1}{2}(\mathbf{S}_3 + 2\mathbf{S}_3 \times (\mathbf{S}_1 \times \mathbf{S}_2)), \tag{2.33}$$

Using the basis of Eq. (2.10) again, it is now easily checked that $\mathbf{M}_i$ is the same for all lattice sites i, which confirms that $\mathbf{M}$ becomes a unit vector when considering the ground state configuration.

2.1.2 Symmetry and the construction of the Landau free energy

Now that we have found suitable order parameters, we can construct the Landau free energy of the system. The order parameters that we will use are the sublattice magnetization $\mathbf{M}$ and a general nematic order parameter $Q^{\alpha\beta}$; note that we no longer distinguish between different forms such as $Q_\kappa^{\alpha\beta}$ and $Q_S^{\alpha\beta}$ due to the fact that the exact form is just a matter of choice.

In order to construct a Landau free energy from the order parameters $Q^{\alpha\beta}$ and $\mathbf{M}$, we need to find the combinations that are invariant under the symmetry group of the Hamiltonian, in this case $O(3)$. First, we need to know how the order parameters $Q^{\alpha\beta}$ and $\mathbf{M}$ transform under the operation

$$S_i^\alpha \to g^{\alpha\beta} S_i^\beta, \quad g \in O(3), \tag{2.34}$$

where we have used Einstein's convention to sum over repeated indices. Using that $\det(g) = \pm 1$ for all $g \in O(3)$, one can show for any two vectors $\mathbf{A}$ and $\mathbf{B}$

$$g\mathbf{A} \times g\mathbf{B} = \det(g) g(\mathbf{A} \times \mathbf{B}) = \pm g(\mathbf{A} \times \mathbf{B}). \tag{2.35}$$

Referring back to Eq. (2.19), we see that the normal vector $\boldsymbol{\kappa}_\Delta$ transforms as

$$\kappa_\Delta^\alpha \to \pm g^{\alpha\beta} \kappa_\Delta^\beta. \tag{2.36}$$

Combining this with the fact that $g^{\alpha\rho} g^{\beta\sigma} \delta^{\rho\sigma} = \delta^{\alpha\beta}$ and that the dot product $\mathbf{q} \cdot \mathbf{r}_i$ is left invariant, we find that the operation of Eq. (2.34) imposes

$$Q^{\alpha\beta} \to g^{\alpha\rho} g^{\beta\sigma} Q^{\rho\sigma}, \tag{2.37}$$

$$M^\alpha \to g^{\alpha\beta} M^\beta, \tag{2.38}$$

which confirms that $Q^{\alpha\beta}$ and $\mathbf{M}$ transform like a rank-2 tensor and a vector respectively.

To find all combinations of the order parameters $Q^{\alpha\beta}$ and M^α that are left invariant under the above transformation, we consider an arbitrary combination A with $2n$ indices. Since the Landau free energy itself does not carry any indices, each term must be fully contracted. Using that $g^T = g^{-1}$, such a term transforms as

$$\begin{aligned} A^{\alpha_1\alpha_1\alpha_2\alpha_2\ldots\alpha_n\alpha_n} &\to g^{\alpha_1\beta_1} g^{\alpha_1\gamma_1} g^{\alpha_2\beta_2} g^{\alpha_2\gamma_2} \ldots g^{\alpha_n\beta_n} g^{\alpha_n\gamma_n} A^{\beta_1\gamma_1\beta_2\gamma_2\ldots\beta_n\gamma_n} \\ &= g^{\alpha_1\beta_1} (g^{-1})^{\gamma_1\alpha_1} g^{\alpha_2\beta_2} (g^{-1})^{\gamma_2\alpha_2} \ldots g^{\alpha_n\beta_n} (g^{-1})^{\gamma_n\alpha_n} A^{\beta_1\gamma_1\beta_2\gamma_2\ldots\beta_n\gamma_n} \\ &= \delta^{\beta_1\gamma_1} \delta^{\beta_2\gamma_2} \ldots \delta^{\beta_n\gamma_n} A^{\beta_1\gamma_1\beta_2\gamma_2\ldots\beta_n\gamma_n} \\ &= A^{\beta_1\beta_1\beta_2\beta_2\ldots\beta_n\beta_n} \\ &= A^{\alpha_1\alpha_1\alpha_2\alpha_2\ldots\alpha_n\alpha_n}. \end{aligned} \tag{2.39}$$

From this, we conclude that any fully contracted non-zero combination of $Q^{\alpha\beta}$ and M^α is allowed. Since $Q^{\alpha\beta}$ is traceless (so $Q^{\alpha\alpha} = 0$) and $(Q^{\alpha\beta}Q^{\beta\alpha})^2$ is proportional to $Q^{\alpha\beta}Q^{\beta\gamma}Q^{\gamma\rho}Q^{\rho\alpha}$ [10], the Landau free energy up to fourth order is given by

$$\begin{aligned} L &= C_1 M^\alpha M^\alpha + C_2 Q^{\alpha\beta} Q^{\beta\alpha} + C_3 Q^{\alpha\beta} Q^{\beta\gamma} Q^{\gamma\alpha} + C_4 M^\alpha Q^{\alpha\beta} M^\beta + C_5 (M^\alpha M^\alpha)^2 \\ &\quad + C_6 (Q^{\alpha\beta} Q^{\beta\alpha})^2 + C_7 M^\alpha Q^{\alpha\beta} Q^{\beta\gamma} M^\gamma + C_8 M^\alpha M^\alpha Q^{\beta\gamma} Q^{\gamma\beta} \qquad (2.40) \\ &= C_1 |\mathbf{M}|^2 + C_2 \mathrm{Tr}(\mathbf{Q}^2) + C_3 \mathrm{Tr}(\mathbf{Q}^3) + C_4 \mathbf{M} \cdot (\mathbf{Q} \cdot \mathbf{M}) + C_5 |\mathbf{M}|^4 \\ &\quad + C_6 \mathrm{Tr}(\mathbf{Q}^2)^2 + C_7 |\mathbf{Q} \cdot \mathbf{M}|^2 + C_8 |\mathbf{M}|^2 \mathrm{Tr}(\mathbf{Q}^2), \qquad (2.41) \end{aligned}$$

where C_i are unknown coefficients that generally depend on the temperature and the microscopic parameters of the system.

It may be useful to look at the Landau free energy in a particular basis. In the basis with $\boldsymbol{\kappa}_\Delta = \pm\hat{\mathbf{z}}$, the order parameters reduce to the following expressions [10]:

$$\mathbf{Q} = \begin{pmatrix} -\frac{1}{3}S & 0 & 0 \\ 0 & -\frac{1}{3}S & 0 \\ 0 & 0 & \frac{2}{3}S \end{pmatrix}, \tag{2.42}$$

$$\mathbf{M} = \begin{pmatrix} M\cos(\theta) \\ M\sin(\theta) \\ 0 \end{pmatrix}. \tag{2.43}$$

With these, the Landau free energy becomes

$$L = c_1 M^2 + c_2 S^2 + c_3 S^3 + c_4 M^2 S + c_5 M^4 + c_6 S^4 + c_7 M^2 S^2, \tag{2.44}$$

which shows that it is possible to express it in terms of two scalars S and M rather than the much more complicated parameters $Q^{\alpha\beta}$ and $\mathbf{M}$.

2.1.3 Primary and secondary order parameters

In this final part of the section, we will interpret the Landau free energy found above. The simplified expression Eq. (2.44) consists of three parts: a part that depends only on M, a part that depends only on S, and some coupling terms that relate the order parameters to each other. The part depending only on M consists of even order terms only, which implies a second order phase transition, in accordance with the beginning of this chapter. On the other hand, the part that depends only on S also contains an odd order S^3 term, which implies a first order phase transition. This indicates that we should distinguish between *primary* and *secondary* order parameters. The primary order parameter drags the secondary order parameter along, and it is therefore the one that decides the type of the phase transition in most situations. However, even if the primary order parameter never becomes non-zero, the secondary order parameter can still become non-zero on its own, in which case the secondary order parameter will determine the type of the phase transition. Below, we will further look into this concept by means of Monte Carlo simulations.

Before turning to the simulations, it is important to note that we are looking at a two-dimensional system with a continuous symmetry. As we will discuss in Ch. 3, the Mermin-Wagner theorem [13] states that this continuous symmetry cannot be spontaneously broken at any finite temperature, so there cannot be a phase transition at any $T > 0$. Nevertheless, the simulations are done on a finite lattice, such that they still show some ordering for $T > 0$, and this can be used to analyse the relations between the order parameters.

We consider simulations based on a simple Metropolis algorithm of the classical antiferromagnetic Heisenberg model on a distorted triangular lattice with N lattice sites (see appendix A.1 for more information on the methods). The quantities that we measure are the lowest order non-zero contractions of the order parameters. Since the nematic order parameters are traceless, these contractions are the generalized squares $|\mathbf{M}|^2 \equiv (M^\alpha)^2$, $Q_S^{\alpha\beta}Q_S^{\beta\alpha} \equiv (Q_S^{\alpha\beta})^2$ and $Q_\kappa^{\alpha\beta}Q_\kappa^{\beta\alpha} \equiv (Q_\kappa^{\alpha\beta})^2$.

The results of the simulations on the undistorted triangular lattice (with $J_1 = J_2$) with $N = 132$ lattice sites are shown in the left panel of Fig. 2.4. For these simulations, helical boundary conditions are used. Two features stand out. First, the different nematic order parameters show the same qualitative behaviour, suggesting that they are indeed both valid parameters to describe nematic ordering. Second, the sublattice magnetization is the first quantity to start increasing when the temperature is being decreased. This suggests that the sublattice magnetization is the primary order parameter, while the nematic order parameters are only secondary. Note especially the similarities between these results and those of the Kagomé lattice in Ref. [12]. The similarities suggest that the sublattice magnetization M^α on the triangular lattice takes a similar role as the octupolar moment $T^{\alpha\beta\gamma}$ on the Kagomé lattice (we will explain this octupolar ordering in Sec. 2.2.1). In particular, we expect a coupling term in Landau free energy:

$$\Delta L \simeq C M^\alpha Q^{\alpha\beta} M^\beta, \tag{2.45}$$

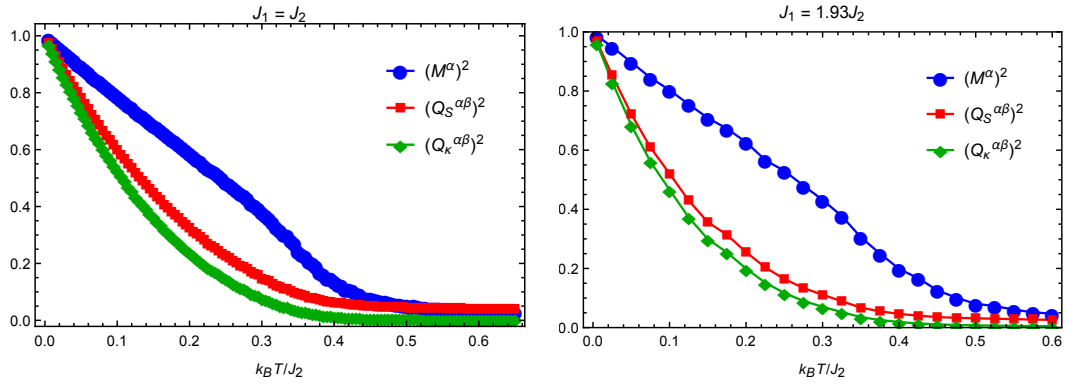

Figure 2.4: Order parameters as functions of temperature on the undistorted triangular lattice (with $J_1 = J_2$) with $N = 132$ lattice sites (left) and on the distorted triangular lattice (with $J_1 = 1.93J_2$) with $N = 288$ lattice sites (right). All quantities are normalized such that they are equal to 1 in the ground state.

where C is a coefficient that can depend on the temperature and the parameters of the Hamiltonian. This is exactly what we have seen before.

The results of the simulations on the distorted triangular lattice with $J_1 = 1.93J_2$ and $N = 288$ lattice sites are shown in the right panel of Fig. 2.4. Here, periodic boundary conditions were used. Note that the results look very similar to those of the undistorted triangular lattice. This suggests that the same conclusions hold as for the undistorted triangular lattice, such that for this model the coupling constants J_1 and J_2 do not have a qualitative effect on the Landau theory.

An explanation for the usage of the value $J_1 = 1.93J_2$ may be in order. As was explained in the first part of this section, the ground state of the antiferromagnetic Heisenberg model on the distorted triangular lattice is generally not periodic in the $\mathbf{a}_1$-direction. Therefore, simulations using periodic boundary conditions (which forces periodic solutions) may not give the correct results. To fix this, the lattice size and the ratio J_1/J_2 have been chosen such that the ground state is approximately periodic on the lattice used in the simulations. Additional information on the Monte Carlo simulations, the problems that were encountered and their solution, and additional results on slightly different models can all be found in appendix A.2.

Let us return to the matter of primary and secondary order parameters. The simulations suggested that the sublattice magnetization is the primary order parameter, while the nematic order parameter is only secondary. This is also implied by their definition: if the sublattice magnetization is non-zero, it automatically means that the spins selected a plane, leading to a non-zero nematic order parameter. On the other hand, it is perfectly possible to have a random coplanar configuration that has non-zero nematic ordering while still having a zero sublattice magnetization. The sublattice magnetization therefore drags the nematic order parameter along when it becomes non-zero, and not the other way around, suggesting that the sublattice magnetization is the primary order parameter.

In the Landau free energy, all of this manifests itself by having the only temperature dependence in the coefficient c_1, leading to

$$L = c_1(T)M^2 + \frac{1}{2}c_2S^2 + \frac{1}{3}c_3S^3 + c_4M^2S + c_5M^4 + \frac{1}{4}c_6S^4 + \frac{1}{2}c_7M^2S^2, \tag{2.46}$$

where the parameters $c_2, \ldots, c_7$ are now constants in T. If we now want to find S in terms of M, we look at a fixed value of M (corresponding to a fixed temperature), which gives

$$L = \frac{1}{2}c_2S^2 + \frac{1}{3}c_3S^3 + \frac{1}{4}c_6S^4 + (c_4S + \frac{1}{2}c_7S^2)M^2 + \text{const.} \tag{2.47}$$

This expression suggests that M^2 now acts as an external field to S, once again implying that a non-zero M results in a non-zero S, and not the other way around. Minimizing L with respect to S now gives

$$c_2S + c_3S^2 + c_6S^3 + (c_4 + c_7S)M^2 = 0, \tag{2.48}$$

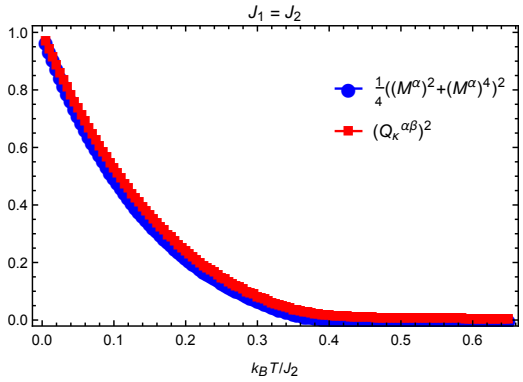

Figure 2.5: Overlap of the lines for a particular series of the magnetization.

which gives us S as a function of M^2. As a next step, it is possible to express the solution of this equation as a power series in M^2.

As an example, we use the results shown in the left panel of Fig. 2.4. To find the relation between these two quantities, different powers and prefactors of the magnetization have been attempted until the data overlapped. This can be seen in Fig. 2.5. The resulting relation is

$$S \sim M^2 + M^4, \tag{2.49}$$

so the simulations agree with the observation that S can be expressed as a power series in M^2. Using this result and plugging it back into the Landau free energy and combining the terms of the same order, we finally arrive at

$$L = A(T)M^2 + BM^4, \tag{2.50}$$

where A and B are the new Landau coefficients.

2.2 Landau theory of the Swedenborgite antiferromagnet

While it turned out in the end that the secondary order parameter can safely be ignored when constructing the Landau free energy of the model from the previous section, this is not a general result. Let us first consider the order parameters that describe the ordering encountered in the different low-temperature phases of the Swedenborgite HAFM. As we have seen in Sec. 1.3, this model has two different low-temperature phases, depending on the value of J_2/J_1: if $J_2/J_1 \geq 3/2$, there is a unique ground state configuration, while for $J_2/J_1 < 3/2$ there is only the selection of a common plane. The latter type of ordering is the same as the nematic ordering encountered in the previous section, so this phase can again be described by the nematic order parameter $Q^{\alpha\beta}$. Additionally, the unique ground state configuration is entirely coplanar as well, so this order parameter is also valid in this region. However, just as we have seen in the previous section, the nematic order parameter is not sufficient to describe all of the ordering of the unique ground state. Since this ground state has a very well defined configuration over the entire lattice, it is once again possible to define a sublattice magnetization $\mathbf{M}$ that rotates each of the spins in such a way that it successfully captures this configuration. We will not actually write down this sublattice magnetization explicitly, as it is not very illuminating; the important result is that the ordering can be described by a vector $\mathbf{M}$ similar to the one from the previous section. It is now immediately apparent that $Q^{\alpha\beta}$ must be secondary to $\mathbf{M}$: both low-temperature phases have non-zero $Q^{\alpha\beta}$, while only the unique ground state has non-zero $\mathbf{M}$, and there is no phase where only $\mathbf{M}$ is non-zero.

While the exact expressions of the order parameters themselves are different, we once again have a rank-2 tensor $Q^{\alpha\beta}$ and a vector $\mathbf{M}$ as our order parameters, so the most general form of the Landau free energy up to fourth order looks the same as before:

$$\begin{aligned} L &= C_1 M^\alpha M^\alpha + C_2 Q^{\alpha\beta} Q^{\beta\alpha} + C_3 Q^{\alpha\beta} Q^{\beta\gamma} Q^{\gamma\alpha} + C_4 M^\alpha Q^{\alpha\beta} M^\beta + C_5 (M^\alpha M^\alpha)^2 \\ &\quad + C_6 (Q^{\alpha\beta} Q^{\beta\alpha})^2 + C_7 M^\alpha Q^{\alpha\beta} Q^{\beta\gamma} M^\gamma + C_8 M^\alpha M^\alpha Q^{\beta\gamma} Q^{\gamma\beta} \qquad (2.51) \\ &= c_1 M^2 + c_2 S^2 + c_3 S^3 + c_4 M^2 S + c_5 M^4 + c_6 S^4 + c_7 M^2 S^2, \qquad (2.52) \end{aligned}$$

where all of the coefficients can now be functions of T, J_1 and J_2. As the order of the low-temperature phase and the types of the phase transition depend on the value of J_2/J_1, at least one of the coefficients must be a function of this fraction.

In the following, we will see how a particular choice of the coefficients can result in the proper phase diagram. Let us first consider $J_2/J_1 < 3/2$. In this region, M will remain zero, so c_5 and c_7 are greater than zero for all temperatures. Moreover, noting that c_6 must be positive and choosing c_3 to be negative, S will always be non-negative, such that c_4 must be positive as well. The coefficient c_1 could become negative for some temperature: the effective quadratic term in M is now given by

$$\left(c_1 + c_4 S + c_7 S^2\right) M^2, \tag{2.53}$$

so c_1 could be negative as long as S is large enough such that the entire prefactor remains positive. Allowing the final coefficient c_2 to change sign at a certain temperature T^*, these observations result in a first order phase transition from a low-temperature nematic phase to a disordered phase (which could be a spin-liquid phase, since this Landau theory cannot distinguish this from a true disordered phase).

Next, we consider $J_2/J_1 \geq 3/2$. In this region, the sublattice magnetization becomes non-zero and drags the nematic order parameter along. As we have seen in the previous section, this can be explained by putting the relevant temperature dependence in c_1. In order for S to be dragged along, the coefficients c_4 and c_7 are now negative, while the coefficients of the highest order terms c_5 and c_6 must of course still be positive. Similar to the $J_2/J_1 < 3/2$ case, we choose c_3 to be negative, while the final coefficient c_2 may still switch sign for some temperature. As in the previous section, minimization of L with respect to S allows us to expand S as a power series in M^2, which returns a Landau free energy of the form of Eq. (2.50). This case leads to a second order phase transition between a unique configuration with non-zero sublattice magnetization (the unique ground state) and a disordered phase.

Combining the above, we have that c_3 is negative while c_5 and c_6 are positive for all fractions J_2/J_1 and temperatures T. In addition, the coupling coefficients c_4 and c_7 are positive below $J_2/J_1 = 3/2$ and negative otherwise, changing sign at this boundary value. The coefficients c_1 and c_2 are both positive for high temperatures, and it depends on the fraction J_2/J_1 which of the two causes a phase transition at a certain temperature.

Note that the above analysis of the coefficients is not unique, and it is just an example of how the coefficients can lead to the phase diagram from Fig. 1.10. However, some of the observations are conclusive: the Landau free energy, which follows entirely from the symmetries of the Hamiltonian, allows for second order phase transitions and first order phase transitions (to a unique configuration and a nematic phase respectively) at certain temperatures and coupling constants. Which of the two happens and what the critical temperature is, depends on the fraction J_2/J_1. These conclusions confirm what we have seen in Sec. 1.3, and we have achieved the goal of this chapter: we have successfully constructed a Landau theory for the Swedenborgite HAFM and used it to understand which phase transitions are possible and what the types of these phase transitions are.

Before we end this chapter, we note that there is still a type of ordering that might appear that we have not yet considered. As we will see in this final part of the chapter, this type of ordering turns out to be absent for the Swedenborgite HAFM, such that the above is still the full story.

2.2.1 Octupolar ordering and its absence

As was briefly mentioned in Sec. 2.1.3, the phase diagram of the Kagomé HAFM contains a phase described by *octupolar ordering* [12]. To see what this is, we take a step back and look at the ground state of the Kagomé antiferromagnet. As we have seen in Sec. 1.2, the building block of the Kagomé lattice is a single triangle. The Hamiltonian of the antiferromagnetic Heisenberg model on this single triangle can be written as

$$H_1 = J \sum_{i,j} \mathbf{S}_i \cdot \mathbf{S}_j = \frac{J}{2} \left(\mathbf{S}_1 + \mathbf{S}_2 + \mathbf{S}_3\right)^2 + \text{const.} \tag{2.54}$$

Just like before, minimization of this energy leads to a 120° configuration of spins. However, unlike what we have seen on triangular lattices, the Kagomé lattice consists of corner-sharing triangles. So if the

configuration of a single triangle is known, the neighbouring triangles are still free to choose their own plane and helicity, rather than being uniquely determined. Therefore, the ground state of the Kagomé HAFM is highly degenerate.

Similar to what we have seen for the Swedenborgite HAFM, Chalker showed that the low-temperature phase of the Kagomé HAFM is dominated by order-by-disorder effects, which select coplanar configurations and lead to a nematic phase [2]. This additional constraint takes away the freedom to select a plane for each triangle, and we are now only allowed to choose the helicity of each triangle (for example the sign choice in Eq. (2.10)). While the total degeneracy is still very large, each spin must now point in one of only three possible directions. Hence, this nematic phase is still far more ordered than random coplanar configurations, and the usual nematic order parameter is not enough to describe the ordering of this phase.

In the XY model, which describes spins as two-dimensional unit vectors, this ordering can successfully be captured by the parameter $w_j = e^{3i\theta_j}$, where θ_j is the angle of the spin in the plane: in the ground state, each spin has $\theta_j \in \{0, 2\pi/3, 4\pi/3\}$, leading to $w_j = 1$ for each spin. For the Heisenberg model, it is more complicated to describe this ordering due to the fact that the common plane is arbitrary. The order parameter cannot be a vector (which describes a particular configuration) or a rank-2 tensor (which describes nematic ordering), so it must at least be a rank-3 tensor. Zhitomirsky found that this ordering, called octupolar ordering, can be described by the *octupolar moment* [12]:

$$T^{\alpha\beta\gamma} = \frac{1}{N}\sum_i \left(S_i^\alpha S_i^\beta S_i^\gamma - \frac{1}{5} S_i^\alpha \delta^{\beta\gamma} - \frac{1}{5} S_i^\beta \delta^{\alpha\gamma} - \frac{1}{5} S_i^\gamma \delta^{\alpha\beta} \right). \tag{2.55}$$

It turns out that this is the primary order parameter of the Kagomé HAFM, and that the nematic order parameter is only secondary.

The question is now whether or not this octupolar ordering also plays a role for the Swedenborgite HAFM. The most important difference between the two lattices is that the ground state degeneracy on the Kagomé lattice originates from the interactions between unit cells, while on the Swedenborgite lattice it is caused by the interactions inside a single unit cell. So contrary to the nematic phase of the Kagomé HAFM, a single building block of the Swedenborgite lattice (i.e. a bipyramid) already results in a very high degeneracy, as we have seen in Sec. 1.3. Moreover, a large part of this degeneracy remains even when restricted to a single plane. As a result, the spins do not have to choose from a finite number of possible directions, such that there is no octupolar ordering.

Since there is no octupolar ordering present in the nematic phase of the Swedenborgite HAFM, we assume that the nematic order parameter $Q^{\alpha\beta}$ is sufficient. There could of course still be a very complicated order parameter that we missed, as there are still constraints that prevent the configurations of the nematic phase to be truely random coplanar configurations, but comparison with the simulations leads us to believe that this is not the case. Therefore, our final conclusion of this chapter is that the analysis from the first part of this section is the proper Landau description for the antiferromagnetic Heisenberg model on the Swedenborgite lattice.

Chapter 3

Mean-field theory

In this chapter, we will develop a mean-field approach in an attempt to derive the phase diagram of the antiferromagnetic Heisenberg model on the Swedenborgite lattice. This approach will only be an approximation, and its results will not be exact in the number of dimensions we are looking at. Still, the methods that we will use in the end are very general for spin models, and they form an excellent framework to provide a first approximation. We will start this chapter by introducing mean-field theory by applying several mean-field methods to the antiferromagnetic Heisenberg model on the undistorted triangular lattice. At the end of this first section, we will relate mean-field theory to Landau theory (see Ch. 2) by means of a Hubbard-Stratonovich transformation. Then in Sec. 3.2, we will revisit one of the mean-field methods and generalize it to a framework that can be applied to any spin model. Using this framework, we will then be able to construct a mean-field theory for the Swedenborgite HAFM and use it to find an approximation for the critical temperature as a function of J_2/J_1. Finally, we will wrap up this chapter by discussing the validity of mean-field theory and its failure for low-dimensional systems.

3.1 Mean-field methods applied to the Heisenberg antiferromagnet on the triangular lattice

We consider the antiferromagnetic Heisenberg model on the undistorted triangular lattice. Even though the Mermin-Wagner theorem [13] states that this model cannot exhibit long-range order at a finite temperature, we will discuss several mean-field methods to describe it. In Sec. 3.4, we will see how the presence of fluctuations (which were ignored) cause mean-field theory to fail in low-dimensional systems, rendering the conclusions drawn from the mean-field methods obsolete. While the methods presented here do not give the correct results for the model at hand, they may be used to approximate higher-dimensional systems.

3.1.1 A simple mean-field approximation

For the first method, we use our knowledge of the ordered phase of the model (the ground state, i.e. the 120° configuration) to see that the lattice can be divided into three sublattices, each with their own magnetization (see again the top-left panel of Fig. 2.3). Let us rewrite the Hamiltonian:

$$\begin{aligned} H &= J \sum_{\langle i,j \rangle} \mathbf{S}_i \cdot \mathbf{S}_j \\ &= \frac{1}{2} \sum_{ij} J_{ij} \mathbf{S}_i \cdot \mathbf{S}_j \\ &= \frac{1}{2} \sum_{ij} J_{ij} [\mathbf{S}_i \cdot \langle \mathbf{S}_j \rangle + \langle \mathbf{S}_i \rangle \cdot \mathbf{S}_j - \langle \mathbf{S}_i \rangle \cdot \langle \mathbf{S}_j \rangle + (\mathbf{S}_i - \langle \mathbf{S}_i \rangle) \cdot (\mathbf{S}_j - \langle \mathbf{S}_j \rangle)] \\ &\simeq \sum_{ij} J_{ij} \mathbf{S}_i \cdot \langle \mathbf{S}_j \rangle + \text{const.} \end{aligned} \tag{3.1}$$

Here, and in the remainder of this thesis, angle brackets around a quantity $\langle \ldots \rangle$ denote the thermal expectation value of the quantity. In the first line, $\langle i,j \rangle$ denote all nearest neighbour pairs. In the second line, J_{ij} is defined to be equal to J if i,j are nearest neighbours, and zero otherwise. The factor $1/2$ is there to cancel double counting of the pairs. In the final line, we neglect the fluctuations term $(\mathbf{S}_i - \langle \mathbf{S}_i \rangle) \cdot (\mathbf{S}_j - \langle \mathbf{S}_j \rangle)$ (which is the mean-field approximation) and we use $J_{ij} = J_{ji}$ to combine the remaining terms. Finally, note that the average $\langle \mathbf{S}_j \rangle \equiv \mathbf{m}_j$ depends on the sublattice to which j belongs.

We will now introduce the sublattices l_1, l_2 and l_3 and the corresponding magnetizations $\mathbf{m}_1$, $\mathbf{m}_2$ and $\mathbf{m}_3$. The Hamiltonian becomes

$$\begin{aligned} H &= \sum_{i \in l_1, j} J_{ij} \mathbf{S}_i \cdot \langle \mathbf{S}_j \rangle + \sum_{i \in l_2, j} J_{ij} \mathbf{S}_i \cdot \langle \mathbf{S}_j \rangle + \sum_{i \in l_3, j} J_{ij} \mathbf{S}_i \cdot \langle \mathbf{S}_j \rangle \\ &= 3J \sum_{i \in l_1} \mathbf{S}_i \cdot (\mathbf{m}_2 + \mathbf{m}_3) + 3J \sum_{i \in l_2} \mathbf{S}_i \cdot (\mathbf{m}_3 + \mathbf{m}_1) + 3J \sum_{i \in l_3} \mathbf{S}_i \cdot (\mathbf{m}_1 + \mathbf{m}_2) \\ &\equiv H_1 + H_2 + H_3. \end{aligned} \tag{3.2}$$

Using the fact that $\mathbf{m}_n = 0$ in the disordered phase and $\mathbf{S}^1_\Delta + \mathbf{S}^2_\Delta + \mathbf{S}^3_\Delta = 0$ in the ground state, we see that we can write

$$H_n = -3J \sum_{i \in l_n} \mathbf{S}_i \cdot \mathbf{m}_n, \tag{3.3}$$

where $n \in \{1,2,3\}$ signifies the sublattice.

We can use Eq. (3.3) to write down self-consistency equations for $\mathbf{m}_n$:

$$\begin{aligned} \mathbf{m}_n = \langle \mathbf{S}_{i \in l_n} \rangle &= \frac{\operatorname{Tr} \mathbf{S}_{i \in l_n} \exp\left[3\beta J \sum\limits_{i \in l_n} \mathbf{S}_i \cdot \mathbf{m}_n \right]}{\operatorname{Tr} \exp\left[3\beta J \sum\limits_{i \in l_n} \mathbf{S}_i \cdot \mathbf{m}_n \right]} \\ \Rightarrow m_n^j &= \frac{3}{N} \frac{1}{3\beta J} \frac{\partial \ln Z_n}{\partial m_n^j}. \end{aligned} \tag{3.4}$$

Here, $j \in \{x,y,z\}$, while the $3/N$ comes from the fact that each sublattice consists of $N/3$ lattice sites. The partition function corresponding to sublattice n is given by

$$\begin{aligned} Z_n &= \operatorname{Tr} \exp\left[3\beta J \sum_{i \in l_n} \mathbf{S}_i \cdot \mathbf{m}_n \right] \\ &= \left(\frac{1}{4\pi} \int_0^{2\pi} \int_0^{\pi} e^{3\beta J m_n \cos\theta} \sin\theta \mathrm{d}\theta \mathrm{d}\phi \right)^{N/3} \\ &= \left(\frac{\sinh(3\beta J m_n)}{3\beta J m_n} \right)^{N/3}, \end{aligned} \tag{3.5}$$

where we used that $\mathbf{S}_i \cdot \mathbf{m}_n = |\mathbf{S}_i||\mathbf{m}_n| \cos\theta_i = m_n \cos\theta_i$, with $m_n \equiv \sqrt{(m_n^x)^2 + (m_n^y)^2 + (m_n^z)^2}$. Plugging this result back into Eq. (3.4), we find

$$m_n^j = \left(\frac{1}{\tanh(3\beta J m_n)} - \frac{1}{3\beta J m_n} \right) \frac{m_n^j}{m_n}. \tag{3.6}$$

The final form of the self-consistency equation for the absolute values of the magnetizations $\mathbf{m}_n$ is thus

$$m_n = \frac{1}{\tanh(3\beta J m_n)} - \frac{1}{3\beta J m_n}. \tag{3.7}$$

This result, assuming that fluctuations can safely be neglected (which they cannot, as we will see in Sec. 3.4), implies the existence of a phase transition. To see this, we can graphically solve Eq. (3.7) for different values of β, which is done in Fig. 3.1. For high temperatures (i.e. small β), the only solution

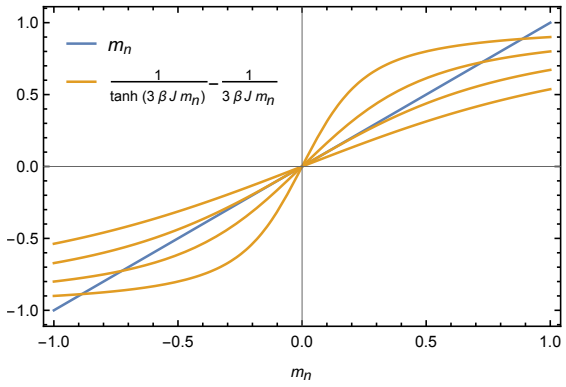

Figure 3.1: Graphic solution of Eq. (3.7) for different values of β.

is $m_n = 0$. However, for lower temperatures there are also solutions for non-zero values of m_n. This implies that the system will go into an ordered phase for sufficiently low temperatures.

Finally, let us calculate the critical temperature that follows from Eq. (3.7). As can be seen from Fig. 3.1, the critical temperature is the temperature for which the derivative of the right-hand side with respect to m_n is equal to 1 for $m_n = 0$. This derivative is given by

$$\frac{1}{3\beta J m_n^2} - \frac{3\beta J}{\sinh^2(3\beta J m_n)}. \tag{3.8}$$

Using the Taylor series

$$\frac{1}{\sinh^2 x} = \frac{1}{x^2} - \frac{1}{3} + \mathcal{O}(x^2), \tag{3.9}$$

we find

$$\lim_{m_n \to 0} \left(\frac{1}{3\beta_c J m_n^2} - \frac{3\beta_c J}{\sinh^2(3\beta_c J m_n)} \right) = \beta_c J = 1, \tag{3.10}$$

so the critical temperature is given by

$$k_B T_c = J. \tag{3.11}$$

3.1.2 Variational mean-field theory

Next, we will consider variational mean-field theory, using the principles described by Falk [14]. However, before we do so, we will rewrite our spin variables in terms of rotated variables. The rotation matrix corresponding to a rotation of angle θ about a unit vector $\hat{\mathbf{u}}_i = (u_{i,x}, u_{i,y}, u_{i,z})$ is given by

$$\mathbf{R}_i(\theta) = \begin{pmatrix} \cos\theta + u_{i,x}^2(1-\cos\theta) & u_{i,x}u_{i,y}(1-\cos\theta) - u_{i,z}\sin\theta & u_{i,x}u_{i,z}(1-\cos\theta) + u_{i,y}\sin\theta \\ u_{i,y}u_{i,x}(1-\cos\theta) + u_{i,z}\sin\theta & \cos\theta + u_{i,y}^2(1-\cos\theta) & u_{i,y}u_{i,z}(1-\cos\theta) - u_{i,x}\sin\theta \\ u_{i,z}u_{i,x}(1-\cos\theta) - u_{i,y}\sin\theta & u_{i,z}u_{i,y}(1-\cos\theta) + u_{i,x}\sin\theta & \cos\theta + u_{i,z}^2(1-\cos\theta) \end{pmatrix}, \tag{3.12}$$

which can straightforwardly be derived by applying a sequence of rotations about the basis vectors $\hat{\mathbf{x}}$, $\hat{\mathbf{y}}$ and $\hat{\mathbf{z}}$. Next, we introduce a new spin variable:

$$\mathbf{M}_i \equiv \mathbf{R}_i(-\mathbf{q}\cdot\mathbf{r}_i)\cdot\mathbf{S}_i, \tag{3.13}$$

where $\mathbf{q}$ is the wave vector corresponding to the periodicity of the ground state configuration. We allow the rotation axis $\hat{\mathbf{u}}_i$ to depend on the lattice site, such that we may in principle include fluctuations. However, we assume that the rotation axis changes slow enough that it can be taken the same for neighbouring lattice sites. In terms of these new variables, the Hamiltonian becomes

$$\begin{aligned} H &= \frac{1}{2}\sum_{ij} J_{ij}(\mathbf{R}_i(\mathbf{q}\cdot\mathbf{r}_i)\cdot\mathbf{M}_i)^T\cdot(\mathbf{R}_i(\mathbf{q}\cdot\mathbf{r}_j)\cdot\mathbf{M}_j) \\ &= \frac{1}{2}\sum_{ij} \mathbf{M}_i\cdot J_{ij}\mathbf{R}_i(\mathbf{q}\cdot(\mathbf{r}_j-\mathbf{r}_i))\cdot\mathbf{M}_j. \end{aligned} \tag{3.14}$$

Since $\mathbf{q}\cdot(\mathbf{r}_j-\mathbf{r}_i)=\pm 2\pi/3$, it is also useful to know how the rotation matrix corresponding to such rotations acts on an arbitrary vector $\mathbf{A}$. It is straightforward to show that

$$\mathbf{R}_i(\pm 2\pi/3)\cdot\mathbf{A}=\frac{1}{2}\left(3(\hat{\mathbf{u}}_i\cdot\mathbf{A})\hat{\mathbf{u}}_i-\mathbf{A}\pm\sqrt{3}(\hat{\mathbf{u}}_i\times\mathbf{A})\right). \tag{3.15}$$

With these preliminaries out of the way, let us consider variational mean-field theory [14]. In this theory, one writes down a free energy according to an unknown probability density ρ. In the mean-field approximation, we assume that this probability density is the product of independent single site probability densities:

$$\rho=\prod_i \rho_i. \tag{3.16}$$

The free energy corresponding to this probability density is given by

$$F_\rho=\operatorname{Tr}\rho H+k_BT\sum_i \operatorname{Tr}\rho_i\ln\rho_i. \tag{3.17}$$

The actual Helmholtz free energy of the system is obtained by minimizing F_ρ with respect to ρ by means of variational differentiation, under the constraint $\operatorname{Tr}\rho=1$. We will now apply this to the model at hand along the lines of Chaikin & Lubensky [10].

Using Eq. (3.16), we immediately see that our free energy functional is given by

$$F_\rho=\frac{1}{2}\sum_{ij}\langle\mathbf{M}_i\rangle\cdot J_{ij}\mathbf{R}_i(\mathbf{q}\cdot(\mathbf{r}_j-\mathbf{r}_i))\cdot\langle\mathbf{M}_j\rangle+k_BT\sum_i\int_0^{2\pi}\int_0^{\pi}\rho_i(\theta_i,\phi_i)\ln(\rho_i(\theta_i,\phi_i))\sin\theta_i\mathrm{d}\theta_i\mathrm{d}\phi_i, \tag{3.18}$$

where the expectation value $\langle\mathbf{M}_i\rangle$ is defined as

$$\begin{aligned}\langle\mathbf{M}_i\rangle\equiv\operatorname{Tr}\rho_i\mathbf{M}_i&=\int\mathrm{d}\Omega_i\mathbf{M}_i(\Omega_i)\rho_i(\Omega_i)\\&=\int_0^{2\pi}\int_0^{\pi}\mathbf{M}_i(\theta_i,\phi_i)\rho_i(\theta_i,\phi_i)\sin\theta_i\mathrm{d}\theta_i\mathrm{d}\phi_i.\end{aligned} \tag{3.19}$$

In these expressions, θ_i and ϕ_i are the angles that fix the direction of the rotated spin variable $\mathbf{M}_i$, and the corresponding solid angle is denoted as Ω_i. Minimizing Eq. (3.18) with respect to ρ_i under the constraint $\operatorname{Tr}\rho_i=1$ gives

$$\frac{\delta F_\rho}{\delta\rho_i}=-\mathbf{M}_i\cdot\mathbf{h}_i^e+k_BT(\ln\rho_i+1)=\lambda_i, \tag{3.20}$$

$$\mathbf{h}_i^e\equiv-\sum_j J_{ij}\mathbf{R}_i(\mathbf{q}\cdot(\mathbf{r}_j-\mathbf{r}_i))\cdot\langle\mathbf{M}_j\rangle. \tag{3.21}$$

Here, λ_i is a Lagrange multiplier used to satisfy the constraint, while $\mathbf{h}_i^e$ is the effective field acting on site i. Solving Eq. (3.20) for ρ_i gives us the probability density:

$$\rho_i=\frac{1}{Z_i}e^{\beta\mathbf{h}_i^e\cdot\mathbf{M}_i}, \tag{3.22}$$

with

$$Z_i=\int\mathrm{d}\Omega_i e^{\beta\mathbf{h}_i^e\cdot\mathbf{M}_i}. \tag{3.23}$$

The next step is to calculate the effective field $\mathbf{h}_i^e$. For convenience, let us write $\langle\mathbf{M}_j\rangle\equiv\boldsymbol{\eta}_j$. The nearest neighbours of the lattice site at position $\mathbf{r}$ are located at $\mathbf{r}+\mathbf{a}_k$. In the basis where $\mathbf{q}=(2\pi/3a,2\pi/\sqrt{3}a)$, the vectors $\mathbf{a}_k$ are given by

$$\begin{aligned}\mathbf{a}_1=a(1,0),\ \mathbf{a}_2=-a(1,0),\ \mathbf{a}_3=-\frac{a}{2}(1,\sqrt{3}),\\ \mathbf{a}_4=\frac{a}{2}(1,\sqrt{3}),\ \mathbf{a}_5=\frac{a}{2}(-1,\sqrt{3}),\ \mathbf{a}_6=-\frac{a}{2}(-1,\sqrt{3}).\end{aligned} \tag{3.24}$$

Hence, for nearest neighbour k, the rotation angle $\mathbf{q}\cdot(\mathbf{r}_j-\mathbf{r}_i)$ is given by $(-1)^{k+1}2\pi/3$. Combining this with Eqs. (3.15) and (3.21), we find

$$\mathbf{h}_i^e \equiv \mathbf{h}^e(\mathbf{r}_i) = -\frac{J}{2}\left[3\left(\hat{\mathbf{u}}_i\cdot\sum_k \boldsymbol{\eta}(\mathbf{r}_i+\mathbf{a}_k)\right)\hat{\mathbf{u}}_i - \sum_k \boldsymbol{\eta}(\mathbf{r}_i+\mathbf{a}_k) - \sqrt{3}\left(\hat{\mathbf{u}}_i\times\sum_k(-1)^k\boldsymbol{\eta}(\mathbf{r}_i+\mathbf{a}_k)\right)\right]. \tag{3.25}$$

To make sense of this expression, we can expand $\boldsymbol{\eta}(\mathbf{r}_i+\mathbf{a}_k)$ for small lattice spacing a:

$$\boldsymbol{\eta}(\mathbf{r}_i+\mathbf{a}_k) = \boldsymbol{\eta}(\mathbf{r}_i) + \frac{\partial\boldsymbol{\eta}(\mathbf{r}_i)}{\partial r^\mu}a_k^\mu + \frac{1}{2}\frac{\partial^2\boldsymbol{\eta}(\mathbf{r}_i)}{\partial r^\mu\partial r^\nu}a_k^\mu a_k^\nu + \mathcal{O}(a^3). \tag{3.26}$$

Here, $\mu,\nu\in\{x,y,z\}$, and summation over μ and ν is implied. It is now straightforward to check that

$$\sum_k \boldsymbol{\eta}(\mathbf{r}_i+\mathbf{a}_k) = 6\boldsymbol{\eta}(\mathbf{r}_i) + \frac{3a^2}{2}\nabla^2\boldsymbol{\eta}(\mathbf{r}_i) + \mathcal{O}(a^3), \tag{3.27}$$

while $\sum_k(-1)^k\boldsymbol{\eta}(\mathbf{r}_i+\mathbf{a}_k)$ vanishes up to second order in a. We conclude that (up to second order in a) the effective field is given by

$$\mathbf{h}^e(\mathbf{r}_i) = -\frac{J}{2}\left[3\left(\hat{\mathbf{u}}_i\cdot\left(6\boldsymbol{\eta}(\mathbf{r}_i)+\frac{3a^2}{2}\nabla^2\boldsymbol{\eta}(\mathbf{r}_i)\right)\right)\hat{\mathbf{u}}_i - 6\boldsymbol{\eta}(\mathbf{r}_i) - \frac{3a^2}{2}\nabla^2\boldsymbol{\eta}(\mathbf{r}_i)\right]. \tag{3.28}$$

If we further take $\hat{\mathbf{u}}_i$ to be perpendicular to $\boldsymbol{\eta}_i$, we finally arrive at

$$\mathbf{h}^e(\mathbf{r}_i) = 3J\boldsymbol{\eta}(\mathbf{r}_i) + \frac{3Ja^2}{4}\left(\nabla^2\boldsymbol{\eta}(\mathbf{r}_i) - 3\left(\hat{\mathbf{u}}_i\cdot\nabla^2\boldsymbol{\eta}(\mathbf{r}_i)\right)\hat{\mathbf{u}}_i\right). \tag{3.29}$$

Now that the effective field has been calculated, let us return to the variational mean-field theory itself. Using Eq. (3.22), we can once again write down a self-consistency equation:

$$\boldsymbol{\eta}_i \equiv \langle\mathbf{M}_i\rangle = \frac{1}{Z_i}\int \mathrm{d}\Omega_i \mathbf{M}_i e^{\beta\mathbf{h}_i^e\cdot\mathbf{M}_i}. \tag{3.30}$$

If we assume that $\boldsymbol{\eta}_i$ uniform, the effective field becomes $\mathbf{h}_i^e = 3J\boldsymbol{\eta}$, and the self-consistency equation becomes

$$\boldsymbol{\eta} = \frac{1}{Z_i}\int \mathrm{d}\Omega_i \mathbf{M}_i e^{3\beta J\boldsymbol{\eta}\cdot\mathbf{M}_i}. \tag{3.31}$$

In essence, this is the same self-consistency equation as Eq. (3.4), and therefore we find

$$|\boldsymbol{\eta}| \equiv \eta = \frac{1}{\tanh(3\beta J\eta)} - \frac{1}{3\beta J\eta}. \tag{3.32}$$

This result demonstrates that the two given mean-field methods both yield the same results, and hence that they both lead to the same (incorrect) conclusions about a phase transition and the corresponding critical temperature.

3.1.3 Mean-field approximation using a Hubbard-Stratonovich transformation and the relation with Landau theory

In this section, we will rewrite the partition function in an exact way by using Gaussian integral identities, then performing a mean-field approximation to extract results from the new form. We start with the Hamiltonian from Eq. (3.14) and introducing some new variables:

$$H = \frac{1}{2}\sum_{ij}\tilde{M}_i A_{ij}\tilde{M}_j. \tag{3.33}$$

Here, $i,j\in\{1,2,...,3N\}$, and the new variables are defined as

$$\tilde{\mathbf{M}} \equiv (\mathbf{M}_1,\mathbf{M}_2,...,\mathbf{M}_N), \tag{3.34}$$

$$\mathbf{A} \equiv \begin{pmatrix} J_{11}\mathbf{R}_1(0) & J_{12}\mathbf{R}_1(\mathbf{q}\cdot(\mathbf{r}_2-\mathbf{r}_1)) & \cdots & J_{1N}\mathbf{R}_1(\mathbf{q}\cdot(\mathbf{r}_N-\mathbf{r}_1)) \\ J_{21}\mathbf{R}_2(\mathbf{q}\cdot(\mathbf{r}_1-\mathbf{r}_2)) & J_{22}\mathbf{R}_2(0) & \cdots & J_{2N}\mathbf{R}_2(\mathbf{q}\cdot(\mathbf{r}_N-\mathbf{r}_2)) \\ \vdots & \vdots & \ddots & \vdots \\ J_{N1}\mathbf{R}_N(\mathbf{q}\cdot(\mathbf{r}_1-\mathbf{r}_N)) & J_{N2}\mathbf{R}_N(\mathbf{q}\cdot(\mathbf{r}_2-\mathbf{r}_N)) & \cdots & J_{NN}\mathbf{R}_N(0) \end{pmatrix}. \tag{3.35}$$

Now consider the following Gaussian integral identity with real degrees of freedom $x_1, ..., x_N$:

$$\begin{aligned} &\int \left(\prod_{i=1}^{N} \frac{\mathrm{d}x_i}{\sqrt{2\pi}}\right) \exp\left[\frac{1}{2}\sum_{ij} x_i G_{ij} x_j - \sum_{ij} b_i G_{ij} x_j\right] \\ &= \frac{1}{\sqrt{\mathrm{Det}(-\mathbf{G})}} \exp\left[-\frac{1}{2}\sum_{ij} b_i G_{ij} b_j\right] \\ &\equiv \mathcal{N} \exp\left[-\frac{1}{2}\sum_{ij} b_i G_{ij} b_j\right]. \end{aligned} \tag{3.36}$$

A derivation of this identity can be found in appendix A.3. Using this integral, we can rewrite the partition function:

$$\begin{aligned} Z &= \left(\prod_i \frac{1}{4\pi} \int_0^{2\pi} \mathrm{d}\phi_i \int_0^{\pi} \mathrm{d}\theta_i \sin\theta_i\right) \exp\left[-\frac{\beta}{2}\sum_{ij} J_{ij}\mathbf{S}_i\cdot\mathbf{S}_j\right] \\ &\equiv \int \mathcal{D}\Omega \exp\left[-\frac{\beta}{2}\sum_{ij} J_{ij}\mathbf{S}_i\cdot\mathbf{S}_j\right] \\ &= \int \mathcal{D}\Omega \exp\left[-\frac{\beta}{2}\sum_{ij} \tilde{M}_i A_{ij} \tilde{M}_j\right] \\ &= \int \mathcal{D}\Omega \frac{1}{\mathcal{N}} \left(\prod_{i=1}^{3N} \frac{\mathrm{d}\tilde{\eta}_i}{\sqrt{2\pi}}\right) \exp\left[\frac{\beta}{2}\sum_{ij} \tilde{\eta}_i A_{ij} \tilde{\eta}_j - \beta \sum_{ij} \tilde{M}_i A_{ij} \tilde{\eta}_j\right]. \end{aligned} \tag{3.37}$$

If we now define $\tilde{\boldsymbol{\eta}} \equiv (\boldsymbol{\eta}_1, \boldsymbol{\eta}_2, ..., \boldsymbol{\eta}_N)$, this expression becomes

$$\begin{aligned} Z &= \int \mathcal{D}\Omega\mathcal{D}\boldsymbol{\eta} \exp\left[\frac{\beta}{2}\sum_{ij} \boldsymbol{\eta}_i \cdot J_{ij}\mathbf{R}_i(\mathbf{q}\cdot(\mathbf{r}_j-\mathbf{r}_i))\cdot\boldsymbol{\eta}_j - \beta\sum_{ij} \mathbf{M}_i \cdot J_{ij}\mathbf{R}_i(\mathbf{q}\cdot(\mathbf{r}_j-\mathbf{r}_i))\cdot\boldsymbol{\eta}_j\right] \\ &= \int \mathcal{D}\Omega\mathcal{D}\boldsymbol{\eta} \exp\left[-\frac{\beta}{2}\sum_i \boldsymbol{\eta}_i\cdot\mathbf{h}_i^e + \beta\sum_i \mathbf{M}_i\cdot\mathbf{h}_i^e\right]. \end{aligned} \tag{3.38}$$

For this last step, we used Eq. (3.21) from last section. The $\boldsymbol{\eta}_i$'s and therefore the effective fields from this section and the previous one are not necessarily the same, but we will see later on that they actually are. The exponent in this final expression only contains linear terms in $\mathbf{M}_i$, and we can therefore perform our original integral over Ω. The integral is essentially the same as the one in Eq. (3.5), so we can immediately evaluate it:

$$\begin{aligned} Z &= \int \mathcal{D}\boldsymbol{\eta} \exp\left[-\frac{\beta}{2}\sum_i \boldsymbol{\eta}_i\cdot\mathbf{h}_i^e\right] \prod_i \frac{\sinh(\beta h_i^e)}{\beta h_i^e} \\ &= \int \mathcal{D}\boldsymbol{\eta} \exp\left[-\frac{\beta}{2}\sum_i \boldsymbol{\eta}_i\cdot\mathbf{h}_i^e + \sum_i \left(\ln\sinh(\beta h_i^e) - \ln(\beta h_i^e)\right)\right], \end{aligned} \tag{3.39}$$

where $h_i^e \equiv |\mathbf{h}_i^e|$. This is our final expression for the partition function Z. The above transformation is a so-called Hubbard-Stratonovich transformation, and it is important to note that the final expression

Eq. (3.39) is exact. Referring back to Eq. (2.5) at the start of Ch. 2, we see that this expression for the partition function is the same as it is for Landau theory, provided that $\boldsymbol{\eta}$ is indeed the order parameter. If this is the case, we can now immediately read off the Landau free energy from the exponent.

Let us now turn to the mean-field approximation. In this case, the mean-field approximation is that we assume that the most probable value of the integrand is the only relevant contribution to the functional integral. In other words: the partition function Z is approximated to be equal to the integrand of the functional integral, evaluated at its maximum value with respect to $\boldsymbol{\eta}_i$. In this approximation, we find the Helmholtz free energy

$$\begin{aligned} F = -k_B T \ln Z &= \min_{\boldsymbol{\eta}_i} \left[\frac{1}{2} \sum_i \boldsymbol{\eta}_i \cdot \mathbf{h}_i^e - k_B T \sum_i \left(\ln \sinh(\beta h_i^e) - \ln(\beta h_i^e) \right) \right] \\ &= \min_{\boldsymbol{\eta}_i} L[\boldsymbol{\eta}_i], \end{aligned} \tag{3.40}$$

where $L[\boldsymbol{\eta}_i]$ is the Landau free energy. Under the assumption that $\boldsymbol{\eta}_i$ is uniform (i.e. $\mathbf{h}_i^e = 3J\boldsymbol{\eta}$), we obtain

$$L = \frac{3JN}{2}\eta^2 - Nk_B T(\ln \sinh(3\beta J\eta) - \ln(3\beta J\eta)), \tag{3.41}$$

again with $|\boldsymbol{\eta}| \equiv \eta$. Minimizing this Landau free energy with respect to η once again gives us Eq. (3.32), confirming that this $\boldsymbol{\eta}$ can indeed be identified as the order parameter $\langle \mathbf{M} \rangle$, and that this mean-field method gives the same results as the previous ones.

Finally, we will look at the situation that $\boldsymbol{\eta}_i$ is not uniform. To do so, consider the continuum limit: the small a limit, with $\boldsymbol{\eta}_i \to \boldsymbol{\eta}(\mathbf{r})$, $\mathbf{h}_i^e \to \mathbf{h}^e(\mathbf{r})$ and $\sum_i \to N/V \int \mathrm{d}\mathbf{r}$. Since we are interested in the region close to the critical point, we expand the Landau free energy for small $\boldsymbol{\eta}(\mathbf{r})$. Using the series

$$\ln \sinh x - \ln x = \frac{x^2}{6} - \frac{x^4}{180} + \mathcal{O}(x^6), \tag{3.42}$$

we find the following Landau free energy:

$$\begin{aligned} L[\boldsymbol{\eta}(\mathbf{r})] &= \frac{N}{V} \int \mathrm{d}\mathbf{r} \left[\frac{1}{2} \boldsymbol{\eta}(\mathbf{r}) \cdot \mathbf{h}^e(\mathbf{r}) - k_B T \left(\frac{\beta^2 |\mathbf{h}^e(\mathbf{r})|^2}{6} - \frac{\beta^4 |\mathbf{h}^e(\mathbf{r})|^4}{180} + ... \right) \right] \\ &\equiv \frac{N}{V} \int \mathrm{d}\mathbf{r} f(\mathbf{r}). \end{aligned} \tag{3.43}$$

Here, $f(\mathbf{r})$ is the Landau free energy density. Additionally, we only keep terms up to lowest non-trivial order in a, such that

$$\boldsymbol{\eta}(\mathbf{r}) \cdot \mathbf{h}^e(\mathbf{r}) = 3J|\boldsymbol{\eta}(\mathbf{r})|^2 + \frac{3Ja^2}{4} \boldsymbol{\eta}(\mathbf{r}) \cdot \nabla^2 \boldsymbol{\eta}(\mathbf{r}) + ..., \tag{3.44}$$

$$|\mathbf{h}^e(\mathbf{r})|^2 = 9J^2|\boldsymbol{\eta}(\mathbf{r})|^2 + \frac{9J^2a^2}{2} \boldsymbol{\eta}(\mathbf{r}) \cdot \nabla^2 \boldsymbol{\eta}(\mathbf{r}) + ..., \tag{3.45}$$

$$|\mathbf{h}^e(\mathbf{r})|^4 = 81J^4|\boldsymbol{\eta}(\mathbf{r})|^4 + ..., \tag{3.46}$$

where we used that $\hat{\mathbf{u}}(\mathbf{r})$ is chosen such that $\boldsymbol{\eta}(\mathbf{r}) \cdot \hat{\mathbf{u}}(\mathbf{r}) = 0$. With these, the Landau free energy becomes

$$L[\boldsymbol{\eta}(\mathbf{r})] = \frac{N}{V} \int \mathrm{d}\mathbf{r} \left[\frac{3Ja^2}{8}(1 - 2\beta J) \boldsymbol{\eta}(\mathbf{r}) \cdot \nabla^2 \boldsymbol{\eta}(\mathbf{r}) + \frac{3J}{2}(1 - \beta J)|\boldsymbol{\eta}(\mathbf{r})|^2 + \frac{9\beta^3 J^4}{20} |\boldsymbol{\eta}(\mathbf{r})|^4 + ... \right]. \tag{3.47}$$

Again, this implies a critical temperature of $k_B T_c = J$, because that is the temperature at which the coefficient in front of the quadratic term changes sign. Close to this temperature, we obtain

$$L[\boldsymbol{\eta}(\mathbf{r})] = \frac{N}{V} \int \mathrm{d}\mathbf{r} \left[-\frac{3Ja^2}{8} \boldsymbol{\eta}(\mathbf{r}) \cdot \nabla^2 \boldsymbol{\eta}(\mathbf{r}) + \frac{3Jt}{2} |\boldsymbol{\eta}(\mathbf{r})|^2 + \frac{9J}{20} |\boldsymbol{\eta}(\mathbf{r})|^4 + ... \right], \tag{3.48}$$

where $t \equiv (T - T_c)/T_c$, showing that the Landau free energy can also fully be derived from the microscopic Hamiltonian. However, we will see in Sec. 3.4 that mean-field theory alone is not enough, hence the interpretation from simply minimizing L does not give the correct results for this two-dimensional system.

3.2 Variational mean-field theory revisited

While the methods covered in the previous section are very useful for a lattice with unit cells containing only a single lattice site, it is not straightforward to generalize them to more complicated lattices. In order to be able to develop a mean-field theory for the Swedenborgite HAFM, we will now revisit the principles of variational mean-field theory and use it to formulate a framework that can be applied to general spin models, including those on a complicated lattice. Doing so, we will closely follow the methods described by Reimers, Berlinsky, and Shi in Ref. [15].

3.2.1 Real space free energy

Previously, we used our knowledge of the ground state of the antiferromagnetic Heisenberg model on the triangular lattice to rewrite the Hamiltonian in terms of rotated spin variables. Now, we will keep the original spin variables, such that the associated magnetization will become periodic rather than constant for the ground state. The advantage of this is that the following procedure is independent of the lattice and can be applied in general.

As before, we consider the Heisenberg Hamiltonian:

$$H = \frac{1}{2}\sum_{ij} J_{ij}\mathbf{S}_i \cdot \mathbf{S}_j, \tag{3.49}$$

where we now sum over all lattice sites i, j, while J_{ij} is defined to be equal to J (with $J > 0$) if i, j are nearest neighbours and zero otherwise. We start by writing down the mean-field free energy F_ρ according to Eq. (3.17), where ρ is again the product of single site probability densities $\rho_i(\theta_i, \phi_i)$, the angles θ_i, ϕ_i are now the angles describing the direction of spin $\mathbf{S}_i$, and the trace is now defined as

$$\mathrm{Tr} \equiv \int \mathcal{D}\Omega = \prod_i \left(\frac{1}{4\pi} \int_0^{2\pi} \mathrm{d}\phi_i \int_0^{\pi} \mathrm{d}\theta_i \sin\theta_i \right). \tag{3.50}$$

As we discussed in Sec. 3.1.2, the actual free energy of the system is obtained by minimizing F_ρ with respect to ρ_i by means of variational differentiation, under the constraint $\mathrm{Tr}\,\rho_i = 1$. Additionally, rather than obtaining a self-consistency equation later on, we now introduce the order parameter by means of another constraint:

$$\mathrm{Tr}\,\rho_i \mathbf{S}_i = \langle \mathbf{S}_i \rangle \equiv \mathbf{m}_i. \tag{3.51}$$

Minimization of F_ρ under the above constraints gives

$$\frac{\delta F_\rho}{\delta \rho_i} = \mathbf{S}_i \cdot \left(\sum_j J_{ij}\mathbf{m}_j \right) + k_B T(\ln \rho_i + 1) = \lambda_i + \mathbf{S}_i \cdot \mathbf{\Lambda}_i. \tag{3.52}$$

Here, λ_i and $\mathbf{\Lambda}_i$ are Lagrange multipliers used to satisfy the constraints. Since these multipliers are unknown constants that are to be found later, they can be used to absorb some of the terms by redefining them. Writing $\mathbf{\Lambda}_i \to \mathbf{\Lambda}_i + \sum_j J_{ij}\mathbf{m}_j$, this equation gives

$$\rho_i = \frac{1}{Z_i} e^{\beta \mathbf{\Lambda}_i \cdot \mathbf{S}_i}, \tag{3.53}$$

with

$$\begin{aligned} Z_i &= \int \mathrm{d}\Omega_i e^{\beta \mathbf{\Lambda}_i \cdot \mathbf{S}_i} \\ &= \frac{\sinh(\beta\Lambda_i)}{\beta\Lambda_i} \end{aligned} \tag{3.54}$$

and $\Lambda_i \equiv |\mathbf{\Lambda}_i|$. Using the above results, we find the free energy

$$\begin{aligned} F &= \frac{1}{2}\sum_{ij} J_{ij}\mathbf{m}_i \cdot \mathbf{m}_j + k_B T \sum_i \left(\beta \mathbf{\Lambda}_i \cdot \operatorname{Tr}\rho_i \mathbf{S}_i - \operatorname{Tr}\rho_i \ln Z_i\right) \\ &= \frac{1}{2}\sum_{ij} J_{ij}\mathbf{m}_i \cdot \mathbf{m}_j + \sum_i \left(\mathbf{\Lambda}_i \cdot \mathbf{m}_i - k_B T \ln\left(\frac{\sinh(\beta\Lambda_i)}{\beta\Lambda_i}\right)\right). \end{aligned} \tag{3.55}$$

The next step is to expand $\mathbf{\Lambda}_i$ in terms of $\mathbf{m}_i$. To do so, we first write down the equation for $\mathbf{m}_i$ in terms of $\mathbf{\Lambda}_i$:

$$\begin{aligned} \mathbf{m}_i &= \operatorname{Tr}\rho_i \mathbf{S}_i = \frac{1}{\beta}\nabla_{\mathbf{\Lambda}_i} \ln Z_i \\ &= \left(\frac{1}{\tanh(\beta\Lambda_i)} - \frac{1}{\beta\Lambda_i}\right)\hat{\mathbf{\Lambda}}_i. \end{aligned} \tag{3.56}$$

The absolute value m_i can thus be expanded as

$$m_i = \frac{\beta\Lambda_i}{3} - \frac{\beta^3\Lambda_i^3}{45} + \mathcal{O}(\Lambda_i^5). \tag{3.57}$$

Inverting this expression gives

$$\beta\Lambda_i = 3m_i + \frac{9}{5}m_i^3 + \mathcal{O}(m_i^5). \tag{3.58}$$

Additionally, this result can be used to find

$$\ln Z_i = \frac{3}{2}m_i^2 + \frac{27}{20}m_i^4 + \mathcal{O}(m_i^6). \tag{3.59}$$

With these expansions, the free energy becomes

$$F = \frac{1}{2}\sum_{ij}(J_{ij} + 3k_B T\delta_{ij})\mathbf{m}_i \cdot \mathbf{m}_j + \frac{9}{20}k_B T\sum_i m_i^4 + \mathcal{O}(m_i^6), \tag{3.60}$$

where δ_{ij} is the Kronecker delta.

This final expression is the general low-field expansion of the mean-field free energy for the antiferromagnetic Heisenberg model on an arbitrary lattice. However, this form of the free energy can be hard to work with on complicated lattices. In order to make sense of it, we can work on the level of unit cells rather than individual lattice sites. To do so, we write $\mathbf{m}_i \to \mathbf{m}_i^a$, $J_{ij} \to J_{ij}^{ab}$ and $\delta_{ij} \to \delta_{ij}^{ab}$. Here i, j refer to the unit cells while a, b refer to the different sites within the unit cells (i.e. the sublattices). For a lattice with unit cells consisting of n lattice sites, this means that i, j go from 1 to $N/n \equiv N_c$ (where N is the total number of lattice sites), while a, b go from 1 to n. With this notation, the free energy simply becomes

$$F = \frac{1}{2}\sum_{ab}\sum_{ij}\left(J_{ij}^{ab} + 3k_B T\delta_{ij}^{ab}\right)\mathbf{m}_i^a \cdot \mathbf{m}_j^b + \frac{9}{20}k_B T\sum_a\sum_i (m_i^a)^4 + \mathcal{O}\left((m_i^a)^6\right). \tag{3.61}$$

3.2.2 Momentum space free energy

Due to the often complicated form of J_{ij}^{ab}, the free energy given in Eq. (3.61) is often still not very useful. Therefore, we will make use of the lattice symmetries by Fourier transforming the free energy with respect to the unit cells. Noting that $\mathbf{m}_i^a = \mathbf{m}_{\mathbf{r}_i}^a$ (where $\mathbf{r}_i$ is the position of unit cell i), $J_{ij}^{ab} = J_{\mathbf{r}_{ij}}^{ab}$ (with $\mathbf{r}_{ij} \equiv \mathbf{r}_i - \mathbf{r}_j$) and $\delta_{ij}^{ab} = \delta_{\mathbf{r}_{ij}}^{ab}$, the Fourier transform is given by

$$\mathbf{m}_{\mathbf{r}_i}^a = \sum_{\mathbf{q}} \mathbf{m}_{\mathbf{q}}^a e^{i\mathbf{q}\cdot\mathbf{r}_i}, \tag{3.62}$$

$$J_{\mathbf{r}_{ij}}^{ab} = \frac{1}{N_c}\sum_{\mathbf{q}} J_{\mathbf{q}}^{ab} e^{i\mathbf{q}\cdot\mathbf{r}_{ij}}, \tag{3.63}$$

$$\delta_{\mathbf{r}_{ij}}^{ab} = \delta^{ab}\frac{1}{N_c}\sum_{\mathbf{q}} e^{i\mathbf{q}\cdot\mathbf{r}_{ij}}. \tag{3.64}$$

The components of the free energy become

$$\begin{aligned}
\sum_{ij} J_{ij}^{ab}\mathbf{m}_i^a\cdot\mathbf{m}_j^b &= \frac{1}{N_c}\sum_{ij}\sum_{\mathbf{q}_1,\mathbf{q}_2,\mathbf{q}_3} J_{\mathbf{q}_1}^{ab}\mathbf{m}_{\mathbf{q}_2}^a\cdot\mathbf{m}_{\mathbf{q}_3}^b e^{i\mathbf{r}_i\cdot(\mathbf{q}_1+\mathbf{q}_2)-i\mathbf{r}_j\cdot(\mathbf{q}_1-\mathbf{q}_3)} \\
&= N_c\sum_{\mathbf{q}} J_{\mathbf{q}}^{ab}\mathbf{m}_{-\mathbf{q}}^a\cdot\mathbf{m}_{\mathbf{q}}^b, \qquad (3.65)\\
\sum_{ij}\delta_{ij}^{ab}\mathbf{m}_i^a\cdot\mathbf{m}_j^b &= \delta^{ab}\frac{1}{N_c}\sum_{ij}\sum_{\mathbf{q}_1,\mathbf{q}_2,\mathbf{q}_3}\mathbf{m}_{\mathbf{q}_2}^a\cdot\mathbf{m}_{\mathbf{q}_3}^b e^{i\mathbf{r}_i\cdot(\mathbf{q}_1+\mathbf{q}_2)-i\mathbf{r}_j\cdot(\mathbf{q}_1-\mathbf{q}_3)} \\
&= \delta^{ab}N_c\sum_{\mathbf{q}}\mathbf{m}_{-\mathbf{q}}^a\cdot\mathbf{m}_{\mathbf{q}}^b, \qquad (3.66)\\
\sum_i (m_i^a)^4 &= \sum_i\left(\mathbf{m}_i^a\cdot\mathbf{m}_i^a\right)^2 \\
&= \sum_i\left(\sum_{\mathbf{q}_1,\mathbf{q}_2}\mathbf{m}_{\mathbf{q}_1}^a\cdot\mathbf{m}_{\mathbf{q}_2}^a e^{i\mathbf{r}_i\cdot(\mathbf{q}_1+\mathbf{q}_2)}\right)^2 \\
&= \sum_i\sum_{\mathbf{q}_1,\mathbf{q}_2,\mathbf{q}_3,\mathbf{q}_4}\left(\mathbf{m}_{\mathbf{q}_1}^a\cdot\mathbf{m}_{\mathbf{q}_2}^a\right)\left(\mathbf{m}_{\mathbf{q}_3}^a\cdot\mathbf{m}_{\mathbf{q}_4}^a\right)e^{i\mathbf{r}_i\cdot(\mathbf{q}_1+\mathbf{q}_2+\mathbf{q}_3+\mathbf{q}_4)} \\
&= N_c\sum_{\mathbf{q}_1,\mathbf{q}_2,\mathbf{q}_3,\mathbf{q}_4}\delta_{\mathbf{q}_1+\mathbf{q}_2+\mathbf{q}_3+\mathbf{q}_4,0}\left(\mathbf{m}_{\mathbf{q}_1}^a\cdot\mathbf{m}_{\mathbf{q}_2}^a\right)\left(\mathbf{m}_{\mathbf{q}_3}^a\cdot\mathbf{m}_{\mathbf{q}_4}^a\right) \\
&\equiv N_c\sum_{\{\mathbf{q}\}}{}'\left(\mathbf{m}_{\mathbf{q}_1}^a\cdot\mathbf{m}_{\mathbf{q}_2}^a\right)\left(\mathbf{m}_{\mathbf{q}_3}^a\cdot\mathbf{m}_{\mathbf{q}_4}^a\right). \qquad (3.67)
\end{aligned}$$

Plugging this back into Eq. (3.61), we see that the free energy per unit cell is equal to

$$F/N_c = \frac{1}{2}\sum_{ab}\sum_{\mathbf{q}}\left(J_{\mathbf{q}}^{ab}+3k_BT\delta^{ab}\right)\mathbf{m}_{-\mathbf{q}}^a\cdot\mathbf{m}_{\mathbf{q}}^b + \frac{9}{20}k_BT\sum_a\sum_{\{\mathbf{q}\}}{}'\left(\mathbf{m}_{\mathbf{q}_1}^a\cdot\mathbf{m}_{\mathbf{q}_2}^a\right)\left(\mathbf{m}_{\mathbf{q}_3}^a\cdot\mathbf{m}_{\mathbf{q}_4}^a\right)+\mathcal{O}\left((m_{\mathbf{q}}^a)^6\right). \qquad (3.68)$$

Next, we will diagonalize the second order term. Since $J_{\mathbf{q}}^{ab}$ is Hermitian, it is diagonalized by

$$J_{\mathbf{q}}^{ab} = \sum_{ij}U_{\mathbf{q}}^{ai}D_{\mathbf{q}}^{ij}(U_{\mathbf{q}}^{-1})^{jb} = \sum_{ij}U_{\mathbf{q}}^{ai}D_{\mathbf{q}}^{ij}(U_{\mathbf{q}}^{\dagger})^{jb}, \qquad (3.69)$$

where i,j now refer to the n normal modes, $U_{\mathbf{q}}^{ai}$ is the unitary diagonalization matrix and

$$D_{\mathbf{q}}^{ij} = \delta^{ij}\lambda_{\mathbf{q}}^i \qquad (3.70)$$

is the diagonal matrix of the eigenvalues of $J_{\mathbf{q}}^{ab}$. It is useful to note that $\mathbf{m}_{-\mathbf{q}}^a = (\mathbf{m}_{\mathbf{q}}^a)^*$ and $(J_{-\mathbf{q}}^{ab})^* = J_{\mathbf{q}}^{ab}$ (and therefore $(U_{-\mathbf{q}}^{ai})^* = U_{\mathbf{q}}^{ai}$), which follows from the fact that their position space counterparts are real. In terms of the normal modes of the system,

$$\mathbf{\Phi}_{\mathbf{q}}^i \equiv \sum_a (U_{\mathbf{q}}^{\dagger})^{ia}\mathbf{m}_{\mathbf{q}}^a, \qquad (3.71)$$

the magnetization becomes

$$\mathbf{m}_{\mathbf{q}}^a = \sum_i U_{\mathbf{q}}^{ai}\mathbf{\Phi}_{\mathbf{q}}^i, \qquad (3.72)$$

and dot products of two magnetizations thus become

$$\begin{aligned}
\sum_a\left(\mathbf{m}_{\mathbf{q}_1}^a\cdot\mathbf{m}_{\mathbf{q}_2}^a\right) &= \sum_a\sum_{ij}U_{\mathbf{q}_1}^{ai}U_{\mathbf{q}_2}^{aj}\mathbf{\Phi}_{\mathbf{q}_1}^i\cdot\mathbf{\Phi}_{\mathbf{q}_2}^j \\
&= \sum_{ij}(U_{\mathbf{q}_1}^T U_{\mathbf{q}_2})^{ij}\mathbf{\Phi}_{\mathbf{q}_1}^i\cdot\mathbf{\Phi}_{\mathbf{q}_2}^j. \qquad (3.73)
\end{aligned}$$

All this can then be used to rewrite the free energy per unit cell in terms of the normal modes:

$$F/N_c = \frac{1}{2}\sum_i \sum_{\mathbf{q}} \left(\lambda^i_{\mathbf{q}} + 3k_BT\right) \mathbf{\Phi}^i_{-\mathbf{q}} \cdot \mathbf{\Phi}^i_{\mathbf{q}} + \frac{9}{20} k_BT \sum_{ijkl} {\sum_{\{\mathbf{q}\}}}' \left(\mathbf{\Phi}^i_{\mathbf{q}_1} \cdot \mathbf{\Phi}^j_{\mathbf{q}_2}\right) \left(\mathbf{\Phi}^k_{\mathbf{q}_3} \cdot \mathbf{\Phi}^l_{\mathbf{q}_4}\right) \sum_a U^{ai}_{\mathbf{q}_1} U^{aj}_{\mathbf{q}_2} U^{ak}_{\mathbf{q}_3} U^{al}_{\mathbf{q}_4} + \mathcal{O}\left((\Phi^i_{\mathbf{q}})^6\right). \tag{3.74}$$

This expression is again the general low-field expansion of the mean-field free energy of the antiferromagnetic Heisenberg model on an arbitrary lattice, but this time in momentum space. The quadratic term of this expansion implies a phase transition. As usual, there is a phase transition between the region where there are non-zero modes (the ordered phase) and the region where there are no non-zero modes (the disordered phase). In accordance with Landau theory, a mode becomes non-zero when the corresponding quadratic coefficient becomes negative. Hence, Eq. (3.74) implies that there is a phase transition at the point where the first of the modes becomes non-zero, which gives

$$k_BT_c = -\min_{\mathbf{q},i} \lambda^i_{\mathbf{q}}/3. \tag{3.75}$$

Moreover, minimizing the free energy for any temperature shows us that the mode corresponding to the smallest possible eigenvalue is the one that is selected by the system. In the next sections, we will investigate the implications of these general results on the triangular lattice and on the Swedenborgite lattice.

3.2.3 A final look at the triangular lattice

Before we move on to the more complicated Swedenborgite lattice, we briefly show how these methods can be applied to the triangular lattice. On the triangular lattice, there is only one lattice site per unit cell, making the problem much simpler. In particular, the matrix $J^{ab}_{\mathbf{q}}$ becomes a scalar $J_{\mathbf{q}}$, and the diagonalization process becomes obsolete. In order to calculate the Fourier transform of the interaction matrix, we need to define a basis. It is most convenient to work in the basis of the lattice vectors

$$\hat{\mathbf{a}}_1 = \begin{pmatrix} 1 \\ 0 \end{pmatrix}, \qquad \hat{\mathbf{a}}_2 = \frac{1}{2}\begin{pmatrix} 1 \\ \sqrt{3} \end{pmatrix} \tag{3.76}$$

and "deform" the lattice such that these vectors are orthogonal, while preserving the interactions. Then, the nearest neighbours are at $\pm a\hat{\mathbf{a}}_1$, $\pm a\hat{\mathbf{a}}_2$ and $\pm a(\hat{\mathbf{a}}_1 - \hat{\mathbf{a}}_2)$, where a is the lattice constant, and the wave vector can be decomposed as $\mathbf{q} = q_1\hat{\mathbf{a}}_1 + q_2\hat{\mathbf{a}}_2$. Let us now calculate $J_{\mathbf{q}}$:

$$\begin{aligned} J_{\mathbf{q}} &= \sum_{\mathbf{r}_{ij}} J_{\mathbf{r}_{ij}} e^{-i\mathbf{q}\cdot\mathbf{r}_{ij}} \\ &= J\left[e^{-iaq_1} + e^{iaq_1} + e^{-iaq_2} + e^{iaq_2} + e^{-ia(q_1-q_2)} + e^{ia(q_1-q_2)}\right] \\ &= 2J\left[\cos(aq_1) + \cos(aq_2) + \cos(a(q_1 - q_2))\right]. \end{aligned} \tag{3.77}$$

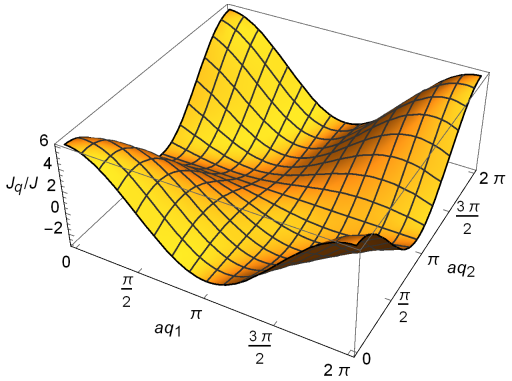

Figure 3.2: Interactions $J_{\mathbf{q}}$ of the antiferromagnetic Heisenberg model on the triangular lattice as a function of the wave vector $\mathbf{q}$.

In the following, we will always absorb a into $\mathbf{q}$. A plot of the resulting expression is shown in Fig. 3.2.

Since the free energy is to be minimized, the mode that will actually appear in the system (provided that the temperature is small enough) is the one that minimizes $J_{\mathbf{q}}$. Doing so, we find $q_1 = 2\pi/3$, $q_2 = 4\pi/3$, or the other way around. These values correspond to a 120° configuration of the magnetization $\mathbf{m}_i$. Plugging this $\mathbf{q}$ back in, we find $J_{\mathbf{q}} = -3J$, which then translates to $k_B T_c = J$. We thus find that there is a phase transition between a disordered phase and an ordered 120° phase, located at the critical temperature $k_B T_c = J$. These results agree with our previous mean-field results.

3.3 Mean-field critical temperature of the Swedenborgite antiferromagnet

In this section, we apply the methods from Sec. 3.2 to the Swedenborgite lattice. To describe the lattice, we will use the same convention as was used in Sec. 1.2. In particular, the basis vectors of the unit cells are given by

$$\hat{\mathbf{a}}_1 = \begin{pmatrix} 1 \\ 0 \\ 0 \end{pmatrix}, \qquad \hat{\mathbf{a}}_2 = \frac{1}{2}\begin{pmatrix} 1 \\ \sqrt{3} \\ 0 \end{pmatrix}, \qquad \hat{\mathbf{a}}_3 = \begin{pmatrix} 0 \\ 0 \\ 1 \end{pmatrix}. \tag{3.78}$$

Using these conventions, referring back to Fig. 1.7, and taking the Fourier transform in the same way as in Sec. 3.2.3, the interaction matrix becomes

$$\mathbf{J}_{\mathbf{q}}/J_1 = \begin{pmatrix} 0 & 1+e^{iq_2} & 1+e^{-i(q_1-q_2)} & \frac{J_2}{J_1} & 0 & 0 & 0 & \frac{J_2}{J_1}e^{iq_3} \\ 1+e^{-iq_2} & 0 & 1+e^{-iq_1} & \frac{J_2}{J_1} & 0 & 0 & 0 & \frac{J_2}{J_1}e^{iq_3} \\ 1+e^{i(q_1-q_2)} & 1+e^{iq_1} & 0 & \frac{J_2}{J_1} & 0 & 0 & 0 & \frac{J_2}{J_1}e^{iq_3} \\ \frac{J_2}{J_1} & \frac{J_2}{J_1} & \frac{J_2}{J_1} & 0 & \frac{J_2}{J_1} & \frac{J_2}{J_1} & \frac{J_2}{J_1} & 0 \\ 0 & 0 & 0 & \frac{J_2}{J_1} & 0 & 1+e^{iq_1} & 1+e^{iq_2} & \frac{J_2}{J_1} \\ 0 & 0 & 0 & \frac{J_2}{J_1} & 1+e^{-iq_1} & 0 & 1+e^{-i(q_1-q_2)} & \frac{J_2}{J_1} \\ 0 & 0 & 0 & \frac{J_2}{J_1} & 1+e^{-iq_2} & 1+e^{i(q_1-q_2)} & 0 & \frac{J_2}{J_1} \\ \frac{J_2}{J_1}e^{-iq_3} & \frac{J_2}{J_1}e^{-iq_3} & \frac{J_2}{J_1}e^{-iq_3} & 0 & \frac{J_2}{J_1} & \frac{J_2}{J_1} & \frac{J_2}{J_1} & 0 \end{pmatrix}. \tag{3.79}$$

Here, J_1 is the in-plane coupling strength, while J_2 is the out-of-plane coupling strength. Next, the eigenvalues of this matrix are considered. Using *Mathematica*, the smallest eigenvalue was found to be at $\mathbf{q} = (2\pi/3, 4\pi/3, 0)$ or $\mathbf{q} = (4\pi/3, 2\pi/3, 0)$ when $J_2/J_1 > 1/\sqrt{2}$, while for $J_2/J_1 \leq 1/\sqrt{2}$ the smallest eigenvalue is equal to -2 for all $\mathbf{q}$. At these $\mathbf{q}$, the smallest eigenvalues are given by

$$\min_{\mathbf{q},i} \lambda_{\mathbf{q}}^i = \min\left(-2, \frac{1}{2}\left(1 - \sqrt{1 + 48\left(\frac{J_2}{J_1}\right)^2}\right)\right) = \begin{cases} -2 & \text{if } J_2/J_1 \leq 1/\sqrt{2} \\ \frac{1}{2}\left(1 - \sqrt{1 + 48\left(\frac{J_2}{J_1}\right)^2}\right) & \text{if } J_2/J_1 > 1/\sqrt{2} \end{cases}. \tag{3.80}$$

The eigenvectors corresponding to these eigenvalues have been calculated as well. The eigenvectors corresponding to the eigenvalue $\lambda_{\mathbf{q}} = -2$ (which is a doubly degenerate eigenvalue for every wave vector $\mathbf{q}$) are given by

$$\left(1, \frac{1 - e^{i(q_1-q_2)}}{e^{iq_1} - 1}, \frac{e^{iq_1}\left(e^{-iq_2} - 1\right)}{e^{iq_1} - 1}, 0, 0, 0, 0\right), \tag{3.81}$$

$$\left(0, 0, 0, 0, 1, \frac{e^{iq_2} - 1}{e^{iq_1} + e^{iq_2}}, \frac{1 - e^{iq_1}}{e^{iq_1} + e^{iq_2}}, 0\right). \tag{3.82}$$

If the modes corresponding to these eigenvectors are non-zero, the denominators of these expressions cause the inverse Fourier transform to diverge. This can only be prevented if the modes are zero, in which case $\mathbf{m}_i^a = 0$ for all lattice sites. We conclude that there can be no transition to a phase with non-zero sublattice magnetization for $J_2/J_1 \leq 1/\sqrt{2}$.

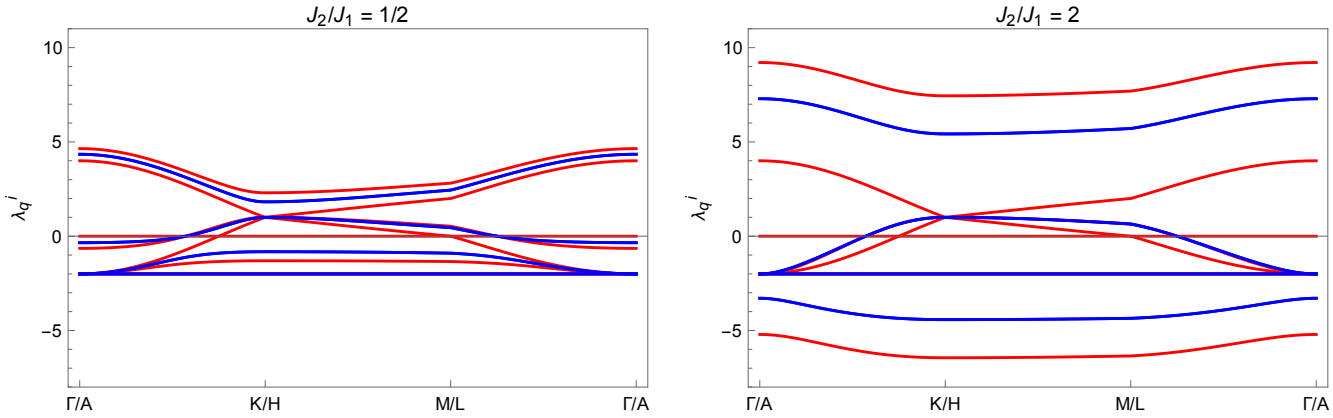

Figure 3.3: Eigenvalues of the interaction matrix $\mathbf{J}_\mathbf{q}/J_1$ of the Swedenborgite HAFM for $J_2/J_1 = 1/2$ (left) and $J_2/J_1 = 2$ (right), along two paths through symmetry points of the first Brillouin zone at fixed q_z. The red path is located at $q_z = 0$; the blue path is the same as the red path, but at $q_z = \pi$. See also Ref. [7].

The eigenvector corresponding to the second eigenvalue of Eq. (3.80) is given by

$$\left(1, 1, 1, -\frac{J_1}{4J_2}\left(1 + \sqrt{1 + 48\left(\frac{J_2}{J_1}\right)^2}\right), 1, 1, 1, -\frac{J_1}{4J_2}\left(1 + \sqrt{1 + 48\left(\frac{J_2}{J_1}\right)^2}\right)\right). \tag{3.83}$$

Fourier transforming this back to real space for $T < T_c$ (i.e. when the corresponding $|\mathbf{\Phi}^i_\mathbf{q}|^2$ is non-zero), we see that $\mathbf{m}^1_i = \mathbf{m}^2_i = \mathbf{m}^3_i = \mathbf{m}^5_i = \mathbf{m}^6_i = \mathbf{m}^7_i$, while $\mathbf{m}^4_i = \mathbf{m}^8_i$ point in the opposite direction from $\mathbf{m}^1_i$. Meanwhile, the values for $\mathbf{q}$ that lead to this solution correspond to a 120° configuration of columns of unit cells. This resulting configuration is exactly the unique ground state configuration of the antiferromagnetic Heisenberg model on the Swedenborgite lattice, as we have seen in Sec. 1.3.

In the above considerations, we used that the magnetizations directly depend on the eigenvectors of the interaction matrix. This works as follows. Referring back to Eq. (3.74), we see that minimization of the free energy gives the quadratic term

$$\frac{1}{2}\left(\min_{\mathbf{q},i} \lambda^i_\mathbf{q} + 3k_BT\right)\mathbf{\Phi}^* \cdot \mathbf{\Phi}, \tag{3.84}$$

where $\mathbf{\Phi} \equiv \mathbf{\Phi}^{i_\text{min}}_{\mathbf{q}_\text{min}}$. In other words: $\mathbf{\Phi}^i_\mathbf{q}$ is only non-zero for the i and $\mathbf{q}$ that minimize $\lambda^i_\mathbf{q}$. From Eq. (3.72), we then see that

$$\mathbf{m}^a_\mathbf{q} = \delta_{\mathbf{q},\mathbf{q}_\text{min}} U^{a\, i_\text{min}}_{\mathbf{q}_\text{min}} \mathbf{\Phi}. \tag{3.85}$$

As the diagonalization matrix $U^{ai}_\mathbf{q}$ is the matrix consisting of the eigenvectors of the interaction matrix, the vector $U^{a\, i_\text{min}}_{\mathbf{q}_\text{min}}$ is simply the eigenvector corresponding to the eigenvalue $\lambda^{i_\text{min}}_{\mathbf{q}_\text{min}}$. As a result, the magnetization $\mathbf{m}^a_\mathbf{q}$ is directly proportional to the eigenvectors that were calculated above.

Finally, we note that the mean-field critical temperature corresponding to the eigenvalues found in this section is

$$k_BT_c/J_1 = \frac{1}{6}\left(\sqrt{1 + 48\left(\frac{J_2}{J_1}\right)^2} - 1\right), \tag{3.86}$$

which is valid for $J_2/J_1 > 1/\sqrt{2}$. Comparing this with the analysis from Sec. 1.3, we see that mean-field theory gets this result wrong in two different ways. First, the mean-field analysis suggests that the unique ground state exists for all $J_2/J_1 > 1/\sqrt{2}$, which is very different from the exact observation that it only exists for $J_2/J_1 \geq 3/2$. It is worth noting that the interaction matrix does not show any special properties at all at $J_2/J_1 = 3/2$. Second, the qualitative behaviour is different: simulations suggest that the critical temperature becomes quadratic in J_2/J_1 for large values of J_2/J_1, while Eq. (3.86) implies that it becomes linear. The reasons for these significant deviations of mean-field theory with the results from Sec. 1.3 will become clear in the final section of this chapter.

3.4 Failure of mean-field theory

As was mentioned before, the Mermin-Wagner theorem states that there can be no spontaneous symmetry breaking of continuous symmetries at any finite temperature in a ($d \leq 2$)-dimensional system, provided that the interactions are sufficiently short-range [13]. This theorem applies to the Heisenberg model: the symmetry that would be broken is $O(3)$ symmetry, which is continuous, and the model only considers nearest neighbour interactions, which is the shortest possible range of interactions. Although the Mermin-Wagner theorem does not prevent phase transitions from happening on the three-dimensional Swedenborgite lattice, the number of dimensions is still low enough for mean-field theory to fail. To see how all of this happens, we will now consider fluctuations and discuss their influence. The methods used in this section are based on Refs. [10, 16, 17].

First note that the $O(3)$ symmetry of the system implies that slowly changing spin rotations only cost little energy. With respect to the mean-field approximation from Sec. 3.1.3, this would mean that there are other low energy configurations that give a significant contribution to the partition function, rather than just the single most probable configuration. To study the effects of such spin rotations, we will use the Landau free energy from Eq. (3.48) and look at the effects from fluctuations. To do so, consider the following parametrization of $\boldsymbol{\eta}(\mathbf{r})$:

$$\boldsymbol{\eta}(\mathbf{r}) = \eta \begin{pmatrix} \sin(\theta(\mathbf{r}))\cos(\phi(\mathbf{r})) \\ \sin(\theta(\mathbf{r}))\sin(\phi(\mathbf{r})) \\ \cos(\theta(\mathbf{r})) \end{pmatrix}. \tag{3.87}$$

Since we are only looking at rotational fluctuations, the absolute value η is taken constant. With this parametrization, the fluctuations term of the Landau free energy density becomes

$$\begin{aligned} -\frac{3Ja^2}{8}\boldsymbol{\eta}(\mathbf{r}) \cdot \nabla^2 \boldsymbol{\eta}(\mathbf{r}) &= \frac{3Ja^2\eta^2}{8}\left[(\nabla\theta(\mathbf{r}))^2 + \sin^2(\theta(\mathbf{r}))(\nabla\phi(\mathbf{r}))^2\right] \\ &\equiv \frac{K}{2}\left[(\nabla\theta)^2 + \sin^2\theta(\nabla\phi)^2\right]. \end{aligned} \tag{3.88}$$

For simplicity, we will now restrict ourselves to fluctuations in a single plane, i.e. fluctuations in ϕ. Next, we add an external field $h_\phi(\mathbf{r})$ coupling to $\phi(\mathbf{r})$ in order to be able to calculate correlation functions. The part of the partition function corresponding to ϕ is given by

$$Z_\phi = \int \mathcal{D}\phi \exp\left[-\beta \int \mathrm{d}\mathbf{r}\left(\frac{\tilde{K}}{2}(\nabla\phi)^2 - h_\phi(\mathbf{r})\phi(\mathbf{r})\right)\right], \tag{3.89}$$

where $\tilde{K} \equiv K\sin^2\theta$. Using this expression, the expectation value of $\phi(\mathbf{r})$ can be written as

$$\begin{aligned} \langle\phi(\mathbf{r})\rangle &= \frac{1}{Z_\phi}\int \mathcal{D}\phi\, \phi(\mathbf{r}) \exp\left[-\beta \int \mathrm{d}\mathbf{r}\left(\frac{\tilde{K}}{2}(\nabla\phi)^2 - h_\phi(\mathbf{r})\phi(\mathbf{r})\right)\right] \\ &= \frac{1}{Z_\phi}\frac{\delta Z_\phi}{\delta\beta h_\phi(\mathbf{r})} = -\frac{\delta F_\phi}{\delta h_\phi(\mathbf{r})}. \end{aligned} \tag{3.90}$$

It is useful to introduce a quantity called the susceptibility χ, which measures how the expectation value of $\phi(\mathbf{r})$ reacts to a change in the external field at $\mathbf{r}'$:

$$\chi(\mathbf{r},\mathbf{r}') \equiv \frac{\delta\langle\phi(\mathbf{r})\rangle}{\delta h_\phi(\mathbf{r}')} = -\frac{\delta^2 F_\phi}{\delta h_\phi(\mathbf{r}')\delta h_\phi(\mathbf{r})}. \tag{3.91}$$

Using Eq. (3.90), we see that the susceptibility is proportional to the correlation function $G(\mathbf{r},\mathbf{r}')$:

$$\begin{aligned} \chi(\mathbf{r},\mathbf{r}') &= \beta\left(\frac{1}{Z_\phi}\frac{\delta^2 Z_\phi}{\delta\beta h_\phi(\mathbf{r}')\delta\beta h_\phi(\mathbf{r})} - \frac{1}{Z_\phi}\frac{\delta Z_\phi}{\delta\beta h_\phi(\mathbf{r}')}\frac{1}{Z_\phi}\frac{\delta Z_\phi}{\delta\beta h_\phi(\mathbf{r})}\right) \\ &= \beta\left(\langle\phi(\mathbf{r})\phi(\mathbf{r}')\rangle - \langle\phi(\mathbf{r})\rangle\langle\phi(\mathbf{r}')\rangle\right) \\ &= \beta\langle(\phi(\mathbf{r}) - \langle\phi(\mathbf{r})\rangle)(\phi(\mathbf{r}') - \langle\phi(\mathbf{r}')\rangle)\rangle \\ &\equiv \beta G(\mathbf{r},\mathbf{r}'). \end{aligned} \tag{3.92}$$

Let us now return to the Landau free energy with the added external field, evaluated at the expectation value. Minimizing it with respect to $\langle\phi(\mathbf{r})\rangle$ gives

$$-\tilde{K}\nabla^2\langle\phi(\mathbf{r})\rangle - h_\phi(\mathbf{r}) = 0. \tag{3.93}$$

Performing a functional derivative of this equation with respect to $h_\phi(\mathbf{r}')$ and using Eq. (3.92), we obtain

$$-\beta\tilde{K}\nabla^2 G(\mathbf{r},\mathbf{r}') = \delta(\mathbf{r}-\mathbf{r}'). \tag{3.94}$$

For $d > 2$ dimensions, one can go to Fourier space to solve this equation. Transforming the result back to real space and making the integral dimensionless gives the result $G(\mathbf{r},\mathbf{r}') \sim r^{2-d}$, where $r \equiv |\mathbf{r}-\mathbf{r}'|$. This means that the correlation function converges to a constant when $r \to \infty$. However, if $d = 2$ this result no longer holds. Using homogeneity and isotropy of the equation gives $G(\mathbf{r},\mathbf{r}') = G(r)$, such that

$$\nabla^2 G(\mathbf{r},\mathbf{r}') = \frac{1}{r}\frac{\partial}{\partial r}\left(r\frac{\partial G(r)}{\partial r}\right). \tag{3.95}$$

For $r \neq 0$, this must be zero, so we find

$$G(\mathbf{r},\mathbf{r}') = c_1 + c_2 \ln r, \tag{3.96}$$

where c_1 and c_2 are constants. To find the value of c_2, we can integrate Eq. (3.94) over a circle with radius r_0 about the origin. Using the divergence theorem

$$\int_V \mathrm{d}V\, \nabla^2 G = \oint_{\partial V} \mathrm{d}S\, \nabla G \cdot \hat{\mathbf{n}} \tag{3.97}$$

and $\nabla G(r) = \frac{\partial G(r)}{\partial r}\hat{\mathbf{r}}$, we find

$$\begin{aligned} -\beta\tilde{K}\oint_{\partial V}\mathrm{d}S\,\frac{c_2}{r} = -\beta\tilde{K}\,2\pi r_0\,\frac{c_2}{r_0} = 1 \\ \Rightarrow c_2 = -\frac{k_B T}{2\pi\tilde{K}}. \end{aligned} \tag{3.98}$$

The correlation function is thus given by

$$G(\mathbf{r},\mathbf{r}') = -\frac{k_B T}{2\pi\tilde{K}}\ln r + c_1. \tag{3.99}$$

The resulting correlation function can be used to find the expectation value of the phase difference between two points. From homogeneity, it follows that $\langle\phi(\mathbf{r})\rangle$ is constant in space. Using this, we find

$$\langle(\phi(\mathbf{r}) - \phi(\mathbf{r}'))^2\rangle = 2G(0) - 2G(r) \sim \ln r. \tag{3.100}$$

This expression suggests the appearance of a divergence for $r \to 0$. However, this does not actually happen, due to the fact that we are still working on a discrete lattice. This lattice imposes a lower cut-off $r > a$, where a is again the lattice spacing. Taking this into account, there is no actual divergence.

The above results show us that the phase difference between two points diverges as $r \to \infty$ for any finite T. As a result, the angles between the two spins, and consequently the two spins themselves, are completely uncorrelated at large length scales. This means that there is no long-range ordering for any finite temperature, such that the system does not undergo a phase transition at all, confirming the prediction from the Mermin-Wagner theorem.

We have now seen that fluctuations prevent phase transitions from happening for $d \leq 2$, rendering any conclusions about phase transitions following from mean-field theory invalid. After all, mean-field theory assumes that we can take the expectation values of neighbours as effective fields acting on a site, while neglecting fluctuations. It is however still possible to find short-range ordering, but this local ordering will not extend over the entire space. This enabled us to find non-zero order parameters in the simulations on a small two-dimensional lattice at finite temperatures in Ch. 2.

The above analysis does not yet explain why mean-field theory also (partially) failed on the Swedenborgite lattice. One reason for the mean-field results to be incorrect is that mean-field theory ignores

the constraint that the spins are defined to be unit vectors. However, another reason is that fluctuations can have a significant influence even for $d > 2$. To check if this is the case, we can turn to the *Ginzburg criterion* [18]:

$$\langle (\delta\eta)^2 \rangle \ll \langle \eta \rangle^2, \tag{3.101}$$

which must hold for all temperatures in the ordered phase. Here, η is an arbitrary scalar order parameter, while

$$\delta\eta \equiv V^{-1} \int_V \mathrm{d}\mathbf{r}\, (\eta(\mathbf{r}) - \langle \eta \rangle) \tag{3.102}$$

is the average fluctuation over some volume V. In terms of the *correlation length* ξ, which gives the range of the correlations, this volume should at least be of the order $V_\xi \equiv \xi^d$. Using $G(r) \sim r^{2-d}$ from the previous example and making the resulting integral dimensionless, we can calculate the left-hand side of the criterion:

$$\langle (\delta\eta)^2 \rangle = V_\xi^{-1} \int_{V_\xi} \mathrm{d}\mathbf{r}\, G(r) \sim \xi^{2-d}. \tag{3.103}$$

The crucial point is that the Ginzburg criterion must also hold in the vicinity of the phase transition if we want to use mean-field theory to describe it, which is where $\langle \eta \rangle$ goes to zero and the correlation length ξ goes to infinity. If we want to satisfy the criterion in this region, ξ^{2-d} must go to zero faster than $\langle \eta \rangle^2$. This leads to the conclusion that there is an *upper critical dimension* below which the fluctuations cannot be ignored. Without explicitly calculating this upper critical dimension, the comparison between mean-field theory and exact observations demonstrate the fact that the dimension of the Swedenborgite lattice is not high enough for the fluctuations to be negligible. In short, the deviations from the exact analysis that we encountered in the previous section are caused by the fact that the fluctuations in the order parameter are larger than the order parameter itself in the vicinity of the phase transition, hence the initial assumption that the fluctuations could be ignored was incorrect.

While we have successfully developed a mean-field theory for the Swedenborgite antiferromagnet, we have now seen that fluctuations play an important role as well. In the next chapter, we will go beyond mean-field theory by thoroughly analysing spin fluctuations.

Chapter 4

Spin waves of the Swedenborgite antiferromagnet

In the previous chapter, we have seen that mean-field theory is insufficient to properly describe the phase transition of the Swedenborgite antiferromagnet in the $J_2/J_1 \to 3/2$ limit. We will therefore attempt a different approach, restricting ourselves to the $J_2/J_1 \geq 3/2$ region: we will start with the unique ground state and add spin fluctuations to it (called *spin waves*), analysing when these fluctuations become strong enough to destroy the ground state configuration. The temperature at which this happens is the temperature at which the configurations can no longer be described as fluctuations about the ground state configuration, such that this is the critical temperature we are looking for. We will first derive the Hamiltonian corresponding to the spin fluctuations, followed by considerations about why we will focus on some of the terms in particular. Then, we will calculate the critical temperature using the lowest order approximation of the Hamiltonian. Finally, the effects of higher order corrections will be considered using two different methods, and we end this chapter by discussing the overall conclusions regarding the goals that were mentioned in Sec. 1.4.

4.1 Spin wave Hamiltonian

In this section, we investigate the energy cost of spin excitations about the ground state of the Swedenborgite HAFM, of which we will later use the results to estimate the critical temperature that separates the unique ground state from the disordered phase. To find the spin wave Hamiltonian, we build on the spin wave analysis by Buhrandt [4], which was done along the lines of Chalker [2].

4.1.1 Real space Hamiltonian

As before, the Hamiltonian of the model at hand is given by

$$H = \frac{1}{2} \sum_{ij} J_{ij} \mathbf{S}_i \cdot \mathbf{S}_j, \tag{4.1}$$

where J_{ij} is equal to J_1 for in-plane nearest neighbour sites i, j, J_2 for intermediate nearest neighbours, and zero otherwise. We now focus on the region $J_2/J_1 \geq 3/2$, such that we can write each spin as $\mathbf{S}_i = \mathbf{S}_{GS,i} + \delta\mathbf{S}_i$, where $\mathbf{S}_{GS,i}$ is the ground state value of spin i; now the fluctuations $\delta\mathbf{S}_i$ are our new thermal variables. As was shown by Buhrandt, it is convenient to work with a local basis where $\hat{\mathbf{z}}_i$ is parallel to the ground state direction $\mathbf{S}_{GS,i}$ of the spin on lattice site i, $\hat{\mathbf{y}}_i$ orthogonal to the ground state plane, and $\hat{\mathbf{x}}_i$ chosen such that the basis is right-handed. In this basis, each spin can be written as

$$\mathbf{S}_i = \left(\epsilon_i^x, \epsilon_i^y, \sqrt{1 - (\epsilon_i^x)^2 - (\epsilon_i^y)^2} \right), \tag{4.2}$$

where ϵ_i^x and ϵ_i^y are the in-plane and out-of-plane spin excitations, respectively. The Hamiltonian thus becomes

$$H = \frac{1}{2}\sum_{ij}\Bigg(\epsilon_i^x J_{ij}(\hat{\mathbf{x}}_i\cdot\hat{\mathbf{x}}_j)\epsilon_j^x + \epsilon_i^y J_{ij}(\hat{\mathbf{y}}_i\cdot\hat{\mathbf{y}}_j)\epsilon_j^y + \sqrt{1-(\epsilon_i^x)^2-(\epsilon_i^y)^2}J_{ij}(\hat{\mathbf{z}}_i\cdot\hat{\mathbf{z}}_j)\sqrt{1-(\epsilon_j^x)^2-(\epsilon_j^y)^2}$$
$$+\epsilon_i^x J_{ij}(\hat{\mathbf{x}}_i\cdot\hat{\mathbf{z}}_j)\sqrt{1-(\epsilon_j^x)^2-(\epsilon_j^y)^2} + \sqrt{1-(\epsilon_i^x)^2-(\epsilon_i^y)^2}J_{ij}(\hat{\mathbf{z}}_i\cdot\hat{\mathbf{x}}_j)\epsilon_j^x\Bigg). \tag{4.3}$$

Here, we used that $\hat{\mathbf{y}}_i$ is perpendicular to both $\hat{\mathbf{x}}_j$ and $\hat{\mathbf{z}}_j$ for all i,j due to our choice of basis. The next step is to consider small excitations and expand this Hamiltonian. The final two terms of the Hamiltonian (i.e. the non-zero cross terms) generate all odd order terms, which we will ignore for now. The actual relevance of these odd order terms will be discussed in Sec. 4.1.3. For our considerations concerning only the even order terms, the Hamiltonian can be written as

$$H = E_{GS} + H_2 + H_4 + \mathcal{O}(\epsilon^6) + H_{odd}, \tag{4.4}$$

where E_{GS} is the ground state energy and H_{odd} contains all odd order terms in ϵ, while H_2 and H_4 are the second and fourth order terms in the ϵ expansion of the Hamiltonian, respectively. To perform the expansion, we use

$$\sqrt{1-(\epsilon_i^x)^2-(\epsilon_i^y)^2} = 1 - \frac{1}{2}\left((\epsilon_i^x)^2+(\epsilon_i^y)^2\right) - \frac{1}{8}\left((\epsilon_i^x)^4+(\epsilon_i^y)^4+2(\epsilon_i^x)^2(\epsilon_i^y)^2\right)+\mathcal{O}(\epsilon^6). \tag{4.5}$$

From this expression, one can calculate that

$$\sqrt{1-(\epsilon_i^x)^2-(\epsilon_i^y)^2}\sqrt{1-(\epsilon_j^x)^2-(\epsilon_j^y)^2} = 1 - \frac{1}{2}\left((\epsilon_i^x)^2+(\epsilon_j^x)^2+(\epsilon_i^y)^2+(\epsilon_j^y)^2\right)$$
$$-\frac{1}{8}\left((\epsilon_i^x)^2-(\epsilon_j^x)^2+(\epsilon_i^y)^2-(\epsilon_j^y)^2\right)^2+\mathcal{O}(\epsilon^6). \tag{4.6}$$

Now that we have a first general expression for the expansion of H in terms of the excitations $\epsilon_i^{x/y}$, we can start looking at H_2 and H_4 individually. Using the above expressions, we find

$$H_2 = \frac{1}{2}\sum_{ij}\left(\epsilon_i^x J_{ij}(\hat{\mathbf{x}}_i\cdot\hat{\mathbf{x}}_j)\epsilon_j^x + \epsilon_i^y J_{ij}(\hat{\mathbf{y}}_i\cdot\hat{\mathbf{y}}_j)\epsilon_j^y - \frac{1}{2}\left((\epsilon_i^x)^2+(\epsilon_j^x)^2+(\epsilon_i^y)^2+(\epsilon_j^y)^2\right)J_{ij}(\hat{\mathbf{z}}_i\cdot\hat{\mathbf{z}}_j)\right) \tag{4.7}$$

Defining

$$\gamma_i \equiv \frac{1}{2}\sum_j J_{ij}(\hat{\mathbf{z}}_i\cdot\hat{\mathbf{z}}_j) \tag{4.8}$$

and using $J_{ij}=J_{ji}$, the final term of H_2 becomes

$$-\frac{1}{2}\sum_i\left((\epsilon_i^x)^2+(\epsilon_i^y)^2\right)\sum_j J_{ij}(\hat{\mathbf{z}}_i\cdot\hat{\mathbf{z}}_j) = -\frac{1}{2}\sum_i\left((\epsilon_i^x)^2+(\epsilon_i^y)^2\right)2\gamma_i$$
$$= -\frac{1}{2}\sum_{ij}\left[\delta_{ij}\left(\epsilon_i^x 2\gamma_i\epsilon_j^x+\epsilon_i^y 2\gamma_i\epsilon_j^y\right)\right]. \tag{4.9}$$

Plugging this back in, we see that the quadratic part of the Hamiltonian is equal to

$$H_2 = \frac{1}{2}\sum_{ij}\left(\epsilon_i^x J_{ij}(\hat{\mathbf{x}}_i\cdot\hat{\mathbf{x}}_j)\epsilon_j^x+\epsilon_i^y J_{ij}(\hat{\mathbf{y}}_i\cdot\hat{\mathbf{y}}_j)\epsilon_j^y-\delta_{ij}\left(\epsilon_i^x 2\gamma_i\epsilon_j^x+\epsilon_i^y 2\gamma_i\epsilon_j^y\right)\right)$$
$$= \frac{1}{2}\sum_{ij}\left(\epsilon_i^x M_{ij}^x\epsilon_j^x+\epsilon_i^y M_{ij}^y\epsilon_j^y\right), \tag{4.10}$$

where we defined

$$M_{ij}^x \equiv J_{ij}(\hat{\mathbf{x}}_i\cdot\hat{\mathbf{x}}_j) - 2\gamma_i\delta_{ij}, \tag{4.11}$$
$$M_{ij}^y \equiv J_{ij}(\hat{\mathbf{y}}_i\cdot\hat{\mathbf{y}}_j) - 2\gamma_i\delta_{ij}. \tag{4.12}$$

We can also rewrite the quartic part of the Hamiltonian in a similar fashion. Referring back to Eqs. (4.3) and (4.6) and using again that J_{ij} is symmetric, we find

$$\begin{aligned}
H_4 &= -\frac{1}{16}\sum_{ij}\left((\epsilon_i^x)^2-(\epsilon_j^x)^2+(\epsilon_i^y)^2-(\epsilon_j^y)^2\right)^2 J_{ij}(\hat{\mathbf{z}}_i\cdot\hat{\mathbf{z}}_j)\\
&= -\frac{1}{8}\sum_{ij}\left[(\epsilon_i^x)^4+(\epsilon_i^y)^4+2(\epsilon_i^x)^2(\epsilon_i^y)^2-(\epsilon_i^x)^2(\epsilon_j^x)^2-(\epsilon_i^y)^2(\epsilon_j^y)^2-2(\epsilon_i^x)^2(\epsilon_j^y)^2\right]J_{ij}(\hat{\mathbf{z}}_i\cdot\hat{\mathbf{z}}_j)\\
&= \frac{1}{8}\sum_{ij}\left[(\epsilon_i^x)^2(\epsilon_j^x)^2+(\epsilon_i^y)^2(\epsilon_j^y)^2+2(\epsilon_i^x)^2(\epsilon_j^y)^2\right](J_{ij}(\hat{\mathbf{z}}_i\cdot\hat{\mathbf{z}}_j)-2\gamma_i\delta_{ij})\\
&= \frac{1}{8}\sum_{ij}\left[(\epsilon_i^x)^2M_{ij}^z(\epsilon_j^x)^2+(\epsilon_i^y)^2M_{ij}^z(\epsilon_j^y)^2+(\epsilon_i^x)^2M_{ij}^z(\epsilon_j^y)^2+(\epsilon_i^y)^2M_{ij}^z(\epsilon_j^x)^2\right], \qquad (4.13)
\end{aligned}$$

where

$$M_{ij}^z \equiv J_{ij}(\hat{\mathbf{z}}_i\cdot\hat{\mathbf{z}}_j)-2\gamma_i\delta_{ij}. \qquad (4.14)$$

Before we continue our analysis, a few remarks are in order. First, it will be necessary to know what the dot products $(\hat{\mathbf{x}}_i\cdot\hat{\mathbf{x}}_j)$, $(\hat{\mathbf{y}}_i\cdot\hat{\mathbf{y}}_j)$ and $(\hat{\mathbf{z}}_i\cdot\hat{\mathbf{z}}_j)$ are. Referring back to the unique ground state configuration as seen in Sec. 1.3 (i.e. the 120° configuration of columns) and noting that $\hat{\mathbf{z}}_i = \mathbf{S}_{GS,i}$, we immediately find

$$(\hat{\mathbf{z}}_i\cdot\hat{\mathbf{z}}_j) = \begin{cases} 1 & i \text{ and } j \in \text{ same Kagomé layer, same bipyramid} \\ -1/2 & i \text{ and } j \in \text{ same Kagomé layer, different bipyramids} \\ -1 & i \text{ or } j \in \text{ triangular layer, other in adjacent Kagomé layer} \end{cases} \qquad (4.15)$$

for i,j nearest neighbours. In addition, $(\hat{\mathbf{x}}_i\cdot\hat{\mathbf{x}}_j) = (\hat{\mathbf{z}}_i\cdot\hat{\mathbf{z}}_j)$ and $(\hat{\mathbf{y}}_i\cdot\hat{\mathbf{y}}_j) = 1$ for all i,j. Hence, we see that $M_{ij}^z = M_{ij}^x$, such that we only have to consider M_{ij}^x and M_{ij}^y. Additionally, with these dot products γ_i becomes

$$\gamma_i = \begin{cases} J_1/2 - J_2 & i \in \text{Kagomé layer} \\ -3J_2 & i \in \text{triangular layer.} \end{cases} \qquad (4.16)$$

Second, it is more convenient to work on the level of unit cells rather than individual lattice sites, similar to what we have done in Sec. 3.2. Letting i,j refer to the unit cells while a,b refer to the different sites within the unit cells (i.e. the sublattices), we find

$$H_2 = \frac{1}{2}\sum_{ab}\sum_{ij}\left(\epsilon_i^{xa}M_{ij}^{xab}\epsilon_j^{xb}+\epsilon_i^{ya}M_{ij}^{yab}\epsilon_j^{yb}\right), \qquad (4.17)$$

$$H_4 = \frac{1}{8}\sum_{ab}\sum_{ij}\left[(\epsilon_i^{xa})^2M_{ij}^{xab}(\epsilon_j^{xb})^2+(\epsilon_i^{ya})^2M_{ij}^{xab}(\epsilon_j^{yb})^2+(\epsilon_i^{xa})^2M_{ij}^{xab}(\epsilon_j^{yb})^2+(\epsilon_i^{ya})^2M_{ij}^{xab}(\epsilon_j^{xb})^2\right]. \qquad (4.18)$$

Here, a,b go from 1 to 8 (as there are 8 lattice sites per unit cell), while i,j go from 1 to N_c, where N_c is defined as the total number of unit cells.

4.1.2 Momentum space Hamiltonian

Due to the complicated form of the interaction matrices M_{ij}^{xab} and M_{ij}^{yab}, it is necessary to exploit the symmetry of the ground state by Fourier transforming the Hamiltonian on the level of unit cells. Noting that $\epsilon_i^{x/ya} = \epsilon_{\mathbf{r}_i}^{x/ya}$ (where $\mathbf{r}_i$ is the position of unit cell i), $M_{ij}^{xab} = M_{\mathbf{r}_{ij}}^{xab}$ (with $\mathbf{r}_{ij} \equiv \mathbf{r}_i - \mathbf{r}_j$) and $M_{ij}^{yab} = M_{\mathbf{r}_{ij}}^{yab}$, the Fourier transform is given by

$$\epsilon_{\mathbf{r}_i}^{x/ya} = \sum_{\mathbf{q}}\epsilon_{\mathbf{q}}^{x/ya}e^{i\mathbf{q}\cdot\mathbf{r}_i}, \qquad (4.19)$$

$$M_{\mathbf{r}_{ij}}^{xab} = \frac{1}{N_c}\sum_{\mathbf{q}}M_{\mathbf{q}}^{xab}e^{i\mathbf{q}\cdot\mathbf{r}_{ij}}, \qquad (4.20)$$

$$M_{\mathbf{r}_{ij}}^{yab} = \frac{1}{N_c}\sum_{\mathbf{q}}M_{\mathbf{q}}^{yab}e^{i\mathbf{q}\cdot\mathbf{r}_{ij}}. \qquad (4.21)$$

Here, the lattice spacing a has once again been absorbed by the wave vector $\mathbf{q}$. In terms of these variables, the quadratic and quartic parts of the Hamiltonian become

$$\begin{aligned} H_2 &= \frac{1}{2N_c}\sum_{ab}\sum_{ij}\sum_{\mathbf{q}_1,\mathbf{q}_2,\mathbf{q}_3}\left(\epsilon^{xa}_{\mathbf{q}_1}M^{xab}_{\mathbf{q}_2}\epsilon^{xb}_{\mathbf{q}_3}+\epsilon^{ya}_{\mathbf{q}_1}M^{yab}_{\mathbf{q}_2}\epsilon^{yb}_{\mathbf{q}_3}\right)e^{i\mathbf{r}_i\cdot(\mathbf{q}_1+\mathbf{q}_2)}e^{i\mathbf{r}_j\cdot(\mathbf{q}_3-\mathbf{q}_2)} \\ &= \frac{N_c}{2}\sum_{\mathbf{q}}\sum_{ab}\left(\epsilon^{xa}_{-\mathbf{q}}M^{xab}_{\mathbf{q}}\epsilon^{xb}_{\mathbf{q}}+\epsilon^{ya}_{-\mathbf{q}}M^{yab}_{\mathbf{q}}\epsilon^{yb}_{\mathbf{q}}\right) \\ &= \frac{N_c}{2}\sum_{\mathbf{q}}\sum_{ab}\left((\epsilon^{xa}_{\mathbf{q}})^*M^{xab}_{\mathbf{q}}\epsilon^{xb}_{\mathbf{q}}+(\epsilon^{ya}_{\mathbf{q}})^*M^{yab}_{\mathbf{q}}\epsilon^{yb}_{\mathbf{q}}\right), \end{aligned} \tag{4.22}$$

$$\begin{aligned} H_4 = \frac{N_c}{8}\sum_{\mathbf{q}_1,\mathbf{q}_2,\mathbf{q}_3}\sum_{ab}\Big(&(\epsilon^{xa}_{\mathbf{q}_1+\mathbf{q}_3})^*\epsilon^{xa}_{\mathbf{q}_1}M^{xab}_{\mathbf{q}_3}(\epsilon^{xb}_{\mathbf{q}_2-\mathbf{q}_3})^*\epsilon^{xb}_{\mathbf{q}_2}+(\epsilon^{ya}_{\mathbf{q}_1+\mathbf{q}_3})^*\epsilon^{ya}_{\mathbf{q}_1}M^{xab}_{\mathbf{q}_3}(\epsilon^{yb}_{\mathbf{q}_2-\mathbf{q}_3})^*\epsilon^{yb}_{\mathbf{q}_2} \\ &+(\epsilon^{xa}_{\mathbf{q}_1+\mathbf{q}_3})^*\epsilon^{xa}_{\mathbf{q}_1}M^{xab}_{\mathbf{q}_3}(\epsilon^{yb}_{\mathbf{q}_2-\mathbf{q}_3})^*\epsilon^{yb}_{\mathbf{q}_2}+(\epsilon^{ya}_{\mathbf{q}_1+\mathbf{q}_3})^*\epsilon^{ya}_{\mathbf{q}_1}M^{xab}_{\mathbf{q}_3}(\epsilon^{xb}_{\mathbf{q}_2-\mathbf{q}_3})^*\epsilon^{xb}_{\mathbf{q}_2}\Big), \end{aligned} \tag{4.23}$$

where we used the reality condition $(\epsilon^{x/ya}_{\mathbf{q}})^* = \epsilon^{x/ya}_{-\mathbf{q}}$, and the calculation of H_4 was done in exactly the same was as shown for H_2.

In the above expressions, the ϵ's are the variables (now describing *collective* excitations called spin waves), while the 8×8 interaction matrices $M^{xab}_{\mathbf{q}}$ and $M^{yab}_{\mathbf{q}}$ are determined by the ground state. They can be calculated using the inverse Fourier transforms:

$$M^{x/yab}_{\mathbf{q}} = \sum_{\mathbf{r}} M^{x/yab}_{\mathbf{r}} e^{-i\mathbf{q}\cdot\mathbf{r}}. \tag{4.24}$$

In terms of the basis vectors

$$\hat{\mathbf{a}}_1 = \begin{pmatrix}1\\0\\0\end{pmatrix}, \qquad \hat{\mathbf{a}}_2 = \frac{1}{2}\begin{pmatrix}1\\\sqrt{3}\\0\end{pmatrix}, \qquad \hat{\mathbf{a}}_3 = \begin{pmatrix}0\\0\\1\end{pmatrix} \tag{4.25}$$

and using the information from Sec. 4.1.1, the interaction matrices become

$$\mathbf{M}^x_{\mathbf{q}}/J_1 = \begin{pmatrix}
2\frac{J_2}{J_1}-1 & 1-\frac{1}{2}e^{iq_2} & 1-\frac{1}{2}e^{-i(q_1-q_2)} & -\frac{J_2}{J_1} & 0 & 0 & 0 & -\frac{J_2}{J_1}e^{iq_3} \\
1-\frac{1}{2}e^{-iq_2} & 2\frac{J_2}{J_1}-1 & 1-\frac{1}{2}e^{-iq_1} & -\frac{J_2}{J_1} & 0 & 0 & 0 & -\frac{J_2}{J_1}e^{iq_3} \\
1-\frac{1}{2}e^{i(q_1-q_2)} & 1-\frac{1}{2}e^{iq_1} & 2\frac{J_2}{J_1}-1 & -\frac{J_2}{J_1} & 0 & 0 & 0 & -\frac{J_2}{J_1}e^{iq_3} \\
-\frac{J_2}{J_1} & -\frac{J_2}{J_1} & -\frac{J_2}{J_1} & 6\frac{J_2}{J_1} & -\frac{J_2}{J_1} & -\frac{J_2}{J_1} & -\frac{J_2}{J_1} & 0 \\
0 & 0 & 0 & -\frac{J_2}{J_1} & 2\frac{J_2}{J_1}-1 & 1-\frac{1}{2}e^{iq_1} & 1-\frac{1}{2}e^{iq_2} & -\frac{J_2}{J_1} \\
0 & 0 & 0 & -\frac{J_2}{J_1} & 1-\frac{1}{2}e^{-iq_1} & 2\frac{J_2}{J_1}-1 & 1-\frac{1}{2}e^{-i(q_1-q_2)} & -\frac{J_2}{J_1} \\
0 & 0 & 0 & -\frac{J_2}{J_1} & 1-\frac{1}{2}e^{-iq_2} & 1-\frac{1}{2}e^{i(q_1-q_2)} & 2\frac{J_2}{J_1}-1 & -\frac{J_2}{J_1} \\
-\frac{J_2}{J_1}e^{-iq_3} & -\frac{J_2}{J_1}e^{-iq_3} & -\frac{J_2}{J_1}e^{-iq_3} & 0 & -\frac{J_2}{J_1} & -\frac{J_2}{J_1} & -\frac{J_2}{J_1} & 6\frac{J_2}{J_1}
\end{pmatrix}, \tag{4.26}$$

$$\mathbf{M}^y_{\mathbf{q}}/J_1 = \begin{pmatrix}
2\frac{J_2}{J_1}-1 & 1+e^{iq_2} & 1+e^{-i(q_1-q_2)} & \frac{J_2}{J_1} & 0 & 0 & 0 & \frac{J_2}{J_1}e^{iq_3} \\
1+e^{-iq_2} & 2\frac{J_2}{J_1}-1 & 1+e^{-iq_1} & \frac{J_2}{J_1} & 0 & 0 & 0 & \frac{J_2}{J_1}e^{iq_3} \\
1+e^{i(q_1-q_2)} & 1+e^{iq_1} & 2\frac{J_2}{J_1}-1 & \frac{J_2}{J_1} & 0 & 0 & 0 & \frac{J_2}{J_1}e^{iq_3} \\
\frac{J_2}{J_1} & \frac{J_2}{J_1} & \frac{J_2}{J_1} & 6\frac{J_2}{J_1} & \frac{J_2}{J_1} & \frac{J_2}{J_1} & \frac{J_2}{J_1} & 0 \\
0 & 0 & 0 & \frac{J_2}{J_1} & 2\frac{J_2}{J_1}-1 & 1+e^{iq_1} & 1+e^{iq_2} & \frac{J_2}{J_1} \\
0 & 0 & 0 & \frac{J_2}{J_1} & 1+e^{-iq_1} & 2\frac{J_2}{J_1}-1 & 1+e^{-i(q_1-q_2)} & \frac{J_2}{J_1} \\
0 & 0 & 0 & \frac{J_2}{J_1} & 1+e^{-iq_2} & 1+e^{i(q_1-q_2)} & 2\frac{J_2}{J_1}-1 & \frac{J_2}{J_1} \\
\frac{J_2}{J_1}e^{-iq_3} & \frac{J_2}{J_1}e^{-iq_3} & \frac{J_2}{J_1}e^{-iq_3} & 0 & \frac{J_2}{J_1} & \frac{J_2}{J_1} & \frac{J_2}{J_1} & 6\frac{J_2}{J_1}
\end{pmatrix}. \tag{4.27}$$

With Eqs. (4.22) and (4.23) and the above interaction matrices, our momentum space expansion of the Hamiltonian is complete.

4.1.3 On the relevance of odd order terms

So far, we have ignored the odd order terms of the expansion of the Hamiltonian. In general, the odd order terms cannot be ignored, and in this section we will discuss the relevance of these terms. The part of the Hamiltonian generating these terms is given by

$$\begin{aligned} H_{odd} &= \frac{1}{2}\sum_{ij}\left(\epsilon_i^x J_{ij}(\hat{\mathbf{x}}_i\cdot\hat{\mathbf{z}}_j)\sqrt{1-(\epsilon_j^x)^2-(\epsilon_j^y)^2}+\sqrt{1-(\epsilon_i^x)^2-(\epsilon_i^y)^2}J_{ij}(\hat{\mathbf{z}}_i\cdot\hat{\mathbf{x}}_j)\epsilon_j^x\right) \\ &= \sum_{ij}\epsilon_i^x J_{ij}(\hat{\mathbf{x}}_i\cdot\hat{\mathbf{z}}_j)\sqrt{1-(\epsilon_j^x)^2-(\epsilon_j^y)^2}, \end{aligned} \tag{4.28}$$

where we used the fact that J_{ij} is symmetric for the last step. Before considering the odd order terms in general, let us first look at the linear term,

$$H_1 = \sum_{ij}\epsilon_i^x J_{ij}(\hat{\mathbf{x}}_i\cdot\hat{\mathbf{z}}_j). \tag{4.29}$$

Since we are considering an expansion about the ground state (i.e. about the minimum of H), we know that this linear term must vanish. This can also be shown explicitly. For nearest neighbours, the dot product $(\hat{\mathbf{x}}_i\cdot\hat{\mathbf{z}}_j)$ is only non-zero if i,j belong to different bipyramids, and consequently they must both be part of the same Kagomé layer if the dot product is to be non-zero. Using that each Kagomé lattice site i has two nearest neighbours that are part of different bipyramids (call them i_1 and i_2), we can write

$$H_1 = J_1\sum_{i\in\text{Kagomé}}\epsilon_i^x\left((\hat{\mathbf{x}}_i\cdot\hat{\mathbf{z}}_{i_1})+(\hat{\mathbf{x}}_i\cdot\hat{\mathbf{z}}_{i_2})\right). \tag{4.30}$$

Making use of our knowledge of the ground state configuration, we know that $\hat{\mathbf{z}}_{i_1}$ and $\hat{\mathbf{z}}_{i_2}$ are at angles $2\pi/3$ and $4\pi/3$ with respect to $\hat{\mathbf{z}}_i$, respectively (or the other way around). Noting that $\hat{\mathbf{x}}_i$ is at an angle of $-\pi/2$ with respect to $\hat{\mathbf{z}}_i$, in the same plane as the other angles, we conclude that the angle between $\hat{\mathbf{x}}_i$ and $\hat{\mathbf{z}}_{i_1}$ is $\pi/6$, while the angle between $\hat{\mathbf{x}}_i$ and $\hat{\mathbf{z}}_{i_2}$ is $5\pi/6$ (or the other way around). Therefore:

$$H_1 = J_1\sum_{i\in\text{Kagomé}}\epsilon_i^x\left(\cos(\pi/6)+\cos(5\pi/6)\right) = J_1\sum_{i\in\text{Kagomé}}\epsilon_i^x\left(\sqrt{3}/2-\sqrt{3}/2\right)=0, \tag{4.31}$$

so the linear term indeed vanishes, as was required.

For general odd order terms, the same argument can be used to write

$$(\hat{\mathbf{x}}_i\cdot\hat{\mathbf{z}}_{i_1}) = \pm\sqrt{3}/2, \qquad (\hat{\mathbf{x}}_i\cdot\hat{\mathbf{z}}_{i_2}) = \mp\sqrt{3}/2, \tag{4.32}$$

which leads to

$$H_{odd} = \pm\frac{\sqrt{3}}{2}J_1\sum_{i\in\text{Kagomé}}\epsilon_i^x\left(\sqrt{1-(\epsilon_{i_1}^x)^2-(\epsilon_{i_1}^y)^2}-\sqrt{1-(\epsilon_{i_2}^x)^2-(\epsilon_{i_2}^y)^2}\right). \tag{4.33}$$

Contrary to the linear term, this expression does not vanish in general, however the odd order terms will still not play a role in the approximations we will consider. As we will see in the next sections, we will only be concerned with two-point functions, i.e. expectation values of the form

$$\left\langle\epsilon_{\mathbf{q}}^{x/ya}(\epsilon_{\mathbf{q}}^{x/yb})^*\right\rangle. \tag{4.34}$$

In accordance with the usual Feynman rules (see also appendices A.4 and A.5), two-point functions can be calculated by constructing Feynman diagrams with two external legs; terms of order n in perturbation theory contain n vertices. Now odd order terms of the Hamiltonian are responsible for the appearance of vertices with an odd number of legs. In order to construct a Feynman diagram for two-point functions using vertices with an odd number of legs, we need an even number of such vertices, hence these vertices do not appear in first order perturbation theory. Since we will not go to higher order than the first in our calculations of the two-point functions, it will indeed not be necessary to consider the odd order terms that appear in the Hamiltonian.

4.2 Lowest order approximation of T_c

Now that the Hamiltonian corresponding to spin fluctuations about the ground state is known, we will see how this result can be used to find the qualitative behaviour and the order of magnitude of the critical temperature T_c in the region $J_2/J_1 \geq 3/2$. To estimate this temperature, we will look for the temperature for which the size of the excitations per lattice site $|\delta \mathbf{S}_i|$ becomes of the order of the size of the spins themselves, $|\mathbf{S}_i| = 1$. The idea is that if the excitations are larger than that, then this approach no longer makes sense, as the spins themselves are supposed to be unit vectors. Hence, if the expectation value of the excitations per lattice site becomes larger than 1 according to this description, then we can no longer describe the system as excitations about the ground state, such that we are then looking at the disordered phase. Explicitly, this criterion for the critical temperature can be written as

$$\sum_{i,a} \left(\left\langle (\epsilon_i^{xa})^2 \right\rangle + \left\langle (\epsilon_i^{ya})^2 \right\rangle \right) \sim 8N_c, \tag{4.35}$$

where N_c is again the total number of unit cells, while 8 is the number of lattice sites per unit cell. Using Eq. (4.19), this can also be written as

$$\frac{1}{8} \sum_a \sum_{\mathbf{q}} \left(\left\langle |\epsilon_{\mathbf{q}}^{xa}|^2 \right\rangle + \left\langle |\epsilon_{\mathbf{q}}^{ya}|^2 \right\rangle \right) \sim 1. \tag{4.36}$$

To obtain approximations for the expectation values that appear in the above criterion, we use that the excitations ϵ are "small" (i.e. smaller than 1) in the region where the system can still be described by excitations about the ground state. Therefore, we use the expansion of the Hamiltonian that was obtained in the previous section. We will now interpret the quadratic part of the Hamiltonian as the "kinetic" terms, while the higher order terms are interpreted as "interaction" terms. At the temperatures for which ϵ is small, the interaction terms will be much smaller than the kinetic terms, and for our lowest order approximation we will therefore restrict ourselves to the kinetic terms only. Note that the approximation that the interaction terms are small is only valid at low temperatures, because otherwise the excitations themselves become large and the higher order terms will dominate. However, the approximation suffices for the region that we are interested in, as it only breaks down at the temperature scale at which the entire description starts to fail, which is exactly the temperature scale we are looking for.

Let us now approximate the Hamiltonian by its lowest order non-trivial terms, i.e. the kinetic terms. Referring back to the previous section, the Hamiltonian is now given by

$$H = E_{GS} + H_2 = E_{GS} + \frac{N_c}{2} \sum_{\mathbf{q}} \sum_{ab} \left((\epsilon_{\mathbf{q}}^{xa})^* M_{\mathbf{q}}^{xab} \epsilon_{\mathbf{q}}^{xb} + (\epsilon_{\mathbf{q}}^{ya})^* M_{\mathbf{q}}^{yab} \epsilon_{\mathbf{q}}^{yb} \right). \tag{4.37}$$

Before we move on to finding the critical temperature, we take a moment to discuss the implications of this Hamiltonian. In order to find the energy spectrum of small spin excitations, we can calculate the eigenvalues of the matrices $\mathbf{M}_{\mathbf{q}}^x$ and $\mathbf{M}_{\mathbf{q}}^y$; the energy per unit cell of the corresponding mode is then given by half the eigenvalue of the matrix. This has been done using *Mathematica*, and the results are shown in Fig. 4.1. We find that there is a doubly degenerate flat band with energy per unit cell

$$E_{\mathbf{q}}^i / J_1 N_c = J_2/J_1 - 3/2 \tag{4.38}$$

corresponding to two out-of-plane modes. From this, we immediately see that our approach does not work for $J_2/J_1 < 3/2$: in that region, there are modes with negative energy, so the configuration to which we are adding the excitations no longer minimizes the Hamiltonian, and therefore it is no longer the ground state. Moreover, the flat band has zero energy when $J_2/J_1 = 3/2$, leading to the conclusion that zero energy has a very large density of states when $J_2/J_1 = 3/2$. As we will see below, this leads to a zero critical temperature for this value of J_2/J_1.

Returning to the matter of the critical temperature, let us now calculate the expectation values that appear in Eq. (4.36). Introducing the *Green's function* $\mathbf{G}_{\mathbf{q}}^{x/y}$ according to $(\mathbf{G}_{\mathbf{q}}^{x/y})^{-1} \equiv -\frac{\beta N_c}{2} \mathbf{M}_{\mathbf{q}}^{x/y}$ and introducing external fields $h_{\mathbf{q}}^{x/ya}$ (which we will set to zero later on), the Hamiltonian can be written as

$$\begin{aligned} -\beta H = -\beta E_{GS} + \sum_{\mathbf{q}} \big[&(\boldsymbol{\epsilon}_{\mathbf{q}}^x)^* \cdot (\mathbf{G}_{\mathbf{q}}^x)^{-1} \cdot \boldsymbol{\epsilon}_{\mathbf{q}}^x + (\boldsymbol{\epsilon}_{\mathbf{q}}^y)^* \cdot (\mathbf{G}_{\mathbf{q}}^y)^{-1} \cdot \boldsymbol{\epsilon}_{\mathbf{q}}^y + (\boldsymbol{\epsilon}_{\mathbf{q}}^x)^* \cdot \mathbf{h}_{\mathbf{q}}^x + (\mathbf{h}_{\mathbf{q}}^x)^* \cdot \boldsymbol{\epsilon}_{\mathbf{q}}^x \\ &+ (\boldsymbol{\epsilon}_{\mathbf{q}}^y)^* \cdot \mathbf{h}_{\mathbf{q}}^y + (\mathbf{h}_{\mathbf{q}}^y)^* \cdot \boldsymbol{\epsilon}_{\mathbf{q}}^y \big], \end{aligned} \tag{4.39}$$

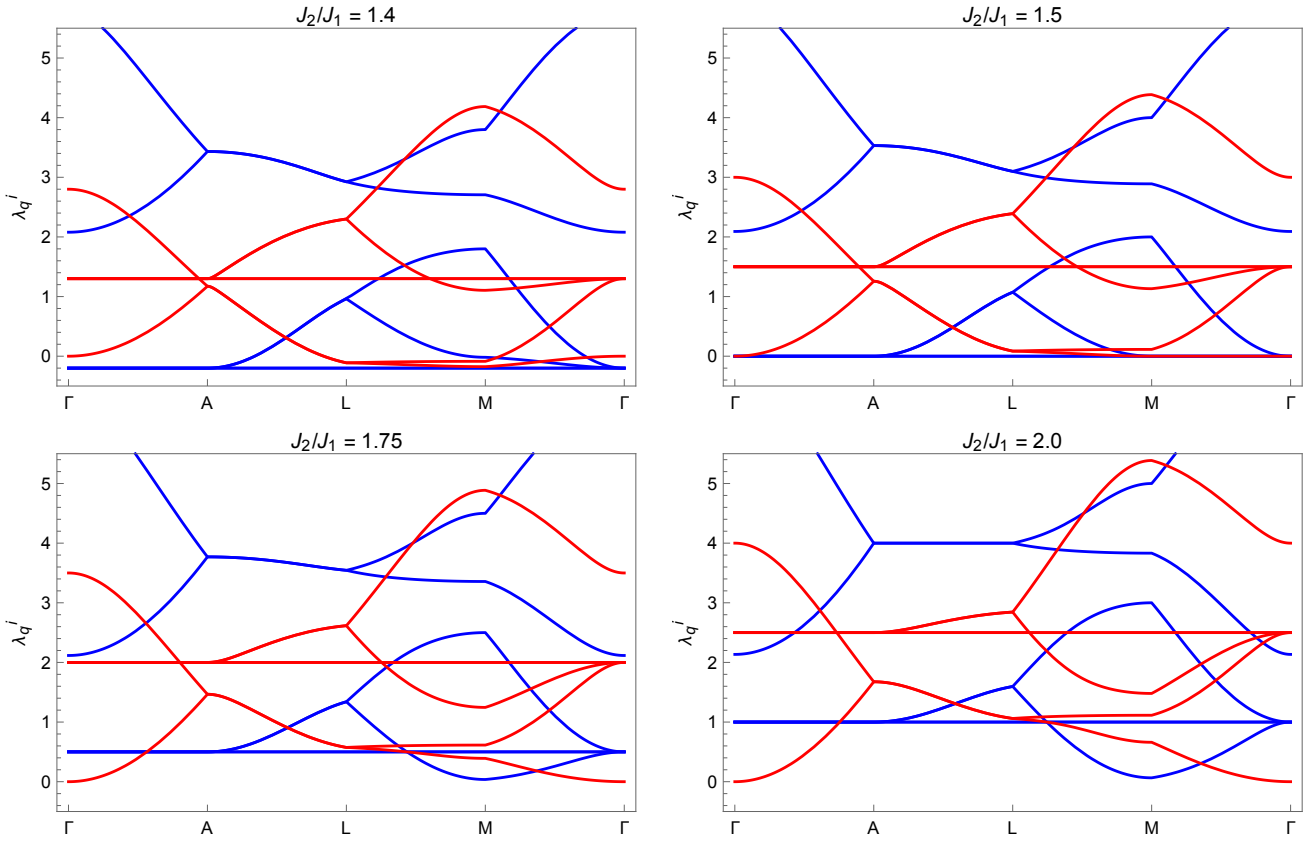

Figure 4.1: Eigenvalues of the matrices $\mathbf{M}^x_{\mathbf{q}}/J_1$ (in red, corresponding to in-plane excitations) and $\mathbf{M}^y_{\mathbf{q}}/J_1$ (in blue, corresponding to out-of-plane excitations) for different values of J_2/J_1, along a path through symmetry points of the first Brillouin zone. Notice how there are excitations with negative energy if $J_2/J_1 < 3/2$, and that there is a doubly degenerate flat band that scales linearly with J_2/J_1 that becomes zero at $J_2/J_1 = 3/2$. See also Ref. [4].

where $\boldsymbol{\epsilon}^{x/y}_{\mathbf{q}}$ and $\mathbf{h}^{x/y}_{\mathbf{q}}$ are 8-component vectors, while $(\mathbf{G}^{x/y}_{\mathbf{q}})^{-1}$ are 8×8 matrices. The partition function can now be obtained from

$$Z = \int \left(\prod_{a,\mathbf{q}} \frac{\mathrm{d}(\epsilon^{xa}_{\mathbf{q}})^* \mathrm{d}\epsilon^{xa}_{\mathbf{q}}}{2\pi i} \frac{\mathrm{d}(\epsilon^{ya}_{\mathbf{q}})^* \mathrm{d}\epsilon^{ya}_{\mathbf{q}}}{2\pi i} \right) e^{-\beta H} \equiv \int \mathcal{D}\epsilon\, e^{-\beta H}. \tag{4.40}$$

Using standard Gaussian integrals (see appendix A.3) and ignoring the constant term $-\beta E_{GS}$ (which will not play a role for any of the expectation values), this becomes

$$Z = \prod_{\mathbf{q}} \left[\frac{1}{\mathrm{Det}\left[-(\mathbf{G}^x_{\mathbf{q}})^{-1}\right]} \frac{1}{\mathrm{Det}\left[-(\mathbf{G}^y_{\mathbf{q}})^{-1}\right]} \exp\left[-(\mathbf{h}^x_{\mathbf{q}})^* \cdot \mathbf{G}^x_{\mathbf{q}} \cdot \mathbf{h}^x_{\mathbf{q}} - (\mathbf{h}^y_{\mathbf{q}})^* \cdot \mathbf{G}^y_{\mathbf{q}} \cdot \mathbf{h}^y_{\mathbf{q}}\right] \right], \tag{4.41}$$

or

$$Z[h, h^*] = \mathcal{N} \exp\left[-\sum_{\mathbf{q}} \left((\mathbf{h}^x_{\mathbf{q}})^* \cdot \mathbf{G}^x_{\mathbf{q}} \cdot \mathbf{h}^x_{\mathbf{q}} + (\mathbf{h}^y_{\mathbf{q}})^* \cdot \mathbf{G}^y_{\mathbf{q}} \cdot \mathbf{h}^y_{\mathbf{q}} \right) \right]. \tag{4.42}$$

From Eqs. (4.39) and (4.40), we also see that

$$\begin{aligned} \left. \frac{\partial^2 \ln Z}{\partial h^{x/ya}_{\mathbf{q}} \partial (h^{x/ya}_{\mathbf{q}})^*} \right|_{h=0} &= \frac{1}{Z} \left. \frac{\partial^2 Z}{\partial h^{x/ya}_{\mathbf{q}} \partial (h^{x/ya}_{\mathbf{q}})^*} \right|_{h=0} - \frac{1}{Z} \frac{\partial Z}{\partial h^{x/ya}_{\mathbf{q}}} \frac{1}{Z} \left. \frac{\partial Z}{\partial (h^{x/ya}_{\mathbf{q}})^*} \right|_{h=0} \\ &= \left\langle |\epsilon^{x/ya}_{\mathbf{q}}|^2 \right\rangle - \left| \left\langle \epsilon^{x/ya}_{\mathbf{q}} \right\rangle \right|^2, \end{aligned} \tag{4.43}$$

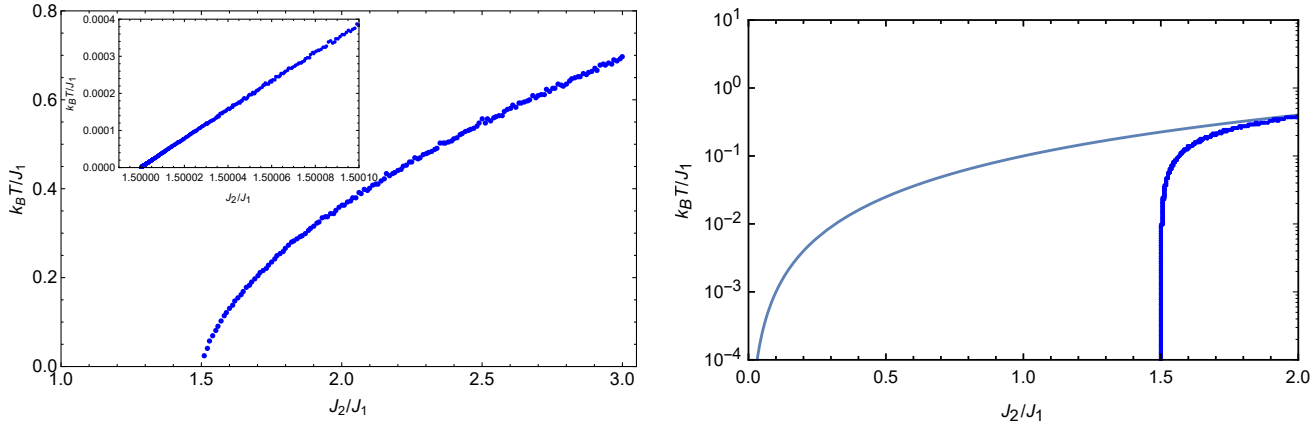

Figure 4.2: Lowest order estimate of the critical temperature k_BT_c/J_1 as a function of the ratio of interaction strengths J_2/J_1. The inset zooms in on the region very close to the boundary value $J_2/J_1 = 3/2$, while the right panel contains a logarithmic plot with the same range as Fig. 1.10. A quadratic curve similar to that of Fig. 1.10 was drawn through it. Note that the numbers on the y-axis are not necessarily correct and that there should likely be a scaling factor of the order 1, since the derivation only gives the qualitative behaviour and the order of magnitude of T_c.

which, using $\langle \epsilon_{\mathbf{q}}^{x/ya} \rangle = 0$ and Eq. (4.42), leads to

$$\left\langle |\epsilon_{\mathbf{q}}^{x/ya}|^2 \right\rangle = -\left(\mathbf{G}_{\mathbf{q}}^{x/y}\right)^{aa} = \frac{2k_BT}{N_c}\left((\mathbf{M}_{\mathbf{q}}^{x/y})^{-1}\right)^{aa}, \tag{4.44}$$

Referring back to the criterion, Eq. (4.36), we finally obtain

$$\frac{k_BT_c}{4N_c}\sum_{\mathbf{q}} \mathrm{Tr}\left[(\mathbf{M}_{\mathbf{q}}^{x})^{-1} + (\mathbf{M}_{\mathbf{q}}^{y})^{-1}\right] \sim 1. \tag{4.45}$$

Considering the continuum limit (i.e. looking at an infinite lattice), the sum over $\mathbf{q}$ can be written as $\frac{N_c}{(2\pi)^3}\int \mathrm{d}\mathbf{q}$, such that

$$\frac{k_BT_c}{J_1} \sim \frac{4(2\pi)^3}{\int \mathrm{d}\mathbf{q}\, \mathrm{Tr}\left[(\mathbf{M}_{\mathbf{q}}^{x}/J_1)^{-1} + (\mathbf{M}_{\mathbf{q}}^{y}/J_1)^{-1}\right]} \tag{4.46}$$

Finally, we can use the fact that the trace is just the sum of the eigenvalues to find that

$$\frac{k_BT_c}{J_1} \sim \frac{4(2\pi)^3}{\sum_i \int \mathrm{d}\mathbf{q}\left(\frac{1}{\lambda_{\mathbf{q}}^{xi}} + \frac{1}{\lambda_{\mathbf{q}}^{yi}}\right)}, \tag{4.47}$$

where $\lambda_{\mathbf{q}}^{x/yi}$ are the eigenvalues of the interaction matrices $\mathbf{M}_{\mathbf{q}}^{x/y}/J_1$ that were given in the previous section.

Now that we have expressions to estimate the critical temperature, we can investigate its behaviour in this lowest order approximation. As we have seen before, there is a doubly degenerate flat band corresponding to out-of-plane fluctuations (i.e. the excitations ϵ_i^{ya}) that goes to zero when J_2/J_1 approaches $3/2$; explicitly, it is given by the eigenvalue $\lambda_{\mathbf{q}}^{yi} = 2(J_2/J_1 - 3/2)$. In the limit that J_2/J_1 goes to $3/2$ from above, these two flat bands dominate the denominator, and a simple calculation shows that

$$\left.\frac{k_BT_c}{J_1}\right|_{(J_2/J_1-3/2)\ll 1} \sim 4(J_2/J_1 - 3/2) \tag{4.48}$$

For the behaviour further away from the point $J_2/J_1 = 3/2$, Mathematica has been used to numerically evaluate the denominator of Eq. (4.47) by adaptive Monte Carlo integration. The results are shown in Fig. 4.2. Fitting these data to a power law, one finds that

$$\frac{k_BT_c}{J_1} \propto (J_2/J_1 - 3/2)^{\alpha}, \tag{4.49}$$

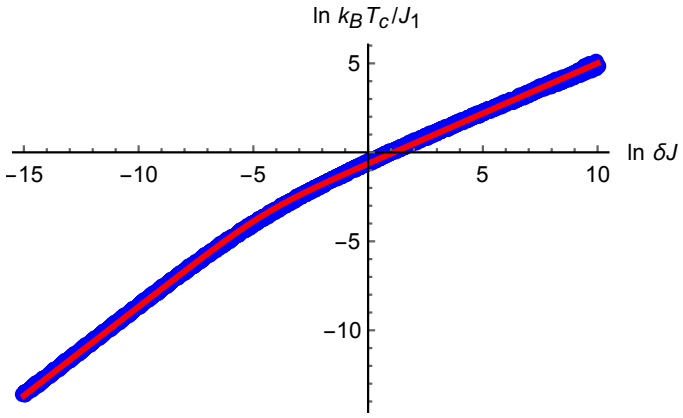

Figure 4.3: Lowest order estimate of the critical temperature $k_B T_c/J_1$ as a function of the ratio of δJ. The red line is a fit through the blue data points, as further explained in the text.

where $\alpha \approx 0.58$. As it seems quite unusual for the large J_2/J_1 behaviour to have a lower leading power than the low J_2/J_1 region (where it is linear), we will end this section by investigating these powers in more detail.

In order to find the leading power, we will look at a double logarithmic plot of the data: rewriting an equation $y = ax^b$ to the variables $Y = \ln y$ and $X = \ln x$, it becomes $e^Y = ae^{bX}$, or $Y = \ln a + bX$, so the leading power can be found by measuring the slope of the corresponding log-log plot. Introducing the variable

$$\delta J \equiv J_2/J_1 - 3/2, \tag{4.50}$$

the double logarithmic plot of the lowest order estimate of the critical temperature is shown in Fig. 4.3. The results from this figure suggest that there are two regions, each with a different leading power. We fit the data to a very simple function that would support such behaviour:

$$\frac{k_B T_c}{J_1} = \frac{c_1 \delta J}{(\delta J + c_2)^{c_3}}, \tag{4.51}$$

where c_1, c_2 and c_3 are fit parameters. In the limit $\delta J \to 0$, this expression becomes linear, while in the limit $\delta J \to \infty$, the leading power becomes $1 - c_3$. Note that this very simple model only serves to show that it is possible to make such behaviour explicit; in reality, this model is far too simple to properly describe the phase transition.

It turns out that the leading power indeed goes to 1 as $\delta J \to 0$, while for $\delta J \to \infty$ it becomes close to a square root. The linear part was already derived above, but this square root remains to be explained.

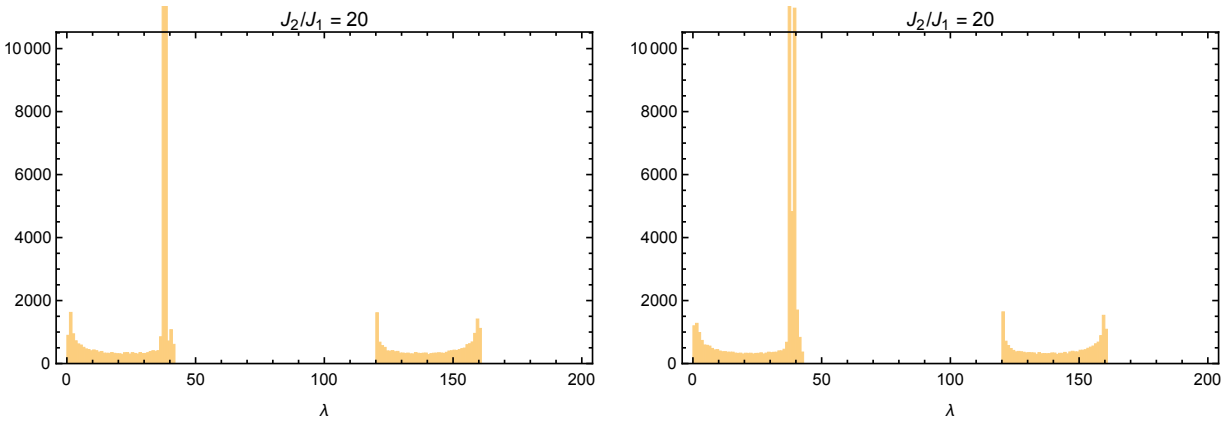

Figure 4.4: Density of states estimates of the matrices $\mathbf{M}^x_{\mathbf{q}}/J_1$ (left) and $\mathbf{M}^y_{\mathbf{q}}/J_1$ (right) for $J_2/J_1 = 20$. The horizontal axis gives the eigenvalues (or the energies); the y-axis gives the number of times that energy appears.

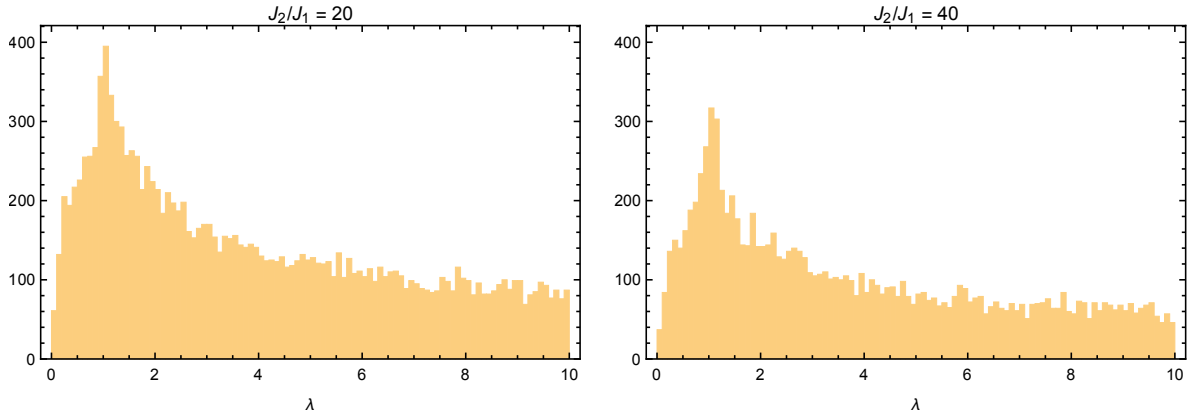

Figure 4.5: Density of states estimate of the matrix $\mathbf{M}^x_{\mathbf{q}}/J_1$ for $J_2/J_1 = 20$ (left) and $J_2/J_1 = 40$ (right), zoomed in on the low energies.

To see where it comes from, we consider the density of states, i.e. the number of states corresponding to a given energy. To find a crude estimate of the density of states, histograms have been made of all the eigenvalues of the matrices $\mathbf{M}^x_{\mathbf{q}}/J_1$ and $\mathbf{M}^y_{\mathbf{q}}/J_1$ for a large number of random values for $\mathbf{q}$. An example is shown in Fig. 4.4. The large peaks that appear originate from the flat bands that we discussed before. At large values of δJ, these peaks are located well away from the low energies, such that they are no longer important, and we should instead be looking at the behaviour of the density of states of low energies. Looking at the density of states for several large values of J_2/J_1, it has been found that the low energy density of states scales with approximately $1/\sqrt{\delta J}$, see for example Fig. 4.5. More explicitly, we have

$$\rho(E, \delta J)\Big|_{\delta J \gg 1} \approx \frac{\rho_0(E)}{\sqrt{\delta J}}, \tag{4.52}$$

for small energies, where $\rho(E, \delta J)$ is the density of states and $\rho_0(E)$ is an unknown function of the energy. Using this result, we can go back to Eq. (4.47). Seeing how the small eigenvalues dominate the integral that appears in this expression, the integral has same the δJ dependence as the low energy density of states. This leads to the conclusion that the right-hand side of the expression scales with approximately $\sqrt{\delta J}$ for large values of δJ, successfully explaining the behaviour seen in Figs. 4.2 and 4.3.

4.3 Higher order contributions

In this section, we will investigate the effects from including the quartic terms of the Hamiltonian in addition to the quadratic terms. Returning to the nomenclature from the previous section, the quartic terms are interpreted as interaction terms. Usually, perturbation theory of such a theory is done in terms of a coupling constant appearing in front of the interaction terms. For our problem, such a coupling constant is absent, but we restrict ourselves to the region where the partition function is almost entirely determined by small ϵ, such that we can still perform the usual perturbation theory. Before we even begin performing such calculations, we can already say something about the effects that the quartic terms will have: looking at Eq. (4.23) and using the fact that $\mathbf{M}^x_{\mathbf{q}}$ only has non-negative eigenvalues, we see that all quartic terms are strictly positive. As a result, the expectation values of the excitations are smaller than they were without the quartic terms for a given temperature, leading to the conclusion that the inclusion of quartic terms will lead to a larger critical temperature. We will now calculate the effects from (quartic) interaction terms in two different ways: first, we include the interactions by approximating them as quadratic corrections, such that the Hamiltonian can once again be treated as non-interacting; second, we will perform perturbation theory directly, using methods from field theory.

4.3.1 Quadratic corrections to the Hamiltonian

We will now estimate the effects of interaction terms by approximating them as corrections to the non-interacting quadratic Hamiltonian. To do so, we will distinguish between the expectation values $\langle\ldots\rangle_0$ according to the non-interacting Hamiltonian $H = E_{GS} + H_2$, and the expectation values $\langle\ldots\rangle$ according to the interacting Hamiltonian $H = E_{GS} + H_2 + H_4$. The idea is to interpret H_4 as a shift in H_2 by finding appropriate approximations of the different parts of H_4 in terms of expectation values. As the non-interacting Hamiltonian is Gaussian, we can use Wick's theorem (see appendix A.4) to find that the non-interacting expectation values of the combinations that appear in Eq. (4.23) can be written as

$$\left\langle (\epsilon^{xa}_{\mathbf{q}_1+\mathbf{q}_3})^* \epsilon^{xa}_{\mathbf{q}_1} (\epsilon^{xb}_{\mathbf{q}_2-\mathbf{q}_3})^* \epsilon^{xb}_{\mathbf{q}_2} \right\rangle_0 = \left\langle (\epsilon^{xa}_{\mathbf{q}_1+\mathbf{q}_3})^* \epsilon^{xa}_{\mathbf{q}_1} \right\rangle_0 \left\langle (\epsilon^{xb}_{\mathbf{q}_2-\mathbf{q}_3})^* \epsilon^{xb}_{\mathbf{q}_2} \right\rangle_0 + \left\langle (\epsilon^{xa}_{\mathbf{q}_1+\mathbf{q}_3})^* \epsilon^{xb}_{\mathbf{q}_2} \right\rangle_0 \left\langle (\epsilon^{xb}_{\mathbf{q}_2-\mathbf{q}_3})^* \epsilon^{xa}_{\mathbf{q}_1} \right\rangle_0 , \tag{4.53}$$

and similarly for the other combinations. We will now consider the first term of Eq. (4.23) as an example. This term can be approximated using

$$\begin{aligned}
(\epsilon^{xa}_{\mathbf{q}_1+\mathbf{q}_3})^* \epsilon^{xa}_{\mathbf{q}_1} (\epsilon^{xb}_{\mathbf{q}_2-\mathbf{q}_3})^* \epsilon^{xb}_{\mathbf{q}_2} &\approx \frac{1}{2} \Big[\left\langle (\epsilon^{xa}_{\mathbf{q}_1+\mathbf{q}_3})^* \epsilon^{xa}_{\mathbf{q}_1} \right\rangle_0 (\epsilon^{xb}_{\mathbf{q}_2-\mathbf{q}_3})^* \epsilon^{xb}_{\mathbf{q}_2} + \left\langle (\epsilon^{xb}_{\mathbf{q}_2-\mathbf{q}_3})^* \epsilon^{xa}_{\mathbf{q}_1} \right\rangle_0 (\epsilon^{xa}_{\mathbf{q}_1+\mathbf{q}_3})^* \epsilon^{xb}_{\mathbf{q}_2} \\
&\quad + \left\langle (\epsilon^{xa}_{\mathbf{q}_1+\mathbf{q}_3})^* \epsilon^{xb}_{\mathbf{q}_2} \right\rangle_0 (\epsilon^{xb}_{\mathbf{q}_2-\mathbf{q}_3})^* \epsilon^{xa}_{\mathbf{q}_1} + \left\langle (\epsilon^{xb}_{\mathbf{q}_2-\mathbf{q}_3})^* \epsilon^{xb}_{\mathbf{q}_2} \right\rangle_0 (\epsilon^{xa}_{\mathbf{q}_1+\mathbf{q}_3})^* \epsilon^{xa}_{\mathbf{q}_1} \Big] \\
&= -\frac{1}{2} \big[G^{xaa}_{\mathbf{q}_1} \delta_{\mathbf{q}_3,0} (\epsilon^{xb}_{\mathbf{q}_2})^* \epsilon^{xb}_{\mathbf{q}_2} + G^{xab}_{\mathbf{q}_1} \delta_{\mathbf{q}_3,\mathbf{q}_2-\mathbf{q}_1} (\epsilon^{xa}_{\mathbf{q}_2})^* \epsilon^{xb}_{\mathbf{q}_2} \\
&\quad + G^{xba}_{\mathbf{q}_2} \delta_{\mathbf{q}_3,\mathbf{q}_2-\mathbf{q}_1} (\epsilon^{xb}_{\mathbf{q}_1})^* \epsilon^{xa}_{\mathbf{q}_1} + G^{xbb}_{\mathbf{q}_2} \delta_{\mathbf{q}_3,0} (\epsilon^{xa}_{\mathbf{q}_1})^* \epsilon^{xa}_{\mathbf{q}_1} \big] .
\end{aligned} \tag{4.54}$$

This is just a more general version of the approximation $a^2 \approx \langle a\rangle_0 a$, and the prefactor is there such that Eq. (4.53) still holds. A better approximation can be obtained by using the expectation values $\langle\ldots\rangle$ rather than $\langle\ldots\rangle_0$, which would lead to self-consistency equations, but the above will suffice for a first approximation. With this approximation, the first term of H_4 (call it $H_{4,1}$) can be written as

$$\begin{aligned}
H_{4,1} &\approx -\frac{N_c}{16} \sum_{\mathbf{q}_1,\mathbf{q}_2} \sum_{ab} \left[M^{xab}_0 \left(G^{xaa}_{\mathbf{q}_1} (\epsilon^{xb}_{\mathbf{q}_2})^* \epsilon^{xb}_{\mathbf{q}_2} + G^{xbb}_{\mathbf{q}_2} (\epsilon^{xa}_{\mathbf{q}_1})^* \epsilon^{xa}_{\mathbf{q}_1} \right) + M^{xab}_{\mathbf{q}_2-\mathbf{q}_1} \left(G^{xab}_{\mathbf{q}_1} (\epsilon^{xa}_{\mathbf{q}_2})^* \epsilon^{xb}_{\mathbf{q}_2} + G^{xba}_{\mathbf{q}_2} (\epsilon^{xb}_{\mathbf{q}_1})^* \epsilon^{xa}_{\mathbf{q}_1} \right) \right] \\
&= -\frac{N_c}{8} \sum_{\mathbf{q}_1,\mathbf{q}_2} \sum_{ab} \left[M^{xab}_0 G^{xaa}_{\mathbf{q}_1} (\epsilon^{xb}_{\mathbf{q}_2})^* \epsilon^{xb}_{\mathbf{q}_2} + M^{xab}_{\mathbf{q}_2-\mathbf{q}_1} G^{xab}_{\mathbf{q}_1} (\epsilon^{xa}_{\mathbf{q}_2})^* \epsilon^{xb}_{\mathbf{q}_2} \right] ,
\end{aligned} \tag{4.55}$$

where we used the fact that $\mathbf{M}^x_{\mathbf{q}}$ is Hermitian. Similarly,

$$(\epsilon^{xa}_{\mathbf{q}_1+\mathbf{q}_3})^* \epsilon^{xa}_{\mathbf{q}_1} (\epsilon^{yb}_{\mathbf{q}_2-\mathbf{q}_3})^* \epsilon^{yb}_{\mathbf{q}_2} \approx -\frac{1}{2} \left[G^{xaa}_{\mathbf{q}_1} \delta_{\mathbf{q}_3,0} (\epsilon^{yb}_{\mathbf{q}_2})^* \epsilon^{yb}_{\mathbf{q}_2} + G^{ybb}_{\mathbf{q}_2} \delta_{\mathbf{q}_3,0} (\epsilon^{xa}_{\mathbf{q}_1})^* \epsilon^{xa}_{\mathbf{q}_1} \right] \tag{4.56}$$

can be used to write the third term of H_4 as

$$H_{4,3} \approx -\frac{N_c}{16} \sum_{\mathbf{q}_1,\mathbf{q}_2} \sum_{ab} \left[M^{xab}_0 \left(G^{xaa}_{\mathbf{q}_1} (\epsilon^{yb}_{\mathbf{q}_2})^* \epsilon^{yb}_{\mathbf{q}_2} + G^{ybb}_{\mathbf{q}_2} (\epsilon^{xa}_{\mathbf{q}_1})^* \epsilon^{xa}_{\mathbf{q}_1} \right) \right] \tag{4.57}$$

Using similar approximations for the remainder of H_4 and putting all results together, we find

$$\begin{aligned}
H_4 &\approx -\frac{N_c}{8} \sum_{\mathbf{q}_1,\mathbf{q}_2} \sum_{ab} \big[M^{xab}_0 \left(G^{xaa}_{\mathbf{q}_1} (\epsilon^{xb}_{\mathbf{q}_2})^* \epsilon^{xb}_{\mathbf{q}_2} + G^{yaa}_{\mathbf{q}_1} (\epsilon^{yb}_{\mathbf{q}_2})^* \epsilon^{yb}_{\mathbf{q}_2} + G^{xaa}_{\mathbf{q}_1} (\epsilon^{yb}_{\mathbf{q}_2})^* \epsilon^{yb}_{\mathbf{q}_2} \right. \\
&\quad \left. + G^{yaa}_{\mathbf{q}_1} (\epsilon^{xb}_{\mathbf{q}_2})^* \epsilon^{xb}_{\mathbf{q}_2} \right) + M^{xab}_{\mathbf{q}_2-\mathbf{q}_1} \left(G^{xab}_{\mathbf{q}_1} (\epsilon^{xa}_{\mathbf{q}_2})^* \epsilon^{xb}_{\mathbf{q}_2} + G^{yab}_{\mathbf{q}_1} (\epsilon^{ya}_{\mathbf{q}_2})^* \epsilon^{yb}_{\mathbf{q}_2} \right) \big] \\
&= \frac{N_c}{2} \sum_{\mathbf{q}} \sum_{ab} \left[(\epsilon^{xa}_{\mathbf{q}})^* V^{xab}_{\mathbf{q}} \epsilon^{xb}_{\mathbf{q}} + (\epsilon^{ya}_{\mathbf{q}})^* V^{yab}_{\mathbf{q}} \epsilon^{yb}_{\mathbf{q}} \right] ,
\end{aligned} \tag{4.58}$$

where

$$V^{xab}_{\mathbf{q}} \equiv -\frac{1}{4} \sum_{\mathbf{q}'} \left[M^{xab}_{\mathbf{q}-\mathbf{q}'} G^{xab}_{\mathbf{q}'} + \delta^{ab} \sum_c M^{xac}_0 \left(G^{xcc}_{\mathbf{q}'} + G^{ycc}_{\mathbf{q}'} \right) \right] , \tag{4.59}$$

$$V^{yab}_{\mathbf{q}} \equiv -\frac{1}{4} \sum_{\mathbf{q}'} \left[M^{xab}_{\mathbf{q}-\mathbf{q}'} G^{yab}_{\mathbf{q}'} + \delta^{ab} \sum_c M^{xac}_0 \left(G^{xcc}_{\mathbf{q}'} + G^{ycc}_{\mathbf{q}'} \right) \right] . \tag{4.60}$$

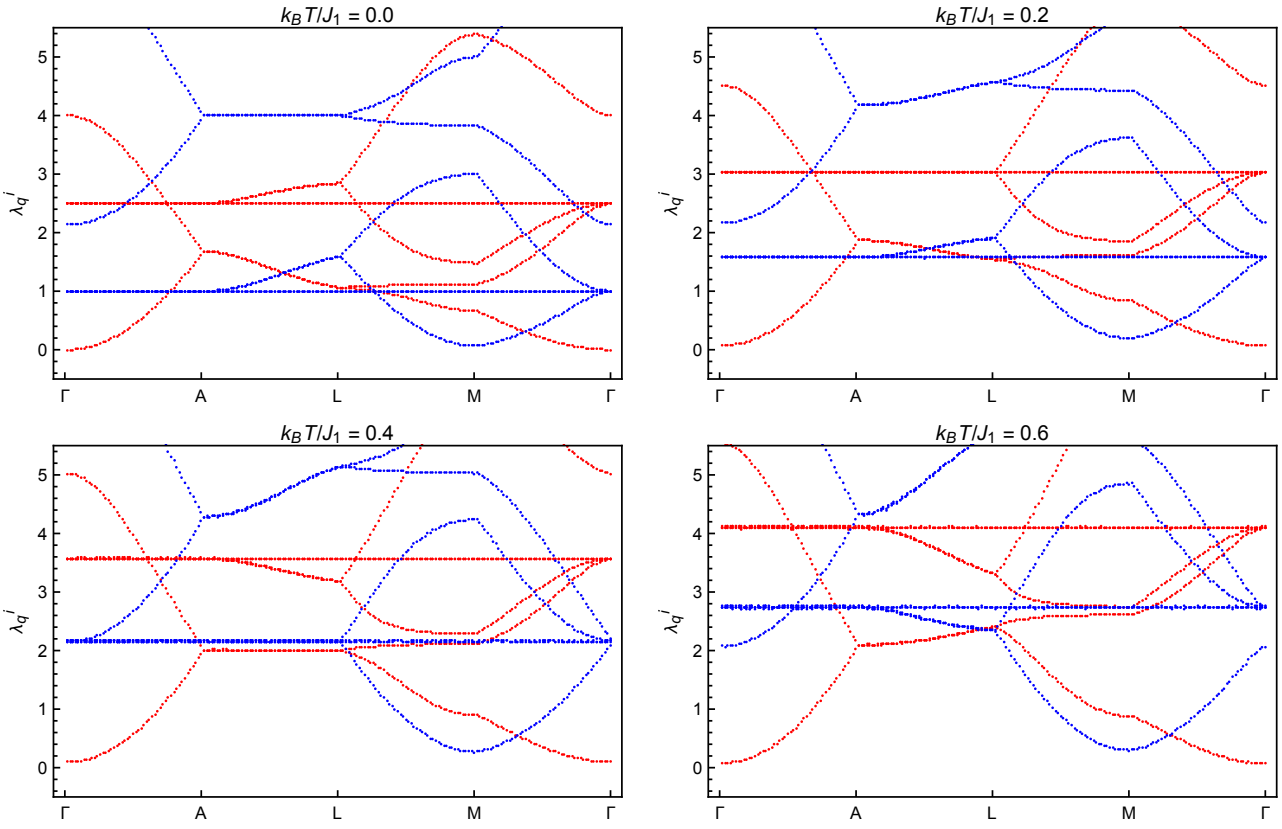

Figure 4.6: Eigenvalues of the matrices $\left(\mathbf{M}_\mathbf{q}^x/J_1 + \frac{k_BT_c}{J_1}\mathbf{v}_\mathbf{q}^x\right)$ (red) and $\left(\mathbf{M}_\mathbf{q}^y/J_1 + \frac{k_BT_c}{J_1}\mathbf{v}_\mathbf{q}^y\right)$ (blue) for $J_2/J_1 = 2.0$ and different temperatures, along a path through symmetry points of the first Brillouin zone. Note that the top-left panel is the same as the bottom-right panel of Fig. 4.1.

Note that $\mathbf{G}_\mathbf{q}^{x/y} = -\frac{2k_BT}{N_c}(\mathbf{M}_\mathbf{q}^{x/y})^{-1}$ still holds. Finally, we see that in our approximation the Hamiltonian becomes

$$H = E_{GS} + H_2 + H_4 \approx E_{GS} + \frac{N_c}{2}\sum_\mathbf{q}\sum_{ab}\left[(\epsilon_\mathbf{q}^{xa})^*\left(M_\mathbf{q}^{xab} + V_\mathbf{q}^{xab}\right)\epsilon_\mathbf{q}^{xb} + (\epsilon_\mathbf{q}^{ya})^*\left(M_\mathbf{q}^{yab} + V_\mathbf{q}^{yab}\right)\epsilon_\mathbf{q}^{yb}\right]. \quad (4.61)$$

The Hamiltonian now has the same form as it had for the lowest order approximation, but the interaction matrices $\mathbf{M}_\mathbf{q}^{x/y}$ have been replaced with $\mathbf{M}_\mathbf{q}^{x/y} + \mathbf{V}_\mathbf{q}^{x/y}$. Therefore, the same methods can be used to approximate the critical temperature. It is important to note that the matrices $\mathbf{V}_\mathbf{q}^{x/y}$ scale linearly with the temperature, so it is convenient to introduce dimensionless matrices $\mathbf{v}_\mathbf{q}^{x/y}$ and write them as $\mathbf{V}_\mathbf{q}^{x/y} = k_BT\mathbf{v}_\mathbf{q}^{x/y}$. Repeating the calculations from the previous section, the criterion for the critical temperature becomes

$$\frac{k_BT_c}{4(2\pi)^3J_1}\int \mathrm{d}\mathbf{q}\,\mathrm{Tr}\left[\left(\mathbf{M}_\mathbf{q}^x/J_1 + \frac{k_BT_c}{J_1}\mathbf{v}_\mathbf{q}^x\right)^{-1} + \left(\mathbf{M}_\mathbf{q}^y/J_1 + \frac{k_BT_c}{J_1}\mathbf{v}_\mathbf{q}^y\right)^{-1}\right] \sim 1. \quad (4.62)$$

Contrary to what we have done in the previous section, it is not straightforward to solve T_c from this expression. This is due to the fact that the inverse matrices that appear in the integrals depend on the temperature as well, in addition to the temperature dependence that appears outside the integral. One way to solve this equation is to calculate the left-hand side of the equation for many different temperatures and see when it becomes of the order 1. However, this proves to be very difficult due to the fact that we are working with six-dimensional integrals and inverse matrices. To do this numerically, one would have to calculate a three-dimensional integral of an 8×8 matrix and take its inverse for each value of $\mathbf{q}$ that is part of the overall three-dimensional integral. This would then have to be repeated for

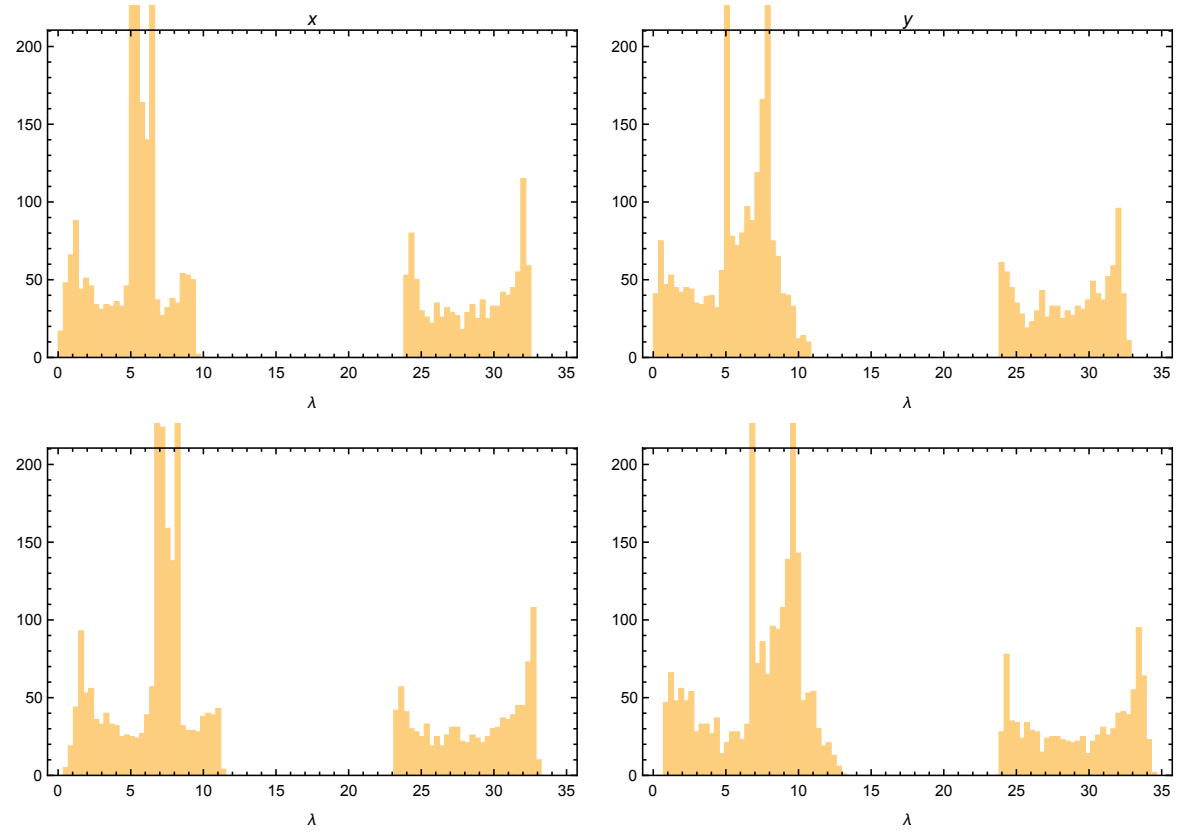

Figure 4.7: Density of states estimates at $J_2/J_1 = 4.0$ for the matrices $\left(\mathbf{M}^x_{\mathbf{q}}/J_1 + \frac{k_BT}{J_1}\mathbf{v}^x_{\mathbf{q}}\right)$ (left column) and $\left(\mathbf{M}^y_{\mathbf{q}}/J_1 + \frac{k_BT}{J_1}\mathbf{v}^y_{\mathbf{q}}\right)$ (right column), with $k_BT/J_1 = 0$ (top row) and $k_BT/J_1 = 1$ (bottom row).

many temperatures and then again for many values of J_2/J_1 in order to find T_c as a function of J_2/J_1. Rather than going through this trouble, we will now investigate the implications of Eq. (4.62) without explicitly solving it.

Let us first look at low temperatures. In this case, the prefactors that appear in front of the $\mathbf{v}^{x/y}_{\mathbf{q}}$ matrices are small, so their influence on the integral becomes small as well. This leads to the conclusion that for very small temperatures the left-hand side becomes the same as it was in the previous section. Now since the critical temperature goes to zero in the limit $J_2/J_1 \to 3/2$, this means that the interaction terms do not influence the critical temperature in this limit, and we find that it is still given by Eq. (4.48) despite the inclusion of interaction terms.

To see what the influence of interactions is at higher temperatures, we look at the eigenvalues of the matrices $\left(\mathbf{M}^{x/y}_{\mathbf{q}}/J_1 + \frac{k_BT}{J_1}\mathbf{v}^{x/y}_{\mathbf{q}}\right)$ for different temperatures at a fixed value of J_2/J_1. The eigenvalues for $J_2/J_1 = 2.0$ are shown in Fig. 4.6. As can be seen from the figure, most eigenvalues move further away from zero for increasing temperature. While the lowest order results say that the critical temperature is of the order $k_BT/J_1 \sim 0.4$ (see the plots from the previous section), we see that the eigenvalues changed significantly for this temperature. Since the eigenvalues are now further away from zero, the integral from Eq. (4.62) is smaller, and it requires a larger temperature for the left-hand side to become of the order 1. This confirms the early observations from the beginning of this section.

Finally, let us take a look at the influence of the quartic terms on the density of states. Fig. 4.7 shows the density of states of the matrices $\left(\mathbf{M}^{x/y}_{\mathbf{q}}/J_1 + \frac{k_BT}{J_1}\mathbf{v}^{x/y}_{\mathbf{q}}\right)$ for zero temperature (top row) and for $k_BT/J_1 = 1$ (bottom row) at the fixed value $J_2/J_1 = 4.0$. It is again immediately clear that the density of states is generally shifted to the right for increasing temperature, i.e. the most abundant energies are higher than before. This leads again to the conclusion that the expectation values of the squared excitations are smaller than in the lowest order approximation, leading to a larger critical temperature.

4.3.2 Direct perturbation theory of the correlation functions

It is also possible to apply perturbation theory directly to the expectation values that are required for approximating the critical temperature. Starting with the Hamiltonian $H = E_{GS} + H_2 + gH_4$, where g is a dimensionless coupling constant, it is shown in appendix A.5 that the relevant expectation values can be calculated by using Feynman diagrams:

$$\left\langle \epsilon_{\mathbf{q}}^{xa} (\epsilon_{\mathbf{q}}^{xb})^* \right\rangle =$$

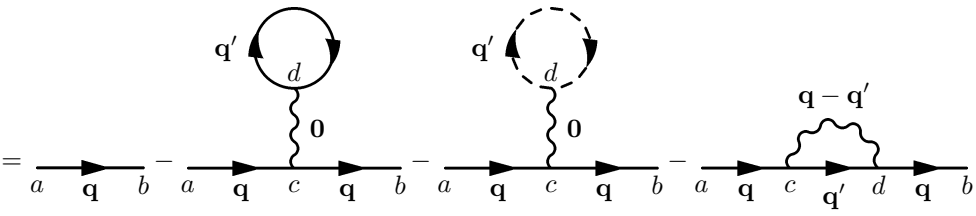

$$+ \mathcal{O}(g^2)$$

$$= -G_{\mathbf{q}}^{xab} + \frac{gN_c}{4k_BT} \sum_{\mathbf{q}'} \sum_{cd} \Big[M_0^{xcd} \left(G_{\mathbf{q}}^{xac} G_{\mathbf{q}}^{xcb} G_{\mathbf{q}'}^{xdd} + G_{\mathbf{q}}^{xac} G_{\mathbf{q}}^{xcb} G_{\mathbf{q}'}^{ydd} \right) + M_{\mathbf{q}-\mathbf{q}'}^{xcd} G_{\mathbf{q}}^{xac} G_{\mathbf{q}'}^{xcd} G_{\mathbf{q}}^{xdb} \Big] + \mathcal{O}(g^2) \tag{4.63}$$

and

$$\left\langle \epsilon_{\mathbf{q}}^{ya} (\epsilon_{\mathbf{q}}^{yb})^* \right\rangle =$$

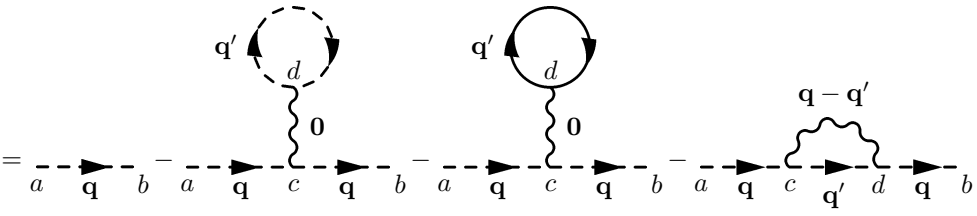

$$+ \mathcal{O}(g^2)$$

$$= -G_{\mathbf{q}}^{yab} + \frac{gN_c}{4k_BT} \sum_{\mathbf{q}'} \sum_{cd} \Big[M_0^{xcd} \left(G_{\mathbf{q}}^{yac} G_{\mathbf{q}}^{ycb} G_{\mathbf{q}'}^{ydd} + G_{\mathbf{q}}^{yac} G_{\mathbf{q}}^{ycb} G_{\mathbf{q}'}^{xdd} \right) + M_{\mathbf{q}-\mathbf{q}'}^{xcd} G_{\mathbf{q}}^{yac} G_{\mathbf{q}'}^{ycd} G_{\mathbf{q}}^{ydb} \Big] + \mathcal{O}(g^2), \tag{4.64}$$

where

$$-G_{\mathbf{q}}^{x/yab} = \left\langle \epsilon_{\mathbf{q}}^{x/ya} (\epsilon_{\mathbf{q}}^{x/yb})^* \right\rangle_0 = \frac{2k_BT}{N_c} \left((\mathbf{M}_{\mathbf{q}}^{x/y})^{-1} \right)^{ab} \tag{4.65}$$

is the non-interacting Green's function. The diagrams should be interpreted according to Table 4.1, and we sum over all internal indices and momenta. For our problem, we have $g = 1$, so the above expansions cannot be used in general. However, restricting ourselves to the temperatures corresponding to small excitations ϵ (i.e. low temperatures), we can rewrite it as a temperature expansion:

$$\begin{aligned} \left\langle \epsilon_{\mathbf{q}}^{xa} (\epsilon_{\mathbf{q}}^{xb})^* \right\rangle = \frac{2k_BT}{N_c} \left((\mathbf{M}_{\mathbf{q}}^{x})^{-1} \right)^{ab} - \frac{2k_B^2T^2}{N_c^2} \sum_{\mathbf{q}'} \sum_{cd} \Big[M_0^{xcd} \Big(& \left((\mathbf{M}_{\mathbf{q}}^{x})^{-1} \right)^{ac} \left((\mathbf{M}_{\mathbf{q}}^{x})^{-1} \right)^{cb} \left((\mathbf{M}_{\mathbf{q}'}^{x})^{-1} \right)^{dd} \\ & + \left((\mathbf{M}_{\mathbf{q}}^{x})^{-1} \right)^{ac} \left((\mathbf{M}_{\mathbf{q}}^{x})^{-1} \right)^{cb} \left((\mathbf{M}_{\mathbf{q}'}^{y})^{-1} \right)^{dd} \Big) \\ & + M_{\mathbf{q}-\mathbf{q}'}^{xcd} \left((\mathbf{M}_{\mathbf{q}}^{x})^{-1} \right)^{ac} \left((\mathbf{M}_{\mathbf{q}'}^{x})^{-1} \right)^{cd} \left((\mathbf{M}_{\mathbf{q}}^{x})^{-1} \right)^{db} \Big] + \mathcal{O}\left((k_BT)^3 \right), \end{aligned} \tag{4.66}$$

Expression	Diagram
$-G_{\mathbf{q}}^{xab}$	$a \xrightarrow[\mathbf{q}]{} b$
$-G_{\mathbf{q}}^{yab}$	$a \dashrightarrow[\mathbf{q}]{} b$
$M_{\mathbf{q}}^{xab}$	$a \sim\sim\sim[\mathbf{q}]\sim\sim\sim b$

Table 4.1: Definitions of the different components of the Feynman diagrams.

and similarly for the out-of-plane excitations. Taking the continuum limit, the expectation value of the squared excitations per lattice site (i.e. the left-hand side of Eq. (4.36)) can now be calculated:

$$\begin{aligned}
&\frac{1}{8}\sum_a\sum_{\mathbf{q}}\left(\left\langle|\epsilon_{\mathbf{q}}^{xa}|^2\right\rangle+\left\langle|\epsilon_{\mathbf{q}}^{ya}|^2\right\rangle\right)\\
&\quad=\frac{k_BT}{4(2\pi)^3J_1}\int\mathrm{d}\mathbf{q}\,\mathrm{Tr}\left[\left(\mathbf{M}_{\mathbf{q}}^x/J_1\right)^{-1}+\left(\mathbf{M}_{\mathbf{q}}^y/J_1\right)^{-1}\right]-\frac{k_B^2T^2}{4(2\pi)^6J_1^2}\int\mathrm{d}\mathbf{q}\mathrm{d}\mathbf{q}'\sum_{abc}\Big[\\
&\qquad\qquad M_0^{xbc}/J_1\left(\left((\mathbf{M}_{\mathbf{q}}^x/J_1)^{-1}\right)^{ab}\left((\mathbf{M}_{\mathbf{q}}^x/J_1)^{-1}\right)^{ba}\left((\mathbf{M}_{\mathbf{q}'}^x/J_1)^{-1}\right)^{cc}\right.\\
&\qquad\qquad\left.+\left((\mathbf{M}_{\mathbf{q}}^x/J_1)^{-1}\right)^{ab}\left((\mathbf{M}_{\mathbf{q}}^x/J_1)^{-1}\right)^{ba}\left((\mathbf{M}_{\mathbf{q}'}^y/J_1)^{-1}\right)^{cc}+(x\leftrightarrow y)\right)\\
&\qquad\qquad+M_{\mathbf{q}-\mathbf{q}'}^{xbc}/J_1\left(\left((\mathbf{M}_{\mathbf{q}}^x/J_1)^{-1}\right)^{ab}\left((\mathbf{M}_{\mathbf{q}'}^x/J_1)^{-1}\right)^{bc}\left((\mathbf{M}_{\mathbf{q}}^x/J_1)^{-1}\right)^{ca}+(x\leftrightarrow y)\right)\Big]\\
&\qquad\qquad+\mathcal{O}\left((k_BT/J_1)^3\right)\\
&\quad\equiv\frac{k_BT}{J_1}I_1-\frac{k_B^2T^2}{J_1^2}I_2+\mathcal{O}\left((k_BT/J_1)^3\right),
\end{aligned}\tag{4.67}$$

where I_1 and I_2 are positive dimensionless integrals that depend only on the fraction J_2/J_1. Note that I_1 is the same integral as the one that we encountered for the lowest order calculations in Sec. 4.2. Without explicitly evaluating the integral I_2 (which again proves to be difficult), we can draw a conclusion: since the quadratic term in this expansion is purely negative, we see that the fluctuations are suppressed by the presence of interaction terms. This is the same conclusion as the one we encountered in the first part of this section.

The temperature expansion Eq. (4.67) can be used to find the temperature scale at which the system can no longer be described as spin fluctuations about the ground state, similar to what we have done in the previous sections. This can again be done by investigating when this approximation for the size of the excitations no longer makes sense, for example when they become of the order 1 or when the quadratic term becomes dominant (in which case increasing temperature would lead to decreasing excitations according to Eq. (4.67)). However, this temperature expansion can only be used to find the critical temperature in the region in which the critical temperature is small, which is the region close to the boundary value $J_2/J_1=3/2$. Further away from this point, the critical temperature becomes large, and we can no longer expand the expectation values as functions of small temperature. We can therefore only be certain of the results in the vicinity of $J_2/J_1=3/2$.

4.4 Conclusions and outlook

In this first part of the thesis, we have investigated the phase transitions that appear in the antiferromagnetic Heisenberg model on the Swedenborgite lattice. In particular, we focused on the phase transition separating the unique ground state from a disordered phase in the limit that the fraction of out-of-plane and in-plane interaction strengths J_2/J_1 goes to 3/2 from above.

We have first seen how Landau theory can be used to understand the types of phase transitions that appear in the system. It followed that the symmetries of the model allow for a first and a second order phase transition, separating a disordered phase from a coplanar (nematic) phase and a unique configuration, respectively. Which of the two happens can depend on the ratio J_2/J_1, although the way in which it depends on this ratio does not follow from phenomenological Landau theory alone.

Next, we constructed a mean-field theory to describe the second order phase transition to the unique ground state. Mean-field theory confirmed that the low-temperature phase is indeed the unique ground state that was found in Sec. 1.3, and that the system can only be in this phase if J_2/J_1 is greater than a specific boundary value. However, we found that mean-field theory returns a boundary value and a critical temperature that do not agree with the exact analysis and the simulations that lead to the phase diagram shown in Fig. 1.10. The reason of these deviations was explained by the observation that the fluctuations of the order parameter are larger than the order parameter itself in the region close to the phase transition, hence the assumption that these fluctuations could be ignored when describing the phase transition was incorrect.

Finally, we developed a method to find both the order of magnitude and the qualitative behaviour of the critical temperature of the second order phase transition by looking at spin waves on the ground state configuration. From this analysis, we concluded that the critical temperature is linearly proportional to $(J_2/J_1 - 3/2)$ in the limit that $J_2/J_1 \to 3/2$ from above. The spin wave analysis also showed there are modes with negative energy when J_2/J_1 is smaller than $3/2$, confirming that the unique ground state configuration is no longer the ground state in this region. For larger values of J_2/J_1, we found that the critical temperature behaves approximately like a square root in the lowest order approximation, but also that higher order corrections increase this critical temperature to larger values. How exactly the critical temperature behaves in general could not be found, and therefore the only certain conclusion from the spin wave analysis is that the critical temperature is linear in $(J_2/J_1 - 3/2)$ when $J_2/J_1 \to 3/2$ from above. Referring to the goals formulated in Sec. 1.4, we see that this conclusion successfully answers the questions of this part of the thesis. In particular, we found that the critical temperature is well defined at the boundary $J_2/J_1 = 3/2$, namely that it goes to zero, due to the fact that spin excitations about the ground state diverge for any non-zero temperature at this point. Combining this with the analysis from Ch. 1, we conclude that the spin-liquid phase indeed extends to the region $J_2/J_1 > 3/2$, which is what we expected for entropic reasons.

Even with the combined results from Buhrandt in Ref. [4] and this work, there is still a region that has not yet been studied in detail: it remains unclear how the first order phase transition to the nematic phase behaves in the limit $J_2/J_1 \to 0$. Future work could therefore focus on finding the critical temperature in this limit. This is however not straightforward, since mean-field theory cannot be used in the forms presented here when concerned with nematic ordering, and one would have to develop a more complicated theory. Additionally, the spin-wave analysis cannot simply be repeated in this limit, as there is no unique ground state to add the spin fluctuations to. Moreover, order-by-disorder effects are the reason for nematic ordering to appear, so it would be necessary to find a way to include these effects. Overcoming these obstacles and successfully completing the phase diagram in the limit $J_2/J_1 \to 0$ may prove useful in understanding the relation between the two-dimensional Kagomé antiferromagnet and the three-dimensional Swedenborgite antiferromagnet.

Part II

Quasiparticle interference in a topological insulator

Chapter 5

Introduction to Part II

The second part of this thesis deals with an entirely different subject than the first part, namely with so-called *quasiparticle interference* in a topological insulator. In short, this means that we will look at interference effects due to the scattering of electrons in a material that is an electrical insulator in its bulk, but a conductor on its surface. We will focus our attention on scattering of electrons that is caused by impurities on the surface of the material. Such a surface impurity can be many things: it can be a defect or a vacancy of the underlying lattice (leading to a strong impurity), it can be a weak attractive or repulsive potential due to doping, or it can even be a magnetic impurity that couples differently to particles with a different spin. As was shown experimentally by Hoffman *et al.* [19], the presence of impurities can lead to the emergence of patterns in the spatially resolved quasiparticle density of states that are very similar to familiar optical interference patterns.

The main goal of the remainder of this thesis is to explain experimental results concerning quasiparticle interference by using a theoretical model. With this purpose in mind, Part II consists of two chapters: one introducing the physical concepts, models and techniques necessary to understand the general problem, and one in which we apply these preliminaries to find a model description of quasiparticle interference in the topological insulator $Cu_xBi_2Te_3$.

The first of the two chapters (i.e. this chapter) will first introduce tight-binding models and band theory, both of which are very useful for explaining the electrical properties of a material. At the end of the first section, we will discuss how more complicated models can be approximated by a simple square lattice tight-binding model, while still retaining the same properties in the region of interest. Then, the concepts of Green's functions and the density of states will be introduced, providing very powerful methods for calculating observable quantities corresponding to a given model. Finally, we will introduce the concepts of impurity scattering and the T-matrix, which provide the techniques necessary to find the quasiparticle interference patterns that the presence of impurities leads to.

In Ch. 6, we will first properly formulate the problem and our goals regarding experimental results and the model description of the experimental circumstances. Afterwards, we will discuss a model Hamiltonian, and then we use this Hamiltonian and the previously introduced techniques in order to numerically calculate the quasiparticle interference patterns. Having calculated the consequences of impurity scattering in the proposed model, we will discuss the meaning of these results and compare them to the experimental results. In the final section, we review the conclusions drawn from the discussion.

5.1 Tight-binding models and electronic band structure

In solid-state physics, the electrical properties of a material (such as electrical resistivity and conductivity) are often successfully described by a *tight-binding* model. Such models assume that the electrons in the system are all tightly bound to their corresponding atoms. As the materials of interest are crystalline solids, this means that the electrons are confined to a well-defined lattice. In addition to these spatial restrictions, tight-binding models assume that the interactions between electrons from different lattice sites are "limited". In particular, this refers to the interactions having a maximum range (i.e. being sufficiently short-ranged), for example by only considering nearest and next-nearest neighbour interactions, or even by restricting ourselves to just nearest neighbour interactions.

In this section, we will first work out an example of a simple tight-binding model. The results from this example will then be used to introduce the concepts of band theory, providing suitable models to explain the properties of, among other things, semiconductors and topological insulators. Finally, we will see how an approximate low-energy Hamiltonian can be mapped to a square lattice to capture its relevant physics without knowledge of the full Hamiltonian, using graphene as an example.

5.1.1 The square lattice tight-binding model

The electrical properties of a material are a direct result of the quantum mechanical nature of electrons. In particular, electrons are fermions, such that the Pauli exclusion principle prohibits more than two electrons (one for each spin state) to occupy the same orbital. To illustrate how a tight-binding model can incorporate quantum properties to capture electrical properties, we will first consider a simple second-quantized tight-binding model on a square lattice with only nearest neighbour interactions. To do so, we introduce the fermionic creation and annihilation operators $c^\dagger_{\sigma ij}$ and $c_{\sigma ij}$, where $\sigma \in \{\uparrow, \downarrow\}$ indicates the spin of the electron, and i, j denote the position on the lattice according to

$$\mathbf{r}_{ij} = a\left(i\hat{\mathbf{x}} + j\hat{\mathbf{y}}\right), \quad i, j \in \mathbb{Z}, \tag{5.1}$$

with $\mathbf{r}_{ij}$ being the position vector and a being the lattice constant. When acting on a many-body state, the annihilation operator removes an electron from its corresponding orbital, spin state and lattice site, while the creation operator adds one. These fermionic operators satisfy the anticommutation relations

$$\{c_{\sigma ij}, c^\dagger_{\sigma ij}\} = c_{\sigma ij}c^\dagger_{\sigma ij} + c^\dagger_{\sigma ij}c_{\sigma ij} = 1, \qquad \{c_{\sigma ij}, c_{\sigma ij}\} = 0, \qquad \{c^\dagger_{\sigma ij}, c^\dagger_{\sigma ij}\} = 0, \tag{5.2}$$

while all anticommutation relations between different orbitals, spin states or lattice sites vanish. The Pauli exclusion principle is immediately apparent from these relations: $(c_{\sigma ij})^2 = (c^\dagger_{\sigma ij})^2 = 0$, which means that a particular state can only be occupied by one or zero electrons. For simplicity, we will now first restrict ourselves to a single available orbital on each lattice site, the operators of which are $c^\dagger_{\sigma ij}$ and $c_{\sigma ij}$. Since we only allow electrons to be created and annihilated on the lattice sites (and nowhere else), we are indeed considering electrons that are tightly bound to the atoms and their lattice.

Now that we have introduced the necessary fermionic operators, we can construct the second-quantized Hamiltonian. The only term we should include is a "hopping" term, such that it is energetically favourable for electrons to hop to a neighbouring lattice site. The Hamiltonian of this simple example is thus given by

$$H = \sum_{\sigma, ij}\left[-tc^\dagger_{\sigma ij}c_{\sigma\, i+1\, j} - tc^\dagger_{\sigma ij}c_{\sigma i\, j+1} + h.c.\right], \tag{5.3}$$

where t is the (real) hopping strength. The hopping in different directions and with different spin states all have the same hopping strength, so this Hamiltonian describes an isotropic and non-magnetic model.

The electrical properties can be found in the dispersion relation. This dispersion relation is derived by Fourier transforming the Hamiltonian. We define the Fourier transforms as follows:

$$c_{\sigma ij} = \frac{1}{\sqrt{N_x}}\sum_{k_x} c_{\sigma k_x j}e^{ik_x x_i} \qquad \Longleftrightarrow \qquad c_{\sigma k_x j} = \frac{1}{\sqrt{N_x}}\sum_i c_{\sigma ij}e^{-ik_x x_i}, \tag{5.4}$$

and similarly for the other direction. Here, N_x is the number of lattice sites in the $\hat{\mathbf{x}}$-direction, $x_i = ai$ is the position in the $\hat{\mathbf{x}}$-direction, and $ak_x = 2\pi n/N_x$ with $n \in \{0, 1, \ldots, N_x - 1\}$. Making use of the Kronecker delta

$$\delta_{ij} = \frac{1}{N}\sum_k e^{ik(x_i - x_j)}, \tag{5.5}$$

and the identity $\cos x = (e^{ix} + e^{-ix})/2$, we immediately find

$$\begin{aligned} H &= \sum_{\sigma, k_x, j}\left[-2t\cos(ak_x)c^\dagger_{\sigma k_x j}c_{\sigma k_x j} - tc^\dagger_{\sigma k_x j}c_{\sigma k_x j+1} - tc^\dagger_{\sigma k_x j+1}c_{\sigma k_x j}\right] \\ &= \sum_{\sigma, \mathbf{k}} c^\dagger_{\sigma\mathbf{k}}\left[-2t\cos(ak_x) - 2t\cos(ak_y)\right]c_{\sigma\mathbf{k}} \\ &\equiv \sum_{\sigma, \mathbf{k}} c^\dagger_{\sigma\mathbf{k}}\mathcal{H}_{\mathbf{k}}c_{\sigma\mathbf{k}} \end{aligned} \tag{5.6}$$

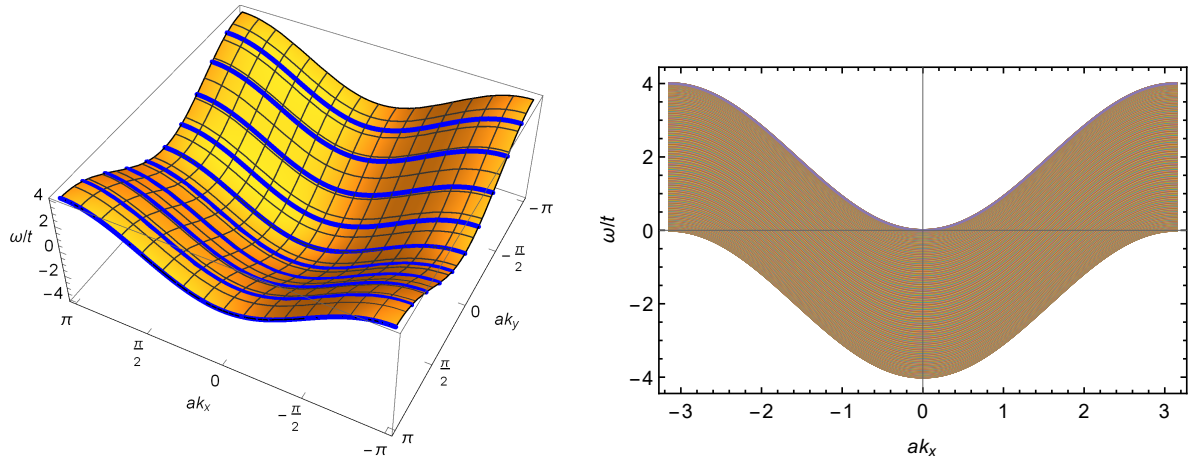

Figure 5.1: Band structure of the square lattice tight-binding model as a function of momentum. Left: the allowed energies in the continuum limit, together with those from a discretized model with $N_y = 10$ (blue lines). Right: allowed energies from a model with free boundary conditions in the $\hat{\mathbf{y}}$-direction and $N_y = 500$.

For future reference, we note that the first line of Eq. (5.6) can be written as

$$H = \sum_{\sigma,k_x} \begin{pmatrix} c^\dagger_{\sigma k_x 1} & c^\dagger_{\sigma k_x 2} & \cdots & c^\dagger_{\sigma k_x N_y} \end{pmatrix} \begin{pmatrix} -2t\cos(ak_x) & -t & 0 & \cdots \\ -t & -2t\cos(ak_x) & -t & \cdots \\ 0 & -t & -2t\cos(ak_x) & \ddots \\ \vdots & \vdots & \ddots & \ddots \end{pmatrix} \begin{pmatrix} c_{\sigma k_x 1} \\ c_{\sigma k_x 2} \\ \vdots \\ c_{\sigma k_x N_y} \end{pmatrix}$$
$$\equiv \sum_{\sigma,k_x} \mathcal{C}^\dagger_{\sigma k_x} \mathcal{H}_{k_x} \mathcal{C}_{\sigma k_x}. \tag{5.7}$$

Also note that we assumed free boundary conditions in the $\hat{\mathbf{y}}$-direction for this final expression. Periodic boundary conditions can be incorporated by placing another $-t$ in the top-right and bottom-left corners of the matrix.

One thing that is immediately clear from the Fourier transformed Hamiltonian is that it is diagonal in $\mathbf{k}$: both the creation and the annihilation operators carry the same value for $\mathbf{k}$ in each term of the sum, and the matrix elements $\mathcal{H}_{\mathbf{k}}$ are only a function of a single $\mathbf{k}$ (rather than $\mathbf{k}$ and $\mathbf{k}'$). This is a result of the number of considered bonds scaling linearly with the number of lattice sites, rather than quadratically (neglecting boundary effects). The observation that the Hamiltonian is diagonal in $\mathbf{k}$ can now be used to find the dispersion relation: calculating the expectation value of the Hamiltonian corresponding to a many-body state with a well-defined momentum $\mathbf{k}$, one finds that its energy is given by

$$\omega = -2t\cos(ak_x) - 2t\cos(ak_y). \tag{5.8}$$

However, it is also possible to consider the allowed energies as a function of k_x only. For periodic boundary conditions in both directions, the allowed energies can be obtained directly from Eq. (5.8) by plugging in $ak_y = 2\pi n/N_y$, again with $n \in \{0, 1, \ldots, N_y - 1\}$. The energies from Eq. (5.8) and the corresponding discretization in the $\hat{\mathbf{y}}$-direction are shown in the left panel of Fig. 5.1. For free boundary conditions in the $\hat{\mathbf{y}}$-direction, the same arguments can be used to find that the allowed energies as a function of k_x are given by the eigenvalues of the matrix $\mathcal{H}_{k_x}$ from Eq. (5.7). This is shown in the right panel of Fig. 5.1. As can be seen from this figure, the square lattice tight-binding model leads to the existence of an *energy band* of allowed energies: all possible states have an energy between $\omega = -4t$ and $\omega = 4t$, and all energies in this range are allowed.

5.1.2 Band theory, electrical properties and topological insulators

The existence of a band structure is a very general feature in solid-state physics, of which tight-binding models are an example. Before we discuss the physical implications and consequences of band structures,

we first introduce a more general tight-binding Hamiltonian. Introducing creation and annihilation operators for each orbital and spin state on every site i of a d-dimensional lattice, the full annihilation operator corresponding to lattice site i is given by

$$\psi_i = \begin{pmatrix} a_{\uparrow i} \\ a_{\downarrow i} \\ b_{\uparrow i} \\ \vdots \end{pmatrix}. \tag{5.9}$$

Here, the first letter (i.e. a, b, etc.) denotes the orbital, while the arrow signifies the spin state. Using our previous observation that the Hamiltonian of a tight-binding model is diagonal in $\mathbf{k}$, the Hamiltonian can be written as

$$H = \sum_{\mathbf{k}} \psi_{\mathbf{k}}^\dagger \mathcal{H}_{\mathbf{k}} \psi_{\mathbf{k}}. \tag{5.10}$$

The quantity $\mathcal{H}_{\mathbf{k}}$ that appears in this expression (often also simply called "the Hamiltonian", as it gives the momentum space matrix elements of the full Hamiltonian) is now a $2n \times 2n$ matrix, where n is the number of considered orbitals. The band structure of a given tight-binding model is entirely encoded in this matrix $\mathcal{H}_{\mathbf{k}}$. It should be noted that the general Hamiltonian from Eq. (5.10) is a direct result of Bloch's theorem (see for example Ref. [20]). Following from the fact that we are working on a crystal lattice, it tells us that the basis of the wave functions consists of the eigenstates of this Hamiltonian (which are Bloch waves with a well-defined wave vector $\mathbf{k}$), and the energies of each of these states are the eigenvalues of the matrix $\mathcal{H}_{\mathbf{k}}$.

The band structure that follows from the Hamiltonian $\mathcal{H}_{\mathbf{k}}$ often consists of several different energy bands. Examples of possible band structures are shown in Fig. 5.2. In order to understand how these band structures lead to certain electrical properties, one has to take into account that systems consisting of many electrons are described by the Fermi-Dirac distribution,

$$f(\omega) = \frac{1}{e^{(\omega-\mu)/k_B T} + 1}, \tag{5.11}$$

where ω is the energy corresponding to a given state, μ is the chemical potential, k_B is the Boltzmann constant and T is the temperature. The distribution $f(\omega)$ gives the probability that a state with energy ω is occupied. An important concept to introduce is that of the *Fermi level*, which is defined as the energy for which $f(\omega)$ is exactly equal to $1/2$, thus providing a natural energy scale that separates the occupied from the unoccupied states. From Eq. (5.11), it immediately follows that $\omega_F = \mu$ is the Fermi level by definition. For zero temperature, every state below the Fermi level is filled, while all states above the Fermi level are empty. On the other hand, if the system is at a finite temperature, some of the electrons from low-energy states are excited to high-energy states by thermal fluctuations. Together with the band structure, this determines whether or not a material conducts electricity. For example, if the Fermi level is located inside an energy band, electrons close to the Fermi level can easily transition to different states with a similar energy. This is what happens in a metal. However, it is also possible for the Fermi level to be located between different bands. This can lead to many interesting materials, such as conventional insulators, semiconductors and topological insulators.

The two bands closest to the Fermi level are called the valence band and the conduction band, see again Fig. 5.2. If the gap between these two bands (called the *band gap*) is large, then it is very unlikely for electrons to "jump" from the valence band to the conduction band. As a result, almost all states of the valence band are occupied, while the conduction band remains empty, such that the electrons have very limited freedom. Materials with a large band gap are thus electrical insulators. If the gap is small, a portion of the electrons can make it across the gap. The result is a semiconductor: a material with a much larger resistivity than a metal, but a much smaller resistivity than an insulator. Semiconductors are particularly useful due to how easily their conductivity can be influenced, for example by increasing the temperature (allowing more electrons to jump to the conduction band) or by applying an electric field (moving the conduction band closer to the Fermi level). A possible band structure of an insulator or a semiconductor (depending on the size of the band gap) is shown in the left panel of Fig. 5.2. In this example, electrons near the bottom of the conduction band have a quadratic dispersion, so they behave like free (but massive) particles. However, the effective mass of these excitations is often different than

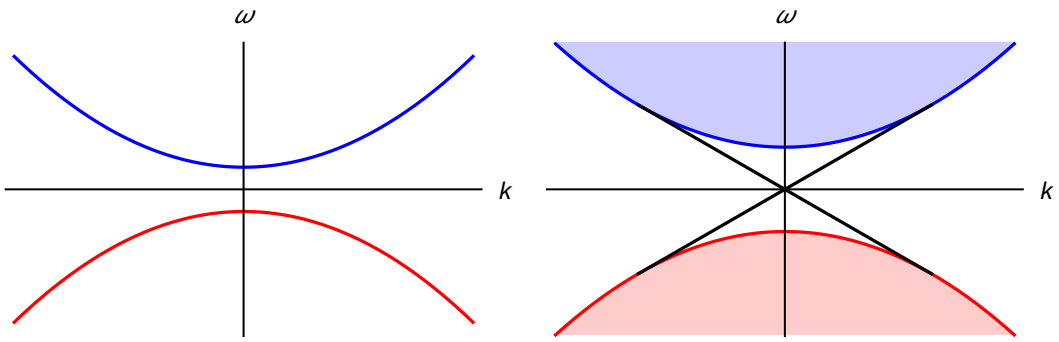

Figure 5.2: Examples of possible band structures. The valence band is shown in red, the conduction band is plotted in blue, and the horizontal axis denotes the Fermi level. The left plot is an example of a semiconductor or an insulator (depending on the size of the band gap), while the right one is an example of a topological insulator, with black lines denoting the edge states.

that of a free electron, so we are instead looking at electron *quasiparticles*. In addition to the presence of these electron quasiparticles, the conduction band electrons leave behind *holes* in the valence band. A nearly full valence band can be described by interpreting these holes as the "particles" (or quasiparticles) of interest, rather than looking at all of the individual electrons, and they have a negative energy with respect to the Fermi level. In the example of the figure, there is particle-hole symmetry, so the holes near the top of the valence band also have a quadratic dispersion. The holes can therefore be interpreted as free particles as well.

In some cases, the bulk of a material and its surface (or edges) have very different properties. This is what happens in a so-called *topological insulator*. With periodic boundary conditions, the band structure of such a material looks very similar to that of an insulator. However, when the surface of the material is considered as well (rather than just looking at the bulk, for example by using free boundary conditions), *edge states* appear that connect the valence band and the conduction band. An example of this is shown in the right panel of Fig. 5.2. The presence of such edge states leads to the remarkable feature that the bulk of the material is an insulator, while its surface behaves as a conductor. In the next chapter, we will consider a specific topological insulator, and we will encounter (among other things) some of the consequences of the existence of bulk states and edge states.

5.1.3 Mapping complicated models to a square lattice

In the final part of this section, we will discuss how more complicated models can be mapped to a simple square lattice tight-binding model without making use of their actual microscopic structure, while retaining much of the important physics. To do so, we will use graphene as an example. A derivation of the tight-binding band structure of graphene and its small-$\mathbf{k}$ approximation, as well as a brief discussion of Dirac points and the corresponding linear dispersion, can be found in appendix B.1.

As a starting point, we use the low-energy Hamiltonian of graphene, close to one of the Dirac points (where the valence band and the conduction band touch). Up to a factor $\hbar$ (which we set to one), this Hamiltonian is given by

$$\mathcal{H}_{\mathbf{k}} = v_F \boldsymbol{\sigma} \cdot \mathbf{k}. \tag{5.12}$$

Here, v_F is called the Fermi velocity, and $\boldsymbol{\sigma}$ is the two-dimensional vector of Pauli matrices,

$$\sigma_1 = \begin{pmatrix} 0 & 1 \\ 1 & 0 \end{pmatrix}, \qquad \sigma_2 = \begin{pmatrix} 0 & -i \\ i & 0 \end{pmatrix}. \tag{5.13}$$

In order to find a tight-binding model that has the same small-$\mathbf{k}$ Hamiltonian as graphene, we replace $ak_{x/y}$ by $\sin(ak_{x/y})$. Note that this particular choice is not unique, but it does not matter for the final results, as long as we restrict ourselves to the region close to the origin. Performing Fourier transforms according to Eq. (5.4), we find:

$$H = \frac{v_F}{a} \sum_{\sigma,\mathbf{k}} \begin{pmatrix} a^\dagger_{\sigma\mathbf{k}} & b^\dagger_{\sigma\mathbf{k}} \end{pmatrix} \begin{pmatrix} 0 & \sin(ak_x) - i\sin(ak_y) \\ \sin(ak_x) + i\sin(ak_y) & 0 \end{pmatrix} \begin{pmatrix} a_{\sigma\mathbf{k}} \\ b_{\sigma\mathbf{k}} \end{pmatrix}$$

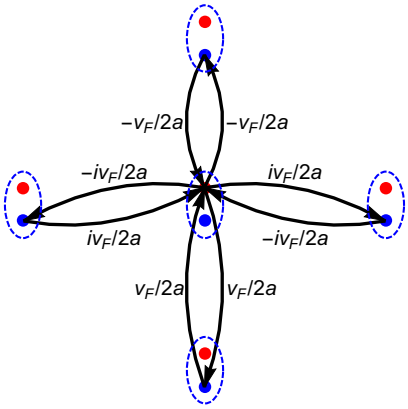

Figure 5.3: Schematic view of a single term of the square lattice tight-binding model that leads to the same low-energy Hamiltonian as graphene. The red and blue dots enclosed by dashed lines denote the two different orbitals located at each lattice site, while the arrows denote the different hopping terms, together with the corresponding hopping parameter. The direction of the arrows signify which particle is created and which one is annihilated.

$$
\begin{aligned}
&= \frac{v_F}{a} \sum_{\sigma,\mathbf{k}} \left[a^\dagger_{\sigma\mathbf{k}} b_{\sigma\mathbf{k}} \left(\sin(ak_x) - i \sin(ak_y) \right) + h.c. \right] \\
&= \frac{v_F}{2a} \sum_{\sigma,k_x,j} \left[2\sin(ak_x) a^\dagger_{\sigma k_x j} b_{\sigma k_x j} - a^\dagger_{\sigma k_x j} b_{\sigma k_x j+1} + a^\dagger_{\sigma k_x j} b_{\sigma k_x j-1} + h.c. \right] \\
&= \frac{v_F}{2a} \sum_{\sigma,ij} \left[-i\, a^\dagger_{\sigma ij} b_{\sigma i+1\, j} + i\, a^\dagger_{\sigma ij} b_{\sigma i-1\, j} - a^\dagger_{\sigma ij} b_{\sigma i\, j+1} + a^\dagger_{\sigma ij} b_{\sigma i\, j-1} + h.c. \right] .
\end{aligned} \tag{5.14}
$$

Similar to the example in the first part of this section, i, j denote the position on a square lattice according to Eq. (5.1). The final line of Eq. (5.14) describes a tight-binding model on a square lattice, each lattice site consisting of two orbitals and each bond having a different and sometimes complex hopping parameter. All interactions corresponding to a single term of the overall sum are shown in Fig. 5.3. The fact that this result now describes a square lattice tight-binding model comes from the choice to replace $ak_{x/y}$ by a simple sine rather than something more complicated.

Now that we have mapped graphene to a square lattice, we should check if this approximate model gives the same band structure in the region of interest as the actual model that follows from graphene's honeycomb lattice. Let us first find the band structure of the approximate model as a function of k_x. Defining the annihilation operator

$$
\psi_{\sigma k_x j} \equiv \begin{pmatrix} a_{\sigma k_x j} \\ b_{\sigma k_x j} \end{pmatrix} \tag{5.15}
$$

and using the third line of Eq. (5.14), the Hamiltonian can be written as

$$
\begin{aligned}
H &= \frac{v_F}{2a} \sum_{\sigma,k_x,j} \left[2\sin(ak_x) a^\dagger_{\sigma k_x j} b_{\sigma k_x j} - a^\dagger_{\sigma k_x j} b_{\sigma k_x j+1} + b^\dagger_{\sigma k_x j} a_{\sigma k_x j+1} + h.c. \right] \\
&= \sum_{\sigma,k_x} \begin{pmatrix} \psi^\dagger_{\sigma k_x 1} & \psi^\dagger_{\sigma k_x 2} & \cdots & \psi^\dagger_{\sigma k_x N_y} \end{pmatrix} \begin{pmatrix} h_0(k_x) & h_1 & 0 & \cdots \\ h_1^\dagger & h_0(k_x) & h_1 & \cdots \\ 0 & h_1^\dagger & h_0(k_x) & \ddots \\ \vdots & \vdots & \ddots & \ddots \end{pmatrix} \begin{pmatrix} \psi_{\sigma k_x 1} \\ \psi_{\sigma k_x 2} \\ \vdots \\ \psi_{\sigma k_x N_y} \end{pmatrix} ,
\end{aligned} \tag{5.16}
$$

where

$$
h_0(k_x) = \begin{pmatrix} 0 & \frac{v_F}{a} \sin(ak_x) \\ \frac{v_F}{a} \sin(ak_x) & 0 \end{pmatrix} , \qquad h_1 = \begin{pmatrix} 0 & -\frac{v_F}{2a} \\ \frac{v_F}{2a} & 0 \end{pmatrix} , \qquad h_1^\dagger = \begin{pmatrix} 0 & \frac{v_F}{2a} \\ -\frac{v_F}{2a} & 0 \end{pmatrix} . \tag{5.17}
$$

Note that in the first line of Eq. (5.16), we switched the term $a^\dagger_{\sigma k_x j} b_{\sigma k_x j-1}$ from Eq. (5.14) with its Hermitian conjugate. Additionally, we wrote $j \to j+1$ in the terms containing the layer $j-1$. This does

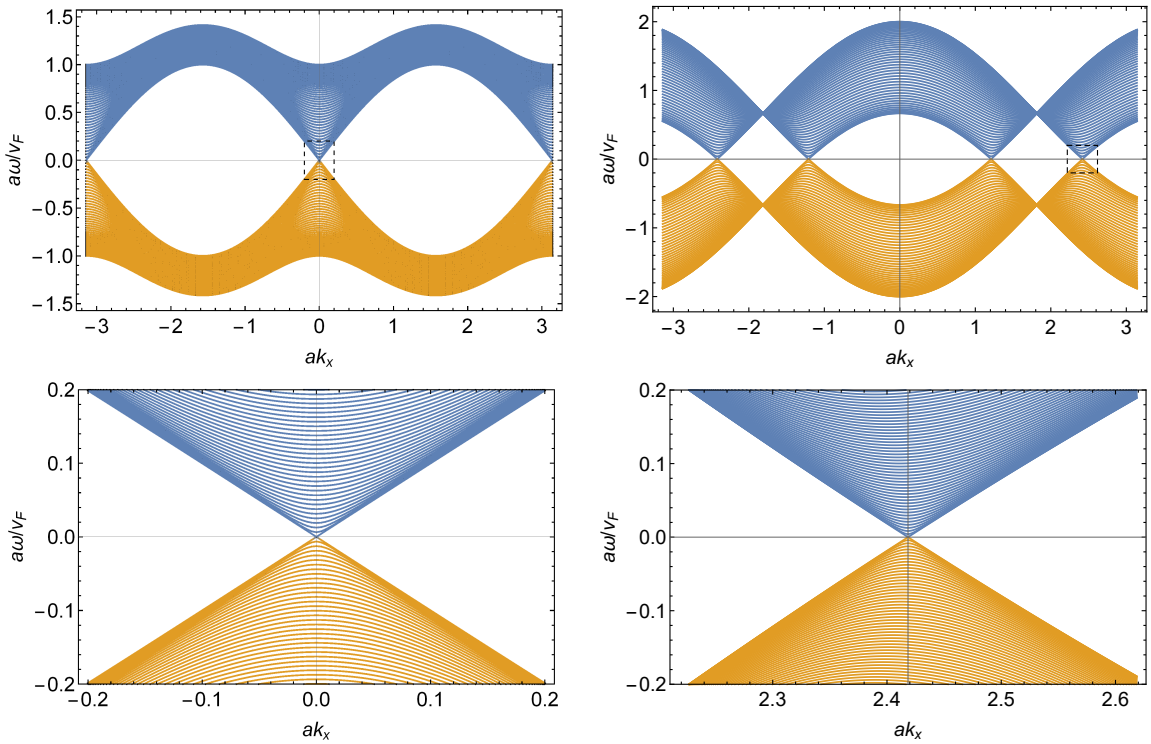

Figure 5.4: Comparison of the band structure of the approximate square lattice model (left) and the actual honeycomb lattice model (right). The top row shows the overall structure in the first Brillouin zone, while the bottom row zooms in on one of the Dirac points (i.e. the regions enclosed by the rectangles in the top panels).

not change any results, as it is just a redistribution of the interaction terms among the different terms of the overall sum.

To keep everything consistent with the full model, we will now consider periodic boundary conditions by putting an additional matrix h_1 in the bottom-left corner of the Hamiltonian matrix, and an additional $h_1^\dagger$ in the top-right corner. The allowed energies as a function of k_x can now be found by calculating the eigenvalues of the Hamiltonian matrix. The resulting band structure is shown in the left half of Fig. 5.4. Additionally, these allowed energies as a function of k_x have also been calculated for graphene's actual honeycomb lattice by making use of the dispersion relation

$$\omega = \pm\frac{2v_F}{3a}\sqrt{3 + 2\cos(\sqrt{3}ak_x) + 4\cos(\sqrt{3}ak_x/2)\cos(3ak_y/2)}, \tag{5.18}$$

the derivation of which can be found in the appendix. The energies have been plotted as a function of k_x with $ak_y = 2\pi n/N_y$, $n \in \{0, 1, \ldots, N_y - 1\}$, where N_y is again the number of "layers" in the $\hat{\mathbf{y}}$-direction. The results are shown in the right half of Fig. 5.4. As can be seen from these results, the complete band structure of the approximate model and the full model are very different. However, in the region of interest (i.e. the low-energy regions in the vicinity of the Dirac points) have almost exactly the same band structure. This confirms that small-$\mathbf{k}$ Hamiltonians can indeed successfully be mapped to a square lattice in order to extract the correct band structure in the region close to the origin. Since the approximate model derived in this section does not use the fact that graphene's underlying lattice is a honeycomb lattice, it also illustrates that these methods work without any knowledge of the underlying lattice, as long as the small-$\mathbf{k}$ Hamiltonian is known.

Finally, it should be noted that approximate models such as the one from this section are very convenient for analyzing the effects of edges. In order to add edge states to the model, one would have to consider Eq. (5.16) with free boundary conditions (i.e. keeping the bottom-left and top-right corners of the matrix empty). Doing so, the edges are simply located at $j = 1$ and $j = N_y$, rather than having some complicated structure by themselves. As we will see later on, this makes it much more straightforward to work with edge states.

5.2 Green's functions and the density of states

Having introduced tight-binding models and band theory, this next section will cover concepts and techniques necessary to analyze such models. In order to derive explicit expressions for the quantities that can be measured experimentally, it is necessary to first introduce the general concept of Green's functions. An elaborate introduction to this concept (and the other subjects from the following two sections) can for example be found in Refs. [21, 22].

As an example, we will first consider the basis of eigenvectors $|\mathbf{r}\rangle$ of the position operator. This can be used to define the position space representation of the wave function corresponding to an arbitrary energy eigenstate $|\psi_n\rangle$ as

$$\psi_n(\mathbf{r}) \equiv \langle \mathbf{r}|\psi_n\rangle. \tag{5.19}$$

Then, the time-independent single particle Schrödinger equation is given by

$$[E_n - H(\mathbf{r})]\,\psi_n(\mathbf{r}) = 0, \tag{5.20}$$

where the operator $H(\mathbf{r})$ is the position space Hamiltonian and the energy E_n is its eigenvalue. We can now define a *Green's function* G by means of the equation

$$[\omega - H(\mathbf{r})]\,G(\mathbf{r},\mathbf{r}',\omega) = \delta(\mathbf{r}-\mathbf{r}'). \tag{5.21}$$

The Green's function that follows from this equation has important physical implications. To see this, we go back to the original vector space of which we have taken the position space representation. In this most general vector space, Eq. (5.21) becomes

$$G(\omega) = (\omega - H)^{-1}. \tag{5.22}$$

The validity of this expression with respect to Eq. (5.21) can easily be verified by making use of the relations

$$\delta(\mathbf{r}-\mathbf{r}')H(\mathbf{r}) = \langle \mathbf{r}|H|\mathbf{r}'\rangle, \tag{5.23}$$

$$G(\mathbf{r},\mathbf{r}',\omega) = \langle \mathbf{r}|G(\omega)|\mathbf{r}'\rangle, \tag{5.24}$$

$$\delta(\mathbf{r}-\mathbf{r}') = \langle \mathbf{r}|\mathbf{r}'\rangle, \tag{5.25}$$

$$\int \mathrm{d}\mathbf{r}\,|\mathbf{r}\rangle\langle\mathbf{r}| = 1. \tag{5.26}$$

The physical significance of the general expression Eq. (5.22) can be extracted by inserting a completeness relation:

$$G(\omega) = (\omega - H)^{-1}\sum_n |\psi_n\rangle\langle\psi_n| = \sum_n \frac{|\psi_n\rangle\langle\psi_n|}{\omega - E_n}, \tag{5.27}$$

where E_n is the energy (i.e. the eigenvalue of H) corresponding to the eigenstate $|\psi_n\rangle$. From this, we conclude that the poles of the Green's function $G(\omega)$ coincide with the eigenvalues of the Hamiltonian H. This observation will turn out to be very useful for calculating the density of states.

The problem with the Green's function is that it is not defined if ω is equal to one of the eigenvalues of H (in this case, the matrix $(\omega - H)$ has a zero eigenvalue and is therefore not invertible). In order to assign a value to the Green's function for these values of ω, we remove the poles by adding an infinitesimal imaginary part $i\delta$ to the (real) energy ω. This can be done in two different ways: one can either let δ go to zero from above or from below, leading to two different Green's functions $G^{\pm}$, where G^{+} is called the *retarded Green's function*, and G^{-} is called the *advanced Green's function*. These two Green's functions are thus given by

$$G^{\pm}(\omega) = \lim_{\delta\to 0^+} G(\omega \pm i\delta) = \lim_{\delta\to 0^+} (\omega \pm i\delta - H)^{-1}. \tag{5.28}$$

Note that ω and δ are both real numbers, while H is still an operator (or a matrix). The retarded and advanced Green's functions are only different from each other at the poles of the original Green's function; for all other values of ω, the infinitesimal δ is much smaller than all $(\omega - E_n)$ and can therefore safely be ignored.

Now that we have defined the general Green's functions, they can be used to calculate the *density of states*. The density of states (or DOS) is defined as

$$\rho(\omega) \equiv \sum_n \delta(\omega - E_n), \tag{5.29}$$

such that the number of particles with energy between ω_1 and ω_2 is given by

$$\int_{\omega_1}^{\omega_2} \mathrm{d}\omega\, \rho(\omega). \tag{5.30}$$

The *local* density of states (or LDOS) corresponding to a given position $\mathbf{r}$ can be calculated in a similar way:

$$\rho(\mathbf{r}, \omega) \equiv \sum_n \delta(\omega - E_n) \left|\langle \mathbf{r}|\psi_n\rangle\right|^2, \tag{5.31}$$

where $\left|\langle \mathbf{r}|\psi_n\rangle\right|^2$ gives the probability to find a particle at position $\mathbf{r}$. From the normalization of the wave function, it follows that $\rho(\omega) = \int \mathrm{d}\mathbf{r}\, \rho(\mathbf{r}, \omega)$.

In order to express the density of states in terms of a Green's function, we consider the following expression for the Dirac delta function:

$$\delta(x) = \lim_{\delta \to 0^+} \frac{1}{\pi} \frac{\delta}{x^2 + \delta^2}. \tag{5.32}$$

To prove this equation, we note that the right-hand side is equal to zero if $x \neq 0$, while it goes to infinity if $x = 0$. This is precisely the behaviour of the delta function, so we only have to show that the normalization on the right-hand side is correct. To do so, we integrate the right-hand side over x:

$$\begin{aligned}
\lim_{\delta \to 0^+} \int_{-\infty}^{\infty} \mathrm{d}x\, \frac{1}{\pi\delta} \frac{1}{(x/\delta)^2 + 1} &= \lim_{\delta \to 0^+} \int_{-\infty}^{\infty} \mathrm{d}y\, \frac{1}{\pi} \frac{1}{y^2 + 1} \\
&= \int_{-\pi/2}^{\pi/2} \frac{\mathrm{d}u}{\cos^2 u} \frac{1}{\pi} \frac{1}{\tan^2 u + 1} \\
&= 1.
\end{aligned} \tag{5.33}$$

The substitutions used here are $x = y\delta$ and $y = \tan u$. In addition to Eq. (5.32), we also use the identity

$$\frac{1}{x \pm i\delta} = \frac{x \mp i\delta}{x^2 + \delta^2}. \tag{5.34}$$

With these two identities, we return to Eq. (5.31):

$$\begin{aligned}
\rho(\mathbf{r}, \omega) &= \lim_{\delta \to 0^+} \sum_n \frac{1}{\pi} \frac{\delta}{(\omega - E_n)^2 + \delta^2} \langle \mathbf{r}|\psi_n\rangle\langle\psi_n|\mathbf{r}\rangle \\
&= \mp \frac{1}{\pi} \lim_{\delta \to 0^+} \sum_n \mathrm{Im} \frac{1}{\omega \pm i\delta - E_n} \langle \mathbf{r}|\psi_n\rangle\langle\psi_n|\mathbf{r}\rangle \\
&= \mp \frac{1}{\pi} \mathrm{Im} \lim_{\delta \to 0^+} \sum_n \langle \mathbf{r}| \frac{1}{\omega \pm i\delta - E_n} |\psi_n\rangle\langle\psi_n|\mathbf{r}\rangle \\
&= \mp \frac{1}{\pi} \mathrm{Im} \lim_{\delta \to 0^+} \sum_n \langle \mathbf{r}|(\omega \pm i\delta - H)^{-1}|\psi_n\rangle\langle\psi_n|\mathbf{r}\rangle \\
&= \mp \frac{1}{\pi} \mathrm{Im} \lim_{\delta \to 0^+} \langle \mathbf{r}|(\omega \pm i\delta - H)^{-1}|\mathbf{r}\rangle \\
&= \mp \frac{1}{\pi} \mathrm{Im}\, G^{\pm}(\mathbf{r}, \mathbf{r}, \omega).
\end{aligned} \tag{5.35}$$

Note that the quantity $\langle \mathbf{r}|(\omega \pm i\delta - H)^{-1}|\mathbf{r}\rangle$ that appears on the second to last line is simply the **rr** diagonal matrix element of the operator $(\omega \pm i\delta - H)^{-1}$. Therefore, we can now immediately find the total density of states, independent of the basis:

$$\begin{aligned}\rho(\omega) &= \mp\frac{1}{\pi}\mathrm{Im}\,\mathrm{Tr}\lim_{\delta\to 0^+}(\omega \pm i\delta - H)^{-1} \\ &= \mp\frac{1}{\pi}\mathrm{Im}\,\mathrm{Tr}\,G^{\pm}(\omega).\end{aligned} \tag{5.36}$$

As we have seen before, the local Hamiltonian (and consequently the local Green's functions $G^{\pm}(\mathbf{r},\mathbf{r}',\omega)$) often still has a matrix structure, for example due to the presence of several allowed orbitals. If this is the case, we simply take the trace over the remaining matrix structure, for the same reason as in Eq. (5.36). Also note that $G^{\pm}(\mathbf{r},\mathbf{r}',\omega) = G^{\pm}(\mathbf{r}-\mathbf{r}',\omega)$ for a translationally invariant system, such that the corresponding local density of states is constant in space.

Finally, we explicitly write the Hamiltonian as a function of the momentum $\mathbf{k}$ (or in other words: we consider the matrix elements $\mathcal{H}_{\mathbf{k}} \equiv \langle \mathbf{k}|H|\mathbf{k}\rangle$) to find the *spectral-weight function*:

$$\rho(\mathbf{k},\omega) = \mp\frac{1}{\pi}\mathrm{Im}\,\mathrm{Tr}\lim_{\delta\to 0^+}(\omega \pm i\delta - \mathcal{H}_{\mathbf{k}})^{-1}. \tag{5.37}$$

This function gives us the probability density as a function of both the momentum and the energy, and is very useful for finding the band structure of a given Hamiltonian. For the remainder of this thesis, the Hamiltonian $\mathcal{H}_{\mathbf{k}}$ that appears in this expression will always be the Hamiltonian matrix corresponding to the quadratic Hamiltonian from equation (5.10).

Let us return for a moment to the discussion from the final part of the previous section, where we found that complicated lattice models can successfully be mapped to a square lattice, and that edges located at the "layers" $j = 1$ and $j = N_y$ can then be added by simply considering free boundary conditions in one of the directions. The matrix corresponding to such a model (for example the one from Eq. (5.16)) has a very clear structure, with the indices of the matrix corresponding to the layers. From the general expression for the Green's function Eq. (5.22), we see that the Green's function has this same clear structure as the Hamiltonian. As a result, the *surface* Green's function (i.e. the Green's function corresponding to the single layer $j = 1$ or $j = N_y$) is given by the top-left or bottom-right corner of the total Green's function. Note however that the components of the Hamiltonian matrix in Eq. (5.16) are themselves matrices, so the individual components of the total Green's function are $n \times n$ matrices as well, where n is the number of available states per lattice site. The surface Green's function, which is a single component of the total Green's function, is therefore also an $n \times n$ matrix. Using this surface component of the total Green's function, the surface spectral-weight function can now be calculated by replacing the total Green's function $(\omega \pm i\delta - \mathcal{H}_{\mathbf{k}})^{-1}$ in Eq. (5.37) with the surface Green's function.

5.3 Impurity scattering and quasiparticle interference

In the previous section, we have seen how the density of states can be calculated for an arbitrary Hamiltonian H. However, in practice it is not always completely straightforward to actually do the calculation, for example in the presence of an impurity. Let us now consider a purely *quadratic* Hamiltonian of the form $H = H_0 + H_I$, such that the (retarded) Green's function corresponding to the "bare" Hamiltonian H_0 is known to be $G_0^+(\omega)$, and H_I is the impurity Hamiltonian. The total Green's function can now be calculated:

$$\begin{aligned}G^+(\omega) &= \lim_{\delta\to 0^+}(\omega + i\delta - H)^{-1} \\ &= \lim_{\delta\to 0^+}(\omega + i\delta - H_0 - H_I)^{-1} \\ &= \lim_{\delta\to 0^+}\left((\omega + i\delta - H_0)(1 - (\omega + i\delta - H_0)^{-1}H_I)\right)^{-1} \\ &= \left(1 - G_0^+(\omega)H_I\right)^{-1}G_0^+(\omega) \\ &= G_0^+(\omega) + G_0^+(\omega)H_IG_0^+(\omega) + G_0^+(\omega)H_IG_0^+(\omega)H_IG_0^+(\omega) + \ldots.\end{aligned} \tag{5.38}$$

Expression	Diagram
$G^+(\omega)$	
$G_0^+(\omega)$	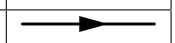
H_I	
$T(\omega)$	

Table 5.1: Definitions of the different components of the Feynman diagrams.

These equations become more insightful by writing them in terms of Feynman diagrams, according to Table 5.1. Doing so, the final line of Eq. (5.38) becomes

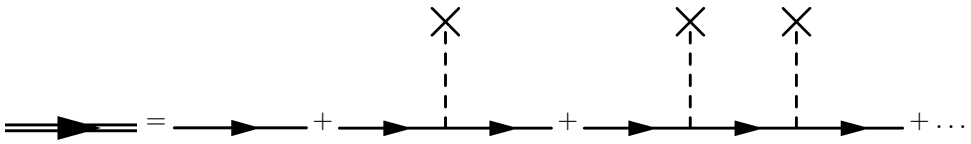

(5.39)

The physical interpretation of this equation is as follows: in absence of "interactions", the propagator is given by the bare Green's function $G_0^+(\omega)$. However, the propagator can now also be scattered on the impurity H_I; moreover, this can happen an arbitrary number of times, resulting in Eq. (5.39). In terms of an incoming particle, it can scatter on the potential H_I several times before leaving, and the complete propagator thus includes all of these possibilities.

In order to calculate the total Green's function, we introduce the concept of the T-matrix. We define the T-matrix such that it captures the probability amplitude of an arbitrary number of times the propagator is scattered on H_I:

$$G^+(\omega) \equiv G_0^+(\omega) + G_0^+(\omega)T(\omega)G_0^+(\omega). \tag{5.40}$$

Comparing this expression to the previous ones, we find that the T-matrix is given by

$$\begin{aligned} T(\omega) \equiv \text{ } &= H_I + H_I G_0^+(\omega) H_I + H_I G_0^+(\omega) H_I G_0^+(\omega) H_I + \dots \\ &= \left(1 - H_I G_0^+(\omega)\right)^{-1} H_I \\ &= \left(1 - \right)^{-1} . \end{aligned} \tag{5.41}$$

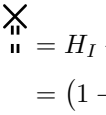

Now that we have developed a general recipe for the calculation of the Green's function in the presence of a scattering potential H_I, we will apply this to the problem of scattering on a single local impurity at the origin. The position space matrix elements of the scattering potential are now given by

$$H_I(\mathbf{r}) = V\delta(\mathbf{r}), \tag{5.42}$$

where V is the impurity strength. Again, it is very possible that V still has a matrix structure, for example if there are several available orbitals or spin states. In terms of Feynman diagrams, the local Green's function $G^+(\mathbf{r}, \mathbf{r}', \omega)$ becomes

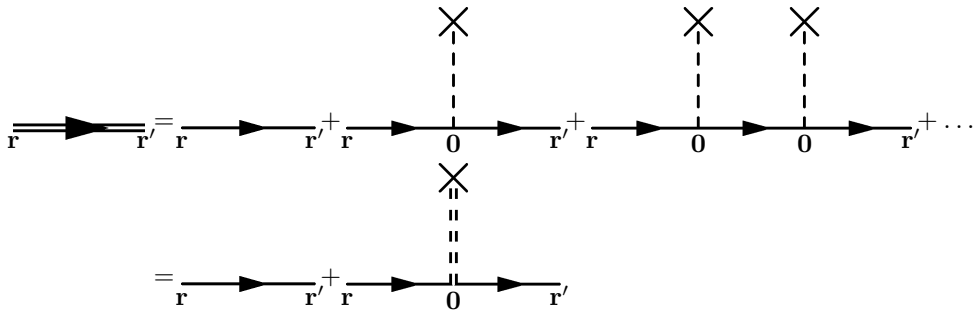

(5.43)

Making use of the T-matrix formalism and assuming the bare Hamiltonian to be translationally invariant, we find

$$G^+(\mathbf{r},\mathbf{r}',\omega) = G_0^+(\mathbf{r}-\mathbf{r}',\omega) + G_0^+(\mathbf{r},\omega)T(\omega)G_0^+(-\mathbf{r}',\omega), \tag{5.44}$$

with

$$T(\omega) = \left(1 - VG_0^+(0,\omega)\right)^{-1} V. \tag{5.45}$$

It is immediately apparent that the resulting Green's function is no longer translationally invariant, as the second term cannot be written in terms of a single variable $(\mathbf{r}-\mathbf{r}')$. This is due to the fact that we are considering a *local* impurity (namely one located at the origin), and so the system itself is no longer translationally invariant.

With the above expression for the local Green's function, we can calculate the changes in the local density of states due to the presence of the impurity. Using the results from the previous section, we find the following expression for the local density of states:

$$\begin{aligned}\rho(\mathbf{r},\omega) &= -\frac{1}{\pi}\mathrm{Im}\,\mathrm{Tr}\,G_0^+(0,\omega) - \frac{1}{\pi}\mathrm{Im}\,\mathrm{Tr}\left[G_0^+(\mathbf{r},\omega)T(\omega)G_0^+(-\mathbf{r},\omega)\right] \\ &\equiv \rho_0(\omega) + \rho_I(\mathbf{r},\omega).\end{aligned} \tag{5.46}$$

Here, the spatially constant $\rho_0(\omega)$ is the local density of states due to the "bare" Hamiltonian, while $\rho_I(\mathbf{r},\omega)$ is the correction to the local density of states due to the presence of the impurity located at the origin. Experimentally, the local features are the ones that are measured, so the correction term $\rho_I(\mathbf{r},\omega)$ is the most relevant for the problem at hand. These features are then often best analyzed by taking the Fourier transform, i.e.

$$\rho_I(\mathbf{q},\omega) = \int \mathrm{d}\mathbf{r}\,\rho_I(\mathbf{r},\omega)e^{-i\mathbf{q}\cdot\mathbf{r}}. \tag{5.47}$$

Note that this Fourier transformed local density of states (or FT-LDOS) is very different from the spectral-weight function that we previously discussed: in absence of an impurity, the spectral-weight function would still depend on the momentum $\mathbf{k}$, explicitly giving the probability density as a function of $\mathbf{k}$ for a given energy. On the other hand, the FT-LDOS would be featureless in absence of an impurity, as it is simply the Fourier transform of the spatial features of the LDOS, and it does therefore not directly give a probability density. Moreover, the $\mathbf{q}$ that appears in Eq. (5.47) does not refer to an actual momentum, and instead it is simply an arbitrary wave number.

Often, it is most convenient to work with the momentum space representation of H_0, such that one starts with a Green's function of the form $G_0^+(\mathbf{k},\omega)$. Starting with this Green's function, there are two ways to calculate the FT-LDOS. The most obvious way is to simply calculate its inverse Fourier transform to get $G_0^+(\mathbf{r},\omega)$, using

$$G_0^+(\mathbf{r},\omega) = \int \frac{\mathrm{d}\mathbf{k}}{(2\pi/a)^d}\,G_0^+(\mathbf{k},\omega)e^{i\mathbf{r}\cdot\mathbf{k}} \qquad \Longleftrightarrow \qquad G_0^+(\mathbf{k},\omega) = \sum_{\mathbf{r}} G_0^+(\mathbf{r},\omega)e^{-i\mathbf{r}\cdot\mathbf{k}}. \tag{5.48}$$

Then, one could calculate $\rho_I(\mathbf{r},\omega)$ and Fourier transform it back to get $\rho_I(\mathbf{q},\omega)$. Note that the above Fourier transform is taken in the continuum limit, such that the sum over $\mathbf{k}$ becomes an integral due to the fact that the step size $2\pi/N$ becomes infinitesimal. However, it is also possible to write the FT-LDOS in terms of a convolution of $G_0^+(\mathbf{k},\omega)$ with itself. This works as follows:

$$\begin{aligned}G_I(\mathbf{r},\omega) &\equiv G_0^+(\mathbf{r},\omega)T(\omega)G_0^+(-\mathbf{r},\omega) \\ &= \int \frac{\mathrm{d}\mathbf{k}}{(2\pi/a)^d}\frac{\mathrm{d}\mathbf{k}'}{(2\pi/a)^d}\,G_0^+(\mathbf{k},\omega)T(\omega)G_0^+(\mathbf{k}',\omega)e^{i\mathbf{r}\cdot(\mathbf{k}-\mathbf{k}')},\end{aligned} \tag{5.49}$$

where d is the number of dimensions of the system. We can then Fourier transform it to find

$$\begin{aligned}G_I(\mathbf{q},\omega) &= \int \mathrm{d}\mathbf{r}\,G_I(\mathbf{r},\omega)e^{-i\mathbf{q}\cdot\mathbf{r}} \\ &= \int \frac{\mathrm{d}\mathbf{k}'}{(2\pi/a)^d}\,G_0^+(\mathbf{q}+\mathbf{k}',\omega)T(\omega)G_0^+(\mathbf{k}',\omega),\end{aligned} \tag{5.50}$$

which is called a *convolution*. We can now write the FT-LDOS in terms of this convolution:

$$\begin{aligned}\rho_I(\mathbf{q},\omega) &= \int \mathrm{d}\mathbf{r}\ \left[-\frac{1}{\pi}\mathrm{Im}\,\mathrm{Tr}\,G_I(\mathbf{r},\omega)\right] e^{-i\mathbf{q}\cdot\mathbf{r}} \\ &= \frac{i}{2\pi}\mathrm{Tr}\int \mathrm{d}\mathbf{r}\ \left[G_I(\mathbf{r},\omega) - (G_I(\mathbf{r},\omega))^*\right] e^{-i\mathbf{q}\cdot\mathbf{r}} \\ &= \frac{i}{2\pi}\mathrm{Tr}\left[G_I(\mathbf{q},\omega) - (G_I(-\mathbf{q},\omega))^*\right]. \end{aligned} \tag{5.51}$$

Both of these methods are entirely equivalent, and it is just a matter of choice which one to use. While the method using the convolution requires the evaluation of only one integral rather than the two Fourier transforms required for the first method, this single integral is generally more time-consuming than the calculation of Fourier transforms (for example by using an FFT algorithm), and it therefore depends on the problem at hand which of the methods is more efficient.

The above discussion concerning the T-matrix formalism and how it can be used to calculate the local density of states contains everything we will need to analyze the effects of the presence of a local lattice impurity. The type of impurity has not yet been specified, so we are free to implement all kinds of impurities: weak or strong, magnetic or non-magnetic, coupling differently to different orbitals, or even more exotic ones. The resulting correction to the local density of states $\rho_I(\mathbf{r},\omega)$ changes the probability to find a quasiparticle at a given position. This change in the probability also changes the conductance at that position, which can be measured experimentally, providing a way to compare experimental data to the theoretical results. As we will see in the next chapter, the quasiparticle LDOS maps originating from the presence of a local impurity often contains interference patterns. In order to better understand these quasiparticle interference (or QPI) patterns, we will then Fourier transform these LDOS maps (i.e. calculate the FT-LDOS) and analyze the results. Finally, we will use the results from this analysis to draw conclusions about the scattering processes that may happen in the considered material.

Chapter 6

Model description of quasiparticle interference in the topological insulator $Cu_xBi_2Te_3$

In this final chapter, we will apply the concepts and techniques from the previous chapter to find a suitable model description of experimentally realized quasiparticle interference in the Cu doped three-dimensional topological insulator Bi_2Te_3. The experiments that provide the motivation of this chapter were done by Van Heumen *et al.* in Ref. [23]. The results from their experiments are also the ones to which we will compare our model results.

The problem that was encountered by Van Heumen in his theoretical model description of the experimental circumstances is that the model and the experiments often seem to disagree about the overall rotational orientation of the QPI patterns. In particular, where the experiments show that the QPI peaks always appear along the $\Gamma \to M$ direction, the model results often imply that these peaks should be located along the $\Gamma \to K$ direction (see appendix B.1 for the definition of these symmetry points of the first Brillouin zone). The main goal of this chapter is to find a model, the corresponding model parameters and the impurity that lead to the correct orientation of the QPI patterns. In doing so, the model parameters have to be chosen such that the band structure coincides with the one found from the experiments, in the small-$\mathbf{k}$ region close to the Γ point. An additional goal is to confirm the existence of different energy windows for the scattering processes, of which the observation was also highlighted in Ref. [23]. In order to achieve these goals, we will first discuss a model Hamiltonian and show that it indeed contains the necessary edge states. Then, we will choose suitable model parameters such that the band structure is the same as that of $Cu_xBi_2Te_3$, after which we will use everything discussed so far to calculate the QPI patterns. Finally, we will discuss the meaning of the results and compare them to the experiments, and we close the chapter by drawing conclusions that follow from this discussion.

6.1 The model Hamiltonian

In this section, we will choose a model Hamiltonian to describe the experimental setup and rewrite it along the lines of Sec. 5.1.3, such that we will be able to analyze surface effects. In Ref. [24], the microscopic lattice structure and the symmetries of the topological insulator Bi_2Te_3 have been used to derive its most general Hamiltonian, up to third order in $\mathbf{k}$ (where $\mathbf{k} = 0$ corresponds to the Γ point). As we have seen in Sec. 5.1.3, a small-$\mathbf{k}$ Hamiltonian is sufficient for deriving the physics in the region we are interested in, and we will therefore use the Hamiltonian from Ref. [24] as our starting point to describe the undoped material:

$$H = \sum_{\mathbf{k}} \psi^\dagger_{\mathbf{k}} \mathcal{H}_{\mathbf{k}} \psi_{\mathbf{k}}, \tag{6.1}$$

where

$$\mathcal{H}_{\mathbf{k}} = \epsilon(\mathbf{k})\mathbb{I}_4 + \mathcal{M}(\mathbf{k})\Gamma_5 + \mathcal{B}(k_z)\Gamma_4 k_z + \mathcal{A}(k_{||})(k_y\Gamma_1 - k_x\Gamma_2) + R_1\Gamma_3(k_x^3 - 3k_xk_y^2) + R_2\Gamma_4(3k_yk_x^2 - k_y^3). \tag{6.2}$$

Here, $k_{||}^2 \equiv k_x^2 + k_y^2$ is the "in-plane" part of $\mathbf{k}$, and the functions are given by

$$\begin{aligned} \epsilon(\mathbf{k}) &= C_0 + C_1 k_z^2 + C_2 k_{||}^2, & \mathcal{M}(\mathbf{k}) &= M_0 + M_1 k_z^2 + M_2 k_{||}^2, \\ \mathcal{B}(k_z) &= B_0 + B_2 k_z^2, & \mathcal{A}(k_{||}) &= A_0 + A_2 k_{||}^2. \end{aligned} \tag{6.3}$$

Moreover, $\mathbb{I}_4$ is the 4×4 identity matrix, while Γ_i are the Euclidean gamma matrices, satisfying the Clifford algebra $\{\Gamma_i, \Gamma_j\} = 2\delta_{ij}\mathbb{I}_4$. The parameters C_i, M_i, B_i, A_i and R_i are unknown and have to be chosen in agreement with experiments. It should again be stressed that the above model Hamiltonian only describes the *undoped* material; the effects of the Cu doping will be added later on by including an impurity Hamiltonian H_I.

As can also be seen from the model Hamiltonian, Bi_2Te_3 is layered in the $\hat{\mathbf{z}}$-direction, such that k_z is decoupled from k_x and k_y. This gives rise to a natural surface for possible surface experiments on this material. In order to calculate observables specifically on this surface, we will now describe the material using a one-dimensional tight-binding model of layers. Note however that there is no unique way to do so, as there are several different models that lead to the same effective Hamiltonian of Eq. (6.2).

First, we calculate the localized four-component spinors by means of a Fourier transform:

$$\psi_{\mathbf{k}} \equiv \psi_{\mathbf{k}_{||}k_z} = \frac{1}{\sqrt{N_z}} \sum_j \psi_{\mathbf{k}_{||}j} e^{-ik_z z_j} \qquad \Longleftrightarrow \qquad \psi_{\mathbf{k}_{||}j} = \frac{1}{\sqrt{N_z}} \sum_{k_z} \psi_{\mathbf{k}_{||}k_z} e^{ik_z z_j}, \tag{6.4}$$

where N_z is the number of layers. Next, we replace all powers $(ak_z)^n$ that appear in Eq. (6.2) by functions $f_n(ak_z)$ that satisfy $f_n(ak_z) = (ak_z)^n + \mathcal{O}(k_z^4)$, where a is the lattice constant (i.e. the distance between the layers). This enables us to calculate the Fourier transforms. Restricting ourselves to a few particularly convenient choices for $f_n(ak_z)$, we find

$$\begin{aligned} \sum_{k_z} \psi_{\mathbf{k}}^\dagger c\, \psi_{\mathbf{k}} &= \frac{1}{N_z} \sum_{k_z, ij} \psi_{\mathbf{k}_{||}i}^\dagger c\, \psi_{\mathbf{k}_{||}j} e^{ik_z(z_i - z_j)} \\ &= \sum_i \psi_{\mathbf{k}_{||}i}^\dagger c\, \psi_{\mathbf{k}_{||}i}, \end{aligned} \tag{6.5}$$

$$\begin{aligned} \sum_{k_z} \psi_{\mathbf{k}}^\dagger c\, k_z \psi_{\mathbf{k}} &\to \sum_{k_z} \psi_{\mathbf{k}}^\dagger \frac{c}{3a} [4 - \cos(ak_z)] \sin(ak_z) \psi_{\mathbf{k}} \\ &= \frac{1}{N_z} \sum_{k_z, ij} \psi_{\mathbf{k}_{||}i}^\dagger \frac{c}{a} \psi_{\mathbf{k}_{||}j} \left[-\frac{2i}{3} e^{iak_z} + \frac{2i}{3} e^{-iak_z} + \frac{i}{12} e^{2iak_z} - \frac{i}{12} e^{-2iak_z} \right] e^{ik_z(z_i - z_j)} \\ &= \sum_i \left[\psi_{\mathbf{k}_{||}i}^\dagger \left(-\frac{2ic}{3a} \right) \psi_{\mathbf{k}_{||}i+1} + \psi_{\mathbf{k}_{||}i}^\dagger \left(\frac{ic}{12a} \right) \psi_{\mathbf{k}_{||}i+2} + h.c. \right], \end{aligned} \tag{6.6}$$

$$\begin{aligned} \sum_{k_z} \psi_{\mathbf{k}}^\dagger c\, k_z^2 \psi_{\mathbf{k}} &\to \sum_{k_z} \psi_{\mathbf{k}}^\dagger \frac{2c}{a^2} [1 - \cos(ak_z)] \psi_{\mathbf{k}} \\ &= \frac{1}{N_z} \sum_{k_z, ij} \psi_{\mathbf{k}_{||}i}^\dagger \frac{c}{a^2} \psi_{\mathbf{k}_{||}j} \left[2 - e^{iak_z} - e^{-iak_z} \right] e^{ik_z(z_i - z_j)} \\ &= \sum_i \left[\psi_{\mathbf{k}_{||}i}^\dagger \left(\frac{2c}{a^2} \right) \psi_{\mathbf{k}_{||}i} + \psi_{\mathbf{k}_{||}i}^\dagger \left(-\frac{c}{a^2} \right) \psi_{\mathbf{k}_{||}i+1} + \psi_{\mathbf{k}_{||}i+1}^\dagger \left(-\frac{c}{a^2} \right) \psi_{\mathbf{k}_{||}i} \right], \end{aligned} \tag{6.7}$$

$$\begin{aligned} \sum_{k_z} \psi_{\mathbf{k}}^\dagger c\, k_z^3 \psi_{\mathbf{k}} &\to \sum_{k_z} \psi_{\mathbf{k}}^\dagger \frac{2c}{a^3} [1 - \cos(ak_z)] \sin(ak_z) \psi_{\mathbf{k}} \\ &= \frac{1}{N_z} \sum_{k_z, ij} \psi_{\mathbf{k}_{||}i}^\dagger \frac{c}{a^3} \psi_{\mathbf{k}_{||}j} \left[-ie^{iak_z} + ie^{-iak_z} + \frac{i}{2} e^{2iak_z} - \frac{i}{2} e^{-2iak_z} \right] e^{ik_z(z_i - z_j)} \\ &= \sum_i \left[\psi_{\mathbf{k}_{||}i}^\dagger \left(-\frac{ic}{a^3} \right) \psi_{\mathbf{k}_{||}i+1} + \psi_{\mathbf{k}_{||}i}^\dagger \left(\frac{ic}{2a^3} \right) \psi_{\mathbf{k}_{||}i+2} + h.c. \right], \end{aligned} \tag{6.8}$$

where c is an arbitrary Hermitian matrix. Defining

$$h_{||}(\mathbf{k}_{||}) \equiv \left(C_0 + C_2 k_{||}^2 \right) \mathbb{I}_4 + \left(M_0 + M_2 k_{||}^2 \right) \Gamma_5 + \mathcal{A}(k_{||})(k_y \Gamma_1 - k_x \Gamma_2) + R_1 \Gamma_3 (k_x^3 - 3k_x k_y^2) + R_2 \Gamma_4 (3k_y k_x^2 - k_y^3), \tag{6.9}$$

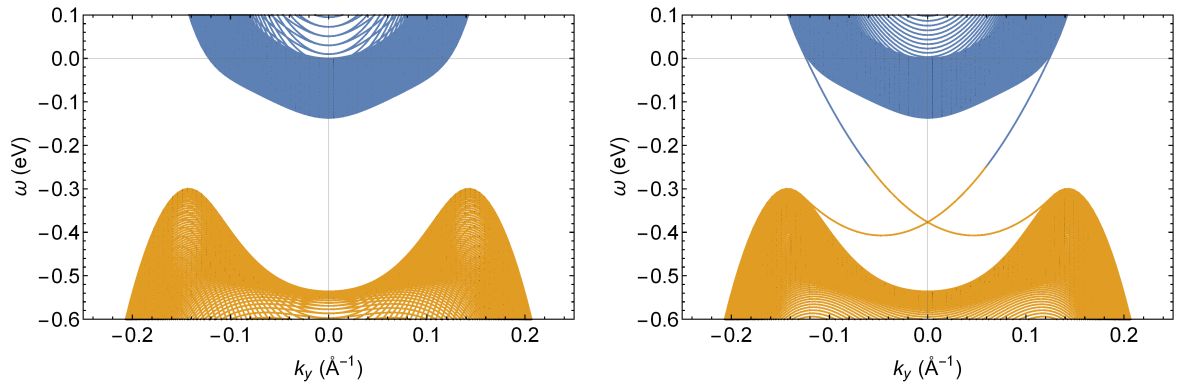

Figure 6.1: Eigenvalues of the Hamiltonian $\mathcal{H}_{\mathbf{k}_{||}}$ for $k_x = 0$ with periodic boundary conditions (left) and with free boundary conditions (right). In the presence of surfaces, edge states appear that connect the two bands.

Eq. (6.2) becomes

$$\mathcal{H}_{\mathbf{k}} = h_{||}(\mathbf{k}_{||}) + C_1 k_z^2 \mathbb{I}_4 + M_1 k_z^2 \Gamma_5 + \mathcal{B}(k_z)\Gamma_4 k_z. \tag{6.10}$$

Combining the above results, we find that the tight-binding Hamiltonian we are looking for is given by

$$\begin{aligned} H &= \sum_{\mathbf{k}_{||},i} \left[\psi^\dagger_{\mathbf{k}_{||}i} h_0(\mathbf{k}_{||}) \psi_{\mathbf{k}_{||}i} + \psi^\dagger_{\mathbf{k}_{||}i} h_1 \psi_{\mathbf{k}_{||}i+1} + \psi^\dagger_{\mathbf{k}_{||}i+1} h_1^\dagger \psi_{\mathbf{k}_{||}i} + \psi^\dagger_{\mathbf{k}_{||}i} h_2 \psi_{\mathbf{k}_{||}i+2} + \psi^\dagger_{\mathbf{k}_{||}i+2} h_2^\dagger \psi_{\mathbf{k}_{||}i} \right] \\ &= \sum_{\mathbf{k}_{||}} \begin{pmatrix} \psi^\dagger_{\mathbf{k}_{||}1} & \psi^\dagger_{\mathbf{k}_{||}2} & \cdots & \psi^\dagger_{\mathbf{k}_{||}N_z} \end{pmatrix} \begin{pmatrix} h_0(\mathbf{k}_{||}) & h_1 & h_2 & 0 & 0 & \cdots \\ h_1^\dagger & h_0(\mathbf{k}_{||}) & h_1 & h_2 & 0 & \cdots \\ h_2^\dagger & h_1^\dagger & h_0(\mathbf{k}_{||}) & h_1 & h_2 & \cdots \\ 0 & h_2^\dagger & h_1^\dagger & h_0(\mathbf{k}_{||}) & h_1 & \ddots \\ 0 & 0 & h_2^\dagger & h_1^\dagger & h_0(\mathbf{k}_{||}) & \ddots \\ \vdots & \vdots & \vdots & \ddots & \ddots & \ddots \end{pmatrix} \begin{pmatrix} \psi_{\mathbf{k}_{||}1} \\ \psi_{\mathbf{k}_{||}2} \\ \vdots \\ \psi_{\mathbf{k}_{||}N_z} \end{pmatrix} \\ &\equiv \sum_{\mathbf{k}_{||}} \psi^\dagger_{\mathbf{k}_{||}} \mathcal{H}_{\mathbf{k}_{||}} \psi_{\mathbf{k}_{||}}, \end{aligned} \tag{6.11}$$

with

$$h_0(\mathbf{k}_{||}) \equiv h_{||}(\mathbf{k}_{||}) + \frac{2C_1}{a^2}\mathbb{I}_4 + \frac{2M_1}{a^2}\Gamma_5, \tag{6.12}$$

$$h_1 \equiv -\frac{C_1}{a^2}\mathbb{I}_4 - \frac{M_1}{a^2}\Gamma_5 - \left(\frac{2B_0}{3a} + \frac{B_2}{a^3}\right) i\Gamma_4, \tag{6.13}$$

$$h_2 \equiv \left(\frac{B_0}{12a} + \frac{B_2}{2a^3}\right) i\Gamma_4. \tag{6.14}$$

Having introduced a localized model, it is now possible to calculate surface observables by using the methods explained in Sec. 5.2. However, we will first check if the model indeed supports the presence of surface states. To do so, we consider periodic boundary conditions in the in-plane directions, and compare the eigenvalues of the Hamiltonian of Eq. (6.11) corresponding to periodic boundary conditions with those corresponding to free boundary conditions in the $\hat{\mathbf{z}}$-direction. These eigenvalues have been calculated along the $\hat{\mathbf{y}}$-direction with $k_x = 0$, using the parameters highlighted in the next section. The eigenvalues are shown in Fig. 6.1. As can be seen in this figure, there can indeed be states that are only present when the system has surfaces, and they connect the valence band to the conduction band. This heavily implies that these states are edge states.

Finally, we require one additional ingredient in order to find QPI patterns: a local surface impurity. The Hamiltonian corresponding to such a surface impurity located at the origin is given by

$$H_I = \psi^\dagger_{\mathbf{r}_{||}=0,i=1} V \psi_{\mathbf{r}_{||}=0,i=1}, \tag{6.15}$$

where V is the 4×4 local impurity matrix, and $\psi_{\mathbf{r}_{||},i}$ is the real space spinor that has also been Fourier transformed in the remaining two directions. Physically, we add this term to the Hamiltonian to include the effects of the Cu doping of our material. However, we only add a single impurity, rather than several impurities. This is justified by the assumption that the impurities are sufficiently separated from each other, such that the QPI patterns they cause are all independent.

6.2 Methods and results

Now that we have a well-defined model to work with, we can use it to calculate experimentally relevant quantities, using the methods from Secs. 5.2 and 5.3. First, we have the bulk retarded Green's function:

$$G^+(\mathbf{k}_{||},\omega) = \lim_{\delta\to 0^+} \left((\omega + i\delta)\mathbb{I}_{4N_z} - \mathcal{H}_{\mathbf{k}_{||}}\right)^{-1}, \tag{6.16}$$

where $\mathcal{H}_{\mathbf{k}_{||}}$ is the matrix that appears in Eq. (6.11). Due to the way that this matrix has been defined, we can immediately identify the 4×4 top-left corner of the bulk Green's function as the surface Green's function, which we will simply call $G(\mathbf{k}_{||},\omega)$ from now on. Setting $B_2/a^2 = -B_0/6$ for simplicity (such that $h_2 = 0$), this surface Green's function can be calculated iteratively using the relation

$$G_N(\mathbf{k}_{||},\omega) = \left(G_1^{-1}(\mathbf{k}_{||},\omega) - h_1 G_{N-1}(\mathbf{k}_{||},\omega)h_1^\dagger\right)^{-1}, \tag{6.17}$$

where $G_N(\mathbf{k}_{||},\omega)$ is the surface Green's function corresponding to a model consisting of N layers; or it can be calculated by using the even more efficient methods derived in Ref. [25]. These very efficient iterative methods for calculating surface Green's functions, explained in detail in appendix B.2, are the ones used for all calculations in this chapter. Having calculated the surface Green's function, we can calculate the surface spectral-weight function as well:

$$\rho(\mathbf{k}_{||},\omega) = -\frac{1}{\pi}\mathrm{Im}\,\mathrm{Tr}\,G(\mathbf{k}_{||},\omega). \tag{6.18}$$

The surface spectral-weight function has been calculated for a system consisting of $2^{15} = 32\,768$ layers with broadening $\delta = 10^{-3}$ eV, using the parameters $C_0 = -1.2$ eV, $C_1/a^2 = 0.295$ eV, $C_2 = 18.67$ eVÅ^2, $M_0 = -1.2$ eV, $M_1/a^2 = 0.43$ eV, $M_2 = 6.845$ eVÅ^2, $B_0/a = 0.33$ eV, $B_2/a^2 = -B_0/6$, $A_0 = 1.8$ eVÅ, $A_2 = 0$, $R_1 = 300$ eVÅ^3 and $R_2 = -140$ eVÅ^3, where B_2 has been chosen such that there are no next-nearest neighbour interactions between the layers. For these calculations, we have defined the gamma matrices as

$$\Gamma_i = \sigma_i \otimes \tau_1, \qquad \Gamma_4 = \sigma_0 \otimes \tau_2, \qquad \Gamma_5 = \sigma_0 \otimes \tau_3, \tag{6.19}$$

$$\sigma_1 = \begin{pmatrix} 0 & 1 \\ 1 & 0 \end{pmatrix}, \qquad \sigma_2 = \begin{pmatrix} 0 & -i \\ i & 0 \end{pmatrix}, \qquad \sigma_3 = \begin{pmatrix} 1 & 0 \\ 0 & -1 \end{pmatrix}, \tag{6.20}$$

where $i \in \{1,2,3\}$ signify the spatial dimensions, σ_0 is the 2×2 identity matrix, σ_i are the Pauli matrices that act in the spin basis, and τ_i are the Pauli matrices corresponding to the orbital degrees of freedom, all in accordance with Ref. [24]. The results from the calculations are shown in Fig. 6.2. The parameters were chosen such that these spectral-weight plots coincide with the ARPES results of $Cu_xBi_2Te_3$ found in Ref. [23]. Note especially that the *Fermi surface* (defined as the constant energy surface in **k**-space that corresponds to the Fermi level) is subject to strong warping. By comparing the QPI patterns shown at the end of this section with those resulting from similar parameter sets that lead to much less warping, it was found that the presence of warping has a strong influence on the scattering processes.

There are a couple of remarks that should be mentioned about these figures. First, the bright lines inside the band gap correspond to edge states, which was already heavily implied by the plots from the previous section. This claim is now further strengthened by the observation that these states are by far the most pronounced states on the surface of the system (after all, we are specifically looking at the *surface* density of states). The presence of these edge states in turn indicates that the model indeed describes a topological insulator. Second, the strong warping of the Fermi surface has been used to identify the $\Gamma \to M$ and the $\Gamma \to K$ directions of the first Brillouin zone. This identification does not follow from these calculations alone, and instead it has been done by comparing these results with

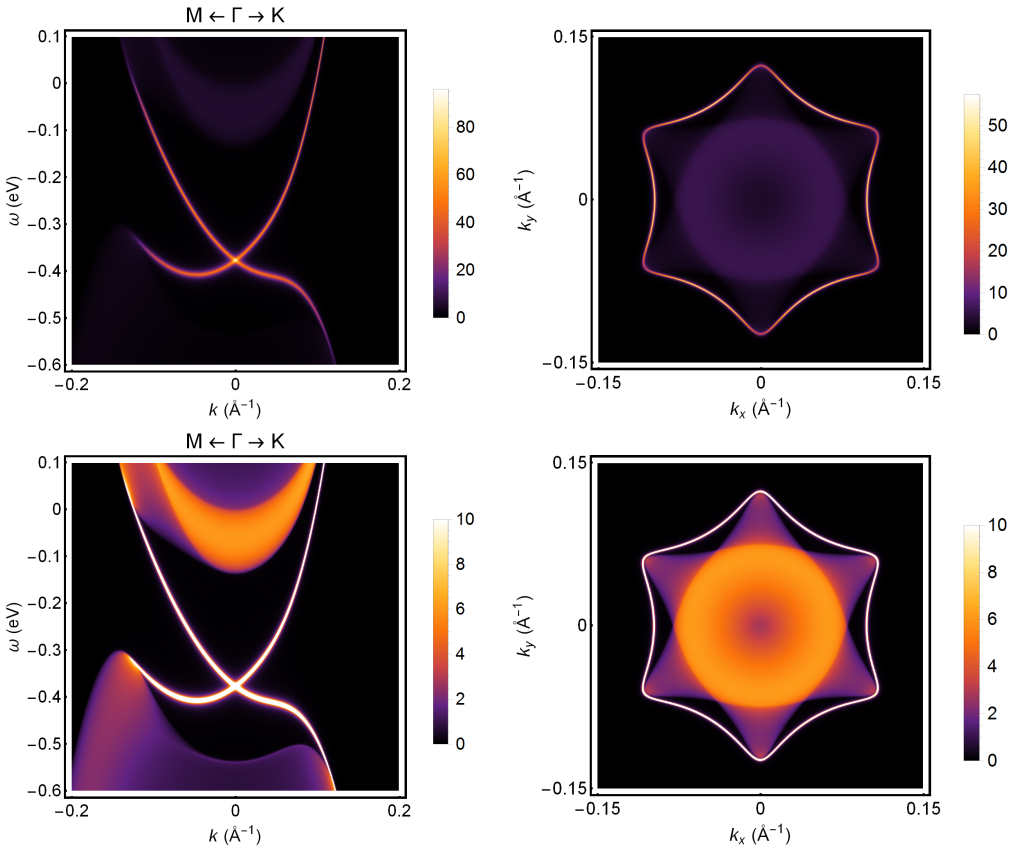

Figure 6.2: Surface spectral-weight function corresponding to the Hamiltonian of Eq. (6.11) with $N_z = 2^{15}$ layers, calculated on a 500×500 grid. Left: band structure along the path $M \leftarrow \Gamma \rightarrow K$ of the first Brillouin zone. Right: constant-energy surface of $\omega = 0$ (i.e. the Fermi surface). The top row shows the full range (using the broadening $\delta = 5 \cdot 10^{-3}$ eV), while the bottom row zooms in on a smaller range for the density of states (with $\delta = 10^{-3}$ eV). Note that the edge states are much more pronounced than is shown in the bottom row.

experiments, see for example Ref. [26]. The conclusion that follows from this comparison is that our k_y-direction corresponds to the $\Gamma \rightarrow M$ direction, while the k_x-direction is the $\Gamma \rightarrow K$ direction.

The next step is to actually find the QPI patterns that appear as a result of the presence of the local impurity that was introduced in Eq. (6.15). This is done by using the techniques outlined in Sec. 5.3. Using T-matrix formalism, the corrections to the surface LDOS due to the presence of a local impurity are found to be given by

$$\rho_I(\mathbf{r}_{||}, \omega) = -\frac{1}{\pi} \mathrm{Im}\, \mathrm{Tr}\left[G_0(\mathbf{r}_{||}, \omega) T(\omega) G_0(-\mathbf{r}_{||}, \omega)\right], \tag{6.21}$$

where $G_0(\mathbf{r}_{||}, \omega)$ is the Fourier transform of the "bare" surface Green's function $G(\mathbf{k}_{||}, \omega)$ in absence of an impurity, while the T-matrix is given by

$$T(\omega) = \left(\mathbb{I}_4 - V G_0(0, \omega)\right)^{-1} V. \tag{6.22}$$

As we have seen before, the "bare" part of the LDOS $\rho_0(\omega)$ is independent of the position $\mathbf{r}$ due to translational symmetry of the undoped system, such that we can safely ignore that term and simply focus on the term $\rho_I(\mathbf{r}_{||}, \omega)$ that arises from the presence of the impurity.

As with most interference patterns, the features from the QPI patterns are most apparent in momentum space. Therefore, we will utilize the FT-LDOS $\rho_I(\mathbf{q}_{||}, \omega)$ in order to analyze the QPI patterns and the corresponding scattering processes. However, while the real space LDOS is an entirely real quantity, the FT-LDOS is a simple Fourier transform and so it can have an imaginary part as well. As we are interested in the amplitudes corresponding to the different wave vectors, we "fix" this by simply plotting the absolute value of the FT-LDOS.

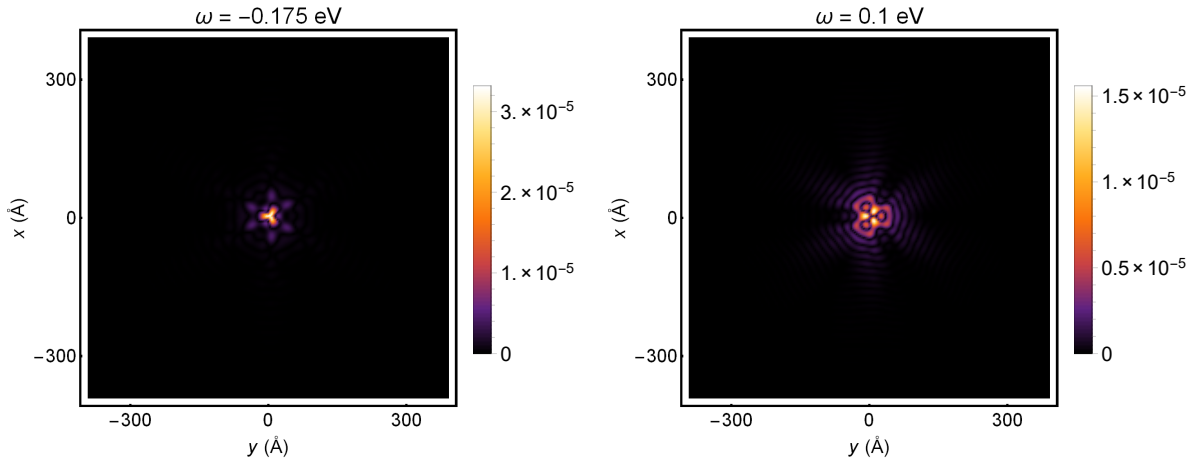

Figure 6.3: Real space LDOS $\rho_I(\mathbf{r}_{||}, \omega)$ for two different energies, calculated using the impurity and parameters mentioned in the text. Note that $\omega = -0.175$ eV is an energy located in the band gap, while $\omega = 0.1$ eV is well into the conduction band.

The surface LDOS and the corresponding FT-LDOS have been calculated for several different energies, with a resolution of $1\,000 \times 1\,000$ points, $q_{x,y}$ going from -0.8 to 0.8 Å^{-1}, $N_z = 2^{15}$ layers, and $\delta = 10^{-2}$ eV. The impurity that was used is the non-magnetic impurity

$$V = V_0 \sigma_0 \otimes \begin{pmatrix} 1 & 0 \\ 0 & 0 \end{pmatrix} = V_0 \begin{pmatrix} 1 & 0 & 0 & 0 \\ 0 & 0 & 0 & 0 \\ 0 & 0 & 1 & 0 \\ 0 & 0 & 0 & 0 \end{pmatrix}, \tag{6.23}$$

where $V_0 = 0.05$ eV is the impurity strength. Physically, this is a weak impurity that couples equally to both spin states (hence being called non-magnetic), while it only couples to one of the two considered orbitals. Note that this weak impurity is in the regime where $T(\omega) \approx V$, such that the precise impurity strength does not influence the shapes of the QPI patterns, only their amplitudes. Two examples of the real space LDOS following from this specific impurity are shown in Fig. 6.3. As can be seen in this figure, the resulting LDOS has three-fold rotational symmetry and depends strongly on the energy scale. In particular, the ripples characteristic to interference patterns become more pronounced for higher energies. The momentum space FT-LDOS corresponding to these real space LDOS plots can be found in Fig. 6.4. From these plots, we see that there are two regions with different QPI patterns: one region that spans the band gap and the bottom part of the conduction band, and another region further into the conduction band. The pattern corresponding to $\omega = -0.05$ eV appears to be a transition between the two regions. Referring back to the observation that the k_y-direction corresponds to the $\Gamma \to M$ direction, the plots also show that the most pronounced QPI peaks appear along the $\Gamma \to M$ direction for all of the energies shown in the figure (except for the transition energy $\omega = -0.05$ eV).

It should be noted that the QPI patterns shown in Fig. 6.4 are very sensitive to the parameters of the model, the type and strength of the impurity, and the energy scale. To illustrate this, the effects of a different type of impurity and of a much stronger impurity are shown in Fig. 6.5. For the left panel, $V = V_0 \mathbb{I}_4$ with $V_0 = 0.05$ eV was used, while the right panel was calculated using the impurity from Eq. (6.23), but with $V_0 = 10^3$ eV. The latter is an example of a very strong impurity, which can be interpreted as a vacancy on the underlying lattice. As can be seen from these examples, these changes in the impurity can have a significant influence on the QPI pattern and its rotational orientation. In both panels, the most pronounced peaks now appear in the $\Gamma \to K$ direction rather than the $\Gamma \to M$ direction. However, a careful look at Fig. 6.4 reveals that the now-dominant peaks in the $\Gamma \to K$ direction were already present in Fig. 6.4, but the peaks in the $\Gamma \to M$ direction were simply stronger. As the impurity clearly has a strong influence on the results, a particular choice had to be made. The type of impurity and the impurity strength that were used for Fig. 6.4 were chosen due to the similarities between these results and the experiments.

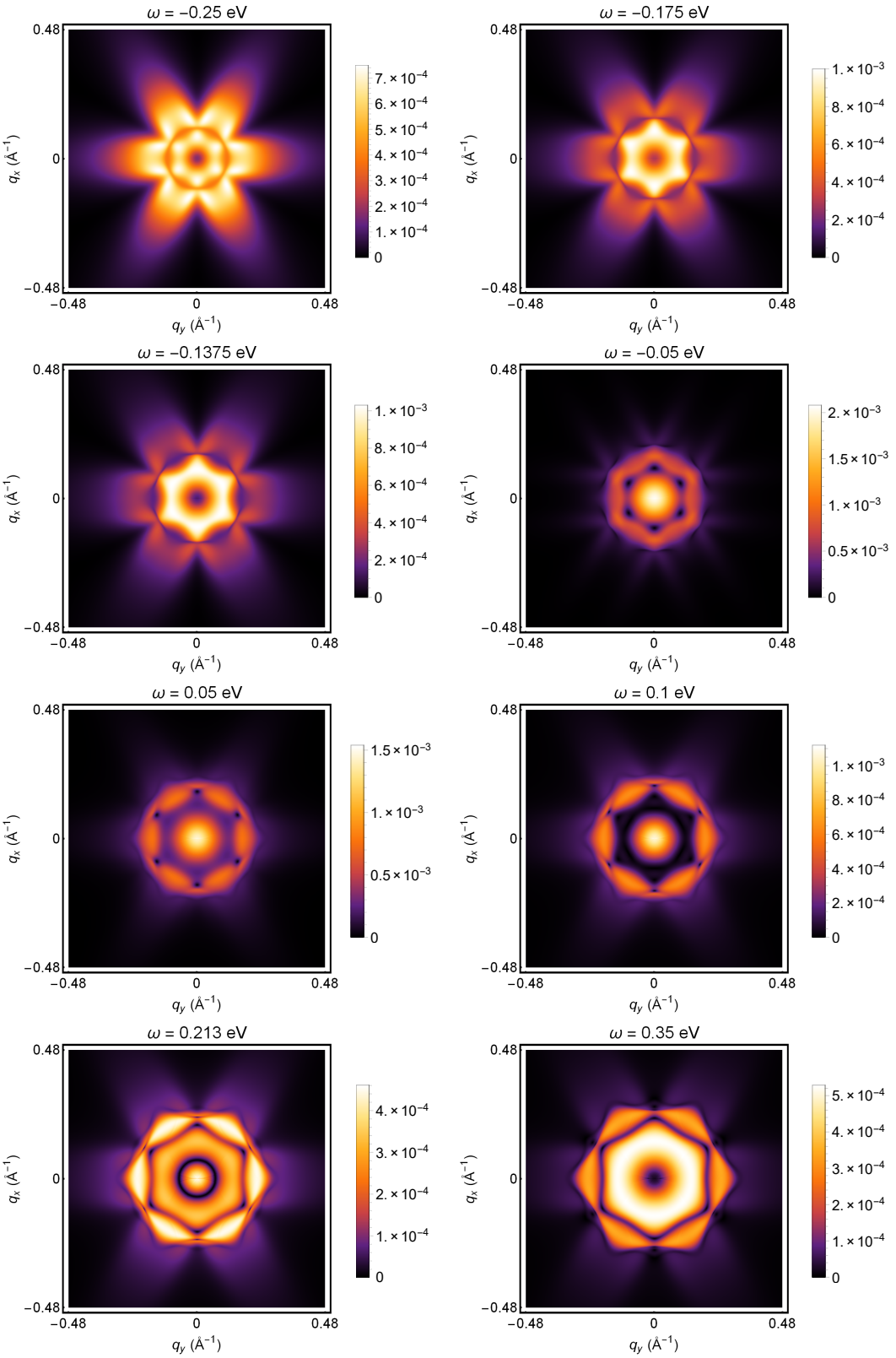

Figure 6.4: Momentum space FT-LDOS $\rho_I(\mathbf{q}_{||}, \omega)$ for eight different energies, again for the impurity and parameters described in the text. Two regions with distinct looking QPI patterns can be observed, with $\omega = -0.05$ eV connecting these regions. The overall six-fold rotational symmetry and the orientation of the patterns are the same in both regions, with the most pronounced peaks being in the $\Gamma \to M$ direction.

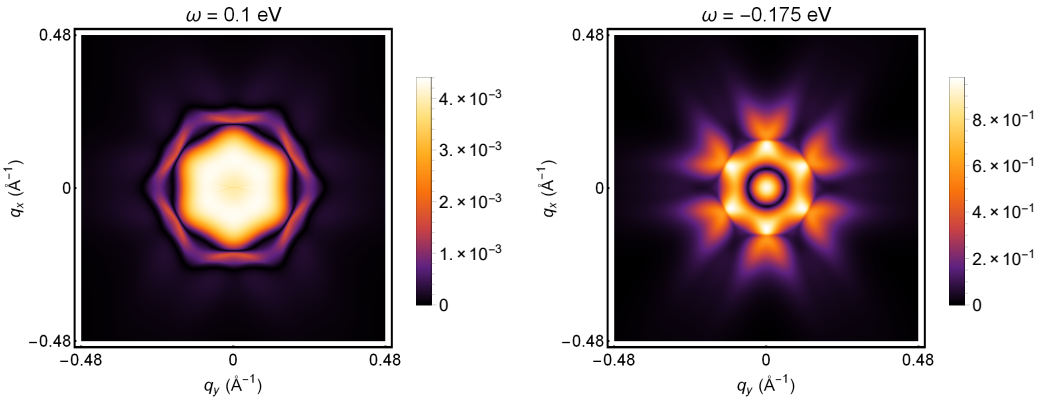

Figure 6.5: Left: FT-LDOS corresponding to the same model, energy and parameters as for one of the pictures of Fig. 6.4, but with a different type of impurity: $V = V_0 \mathbb{I}_4$, with $V_0 = 0.05$ eV. Right: FT-LDOS corresponding to the same model, energy, parameters and impurity as for another one of the pictures of Fig. 6.4, but with a much larger impurity strength $V_0 = 10^3$ eV. These particular energies and impurities were chosen in order to illustrate how strongly these changes in the impurity can influence the QPI patterns.

6.3 Discussion

In this section, we will discuss the results found in the previous section, focusing on the FT-LDOS results shown in Fig. 6.4. One of the first features that stands out is that the QPI patterns all have the same orientation as the Fermi surface. However, the distance of the QPI peaks to the origin is approximately twice as big as the distance of the "ring" from the Fermi surface to the origin (note that the Fermi surface from Fig. 6.2 is rotated by 90 degrees with respect to the plots from Fig. 6.4, where q_x and q_y have been switched with respect to k_x and k_y). This can be explained by *backscattering*: surface particles coming in with momentum $\mathbf{k}$ and hitting the impurity can be bounced back with momentum $-\mathbf{k}$, leading to a change in momentum of $\mathbf{q} = -2\mathbf{k}$. Another interesting feature seen in the FT-LDOS is the distance of the $\Gamma \to M$ peaks to the origin as a function of energy, plotted in Fig. 6.6. In both regions (i.e. the two energy windows with distinct looking QPI patterns that were observed in the previous section), this distance Δq increases with the energy. This is exactly what one would expect from the observation that the spectral-weight function becomes "wider" for larger energies, as can be seen in the left half of Fig. 6.2. However, there is also a jump in Δq between the two regions. Noting that the conduction band is more narrow than the edge states at a given energy, the jump in Δq may be explained by the states from the conduction band becoming more dominant in the scattering processes than the edge states.

The existence of the two energy windows requires an explanation as well. As is argued by Van Heumen in Ref. [23], it is necessary to consider both the edge states and the conduction band. Inside the band gap, there are only edge states, and as a result there can only be scattering between different

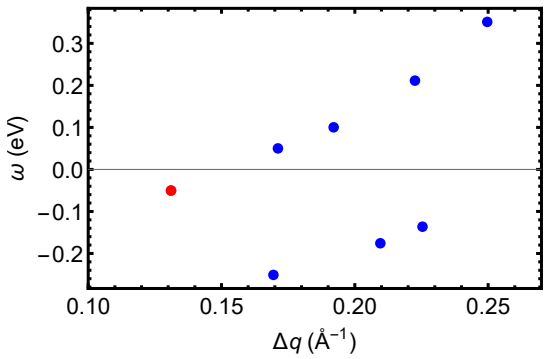

Figure 6.6: Momentum space distance of the most pronounced QPI peaks to the origin, as a function of energy. The jump takes place in the vicinity of $\omega = -0.05$ eV. At this energy, no pronounced peaks are present. The small bump that can still be observed at this energy is denoted by the red dot.

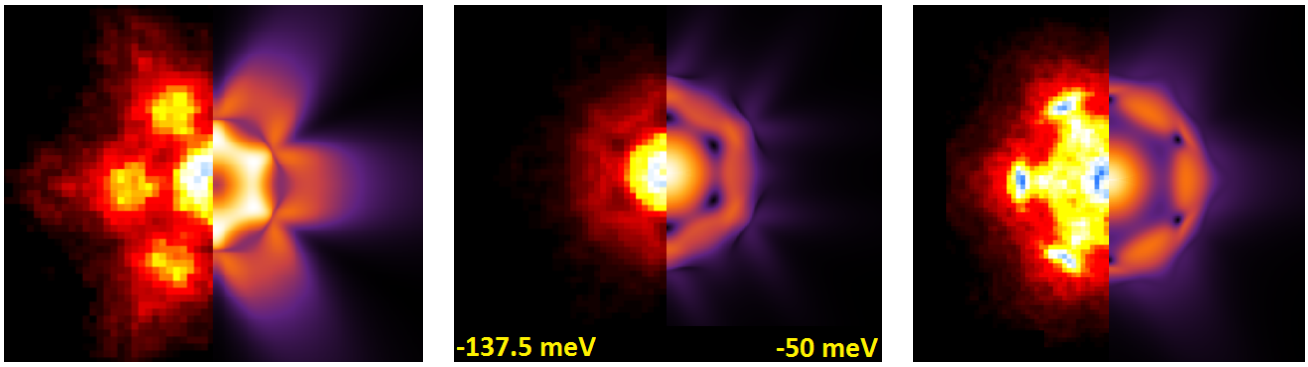

Figure 6.7: Comparison of the model results from Fig. 6.4 with the experimental results from Ref. [23]. The left panel contains the FT-LDOS results corresponding to $\omega = -0.175$ eV (located in the first region), while the right panel shows the results corresponding to $\omega = 0.05$ eV (located in the second region). The central picture compares the transition patterns, where it should be noted that the model and the experiments disagree about the energy at which this transition happens.

edge states. This results in the QPI patterns that were found for low energies. As the energy increases, we eventually reach the bottom of the conduction band. However, as can be seen in Fig. 6.2, the edge states are still much more pronounced than the conduction band, so the scattering between different edge states still dominates the QPI patterns. This continues until we reach $\omega = -0.05$ eV. Around this energy scale, scattering between edge states and the conduction band becomes more important than scattering among edge states only, leading to different QPI patterns. Since states from the conduction band have a smaller momentum than the edge states at the same energy level (see once again Fig. 6.2), this transition leads to a jump in Δq as well. In the experiments from Ref. [23], a third region was observed that was attributed to scattering between different conduction band states becoming the most dominant scattering processes. This region cannot be discerned from our results, due to the fact the model Hamiltonian that we used is only valid for small $\mathbf{k}$ and low energies, such that it does not allow a proper investigation of higher energy scales.

Next, we compare the model results to the experimental results from Ref. [23], see also Fig. 6.7. As was stated in the previous section, all model parameters were chosen such that Fig. 6.2 agrees with the experimental ARPES data. While all energies are the same between the model and the experiments, the momenta are still different. This could be fixed by simply rescaling the model parameters, but it has no physical significance, so we ignore it. Additionally, the QPI patterns from the model are generally in good agreement with those from the experiments. In particular, the model results and the experimental results share the same six-fold rotational symmetry and orientation. In both regions, many of the features from the model are somewhat different and much sharper than those from the experiments, but this is likely due the fact that the model describes a perfect situation that is very difficult to achieve experimentally. For example, the model contains a perfect single layer surface that separates the bulk from a perfect vacuum, which is not a very realistic scenario. On the other hand, the transition pattern (i.e. the one corresponding to $\omega = -0.05$ eV) that connects the two regions appears to be very similar to the one from the experiments. However, the energy at which this transition happens is different: the experiments show that it happens at the lower energy $\omega = -0.1375$ eV. This may again be due to the real surface being less perfect than the one used in the model, or due to the model parameters not being entirely correct. Additionally, it is possible that the impurities on the real material are not always located exactly on the surface, but are instead located a few layers into the bulk, which may lead to different results as well. It would however require a more thorough analysis to be able to draw proper conclusions about the origin of this discrepancy.

Finally, we can say a few words about the nature of the impurity caused by the Cu doping of the material. As was mentioned before, the model results that we found originate from a non-magnetic impurity that only couples to one of the two considered orbitals, see Eq. (6.23). The other orbital is thus undisturbed by the impurity. Moreover, we found that an impurity that couples equally to both orbitals leads to a different rotational orientation of the QPI patterns. Attempts with more types of impurities reveal that only an impurity coupling to the first orbital leads to the orientation of the QPI

patterns from Fig. 6.4, while other types of impurities correspond to different orientations. Since the experiments show that the orientation seen in Fig. 6.4 is the correct one, this therefore suggests that the actual impurities encountered in the experiments only couple to one of the orbitals as well.

6.4 Conclusions and outlook

In the second part of the thesis, we have worked out a model that can be used to describe the experimentally realized quasiparticle interference in the Cu doped topological insulator $Cu_xBi_2Te_3$, which was highlighted in Ref. [23]. Our main goals were to reproduce the orientation of the QPI patterns that was found in the experiments and to confirm the existence of the different energy windows corresponding to different dominant scattering processes.

After discussing all necessary preliminaries in Ch. 5, we introduced a tight-binding model of layers that is capable of describing the material at hand, which was then used to calculate the changes in the surface LDOS due to the presence of a single local surface impurity. There are several conclusions that can be drawn from the results. First, the similarities between the results from the model and from the experiments confirm that the model is able to reproduce the experimental results. This in turn heavily implies that the model properly captures the experimental circumstances. A second related conclusion is that the model is indeed capable of producing QPI patterns with the same six-fold rotational symmetry and orientation as the ones that follow from the experiments. Referring back to the impurity that was necessary to retrieve the correct orientation, we can also conclude that the impurities caused by the Cu doping of the material only couple to the electrons from a single orbital. Finally, the model results confirm that there are at least two energy windows with distinct QPI patterns, which can be explained by the presence of two different scattering processes, namely scattering among edge states versus scattering between edge states and the conduction band. However, besides all of the above conclusions, there are also several quantitative differences between the model results and the experimental results, most importantly the difference in the energy scale separating the two regions. Future work could therefore focus on finding the origins of these differences. Still, everything being taken into account, and despite the fact that the model results are very sensitive to the model parameters and the type and strength of the impurity, the model proved to be very successful in qualitatively reproducing the prominent features from the experimental results.

Appendix

A.1 Comments on the Monte Carlo simulations

In Ch. 2, we have seen the results of Monte Carlo simulations of the antiferromagnetic Heisenberg model on the distorted triangular lattice. We will now comment on some of the aspects related to these simulations. For the general concepts and methods of Monte Carlo simulations in statistical physics, I refer the reader to the book by Newman & Barkema [27].

For our simulations, we used a simple Metropolis algorithm. Starting with a random spin configuration, each simulation step consists of selecting a single random spin and rotating it by a random solid angle within a given opening angle δ. Then, the acceptance ratio is calculated according to the usual Monte Carlo prescriptions, and this ratio is used to determine whether this random move is kept, or the previous configuration is restored. The angle δ is chosen such that the number of accepted and discarded moves are of the same order. First, many simulation steps are done to allow the system to thermalize (i.e. reach thermal equilibrium). After the system is properly thermalized, the simulation continues, but now the relevant quantities are measures as a function of time (the number of simulation steps being a measure of time) and at the end their average values are calculated, giving us the thermal average of these quantities at given values for J_1/J_2 and k_BT/J_2.

As was mentioned in the main text, the simulations were done using different types of boundary conditions. Boundary conditions are necessary because a simulation must always be done on a finite lattice (let us call it the "simulation box"), rather than an infinite lattice, and therefore we require a description for how to handle the boundaries. The boundary conditions that were used are periodic boundary conditions and helical boundary conditions. To see how these work, we consider the square lattice as an example. For periodic boundary conditions, the spin at one end is simply connected to the spin at the corresponding opposite end. For the square lattice, the four neighbours of the lattice site located at position (x, y) are thus found at

$$\begin{aligned} &((x \pm 1) \bmod L, y)\,, \\ &(x, (y \pm 1) \bmod L)\,, \end{aligned} \tag{A.1}$$

where L is the length of the simulation box. While these boundary conditions are quite simple, helical boundary conditions require even less code. Helical boundary conditions are very similar to the usual periodic boundary conditions, but now we simply label each lattice site with a single index i and impose that the neighbours of lattice site i are the sites

$$\begin{aligned} &(i \pm 1) \bmod L, \\ &(i \pm L) \bmod L^2. \end{aligned} \tag{A.2}$$

Whichever of these boundary conditions we choose, they effectively extend the simulation box over the entire space by filling it up with copies of the initial box, only restricting all length scales to be of the order L at most. Fig. A.1 illustrates how the above boundary conditions work on a square lattice. It is straightforward to generalize this example to formulate the boundary conditions on a (distorted) triangular lattice.

Finally, we note that there is a problem that arises for Metropolis simulations on the distorted triangular lattice that was not discussed in the main text: the system sometimes gets stuck in a local minimum. To illustrate this, we look at the extreme case $J_1 = 100J_2$. The ground state is shown in

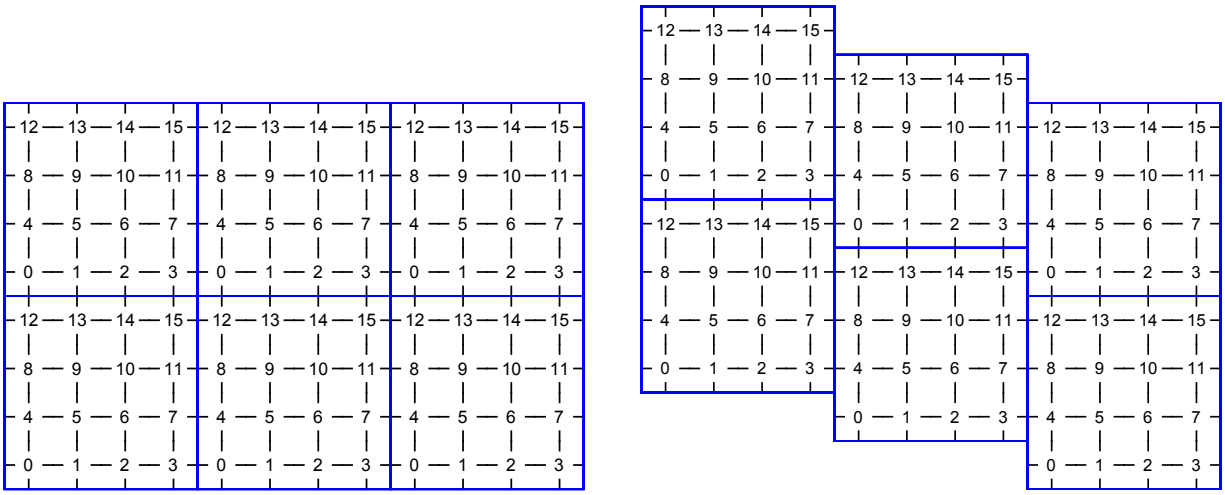

Figure A.1: Example of periodic boundary conditions (left) and helical boundary conditions (right) on a square lattice. A simulation is done in a single box (enclosed by a blue square), which is then extended over the entire space by placing copies of this one box according to the boundary conditions. These concepts can straightforwardly be generalized to the triangular lattice.

the bottom-right panel of Fig. 2.3. In this state and on our finite lattice, it would only cost a relatively small amount of energy to rotate one of the chains out of plane in its entirety. Given the nature of the single spin rotations done in the Metropolis algorithm, it would be very unlikely to change such a configuration back to the ground state configuration. Therefore, if we start with a random configuration and the system takes one of these local minima by chance, the algorithm will sometimes not be able to rotate the chain back to the correct plane in a reasonable amount of time.

A.2 Additional simulation results

We will now look at some additional results from the Monte Carlo simulations. First, let us look at the high temperature values of the order parameters. It is expected that all of the squared order parameters that we measure are greater than zero even when the temperature goes to infinity. This is due to the fact that the quantities are strictly non-negative for each configuration. If we then take the expectation values for $T \to \infty$, all configurations (including ordered configurations, where the squares are non-zero) are equally likely, such that the expectation values are strictly positive. They then go to zero when the lattice size goes to infinity. The left panel of Fig. A.2 shows the results of the undistorted triangular lattice up to a much higher temperature than what was previously considered. We indeed see that the squares remain non-zero even for large temperatures, which is due to the fact that the lattice is finite. However, we see that $(Q_S^{\alpha\beta})^2$ remains significantly larger than $(Q_\kappa^{\alpha\beta})^2$, suggesting that the latter is a more appropriate order parameter.

Next, we consider the ferromagnetic Heisenberg model on the undistorted triangular lattice (so $J_1 = J_2 \to -J$). For this model, we can use the actual magnetization rather than the staggered magnetization that was previously used:

$$\mathbf{M} \equiv \frac{1}{N} \sum_i \mathbf{S}_i. \tag{A.3}$$

The results of the simulations are shown in the right panel of Fig. A.2. As can be seen in the figure, the behaviour is the same as in the antiferromagnetic case, with the exception of $(Q_\kappa^{\alpha\beta})^2$ (which now remains zero by definition). The only apparent difference is that ordering starts to appear at a larger temperature than in the antiferromagnetic case on the same lattice size.

Lastly, we take a moment to look at the finite size effects and compare it to a generalized three-dimensional lattice. In order to find the actual critical temperature, one would have to extrapolate the simulation results to an infinite lattice, and therefore we want to know how the order parameters change

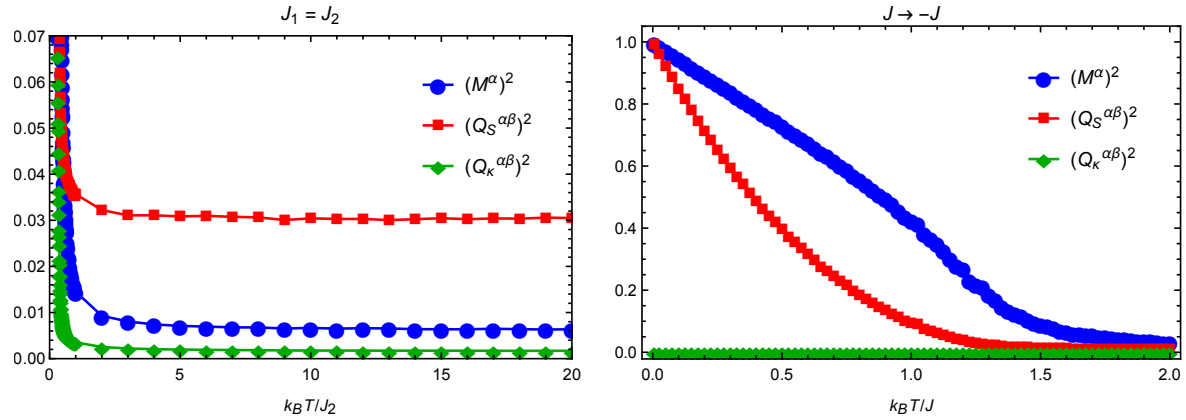

Figure A.2: Left: order parameters as functions of temperature for the antiferromagnetic Heisenberg model on the undistorted triangular lattice using a larger temperature range than before. Right: order parameters as functions of temperature for the ferromagnetic Heisenberg model on the undistorted triangular lattice. Both simulations are done on lattices with $N = 132$ lattice sites.

with increasing lattice size. The left panel of Fig. A.3 shows the finite size scaling of the Heisenberg antiferromagnet on the undistorted triangular lattice, ranging from $N = 72$ to $N = 3540$ lattice sites; the curves move to the left for increasing temperature. While not conclusive from this picture alone, it suggests that the curves are extrapolated all the way to zero in the $N \to \infty$ limit, corresponding to a critical temperature $T_c = 0$. Assuming that this is true, it agrees with the Mermin-Wagner theorem that we encountered in Ch. 3. To see if there is a phase transition at finite temperature in a three-dimensional system, we repeat the same procedure on a generalized three-dimensional lattice, consisting of stacked triangular layers that are coupled antiferromagnetically (such that we simply have antiferromagnetic chains in the third dimension). The results are found in the right panel of Fig. A.3. On this three-dimensional lattice, finite size scaling suggests that there is a finite critical temperature of the order $k_B T_c/J \sim 1$, confirming that a phase transition can indeed exist for this model in three dimensions. Note however that mean-field theory of this model would give $k_B T_c/J = 3$, so mean-field theory once again deviates significantly from the simulations for this three-dimensional model. The above is thus an example of the influence of the number of dimensions on the existence of a phase transition and the validity of mean-field theory, which was explored in Sec. 3.4.

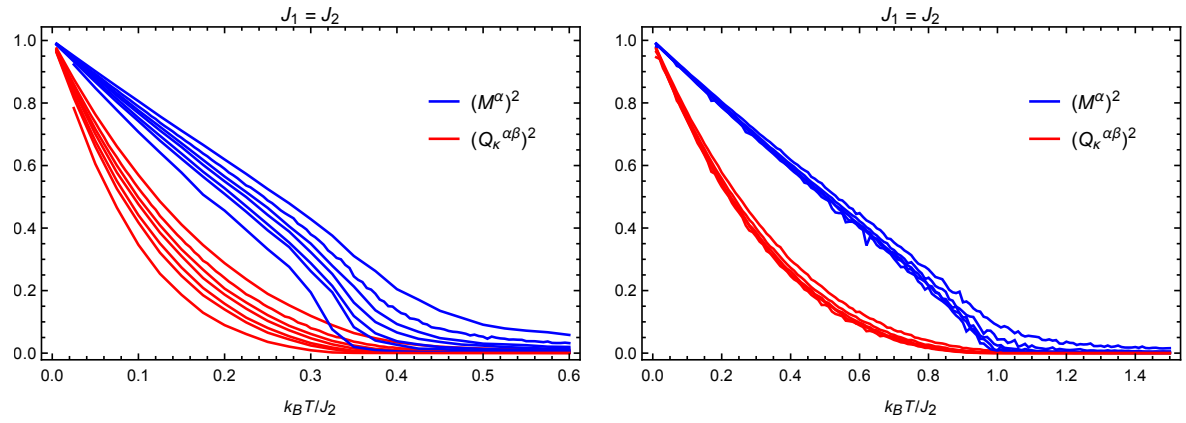

Figure A.3: Finite size scaling of the order parameters of the antiferromagnetic Heisenberg model as a function of temperature on the two-dimensional (undistorted) triangular lattice (left) and on the three-dimensional stacked triangular lattice (right). The simulations on the two-dimensional lattice range from $N = 72$ to $N = 3540$ lattice sites, while those on the three-dimensional lattice range from $N = 216$ to $N = 5832$ lattice sites. Note that the left-most curve is always the one that corresponds to the largest lattice size.

A.3 Gaussian integrals

In the following three sections, we will cover some useful methods, mostly applied to the models from the main text. More information on these methods can be found in Ref. [28].

In the main text, we used Gaussian integrals several times. We will now derive the solutions of these general integrals to support the validity of the corresponding results in the main text. The most basic Gaussian integral is given by

$$\int_{-\infty}^{+\infty} \mathrm{d}x\, e^{-\alpha(x-x_0)^2} = \sqrt{\frac{\pi}{\alpha}}, \tag{A.4}$$

where x is a real variable. This identity is easily verified by switching to polar coordinates. Writing $\alpha \equiv -G^{-1}/2$ and $x_0 \equiv Gb$, it becomes

$$\int_{-\infty}^{+\infty} \mathrm{d}x \exp\left[\frac{1}{2}G^{-1}x^2 - bx\right] = \sqrt{-2\pi G}\exp\left[-\frac{1}{2}Gb^2\right]. \tag{A.5}$$

This result can be generalized to an n-dimensional integral as well. First restricting ourselves to a diagonal matrix $G_{ij} = \delta_{ij}G_{ii}$ (such that the inverse is given by $G^{-1}_{ij} = \delta_{ij}/G_{ii}$), the n different integrals are decoupled, so we find

$$\int \left(\prod_{i=1}^{n} \frac{\mathrm{d}x_i}{\sqrt{2\pi}}\right) \exp\left[\frac{1}{2}\sum_{ij}\left(x_i - \sum_k G_{ik}b_k\right) G^{-1}_{ij} \left(x_j - \sum_k G_{jk}b_k\right)\right] = \frac{1}{\sqrt{\prod_{i=1}^{n}(-G^{-1}_{ii})}} = \frac{1}{\sqrt{\mathrm{Det}(-\mathbf{G}^{-1})}}, \tag{A.6}$$

or

$$\int \left(\prod_{i=1}^{n} \frac{\mathrm{d}x_i}{\sqrt{2\pi}}\right) \exp\left[\frac{1}{2}\sum_{ij} x_i G^{-1}_{ij} x_j - \sum_i b_i x_i\right] = \frac{1}{\sqrt{\mathrm{Det}(-\mathbf{G}^{-1})}} \exp\left[-\frac{1}{2}\sum_{ij} b_i G_{ij} b_j\right]. \tag{A.7}$$

Since we are always working with positive definite (and therefore diagonalizable) matrices in the main text, we know that there exists an orthogonal matrix $\mathbf{O}$ that diagonalizes the matrix $\mathbf{G}^{-1}$, such that the matrix $\mathbf{O}\cdot\mathbf{G}^{-1}\cdot\mathbf{O}^{-1}$ is diagonal. Utilizing the coordinate transformation $\mathbf{x} \to \mathbf{O}\cdot\mathbf{x}'$ and exploiting the fact that $\mathbf{O}$ is orthogonal, it is easily verified that the above identity holds for any positive definite matrix $-\mathbf{G}^{-1}$. Note that if we write $\mathbf{G}^{-1} \to \mathbf{G}$ and $\mathbf{b} \to \mathbf{G}\cdot\mathbf{b}$, we arrive at Eq. (3.36).

In Ch. 4, we also encountered Gaussian integrals with complex variables. The integrals over complex variables are best solved by writing them in terms of the real and imaginary parts of the complex variables, which we will call x and y respectively, such that $z = x + iy$. Then, the Jacobian matrix of the coordinate transformation $z^* = x - iy$, $z = x + iy$ is given by

$$\mathbf{J} = \begin{pmatrix} 1 & -i \\ 1 & i \end{pmatrix}. \tag{A.8}$$

Now we can calculate a Gaussian integral over a single complex variable:

$$\int \mathrm{d}z^*\mathrm{d}z \exp\left[G^{-1}z^*z\right] = \int \mathrm{d}x\,\mathrm{d}y\,\mathrm{Det}(\mathbf{J}) \exp\left[G^{-1}(x^2+y^2)\right] = -2\pi i G. \tag{A.9}$$

Writing $z \to z + Gh$, the right-hand side remains the same, and we can expand the square to find

$$\int \mathrm{d}z^*\mathrm{d}z \exp\left[G^{-1}z^*z + z^*h + h^*z\right] = -2\pi i G \exp\left[-Gh^*h\right]. \tag{A.10}$$

In much the same way as for the real case, this can be generalized to a multidimensional integral, leading to

$$\int \left(\prod_{i=1}^{n} \frac{\mathrm{d}z_i^*\mathrm{d}z_i}{2\pi i}\right) \exp\left[\sum_{ij} z_i^* G^{-1}_{ij} z_j + \sum_i z_i^* h_i + \sum_i h_i^* z_i\right] = \frac{1}{\mathrm{Det}(-\mathbf{G}^{-1})} \exp\left[-\sum_{ij} h_i^* G_{ij} h_j\right], \tag{A.11}$$

where $-\mathbf{G}^{-1}$ is a positive definite Hermitian matrix. This final identity is the one that is used several times in Ch. 4 and the next section.

A.4 Wick's theorem

Wick's theorem is an important tool for calculating expectation values of products of operators with respect to a quadratic Hamiltonian. For the situations at hand, the theorem states that such expectation values are equal to the sum of all possible products of expectation values of two operators. To illustrate how it works, we consider the quadratic Hamiltonian

$$H = \frac{N_c}{2} \sum_{\mathbf{q}} \sum_{ab} \left((\epsilon_{\mathbf{q}}^{xa})^* M_{\mathbf{q}}^{xab} \epsilon_{\mathbf{q}}^{xb} + (\epsilon_{\mathbf{q}}^{ya})^* M_{\mathbf{q}}^{yab} \epsilon_{\mathbf{q}}^{yb} \right). \tag{A.12}$$

Now we define the inverse Green's function $(\mathbf{G}_{\mathbf{q}}^{x/y})^{-1} \equiv -\frac{\beta N_c}{2} \mathbf{M}_{\mathbf{q}}^{x/y}$ and add source terms to the Hamiltonian by introducing the external fields $h_{\mathbf{q}}^{x/ya}$, such that

$$\begin{aligned} -\beta H[h, h^*] = \sum_{\mathbf{q}} \big[&(\boldsymbol{\epsilon}_{\mathbf{q}}^{x})^* \cdot (\mathbf{G}_{\mathbf{q}}^{x})^{-1} \cdot \boldsymbol{\epsilon}_{\mathbf{q}}^{x} + (\boldsymbol{\epsilon}_{\mathbf{q}}^{y})^* \cdot (\mathbf{G}_{\mathbf{q}}^{y})^{-1} \cdot \boldsymbol{\epsilon}_{\mathbf{q}}^{y} + (\boldsymbol{\epsilon}_{\mathbf{q}}^{x})^* \cdot \mathbf{h}_{\mathbf{q}}^{x} + (\mathbf{h}_{\mathbf{q}}^{x})^* \cdot \boldsymbol{\epsilon}_{\mathbf{q}}^{x} \\ &+ (\boldsymbol{\epsilon}_{\mathbf{q}}^{y})^* \cdot \mathbf{h}_{\mathbf{q}}^{y} + (\mathbf{h}_{\mathbf{q}}^{y})^* \cdot \boldsymbol{\epsilon}_{\mathbf{q}}^{y} \big]. \end{aligned} \tag{A.13}$$

As was shown in the previous section and discussed in the main text, the partition function

$$Z[h, h^*] = \int \mathcal{D}\epsilon \, e^{-\beta H[h, h^*]} \tag{A.14}$$

can now be evaluated as

$$Z[h, h^*] = \mathcal{N} \exp\left[- \sum_{\mathbf{q}} \left((\mathbf{h}_{\mathbf{q}}^{x})^* \cdot \mathbf{G}_{\mathbf{q}}^{x} \cdot \mathbf{h}_{\mathbf{q}}^{x} + (\mathbf{h}_{\mathbf{q}}^{y})^* \cdot \mathbf{G}_{\mathbf{q}}^{y} \cdot \mathbf{h}_{\mathbf{q}}^{y} \right) \right] \equiv \mathcal{N} e^{\Delta} \tag{A.15}$$

by means of standard Gaussian integration. From Eqs. (A.13) and (A.14), it is clear that

$$\left\langle \epsilon_{\mathbf{q}_1}^{x/ya_1} (\epsilon_{\mathbf{q}_2}^{x/ya_2})^* \dots \epsilon_{\mathbf{q}_{n-1}}^{x/ya_{n-1}} (\epsilon_{\mathbf{q}_n}^{x/ya_n})^* \right\rangle = \frac{1}{Z} \frac{\partial^n Z}{\partial (h_{\mathbf{q}_1}^{x/ya_1})^* \partial h_{\mathbf{q}_2}^{x/ya_2} \dots \partial (h_{\mathbf{q}_{n-1}}^{x/ya_{n-1}})^* \partial h_{\mathbf{q}_n}^{x/ya_n}} \bigg|_{h=0}, \tag{A.16}$$

where n is an even number. However, the right-hand side of Eq. (A.16) can also be evaluated using Eq. (A.15) and noting that

$$\left\langle \epsilon_{\mathbf{q}}^{x/ya} (\epsilon_{\mathbf{q}'}^{x/yb})^* \right\rangle = -\delta_{\mathbf{q},\mathbf{q}'} \left(\mathbf{G}_{\mathbf{q}}^{x/y} \right)^{ab} \equiv -\delta_{\mathbf{q},\mathbf{q}'} G_{\mathbf{q}}^{x/yab}. \tag{A.17}$$

Looking closely at the above equations, we see that the expectation value from the left-hand side of Eq. (A.16) must indeed consist of products of expectation values of two epsilons.

While it is tedious to derive the exact expressions for the expectation values of products of many epsilons, we will now work out the expectation value of a quartic term as an example:

$$\begin{aligned} \left\langle \epsilon_{\mathbf{q}_1}^{xa} (\epsilon_{\mathbf{q}_2}^{xb})^* \epsilon_{\mathbf{q}_3}^{xc} (\epsilon_{\mathbf{q}_4}^{xd})^* \right\rangle &= \frac{1}{Z} \frac{\partial^4 Z}{\partial (h_{\mathbf{q}_1}^{xa})^* \partial h_{\mathbf{q}_2}^{xb} \partial (h_{\mathbf{q}_3}^{xc})^* \partial h_{\mathbf{q}_4}^{xd}} \bigg|_{h=0} \\ &= \frac{\partial^4 e^{\Delta}}{\partial (h_{\mathbf{q}_1}^{xa})^* \partial h_{\mathbf{q}_2}^{xb} \partial (h_{\mathbf{q}_3}^{xc})^* \partial h_{\mathbf{q}_4}^{xd}} \bigg|_{h=0} \\ &= \frac{\partial^3}{\partial (h_{\mathbf{q}_1}^{xa})^* \partial h_{\mathbf{q}_2}^{xb} \partial (h_{\mathbf{q}_3}^{xc})^*} \left(\left[- \sum_{\alpha} (h_{\mathbf{q}_4}^{x\alpha})^* G_{\mathbf{q}_4}^{x\alpha d} \right] e^{\Delta} \right) \bigg|_{h=0} \\ &= \frac{\partial^2}{\partial (h_{\mathbf{q}_1}^{xa})^* \partial h_{\mathbf{q}_2}^{xb}} \left(\left[-\delta_{\mathbf{q}_3,\mathbf{q}_4} G_{\mathbf{q}_4}^{xcd} + \sum_{\alpha\beta} (h_{\mathbf{q}_4}^{x\alpha})^* G_{\mathbf{q}_4}^{x\alpha d} G_{\mathbf{q}_3}^{xc\beta} h_{\mathbf{q}_3}^{x\beta} \right] e^{\Delta} \right) \bigg|_{h=0}. \end{aligned} \tag{A.18}$$

For the final two derivatives, we use the fact that we set h to zero at the end. As a result, we can simply discard everything that would leave terms containing h. In this particular case, we can ignore the e^{Δ}

part of the second term when taking the final two derivatives, as both derivatives are required to get rid of the existing two h-fields. Continuing the derivation, we find

$$\begin{aligned}\left\langle \epsilon^{xa}_{\mathbf{q}_1}(\epsilon^{xb}_{\mathbf{q}_2})^* \epsilon^{xc}_{\mathbf{q}_3}(\epsilon^{xd}_{\mathbf{q}_4})^* \right\rangle &= \frac{\partial}{\partial (h^{xa}_{\mathbf{q}_1})^*} \left(\left[\sum_\alpha (h^{x\alpha}_{\mathbf{q}_2})^* G^{x\alpha b}_{\mathbf{q}_2} G^{xcd}_{\mathbf{q}_4} \delta_{\mathbf{q}_3,\mathbf{q}_4} + \sum_\alpha (h^{x\alpha}_{\mathbf{q}_4})^* G^{x\alpha d}_{\mathbf{q}_4} G^{xcb}_{\mathbf{q}_3} \delta_{\mathbf{q}_2,\mathbf{q}_3} + \mathcal{O}(h^3) \right] e^{\Delta} \right) \Bigg|_{h=0} \\ &= \left(G^{xab}_{\mathbf{q}_2} G^{xcd}_{\mathbf{q}_4} \delta_{\mathbf{q}_1,\mathbf{q}_2} \delta_{\mathbf{q}_3,\mathbf{q}_4} + G^{xad}_{\mathbf{q}_4} G^{xcb}_{\mathbf{q}_3} \delta_{\mathbf{q}_1,\mathbf{q}_4} \delta_{\mathbf{q}_2,\mathbf{q}_3} + \mathcal{O}(h^2) \right) e^{\Delta} \Big|_{h=0} \\ &= G^{xab}_{\mathbf{q}_2} G^{xcd}_{\mathbf{q}_4} \delta_{\mathbf{q}_1,\mathbf{q}_2} \delta_{\mathbf{q}_3,\mathbf{q}_4} + G^{xad}_{\mathbf{q}_4} G^{xcb}_{\mathbf{q}_3} \delta_{\mathbf{q}_1,\mathbf{q}_4} \delta_{\mathbf{q}_2,\mathbf{q}_3} \\ &= \left\langle \epsilon^{xa}_{\mathbf{q}_1}(\epsilon^{xb}_{\mathbf{q}_2})^* \right\rangle \left\langle \epsilon^{xc}_{\mathbf{q}_3}(\epsilon^{xd}_{\mathbf{q}_4})^* \right\rangle + \left\langle \epsilon^{xa}_{\mathbf{q}_1}(\epsilon^{xd}_{\mathbf{q}_4})^* \right\rangle \left\langle \epsilon^{xc}_{\mathbf{q}_3}(\epsilon^{xb}_{\mathbf{q}_2})^* \right\rangle, \end{aligned} \tag{A.19}$$

which confirms the validity of Wick's theorem for this example.

A.5 Perturbation theory and Feynman diagrams

In the following, we will see explicitly how two-point functions can be calculated perturbatively for a Hamiltonian of the form $H = H_0 + gH_I$, where H_0 is the non-interacting ("bare") Hamiltonian, g is a dimensionless coupling constant, and H_I contains the interaction energy. As a practical example, we will consider the Hamiltonian

$$H_0 = \frac{N_c}{2} \sum_{\mathbf{q}} \sum_{ab} \left((\epsilon^{xa}_{\mathbf{q}})^* M^{xab}_{\mathbf{q}} \epsilon^{xb}_{\mathbf{q}} + (\epsilon^{ya}_{\mathbf{q}})^* M^{yab}_{\mathbf{q}} \epsilon^{yb}_{\mathbf{q}} \right), \tag{A.20}$$

$$\begin{aligned} H_I = \frac{N_c}{8} \sum_{\mathbf{q}_1,\mathbf{q}_2,\mathbf{q}_3} \sum_{ab} \Big(&(\epsilon^{xa}_{\mathbf{q}_1+\mathbf{q}_3})^* \epsilon^{xa}_{\mathbf{q}_1} M^{xab}_{\mathbf{q}_3} (\epsilon^{xb}_{\mathbf{q}_2-\mathbf{q}_3})^* \epsilon^{xb}_{\mathbf{q}_2} + (\epsilon^{ya}_{\mathbf{q}_1+\mathbf{q}_3})^* \epsilon^{ya}_{\mathbf{q}_1} M^{xab}_{\mathbf{q}_3} (\epsilon^{yb}_{\mathbf{q}_2-\mathbf{q}_3})^* \epsilon^{yb}_{\mathbf{q}_2} \\ &+ (\epsilon^{xa}_{\mathbf{q}_1+\mathbf{q}_3})^* \epsilon^{xa}_{\mathbf{q}_1} M^{xab}_{\mathbf{q}_3} (\epsilon^{yb}_{\mathbf{q}_2-\mathbf{q}_3})^* \epsilon^{yb}_{\mathbf{q}_2} + (\epsilon^{ya}_{\mathbf{q}_1+\mathbf{q}_3})^* \epsilon^{ya}_{\mathbf{q}_1} M^{xab}_{\mathbf{q}_3} (\epsilon^{xb}_{\mathbf{q}_2-\mathbf{q}_3})^* \epsilon^{xb}_{\mathbf{q}_2} \Big), \end{aligned} \tag{A.21}$$

and calculate the two-point functions up to first order in g.

We will consider the following two-point functions:

$$\left\langle \epsilon^{x/ya}_{\mathbf{q}} (\epsilon^{x/yb}_{\mathbf{q}})^* \right\rangle = \frac{\int \mathcal{D}\epsilon \, \epsilon^{x/ya}_{\mathbf{q}} (\epsilon^{x/yb}_{\mathbf{q}})^* e^{-\beta H}}{\int \mathcal{D}\epsilon \, e^{-\beta H}}. \tag{A.22}$$

Assuming that the interaction term gH_I is small, the exponents can be approximated as

$$e^{-\beta H} = e^{-\beta H_0} (1 - \beta g H_I) + \mathcal{O}(g^2), \tag{A.23}$$

such that the two-point functions become

$$\begin{aligned} \left\langle \epsilon^{x/ya}_{\mathbf{q}} (\epsilon^{x/yb}_{\mathbf{q}})^* \right\rangle &= \frac{\int \mathcal{D}\epsilon \, \epsilon^{x/ya}_{\mathbf{q}} (\epsilon^{x/yb}_{\mathbf{q}})^* \, (1 - \beta g H_I) \, e^{-\beta H_0}}{\int \mathcal{D}\epsilon \, (1 - \beta g H_I) \, e^{-\beta H_0}} + \mathcal{O}(g^2) \\ &= \frac{\left\langle \epsilon^{x/ya}_{\mathbf{q}} (\epsilon^{x/yb}_{\mathbf{q}})^* \right\rangle_0 - \beta g \left\langle \epsilon^{x/ya}_{\mathbf{q}} (\epsilon^{x/yb}_{\mathbf{q}})^* H_I \right\rangle_0}{1 - \beta g \left\langle H_I \right\rangle_0} + \mathcal{O}(g^2) \\ &= \left\langle \epsilon^{x/ya}_{\mathbf{q}} (\epsilon^{x/yb}_{\mathbf{q}})^* \right\rangle_0 - \beta g \left(\left\langle \epsilon^{x/ya}_{\mathbf{q}} (\epsilon^{x/yb}_{\mathbf{q}})^* H_I \right\rangle_0 - \left\langle \epsilon^{x/ya}_{\mathbf{q}} (\epsilon^{x/yb}_{\mathbf{q}})^* \right\rangle_0 \left\langle H_I \right\rangle_0 \right) + \mathcal{O}(g^2), \end{aligned} \tag{A.24}$$

where $\langle \ldots \rangle_0$ denotes an expectation value according to the bare Hamiltonian H_0. Noting that H_0 is

quadratic, we can calculate the bare expectation values by carefully applying Wick's theorem:

$$\begin{aligned}
&\left\langle \epsilon_{\mathbf{q}}^{x/ya}(\epsilon_{\mathbf{q}}^{x/yb})^* H_I \right\rangle_0 - \left\langle \epsilon_{\mathbf{q}}^{x/ya}(\epsilon_{\mathbf{q}}^{x/yb})^* \right\rangle_0 \langle H_I \rangle_0 \\
&\quad = \frac{N_c}{8} \sum_{\mathbf{q}_1,\mathbf{q}_2,\mathbf{q}_3} \sum_{cd} M_{\mathbf{q}_3}^{xcd} \Big(\left\langle \epsilon_{\mathbf{q}}^{x/ya}(\epsilon_{\mathbf{q}_1+\mathbf{q}_3}^{x/yc})^* \right\rangle_0 \left\langle \epsilon_{\mathbf{q}_1}^{x/yc}(\epsilon_{\mathbf{q}}^{x/yb})^* \right\rangle_0 \left\langle \epsilon_{\mathbf{q}_2}^{x/yd}(\epsilon_{\mathbf{q}_2-\mathbf{q}_3}^{x/yd})^* \right\rangle_0 \\
&\qquad\qquad + \left\langle \epsilon_{\mathbf{q}}^{x/ya}(\epsilon_{\mathbf{q}_1+\mathbf{q}_3}^{x/yc})^* \right\rangle_0 \left\langle \epsilon_{\mathbf{q}_1}^{x/yc}(\epsilon_{\mathbf{q}_2-\mathbf{q}_3}^{x/yd})^* \right\rangle_0 \left\langle \epsilon_{\mathbf{q}_2}^{x/yd}(\epsilon_{\mathbf{q}}^{x/yb})^* \right\rangle_0 \\
&\qquad\qquad + \left\langle \epsilon_{\mathbf{q}}^{x/ya}(\epsilon_{\mathbf{q}_2-\mathbf{q}_3}^{x/yd})^* \right\rangle_0 \left\langle \epsilon_{\mathbf{q}_1}^{x/yc}(\epsilon_{\mathbf{q}}^{x/yb})^* \right\rangle_0 \left\langle \epsilon_{\mathbf{q}_2}^{x/yd}(\epsilon_{\mathbf{q}_1+\mathbf{q}_3}^{x/yc})^* \right\rangle_0 \\
&\qquad\qquad + \left\langle \epsilon_{\mathbf{q}}^{x/ya}(\epsilon_{\mathbf{q}_2-\mathbf{q}_3}^{x/yd})^* \right\rangle_0 \left\langle \epsilon_{\mathbf{q}_1}^{x/yc}(\epsilon_{\mathbf{q}_1+\mathbf{q}_3}^{x/yc})^* \right\rangle_0 \left\langle \epsilon_{\mathbf{q}_2}^{x/yd}(\epsilon_{\mathbf{q}}^{x/yb})^* \right\rangle_0 \\
&\qquad\qquad + \left\langle \epsilon_{\mathbf{q}}^{x/ya}(\epsilon_{\mathbf{q}_1+\mathbf{q}_3}^{x/yc})^* \right\rangle_0 \left\langle \epsilon_{\mathbf{q}_1}^{x/yc}(\epsilon_{\mathbf{q}}^{x/yb})^* \right\rangle_0 \left\langle \epsilon_{\mathbf{q}_2}^{y/xd}(\epsilon_{\mathbf{q}_2-\mathbf{q}_3}^{y/xd})^* \right\rangle_0 \\
&\qquad\qquad + \left\langle \epsilon_{\mathbf{q}}^{x/ya}(\epsilon_{\mathbf{q}_2-\mathbf{q}_3}^{x/yd})^* \right\rangle_0 \left\langle \epsilon_{\mathbf{q}_1}^{y/xc}(\epsilon_{\mathbf{q}_1+\mathbf{q}_3}^{y/xc})^* \right\rangle_0 \left\langle \epsilon_{\mathbf{q}_2}^{x/yd}(\epsilon_{\mathbf{q}}^{x/yb})^* \right\rangle_0 \Big) \\
&\quad = -\frac{N_c}{8} \sum_{\mathbf{q}_1,\mathbf{q}_2,\mathbf{q}_3} \sum_{cd} M_{\mathbf{q}_3}^{xcd} \Big(G_{\mathbf{q}}^{x/yac} G_{\mathbf{q}}^{x/ycb} G_{\mathbf{q}_2}^{x/ydd} \delta_{\mathbf{q},\mathbf{q}_1} \delta_{\mathbf{q}_3,0} + G_{\mathbf{q}}^{x/yac} G_{\mathbf{q}_1}^{x/ycd} G_{\mathbf{q}}^{x/ydb} \delta_{\mathbf{q},\mathbf{q}_2} \delta_{\mathbf{q}_3,\mathbf{q}_2-\mathbf{q}_1} \\
&\qquad\qquad + G_{\mathbf{q}}^{x/yad} G_{\mathbf{q}}^{x/ycb} G_{\mathbf{q}_2}^{x/ydc} \delta_{\mathbf{q},\mathbf{q}_1} \delta_{\mathbf{q}_3,\mathbf{q}_2-\mathbf{q}_1} + G_{\mathbf{q}}^{x/yad} G_{\mathbf{q}_1}^{x/ycc} G_{\mathbf{q}}^{x/ydb} \delta_{\mathbf{q},\mathbf{q}_2} \delta_{\mathbf{q}_3,0} \\
&\qquad\qquad + G_{\mathbf{q}}^{x/yac} G_{\mathbf{q}}^{x/ycb} G_{\mathbf{q}_2}^{y/xdd} \delta_{\mathbf{q},\mathbf{q}_1} \delta_{\mathbf{q}_3,0} + G_{\mathbf{q}}^{x/yad} G_{\mathbf{q}_1}^{y/xcc} G_{\mathbf{q}}^{x/ydb} \delta_{\mathbf{q},\mathbf{q}_2} \delta_{\mathbf{q}_3,0} \Big) \\
&\quad = -\frac{N_c}{8} \sum_{\mathbf{q}'} \sum_{cd} \Big[M_0^{xcd} \Big(G_{\mathbf{q}}^{x/yac} G_{\mathbf{q}}^{x/ycb} G_{\mathbf{q}'}^{x/ydd} + G_{\mathbf{q}}^{x/yad} G_{\mathbf{q}'}^{x/ycc} G_{\mathbf{q}}^{x/ydb} + G_{\mathbf{q}}^{x/yac} G_{\mathbf{q}}^{x/ycb} G_{\mathbf{q}'}^{y/xdd} \\
&\qquad\qquad + G_{\mathbf{q}}^{x/yad} G_{\mathbf{q}'}^{y/xcc} G_{\mathbf{q}}^{x/ydb} \Big) + M_{\mathbf{q}-\mathbf{q}'}^{xcd} \Big(G_{\mathbf{q}}^{x/yac} G_{\mathbf{q}'}^{x/ycd} G_{\mathbf{q}}^{x/ydb} + G_{\mathbf{q}}^{x/yac} G_{\mathbf{q}}^{x/ydb} G_{\mathbf{q}'}^{x/ycd} \Big) \Big] .
\end{aligned} \tag{A.25}$$

Note that if one chooses to look at the x from x/y, then y/x should be interpreted as y (and the other way around). Additionally, for the final term of Eq. (A.25) we used the fact that $\mathbf{M}_{\mathbf{q}}^x$ is Hermitian, combined with the reality condition $(\mathbf{M}_{\mathbf{q}}^x)^* = \mathbf{M}_{-\mathbf{q}}^x$. We can now immediately see that the final two terms are the same. The properties of $\mathbf{M}_{\mathbf{q}}^x$ also lead to $\mathbf{M}_0^x$ being symmetric, from which we conclude that first two terms are the same, as well as the third and the fourth terms. Hence, we find

$$\begin{aligned}
&\left\langle \epsilon_{\mathbf{q}}^{x/ya}(\epsilon_{\mathbf{q}}^{x/yb})^* H_I \right\rangle_0 - \left\langle \epsilon_{\mathbf{q}}^{x/ya}(\epsilon_{\mathbf{q}}^{x/yb})^* \right\rangle_0 \langle H_I \rangle_0 \\
&\quad = -\frac{N_c}{4} \sum_{\mathbf{q}'} \sum_{cd} \Big[M_0^{xcd} \Big(G_{\mathbf{q}}^{x/yac} G_{\mathbf{q}}^{x/ycb} G_{\mathbf{q}'}^{x/ydd} + G_{\mathbf{q}}^{x/yac} G_{\mathbf{q}}^{x/ycb} G_{\mathbf{q}'}^{y/xdd} \Big) + M_{\mathbf{q}-\mathbf{q}'}^{xcd} G_{\mathbf{q}}^{x/yac} G_{\mathbf{q}'}^{x/ycd} G_{\mathbf{q}}^{x/ydb} \Big] .
\end{aligned} \tag{A.26}$$

Plugging this back in, the two-point function becomes

$$\begin{aligned}
\left\langle \epsilon_{\mathbf{q}}^{x/ya}(\epsilon_{\mathbf{q}}^{x/yb})^* \right\rangle = -G_{\mathbf{q}}^{x/yab} + \frac{gN_c}{4k_BT} \sum_{\mathbf{q}'} \sum_{cd} \Big[M_0^{xcd} \Big(G_{\mathbf{q}}^{x/yac} G_{\mathbf{q}}^{x/ycb} G_{\mathbf{q}'}^{x/ydd} + G_{\mathbf{q}}^{x/yac} G_{\mathbf{q}}^{x/ycb} G_{\mathbf{q}'}^{y/xdd} \Big) \\
+ M_{\mathbf{q}-\mathbf{q}'}^{xcd} G_{\mathbf{q}}^{x/yac} G_{\mathbf{q}'}^{x/ycd} G_{\mathbf{q}}^{x/ydb} \Big] + \mathcal{O}(g^2).
\end{aligned} \tag{A.27}$$

To make everything a bit more compact, we can introduce Feynman diagrams. We define the components of the diagrams according to Table 4.1. In addition to these definitions, we sum over all indices belonging to vertices and over all momenta that go around a loop, absorbing all prefactors into the latter. This results in the following expression:

$\left\langle \epsilon_{\mathbf{q}}^{xa}(\epsilon_{\mathbf{q}}^{xb})^* \right\rangle =$ 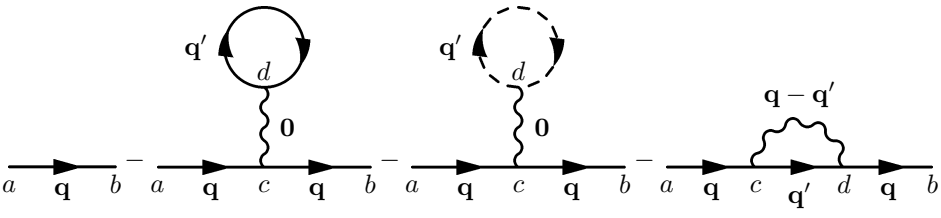

(A.28)

The same expression also holds for the expectation value $\left\langle \epsilon_{\mathbf{q}}^{ya}(\epsilon_{\mathbf{q}}^{yb})^* \right\rangle$, but with the solid and dashed lines interchanged:

$\left\langle \epsilon_{\mathbf{q}}^{xa}(\epsilon_{\mathbf{q}}^{xb})^* \right\rangle =$ 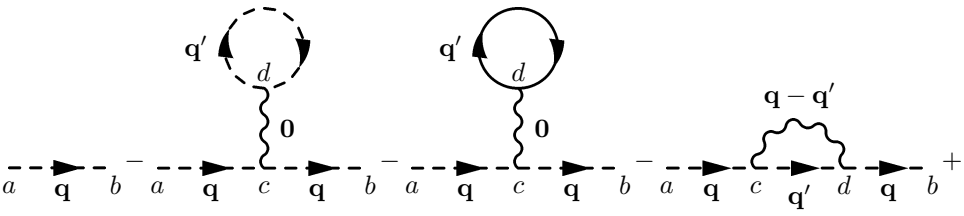

$+ \mathcal{O}(g^2).$ (A.29)

Contracting all of the potentials (i.e. the matrices $M_{\mathbf{q}}^{xab}$) to a single point, we see that all first order terms are indeed of the form

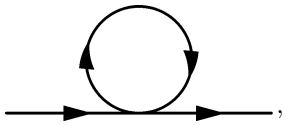 , (A.30)

in accordance with the usual Feynman rules of ϕ^4 theory.

B.1 Tight-binding band structure of graphene

In Ch. 5, we discussed tight-binding models and how they can be used to find the dispersion relation and overall band structure of a material. In this section, we will use these methods to derive the famous dispersion relation of graphene as an example.

The underlying lattice of graphene is the honeycomb lattice, see Fig. B.1. As can be seen in the figure, there are two distinct types of lattice sites, both with different nearest neighbours, and a unit cell consists of one lattice site of each type. Choosing our basis, the vectors between the nearest neighbours are given by

$$\boldsymbol{\delta}_1 = a\begin{pmatrix}0\\1\end{pmatrix}, \qquad \boldsymbol{\delta}_2 = \frac{a}{2}\begin{pmatrix}-\sqrt{3}\\-1\end{pmatrix}, \qquad \boldsymbol{\delta}_3 = \frac{a}{2}\begin{pmatrix}\sqrt{3}\\-1\end{pmatrix}, \tag{B.1}$$

where a is the lattice constant. The lattice vectors are then given by

$$\mathbf{a}_1 = a\begin{pmatrix}\sqrt{3}\\0\end{pmatrix} = \boldsymbol{\delta}_3 - \boldsymbol{\delta}_2, \qquad \mathbf{a}_2 = \frac{a}{2}\begin{pmatrix}\sqrt{3}\\3\end{pmatrix} = \boldsymbol{\delta}_1 - \boldsymbol{\delta}_2. \tag{B.2}$$

Since there are two distinct types of lattice sites, we assign them different creation and annihilation operators: $a^\dagger$ and a for one type, $b^\dagger$ and b for the other. The Hamiltonian of our tight-binding model is now given by

$$H = -t\sum_{\sigma,\langle i,j\rangle}\left[a^\dagger_{\sigma i}b_{\sigma j} + h.c.\right]. \tag{B.3}$$

Here, t is the hopping parameter, $\sigma \in \{\uparrow,\downarrow\}$ is the spin, and $\langle i,j\rangle$ once again denotes the sum over all nearest neighbour pairs. Setting the number of unit cells to be N and taking the Fourier transform according to Eq. (5.4), we immediately find that the Hamiltonian can also be written as

$$\begin{aligned} H &= -t\sum_{\sigma,\mathbf{k}}\left[a^\dagger_{\sigma\mathbf{k}}b_{\sigma,\mathbf{k}}\left(e^{i\mathbf{k}\cdot\boldsymbol{\delta}_1} + e^{i\mathbf{k}\cdot\boldsymbol{\delta}_2} + e^{i\mathbf{k}\cdot\boldsymbol{\delta}_3}\right) + h.c.\right] \\ &= \sum_{\sigma,\mathbf{k}}\begin{pmatrix}a^\dagger_{\sigma\mathbf{k}} & b^\dagger_{\sigma\mathbf{k}}\end{pmatrix}\begin{pmatrix}0 & \Delta_{\mathbf{k}}\\ \Delta^*_{\mathbf{k}} & 0\end{pmatrix}\begin{pmatrix}a_{\sigma\mathbf{k}}\\ b_{\sigma\mathbf{k}}\end{pmatrix}, \end{aligned} \tag{B.4}$$

with

$$\begin{aligned} \Delta_{\mathbf{k}} &\equiv -t\left(e^{i\mathbf{k}\cdot\boldsymbol{\delta}_1} + e^{i\mathbf{k}\cdot\boldsymbol{\delta}_2} + e^{i\mathbf{k}\cdot\boldsymbol{\delta}_3}\right) \\ &= -t\left(e^{iak_y} + e^{-ia(k_y+\sqrt{3}k_x)/2} + e^{-ia(k_y-\sqrt{3}k_x)/2}\right) \\ &= -t\,e^{-iak_y/2}\left(2\cos(\sqrt{3}ak_x/2) + e^{3iak_y/2}\right). \end{aligned} \tag{B.5}$$

The dispersion relation is again given by the eigenvalues of the Hamiltonian. Using the above equations, we find

$$\begin{aligned} \omega = \pm|\Delta_{\mathbf{k}}| &= \pm t\sqrt{4\cos^2(\sqrt{3}ak_x/2) + 4\cos(\sqrt{3}ak_x/2)\cos(3ak_y/2) + 1} \\ &= \pm t\sqrt{3 + 2\cos(\sqrt{3}ak_x) + 4\cos(\sqrt{3}ak_x/2)\cos(3ak_y/2)}. \end{aligned} \tag{B.6}$$

The above dispersion relation gives rise to two different energy bands: one corresponding to the $+$ solution, and one corresponding to the $-$ solution. The resulting bands are shown in Figs. B.2 and B.3. As can be seen from these figures, it turns out that something interesting happens in this model: the two bands touch at the several different points where $\Delta_{\mathbf{k}} = 0$. It is straightforward to see that this happens when the exponent inside the brackets of Eq. (B.5) is equal to ± 1 and the cosine is equal to $\mp 1/2$ (depending on the value of ak_y). We thus find that the bands touch when $ak_y = \pm 2\pi/3$ and $ak_x = \pm 2\pi/3\sqrt{3}$ simultaneously, or alternatively when $ak_y = 0$ and $ak_x = \pm 4\pi/3\sqrt{3}$. These six points are called the *Dirac points*. As we will see below, there are two different types of Dirac points, located at the points K and K′ of the first Brillouin zone. We will now expand the Hamiltonian close to the Dirac points to see what happens in these regions.

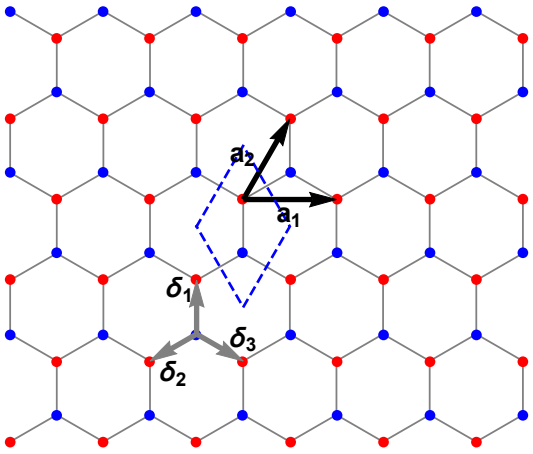

Figure B.1: Schematic view of the honeycomb lattice. There are two different types of lattice sites, denoted by the red and the blue dots. A unit cell (indicated by a blue dashed line) consists of two lattice sites, one of each type. The vectors $\boldsymbol{\delta}_i$ are the vectors between nearest neighbours, while the vectors $\mathbf{a}_i$ are the lattice vectors.

Since $\Delta_\mathbf{k}$ is zero at the Dirac points, its lowest order expansion is given by

$$\Delta_\mathbf{k} = \nabla_\mathbf{k}\Delta_\mathbf{k}\Big|_{\mathbf{k}=\mathbf{k}_0} \cdot (\mathbf{k}-\mathbf{k}_0) + \mathcal{O}((k-k_0)^2), \tag{B.7}$$

where $\mathbf{k}_0$ denotes the wave vector corresponding to a Dirac point. Let us calculate the gradient of $\Delta_\mathbf{k}$:

$$\nabla_\mathbf{k}\Delta_\mathbf{k} = at\, e^{-iak_y/2} \begin{pmatrix} \sqrt{3}\sin(\sqrt{3}ak_x/2) \\ i\cos(\sqrt{3}ak_x/2) - i\, e^{3iak_y/2} \end{pmatrix} \tag{B.8}$$

$$\Rightarrow \nabla_\mathbf{k}\Delta_\mathbf{k}\Big|_{\mathbf{k}=\mathbf{k}_0} = C\frac{3at}{2}\begin{pmatrix} 1 \\ \pm i \end{pmatrix}. \tag{B.9}$$

The $\pm$ that appears in the final line depends on the type of the Dirac point we are looking at (i.e. a K point or a K′ point). Moreover, the constant $C = \pm e^{-iak_{0,y}/2}$ that appears in the final line is a complex number with absolute value 1. Since only the absolute value of $\Delta_\mathbf{k}$ appears in the eigenvalues of the Hamiltonian, this overall constant will not influence any physical quantities, and we can therefore set it to one without losing any information. Redefining $\mathbf{k}$ to be the wave vector with respect to a Dirac point,

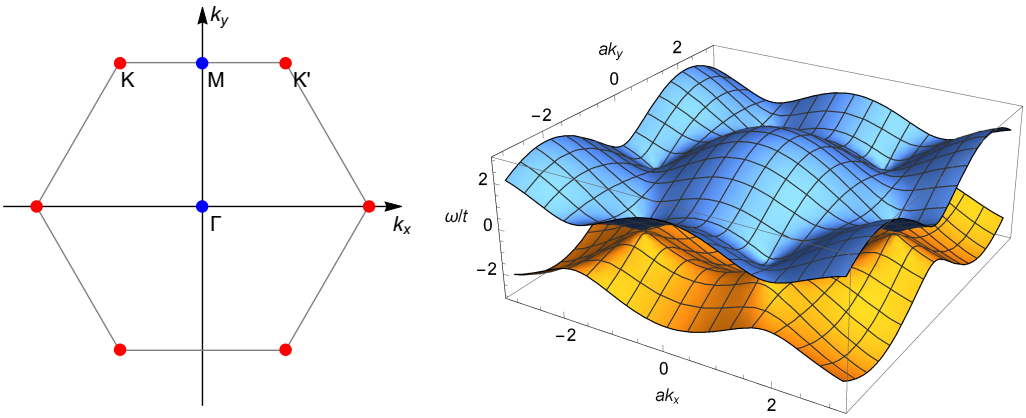

Figure B.2: Left: first Brillouin zone of graphene and the definition of the points Γ, M, K and K′. It is "rotated" by 90 degrees with respect to the underlying lattice. Right: band structure of the model. Note the existence of six points where the bands touch. These Dirac points are denoted by red dots in the left panel.

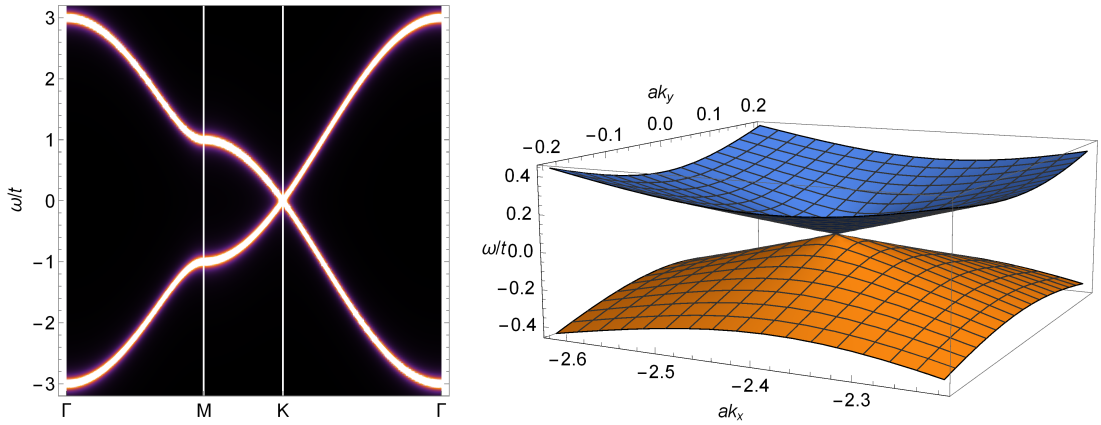

Figure B.3: Left: spectral-weight function of graphene along a path through symmetry points of the first Brillouin zone, showing the band structure. Right: dispersion close to one of the Dirac points (i.e. the K and K′ points of the first Brillouin zone), also known as a Dirac cone.

rather than to the origin in momentum space, we find

$$\Delta_{\mathbf{k}} = \frac{3at}{2}\left(k_x \pm ik_y\right) + \mathcal{O}(k^2), \tag{B.10}$$

where the $\pm$ once again corresponds to the type of the Dirac point. Returning to the Hamiltonian of Eq. (B.4), we find that its matrix is given by

$$\begin{aligned}\mathcal{H}_{\mathbf{k}} &= \begin{pmatrix} 0 & \Delta_{\mathbf{k}} \\ \Delta_{\mathbf{k}}^* & 0 \end{pmatrix} \\ &\approx \frac{3at}{2}\begin{pmatrix} 0 & k_x \pm ik_y \\ k_x \mp ik_y & 0 \end{pmatrix} \\ &= v_F\left(\sigma_1 k_x \mp \sigma_2 k_y\right). \end{aligned} \tag{B.11}$$

Here, $v_F \equiv 3at/2$ is the Fermi velocity (up to a factor $\hbar$, which we set to one), and σ_i are Pauli matrices. As the $\mp$ that appears here does not influence any physical quantities either, we can finally write the Hamiltonian as

$$\mathcal{H}_{\mathbf{k}} = v_F \boldsymbol{\sigma} \cdot \mathbf{k} \tag{B.12}$$

in the vicinity of a Dirac point. From here, it immediately follows that

$$\omega = \pm v_F |\mathbf{k}| \tag{B.13}$$

in the regions of interest. Even though the above model has a spinor structure and even contains Pauli matrices, it should be noted that the spinor components have nothing to do with the actual spin. Instead, they correspond to the two different sublattices (denoted by the red and blue dots in Fig. B.1).

We thus find that the dispersion relation is linear close to the Dirac points. This is quite different from materials such as semiconductors, where the dispersion relation is often quadratic, and it leads to different properties. Physically, this linear dispersion means that the relevant electron and hole quasiparticles behave like massless particles. However, the speed of light in the usual dispersion relation of massless particles has now been replaced by the Fermi velocity v_F. This can also be seen from the observation that Eq. (B.12) is equivalent to the massless Dirac Hamiltonian, which confirms that we are indeed looking at relativistic massless Dirac fermions. The above tight-binding description of graphene is therefore an example of a so-called Dirac semimetal.

Although the low-energy Hamiltonian of Eq. (B.12) is only an approximation of the more general Hamiltonian in the vicinity of the Dirac points, it is still very successful in describing the physics in these regions. This fact is illustrated in Ch. 5 and applied in Ch. 6, where the full Hamiltonian is unknown and the approximate small-$\mathbf{k}$ model has to suffice.

B.2 Efficient iterative methods for the numerical calculation of surface Green's functions

In Ch. 6, we have numerically calculated the surface Green's functions corresponding to systems with a large number of layers. These surface Green's functions are the 4×4 top-left corner of corresponding the bulk Green's functions. Naively, we could therefore calculate a surface Green's function by simply calculating the entire bulk Green's function and then extracting some of the components. However, this method is increasingly inefficient for large numbers of layers, as we would have to calculate the entire inverse of a very large matrix, while only being interested in some of the components. Rather than using this inefficient method, we have therefore used much more efficient iterative methods in order to calculate the surface Green's functions. In this section, we will cover the iterative methods used in the main text. The original derivation of these methods can be found in Ref. [25].

Before turning our attention to the methods themselves, we first introduce the notation we will use in order to avoid confusion. The bulk retarded Green's function corresponding to a system with N_z layers,

$$G^+(\mathbf{k}_{||}, \omega) = \lim_{\delta \to 0^+} \left((\omega + i\delta)\mathbb{I}_{4N_z} - \mathcal{H}_{\mathbf{k}_{||}} \right)^{-1}, \tag{B.14}$$

will simply be denoted by G^{N_z}, such that it can be written as

$$G^{N_z} = \begin{pmatrix} G_{00}^{N_z} & G_{01}^{N_z} & \cdots \\ G_{10}^{N_z} & G_{11}^{N_z} & \cdots \\ \vdots & \vdots & \ddots \end{pmatrix}. \tag{B.15}$$

Here, $G_{ij}^{N_z}$ (with $i, j \in \{0, 1, \ldots, N_z - 1\}$) are 4×4 matrices, and $G_{00}^{N_z}$ is the surface Green's function corresponding to a system with N_z layers.

In order to find the components $G_{00}^{N_z}$ of the bulk Green's function, we consider the inverse of a block matrix of the form

$$\mathbf{M} = \begin{pmatrix} \mathbf{A}_{n\times n} & \mathbf{B}_{n\times m} \\ \mathbf{C}_{m\times n} & \mathbf{D}_{m\times m} \end{pmatrix}, \qquad \mathbf{M}^{-1} \equiv \begin{pmatrix} \mathbf{U}_{n\times n} & \mathbf{V}_{n\times m} \\ \mathbf{W}_{m\times n} & \mathbf{X}_{m\times m} \end{pmatrix}. \tag{B.16}$$

From the definition of the matrix inverse, we find the equations

$$\mathbf{A}_{n\times n} \cdot \mathbf{U}_{n\times n} + \mathbf{B}_{n\times m} \cdot \mathbf{W}_{m\times n} = \mathbb{I}_n, \tag{B.17}$$
$$\mathbf{A}_{n\times n} \cdot \mathbf{V}_{n\times m} + \mathbf{B}_{n\times m} \cdot \mathbf{X}_{m\times m} = 0_{n\times m}, \tag{B.18}$$
$$\mathbf{C}_{m\times n} \cdot \mathbf{U}_{n\times n} + \mathbf{D}_{m\times m} \cdot \mathbf{W}_{m\times n} = 0_{m\times n}, \tag{B.19}$$
$$\mathbf{C}_{m\times n} \cdot \mathbf{V}_{n\times m} + \mathbf{D}_{m\times m} \cdot \mathbf{X}_{m\times m} = \mathbb{I}_m. \tag{B.20}$$

Eqs. (B.17) and (B.19) can then immediately be used to find $\mathbf{U}_{n\times n}$:

$$\begin{aligned} \mathbf{U}_{n\times n} &= \mathbf{A}_{n\times n}^{-1} - \mathbf{A}_{n\times n}^{-1} \cdot \mathbf{B}_{n\times m} \cdot \mathbf{W}_{m\times n} \\ &= \mathbf{A}_{n\times n}^{-1} + \mathbf{A}_{n\times n}^{-1} \cdot \mathbf{B}_{n\times m} \cdot \mathbf{D}_{m\times m}^{-1} \cdot \mathbf{C}_{m\times n} \cdot \mathbf{U}_{n\times n}, \qquad \text{(B.21)} \\ \Rightarrow \mathbf{U}_{n\times n} &= \left(\mathbb{I}_n - \mathbf{A}_{n\times n}^{-1} \cdot \mathbf{B}_{n\times m} \cdot \mathbf{D}_{m\times m}^{-1} \cdot \mathbf{C}_{m\times n} \right)^{-1} \cdot \mathbf{A}_{n\times n}^{-1} \\ &= \left(\mathbf{A}_{n\times n} - \mathbf{B}_{n\times m} \cdot \mathbf{D}_{m\times m}^{-1} \cdot \mathbf{C}_{m\times n} \right)^{-1}, \qquad \text{(B.22)} \end{aligned}$$

which is valid as long as the matrices $\mathbf{D}_{m\times m}$ and $\left(\mathbf{A}_{n\times n} - \mathbf{B}_{n\times m} \cdot \mathbf{D}_{m\times m}^{-1} \cdot \mathbf{C}_{m\times n} \right)$ are invertible. This result can be used to find the surface Green's function. Identifying $\mathbf{M}$ as the matrix $\left((\omega + i\delta)\mathbb{I}_{4N_z} - \mathcal{H}_{\mathbf{k}_{||}} \right)$ and using the Hamiltonian $\mathcal{H}_{\mathbf{k}_{||}}$ from Eq. (6.11) with $h_2 = 0$, we can decompose it by defining

$$\mathbf{A}_{4\times 4} = (\omega + i\delta)\mathbb{I}_4 - h_0(\mathbf{k}_{||}) = \left(G^1 \right)^{-1}, \tag{B.23}$$
$$\mathbf{B}_{4\times 4(N_z-1)} = \begin{pmatrix} -h_1 & 0 & 0 & \cdots \end{pmatrix}, \tag{B.24}$$
$$\mathbf{C}_{4(N_z-1)\times 4} = \begin{pmatrix} -h_1 & 0 & 0 & \cdots \end{pmatrix}^\dagger, \tag{B.25}$$
$$\mathbf{D}_{4(N_z-1)\times 4(N_z-1)} = \left(G^{N_z-1} \right)^{-1}. \tag{B.26}$$

Then, we can use Eq. (B.22) to find the top-left 4×4 block of the inverse of this matrix:

$$\begin{aligned} G_{00}^{N_z} = \mathbf{U}_{4\times 4} &= \Big((\omega + i\delta)\mathbb{I}_4 - h_0(\mathbf{k}_{||}) - (-h_1\ 0\ 0\ \cdots)\, G^{N_z-1}\, (-h_1\ 0\ 0\ \cdots)^\dagger\Big)^{-1} \\ &= \Big((\omega + i\delta)\mathbb{I}_4 - h_0(\mathbf{k}_{||}) - h_1 G_{00}^{N_z-1} h_1^\dagger\Big)^{-1} \end{aligned} \tag{B.27}$$

Together with the Green's function corresponding to a single layer,

$$G^1 = G_{00}^1 = \big((\omega + i\delta)\mathbb{I}_4 - h_0(\mathbf{k}_{||})\big)^{-1}, \tag{B.28}$$

we have thus found a method to iteratively calculate the surface Green's function of a system consisting of N_z layers. With this method, each iterative step adds an additional layer to the bulk Hamiltonian, while the numerical calculation of each step requires an equal amount of time. As a result, the time required to calculate the surface Green's function now only scales linearly with the number of layers N_z, which is a significant improvement over inversion of the entire matrix. It should also be noted that this iterative method is simply a clever way to calculate some components of the inverse matrix by making use of the symmetries of the matrix, and has nothing to do with physics. Consequently, the above relations are valid for any matrix of the same form as our matrix $\big((\omega + i\delta)\mathbb{I}_{4N_z} - \mathcal{H}_{\mathbf{k}_{||}}\big)$.

In the above, we assumed that the next-nearest neighbour coupling h_2 is zero. However, it is straightforward to generalize the methods to also include h_2. Following the same steps, but working with 8×8 blocks $\mathcal{G}_{ij}^{N_z}$ rather than using 4×4 blocks $G_{ij}^{N_z}$, we find

$$\begin{aligned} \mathcal{G}_{00}^{N_z} &= \left((\omega + i\delta)\mathbb{I}_8 - \begin{pmatrix} h_0(\mathbf{k}_{||}) & h_1 \\ h_1^\dagger & h_0(\mathbf{k}_{||}) \end{pmatrix} - \begin{pmatrix} -h_2 & 0 & 0 & \cdots \\ -h_1 & -h_2 & 0 & \cdots \end{pmatrix} G^{N_z-2} \begin{pmatrix} -h_2 & 0 & 0 & \cdots \\ -h_1 & -h_2 & 0 & \cdots \end{pmatrix}^\dagger\right)^{-1} \\ &= \left((\omega + i\delta)\mathbb{I}_8 - \begin{pmatrix} h_0(\mathbf{k}_{||}) & h_1 \\ h_1^\dagger & h_0(\mathbf{k}_{||}) \end{pmatrix} - \begin{pmatrix} h_2 & 0 \\ h_1 & h_2 \end{pmatrix} \mathcal{G}_{00}^{N_z-2} \begin{pmatrix} h_2^\dagger & h_1^\dagger \\ 0 & h_2^\dagger \end{pmatrix}\right)^{-1}, \end{aligned} \tag{B.29}$$

with the initial condition

$$G^2 = \mathcal{G}_{00}^2 = \left((\omega + i\delta)\mathbb{I}_8 - \begin{pmatrix} h_0(\mathbf{k}_{||}) & h_1 \\ h_1^\dagger & h_0(\mathbf{k}_{||}) \end{pmatrix}\right)^{-1}. \tag{B.30}$$

The surface Green's function we are interested in is now given by the 4×4 lop-left quarter of $\mathcal{G}_{00}^{N_z}$.

Although the above methods are already a huge improvement over brute force calculations, there is an even more efficient method, highlighted in Ref. [25], that builds on Eq. (B.27). In the following, we once again set $h_2 = 0$. For reasons that will become clear later on, we start with calculating the component $G_{10}^{N_z}$ of the bulk Green's function. Using Eqs. (B.19), (B.22) and (B.27), we find

$$\begin{aligned} \mathbf{W}_{4(N_z-1)\times 4} &= -\mathbf{D}^{-1}_{4(N_z-1)\times 4(N_z-1)} \cdot \mathbf{C}_{4(N_z-1)\times 4} \cdot \mathbf{U}_{4\times 4} \\ &= -G^{N_z-1}\, (-h_1\ 0\ 0\ \cdots)^\dagger\, G_{00}^{N_z}, \end{aligned} \tag{B.31}$$

from which it follows (by considering the top 4×4 block) that

$$\begin{aligned} G_{10}^{N_z} &= G_{00}^{N_z-1} h_1^\dagger G_{00}^{N_z} \\ &\equiv T G_{00}^{N_z}. \end{aligned} \tag{B.32}$$

Referring back to Eq. (B.27), we see that the surface Green's function corresponding to N_z layers can also be written as

$$G_{00}^{N_z} = \big((\omega + i\delta)\mathbb{I}_4 - h_0(\mathbf{k}_{||}) - h_1 T\big)^{-1}. \tag{B.33}$$

Thus, in order to find the surface Green's function, we have to find an efficient way to calculate the matrix T. We will do so by calculating the component $G_{10}^{N_z}$ in terms of the surface Green's function $G_{00}^{N_z}$ and reading off T according to Eq. (B.32).

Closely following the derivation from Ref. [25], the Green's function Eq. (B.14) can be written in the following way:

$$\begin{pmatrix} (\omega+i\delta)\mathbb{I}_4 - h_0(\mathbf{k}_{||}) & -h_1 & 0 & \cdots \\ -h_1^\dagger & (\omega+i\delta)\mathbb{I}_4 - h_0(\mathbf{k}_{||}) & -h_1 & \cdots \\ 0 & -h_1^\dagger & (\omega+i\delta)\mathbb{I}_4 - h_0(\mathbf{k}_{||}) & \ddots \\ \vdots & \vdots & \ddots & \ddots \end{pmatrix} \begin{pmatrix} G_{00}^{N_z} & G_{01}^{N_z} & \cdots \\ G_{10}^{N_z} & G_{11}^{N_z} & \cdots \\ \vdots & \vdots & \ddots \end{pmatrix} = \mathbb{I}_{4N_z}. \tag{B.34}$$

Some of the equations hidden in this expression are the equations

$$\left((\omega+i\delta)\mathbb{I}_4 - h_0(\mathbf{k}_{||})\right) G_{00}^{N_z} = \mathbb{I}_4 + h_1 G_{10}^{N_z}, \tag{B.35}$$

$$\left((\omega+i\delta)\mathbb{I}_4 - h_0(\mathbf{k}_{||})\right) G_{10}^{N_z} = h_1^\dagger G_{00}^{N_z} + h_1 G_{20}^{N_z}, \tag{B.36}$$

$$\left((\omega+i\delta)\mathbb{I}_4 - h_0(\mathbf{k}_{||})\right) G_{20}^{N_z} = h_1^\dagger G_{10}^{N_z} + h_1 G_{30}^{N_z}, \tag{B.37}$$

$$\vdots$$

$$\left((\omega+i\delta)\mathbb{I}_4 - h_0(\mathbf{k}_{||})\right) G_{N_z-1\,0}^{N_z} = h_1^\dagger G_{N_z-2\,0}^{N_z}, \tag{B.38}$$

or

$$\begin{aligned} G_{n0}^{N_z} &= \left((\omega+i\delta)\mathbb{I}_4 - h_0(\mathbf{k}_{||})\right)^{-1} \left(h_1^\dagger G_{n-1\,0}^{N_z} + h_1 G_{n+1\,0}^{N_z}\right) \\ &\equiv t_0 G_{n-1\,0}^{N_z} + \tilde{t}_0 G_{n+1\,0}^{N_z} \\ &= t_0 \left(t_0 G_{n-2\,0}^{N_z} + \tilde{t}_0 G_{n0}^{N_z}\right) + \tilde{t}_0 \left(t_0 G_{n0}^{N_z} + \tilde{t}_0 G_{n+2\,0}^{N_z}\right), \end{aligned} \tag{B.39}$$

$$\begin{aligned} \Rightarrow G_{n0}^{N_z} &= \left(\mathbb{I}_4 - t_0\tilde{t}_0 - \tilde{t}_0 t_0\right)^{-1} \left(t_0^2 G_{n-2\,0}^{N_z} + \tilde{t}_0^2 G_{n+2\,0}^{N_z}\right) \\ &\equiv t_1 G_{n-2\,0}^{N_z} + \tilde{t}_1 G_{n+2\,0}^{N_z}, \end{aligned} \tag{B.40}$$

for $n \geq 2$. The step from Eq. (B.39) to Eq. (B.40) can be repeated iteratively to find

$$G_{n0}^{N_z} = t_i G_{n-2^i\,0}^{N_z} + \tilde{t}_i G_{n+2^i\,0}^{N_z}, \tag{B.41}$$

for $n \geq 2^i$, with

$$t_i = \left(\mathbb{I}_4 - t_{i-1}\tilde{t}_{i-1} - \tilde{t}_{i-1}t_{i-1}\right)^{-1} t_{i-1}^2, \tag{B.42}$$

$$\tilde{t}_i = \left(\mathbb{I}_4 - t_{i-1}\tilde{t}_{i-1} - \tilde{t}_{i-1}t_{i-1}\right)^{-1} \tilde{t}_{i-1}^2. \tag{B.43}$$

Now we are in a position to calculate $G_{10}^{N_z}$:

$$\begin{aligned} G_{10}^{N_z} &= t_0 G_{00}^{N_z} + \tilde{t}_0 G_{20}^{N_z} \\ &= \left(t_0 + \tilde{t}_0 t_1\right) G_{00}^{N_z} + \tilde{t}_0 \tilde{t}_1 G_{40}^{N_z} \\ &= \left(t_0 + \tilde{t}_0 t_1 + \ldots + \tilde{t}_0 \ldots \tilde{t}_{i-1} t_i\right) G_{00}^{N_z} + \tilde{t}_0 \ldots \tilde{t}_i G_{2^{i+1}\,0}^{N_z}. \end{aligned} \tag{B.44}$$

For a system with $N_z = 2^{i+1}$ layers, $G_{2^{i+1}\,0}^{N_z}$ is the first component of the Green's function that does not exist. From Eqs. (B.35) to (B.38), we see that the place in which this component would appear is simply not present in the equations, and as a result we can equivalently set $G_{2^{i+1}\,0}^{N_z}$ to zero. We therefore conclude that the matrix T_i corresponding to a system with $N_z = 2^{i+1}$ layers is given by the expression

$$\begin{aligned} T_i &= t_0 + \tilde{t}_0 t_1 + \ldots + \tilde{t}_0 \ldots \tilde{t}_{i-1} t_i \\ &= t_0 + \tau_1 t_1 + \ldots + \tau_i t_i \\ &= T_{i-1} + \tau_i t_i, \end{aligned} \tag{B.45}$$

with

$$\begin{aligned} \tau_i &= \tilde{t}_0 \tilde{t}_1 \ldots \tilde{t}_{i-1} \\ &= \tau_{i-1} \tilde{t}_{i-1}. \end{aligned} \tag{B.46}$$

Thus, starting from t_0, $\tilde{t}_0$ (defined in Eq. (B.39)), $T_0 = t_0$ and $\tau_1 = \tilde{t}_0$, we can iteratively calculate T_i using Eqs. (B.42), (B.43), (B.45) and (B.46). If we then plug the resulting T_i into Eq. (B.33), we find the surface Green's function of a system consisting of $N_z = 2^{i+1}$ layers.

Even though the first iterative method that we covered is already quite efficient, this final method is even much more efficient: while each iterative step consists of more calculations and will take more time than for the first method, each step still takes equally long, and now the time required to calculate surface Green's functions only scales logarithmically with the number of layers. This is because each iteration does not simply add a layer to the bulk Hamiltonian, but instead doubles the number of layers of the bulk Hamiltonian. Consequently, with this final method it only requires 19 iterations to consider a system of over one million layers. With the first method, a million layers would require one million iterations (which would take an inconveniently long time), and inverting a four million by four million matrix by brute force would no longer be doable. Due to the extreme efficiency of the final algorithm, that is the one that we use for the calculations of Ch. 6. Finally, it should be noted that this method is once again just a very clever way of calculating components of the inverse matrix, and can be used for any matrix of the same form.

Bibliography

[1] A. P. Ramirez, "Strongly geometrically frustrated magnets," Ann. Rev. Mater. Sci. **24**, 453 (1994).

[2] J. T. Chalker, P. C. W. Holdsworth, and E. F. Shender, "Hidden order in a frustrated system: Properties of the Heisenberg Kagomé antiferromagnet," Phys. Rev. Lett. **68**, 855–858 (1992).

[3] T. H. Han, J. S. Helton, S. Chu, D. G. Nocera, J. A. Rodriguez-Rivera, C. Broholm, and Y. S. Lee, "Fractionalized excitations in the spin-liquid state of a kagome-lattice antiferromagnet," Nature **492**, 406 (2012).

[4] S. Buhrandt, *Magnetic monopoles in chiral magnets & frustrated magnetism on the swedenborgite lattice*, Ph.D. thesis, Utrecht University / University of Cologne (2015).

[5] L. Balents, "Spin liquids in frustrated magnets," Nature **464**, 199 (2010).

[6] J. Villain, R. Bidaux, J. P. Carton, and R. Conte, "Order as an effect of disorder," Journal de Physique **41**, 1263 (1980).

[7] D. D. Khalyavin, P. Manuel, J. F. Mitchell, and L. C. Chapon, "Spin correlations in the geometrically frustrated $R\mathrm{BaCo_4O_7}$ antiferromagnets: Mean-field approach and Monte Carlo simulations," Phys. Rev. B **82**, 094401 (2010).

[8] G. Aminoff, "Über ein neues Mineral von Långban," Zeitschrift für Kristallographie, Mineralogie und Petrographie **60**, 262 (1924).

[9] S. Buhrandt and L. Fritz, "Spin-liquid phase and order by disorder of classical Heisenberg spins on the swedenborgite lattice," Phys. Rev. B **90**, 020403 (2014).

[10] P. M. Chaikin and T. C. Lubensky, *Principles of Condensed Matter Physics* (Cambridge University Press, 1995).

[11] L. D. Landau, "On the theory of phase transitions," Zh. Eksp. Teor. Fiz. **7**, 19 (1937).

[12] M. E. Zhitomirsky, "Octupolar ordering of classical kagome antiferromagnets in two and three dimensions," Phys. Rev. B **78**, 094423 (2008).

[13] N. D. Mermin and H. Wagner, "Absence of Ferromagnetism or Antiferromagnetism in One- or Two-Dimensional Isotropic Heisenberg Models," Phys. Rev. Lett. **17**, 1133–1136 (1966).

[14] H. Falk, "Inequalities of J. W. Gibbs," Am. J. Phys. **38**, 858–869 (1970).

[15] J. N. Reimers, A. J. Berlinsky, and A.-C. Shi, "Mean-field approach to magnetic ordering in highly frustrated pyrochlores," Phys. Rev. B **43**, 865–878 (1991).

[16] N. Goldenfeld, *Lectures on phase transitions and the renormalization group* (Perseus Books Publishing, 1992).

[17] A. Altland and B. Simons, *Condensed Matter Field Theory* (Cambridge University Press, 2006).

[18] V. L. Ginzburg, Sov. Phys. Solid State **2**, 1824 (1960).

[19] J. E. Hoffman, K. McElroy, D.-H. Lee, K. M. Lang, H. Eisaki, S. Uchida, and J. C. Davis, "Imaging Quasiparticle Interference in $Bi_2Sr_2CaCu_2O_{8+\delta}$," Science **297**, 1148–1151 (2002).

[20] C. Kittel, *Introduction to Solid State Physics* (John Wiley & Sons, Inc., 1986).

[21] E. N. Economou, *Green's Functions in Quantum Physics* (Springer, 2006).

[22] G. D. Mahan, *Many-Particle Physics* (Plenum, 1993).

[23] E. van Heumen, S. Johnston, J. Kaas, N. de Jong, F. Massee, J. Oen, E. Rienks, A. Varykhalov, J. B. Goedkoop, Y. Huang, and M. S. Golden, "Multiband quasiparticle interference in the topological insulator $Cu_xBi_2Te_3$," (2011), arXiv:1110.4406 [cond-mat.mes-hall] .

[24] C.-X. Liu, X.-L. Qi, H. Zhang, X. Dai, Z. Fang, and S.-C. Zhang, "Model Hamiltonian for topological insulators," Phys. Rev. B **82**, 045122 (2010).

[25] M. P. López Sancho, J. M. López Sancho, and J. Rubio, "Quick iterative scheme for the calculation of transfer matrices: application to Mo(100)," J. Phys. F: Met. Phys. **14**, 1205 (1984).

[26] Y. L. Chen, J. G. Analytis, J.-H. Chu, Z. K. Liu, S.-K. Mo, X. L. Qi, H. J. Zhang, D. H. Lu, X. Dai, Z. Fang, S. C. Zhang, I. R. Fisher, Z. Hussain, and Z.-X. Shen, "Experimental Realization of a Three-Dimensional Topological Insulator, Bi_2Te_3," Science **325**, 178 (2009).

[27] M. E. J. Newman and G. T. Barkema, *Monte Carlo methods in statistical physics* (Oxford University Press, 1999).

[28] H. T. C. Stoof, K. B. Gubbels, and D. B. M. Dickerscheid, *Ultracold quantum fields* (Springer, 2008).